Department of Civil, Environmental and Geomatic Engineering

University College London

Bond of Basalt Fibre Reinforced Polymer Bars

to Geopolymer Concrete

Giulia Trabacchin

Supervisors:

Dr Mingzhong Zhang

Dr Wendel Sebastian

A thesis submitted for the degree of

Doctor of Philosophy in Sustainable Materials and Structural Engineering

November 2021

Statement of Originality

I, Giulia Trabacchin, confirm that the work presented in this thesis is my own. Where information has been derived from other sources, I confirm that this has been indicated in the thesis.

Signed: Giulia Trabacchin

Date: London, 15th November 2021

IV

Abstract

Geopolymer concrete (GPC), manufactured with industrial by-products (e.g. fly ash and slag) activated by alkaline solutions, has been considered as a promising alternative to Portland cement concrete because of its superior engineering properties and sustainable features (e.g. low CO_2 emissions and reuse of industrial wastes). Basalt fibre reinforced polymer (BFRP) bars have been recently introduced to replace steel reinforcement owing to their light weight, excellent mechanical properties, and high corrosion resistance. The studies on the structural performance of GPC reinforced with BFRP bars have proved its suitability as a substitute for conventional reinforced concrete, while the bond between GPC and BFRP bars which plays a critical role in structural performance and design has not been explored to date.

This thesis aims to investigate experimentally, numerically and theoretically the bond of BFRP bars to GPC. Pull-out tests were conducted to study the bond behaviour of BFRP bars in GPC in terms of bond stress-slip response, bond strength, and failure mechanisms and estimate the effects of different factors including bar diameter, embedment length, bar surface and compressive strength of concrete. Afterwards, 3D finite element modelling of pull-out process using concrete damage plasticity model for GPC and cohesive zone model for BFRP bar-GPC interface was carried out to gain insight into the stress distribution along the bar and failure mechanisms. Furthermore, a theoretical bilinear bond stress-slip model validated with experimental data was proposed to analytically describe the bond between BFRP bars and GPC. Finally, a parametric study was performed to estimate the effects of different factors on the bond behaviour of BFRP bars in GPC, based on which a formula for predicting the bond strength was developed and compared with experimental data and recommendations from existing standard codes for FRP reinforced concrete.

This research provides an in-depth understanding of the interactions between BFRP bars and GPC. The experimental results show that the bond stress-slip curve of BFRP bars to GPC was bilinear, with three characteristic stages (ascending, peak and descending). The bond was mainly offered by mechanical interlocking of the bar ribs against the concrete lugs. The FE and theoretical analysis suggested a nonlinear distribution of the bond stress along the embedded portion of the bar. The proposed bond strength prediction equation, which considered the influence of bar diameter and embedment length, displayed good agreement with the experimental data.

Impact Statement

Geopolymer concrete (GPC) reinforced with basalt fibre reinforced polymer (BFRP) bars has been introduced as a promising alternative to steel reinforced Portland cement concrete (PCC) because of the superior engineering properties, sustainability and durability characteristics of these two innovative materials. However, the full acceptance of BFRP reinforced GPC in the construction industry is contingent on a critical understanding of its structural performance. In particular, within all the engineering aspects, the bond behaviour is a fundamental feature as it assures the load transfer. Yet, to date, the investigation on the bonding mechanisms between BFRP bars and GPC is still lacking. Thus, the main aim of this thesis is to critically characterise the bond behaviour of BFRP bars to GPC, focusing on the effects of different factors on the bond stress-slip relationship, bond strength and failure modes.

From the academic perspective, this study fills some critical gaps existing in the research field. Firstly, the bond interaction between BFRP bars and FA-GGBS based GPC, which has not been addressed before, is studied experimentally considering several influencing factors, providing a database for reference in future studies. Secondly, this study provides the first-ever tensile and bond stresses distribution over the bar length, investigated numerically and analytically using a bilinear bond stress-slip model, offering new insight into the interaction mechanisms between BFRP bars and GPC. Lastly, the analytical and finite element model could be adopted to predict and optimise the overall structural performance of GPC reinforced with BFRP bars.

From the industrial perspective, this research can benefit the future development of sustainable and durable infrastructures by encouraging the application of eco-friendly cement-free concrete and non-corrosive reinforcement. For instance, it is known that the current application of BFRP bars and GPC is limited because of the lack of their inclusion in standard design codes where understanding the bond interaction is a crucial aspect of their development. Thus, based on the findings of this study, the bond strength of BFRP bars in GPC can be accurately determined using the prediction equation proposed. Once further validated with a broader data sample, the empirical equation could be included in the available standards for the service life design of FRP reinforced concrete infrastructures.

Acknowledgements

First, I express my gratitude to my supervisors, Dr Mingzhong Zhang, for the opportunity to work on such a challenging and innovative project, and Dr Wendel Sebastian, for his experienced advice and valuable suggestions. The inspiring technical and philosophical discussions allowed me to deepen my knowledge and grow as a researcher and a person. I also extend my appreciation to Prof. Dina D'Ayala and Prof. Julia Stegemann for their guidance towards the MPhil upgrade. For the support with the experimental program, I gratefully acknowledge Prof. Xiaochun Fan from the Wuhan University of Technology (China), the technical staff from UCL Chadwick Building laboratories, including Warren Gaynor, Leslie Irwin, Dr Shi Shi and Dr Judith Zhou, and Dr. Eral Bele from UCL Mechanical Engineering. Special appreciation goes to Dr Sadjad Naderi for his insightful support and to my research group colleagues who endured this long process with me.

As "It takes a village to raise a child", it is impossible to include all the names of the talented and inspiring people I met during this journey. I am thankful for your encouragement, friendship and advice. The past years have been precious because I shared them with you.

Finally, I express my deepest gratitude to my husband Tommaso, my parents, Maria Grazia and Stefano, and my sister Alessia, for the unconditional love and encouragement they enlightened me with along this path.

x

"γνῶθι σεαυτόν - Know Thyself"

Table of Contents

XV

List of Figures

XIX

List of Tables

List of Abbreviations

AFRP	Aramid fibre reinforced polymer
AL	Alkaline activator
BFRP	Basalt fibre reinforced polymer
CDP	Concrete damage plasticity
CFRP	Carbon fibre reinforced concrete
COV	Coefficient of variation
DAMAGEC	Compressive damage variable
DAMAGET	Tensile damage variable
DIC	Digital image correlation
DOFS	Distributed optical fibre sensing
FA	Fly ash
FB	Failure bar
FE	Free end of the bar
FEM	Finite element model
GFRP	Glass fibre reinforced polymer
GGBS	Ground granulated blast-furnace slag
GPC	Geopolymer concrete
LE	Loaded end of the bar
LR	Loading rate
LVDT	Linear variable differential transducer
PCC	Portland cement concrete
PO	Bar pull-out failure
RC	Reinforced concrete
SC	Splitting of concrete
QUADS	Quadratic nominal stress criterion
SD	Standard deviation
SDEG	Stiffness degradation variable
SH	Sodium hydroxide
SP	Superplasticiser
SS	Sodium silicate

List of Symbols

A_b	Cross-sectional area of the bar
A_{tr}	Area of transversal reinforcement
A_τ	Area underneath the ascending branch (mBPE model)
c	Concrete cover
c_1, c_2	Integrating constants for ascending branch
c_3, c_4	Integrating constants for descending branch
D	Scalar damage of slip
DF	Distance from free end
d	Stiffness degradation variable
d_c, d_t	Damage variable in compression and tension
d_{cs}	Smaller of the distance from the closest concrete surface to the centre of the bar being developed, or two-thirds the centre-to-centre spacing of the bars being developed, mm (CSA-S806) and (CSA-S6)
δ_{mi}	Effective relative displacement
E	Elastic modulus
E_b	Elastic modulus of FRP bar
E_c	Elastic modulus of concrete
E_s	Elastic modulus of steel bar
e	Eccentricity
F	Curve-fitting parameter (Malvar's model)
f_{bod}	Design bond strength of concrete (JSCE)
f_c	Compressive strength of concrete
f_{ck}	Characteristic value for concrete compressing strength
f_{cr}	Cracking strength of concrete
f_{ct}	Splitting tensile strength of concrete
f_f	Tensile strength of FRP bar
f_u	Tensile strength of the bar
f_y	Yield strength of steel bar
G	Curve-fitting parameter (Malvar's model)
G_f	Fracture energy

h	Fitting parameter
IE	Internal energy
K_b	Bond stress concentration factor
K_c	Ratio of the second stress invariant on the tensile meridian to that on the compressive meridian at initial yield for any given value of the pressure invariant
KE	Kinetic energy
k	Bond stiffness
k_{nn}	Bond normal stiffness
k_{ss}, k_{tt}	Bond shear stiffness
k_1	Bar locator factor (CSA-S806-02) and (CSA-S6-14)
k_2	Concrete density factor
k_3	Bar size factor
k_4	Bar fibre factor
k_5	Bar surface profile
k_6	Coating factor (CSA-S6-14)
k_7	Bar size factor (CSA-S6-14)
L_d	Development length
l_d	Embedment length
l_s	Side length of cubic specimen
n	Fitting parameter
p	Curve-fitting parameter (mBPE model)
P, P_m	Pull-out load, maximum pull-out load
r	Slip-ductility ratio
S	Shear modulus of elasticity
s_c	Correction to be applied to the measured loaded end slip
s_d	Slip corresponding to the descending branch
s_e	Slip measured at loaded end prior correction
s_m	Slip correspondent to maximum bond stress
$s_{m,FE}$	Slip correspondent to maximum bond stress at the free end
$s_{m,LE}$	Slip correspondent to maximum bond stress at the loaded end
s_r	Curve-fitting parameter (CMR model)
s_u	Ultimate slip

t_n, t_s, t_t	Traction components in normal and tangential directions
t_n^0, t_s^0, t_t^0	Critical tractions in normal and tangential directions
u_{t0}	Cracking displacement
V_f	Fibre volume fraction
x_p	Coordinate of the peak stress along the bar axis
α	Curve-fitting parameter (mBPE model)
α_1, α_2	Modification factors (JSCE)
β	Curve-fitting parameter (CMR model)
γ	Top modification factor (ACI)
ε_c	Compressive strain
ε_c'	Strain value at the peak stress in compression
ε^{el}	Elastic strain
$\varepsilon_c^{in,h}$	Inelastic hardening strain in compression
ε^{pl}	Plastic strain
ε_u	Rupture strain
ε_y	Yield strain
μ	Viscosity
σ_{b0}	Initial equibiaxial compressive yield stress
σ_c	Compressive stress
σ_{c0}	Concrete initial yield stress in compression
σ_{cu}	Concrete compressive ultimate stress
σ_m	Maximum longitudinal tensile stress of the bar
σ_r	Radial bond stress
σ_{t0}	Concrete tensile failure stress
τ, τ_m	Bond shear stress, Maximum bond stress
$\tau_{ons,FE}$	Bond stress at the onset of slip at the free end
$\tau_{ons,LE}$	Bond stress at the onset of slip at the loaded end
ψ	Dilatation angle

xxx

Chapter 1 Introduction

1.1 Background and research significance

Steel reinforced Portland cement concrete (PCC) is the most widely used construction material globally, because of its advantages, such as cheap ingredients, easy preparation process, ability to be moulded into different shapes, and high compressive strength. However, as the binding material in concrete, Portland cement is responsible for around 7% of global CO_2 emissions due to the elevated temperature (~1450 °C) needed for its manufacturing (Barcelo et al., 2014; Olivier et al., 2016). Another issue with reinforced concrete (RC) is its inadequate durability due to corrosion of the steel reinforcement, which can reduce the steel bar cross-section and cause concrete cracking, deteriorating the RC structures (Raoul et al., 2018). In this regard, maintenance, repair and shortening of the RC structures service life have an estimated cost of $2.5 trillion per year worldwide (Broomfield, 1997; Bowman et al., 2016). Thus, it is urgent to develop and provide novel, sustainable and durable RC structures for society.

Reducing the construction industry impact on the environment is the main goal of sustainable development, which considers issues such as whole life cycle, materials selection and use, recycling, and waste and energy minimisation (Adetunji et al., 2003). To improve the sustainability of concrete, alternative binding materials to Portland cement have been proposed. Among them, geopolymer, also known as alkali-activated materials, made from industrial by-products such as fly ash (FA) and ground granulated blast-furnace slag (GGBS), has been applied in different fields, from waste management to construction industry (Shi et al., 2011). The use of geopolymer in concrete can help reduce CO_2 emissions by up to 80% compared to PCC (Davidovits, 1993). FA and GGBS are widely available. For instance, developing countries such as India and China generate more than 100 million tonnes of FA every year (Dwivedi and Jain, 2014). Existing literature highlights favourable properties for the use of geopolymer concrete (GPC) as a construction material, which exhibits good mechanical properties and high durability in terms of good resistance to corrosion, fire, radiation, acid, and sulphate attacks (Fernández-Jiménez and Palomo, 2006). Scientific research on GPC has significantly increased over the past decades, but knowledge about the structural performance of GPC is still limited, and standard specifications for the design of the GPC mixtures and the structural performance of reinforced GPC have not been implemented yet (Nuruddin et al., 2016; Li et al., 2019). Therefore, more research on the engineering properties and the structural

behaviour is necessary to encourage the application of eco-friendly cement-free GPC as a substitute for PCC in civil infrastructure.

To address the corrosion issue of reinforcing steel and enhance the durability of RC, in recent years, basalt fibre reinforced polymer (BFRP) bars, which fibres are obtained from natural volcanic rock, have been introduced as an alternative reinforcement. In the BFRP composites, the basalt fibres, responsible for load-carrying capacity, are embedded in a polymeric matrix such as vinyl-ester and epoxy resins that transfer the load to the fibres. Besides their sustainability features (Pearson et al., 2011; Wu et al., 2012; Mara et al., 2014; Mohamed et al., 2021), BFRP bars possess promising engineering properties such as light weight, high tensile strength, excellent resistance to acids and corrosion, and to a wide range of temperatures (Serbescu et al., 2014). In addition, BFRP bars are less expensive than carbon fibre reinforced polymers (CFRP) (INFOMINE Research Group, 2007; Lopresto et al., 2011; Inman et al., 2017) and display better durability in an alkaline environment compared with glass fibre reinforced polymer (GFRP) bars (Lee et al., 2014). Moreover, BFRP bars have been successfully applied in PCC (El Refai et al., 2015b; Liu et al., 2017). Hence, because of its improved sustainability and durability, BFRP bar reinforced GPC is a viable alternative to conventional steel reinforced PCC (Fan and Zhang, 2016b, 2016a; Fan et al., 2021). Even though the available studies on the structural performance of GPC reinforced with BFRP bars offer promising results, the knowledge is still limited to the structural behaviour of elements.

To ensure the full acceptance of GPC reinforced with BFRP bars as a composite for civil engineering applications, it is essential to understand key engineering aspects, including the properties of the two materials and their bond behaviour. The bond assures the composite action of the materials that cooperate in the structure load-carrying capacity. It also influences the crack width and spacing (CEB-FIP, 2007). The load transfer between reinforcement and concrete is generally characterised by the local bond stress-slip curve, which can be determined using pull-out or beam-end tests (Sturm and Visintin, 2019). To date, many studies have been conducted to investigate the bond stress-slip behaviour of steel reinforced GPC and BFRP reinforced PCC systems, while the bond between BFRP bars and GPC has not been explored yet. For instance, it has been observed that the bond strength of steel rebars in GPC is approximately 10% to 40% higher than that in PCC, which can be attributed to the more homogeneous and dense microstructure of GPC in comparison with PCC, leading to higher tensile strength and bond strength for similar grades of concrete (Shi and Xie, 1998; Lee and Van Deventer, 2004; Fernández-Jiménez and Palomo, 2006). The bond stress-slip curve for steel reinforced GPC was similar to that of steel reinforced PCC (Castel and Foster, 2015).

Thus, GPC is not only more sustainable than PCC but may also offer superior structural performance.

The bond stress-slip behaviour of fibre reinforced polymer (FRP) in PCC is more complex than steel rebars, owing to the potential influences of fibre type, resin type, anisotropic feature and surface treatment of FRP (CEB-FIP, 2000, 2007; Serbescu et al., 2014). Previous pull-out tests on BFRP reinforced PCC indicated that BFRP bars developed an average bond strength of 75% of GFRP bars but higher residual stress (El Refai et al., 2015b). Excellent bond durability of BFRP bars in PCC was proven where after 45 days of exposure to alkaline environment, vinyl-ester-made BFRP bars and GFRP bars experienced similar bond strength retention (92.4%), while the bond stress retention of epoxy-made BFRP bars was relatively higher (139.5%) (Dong et al., 2018b). Several other studies (Altalmas et al., 2015; El Refai et al., 2015a; Hassan et al., 2016; Dong et al., 2018b) also demonstrated that BFRP bars have comparable or higher bond durability than the similar GFRP bars. The superior bond properties of BFRP bars support their application as internal reinforcement in concrete, although they have not been included in the design codes available for other FRP reinforcements (JSCE, 1997; CAN/CSA S806-12, 2012; ACI 440.1R, 2015; CAN/CSA-S6-14, 2017a).

The use of strain gauges or distributed optical fibre sensors (Henault et al., 2012; Lee and Mulheron, 2012; Marchand et al., 2016; Rolland et al., 2018; Malek et al., 2019) was proved to have limited efficacy for the experimental assessment of bond stress distribution over the embedded length (Lee and Mulheron, 2015). As a complement, analytical and numerical studies can help to gain insights into the bond development and damage evolution during pull-out loading.

In summary, the following aspects have not been exhaustively addressed in the literature:

- Mechanical characterisation of these two innovative materials;
- Experimental estimation of the bond behaviour of BFRP bars to GPC;
- Finite element analysis of bond of BFRP bars to GPC;
- Analytical modelling of the bond stress-slip relationship of BFRP bars in GPC;
- Development of safe and economical design guidelines for BFRP bars and GPC.

Consequently, given the current lack of understanding in the field, the study of bond behaviour between BFRP bars and GPC is of particular interest and is the focus of this research. Fig. 1.1 briefly summarises the motivations of this study. As a result of this work, valuable information on the bond between BFRP bars and GPC will be provided to designers, supporting the application of this new system in structural engineering.
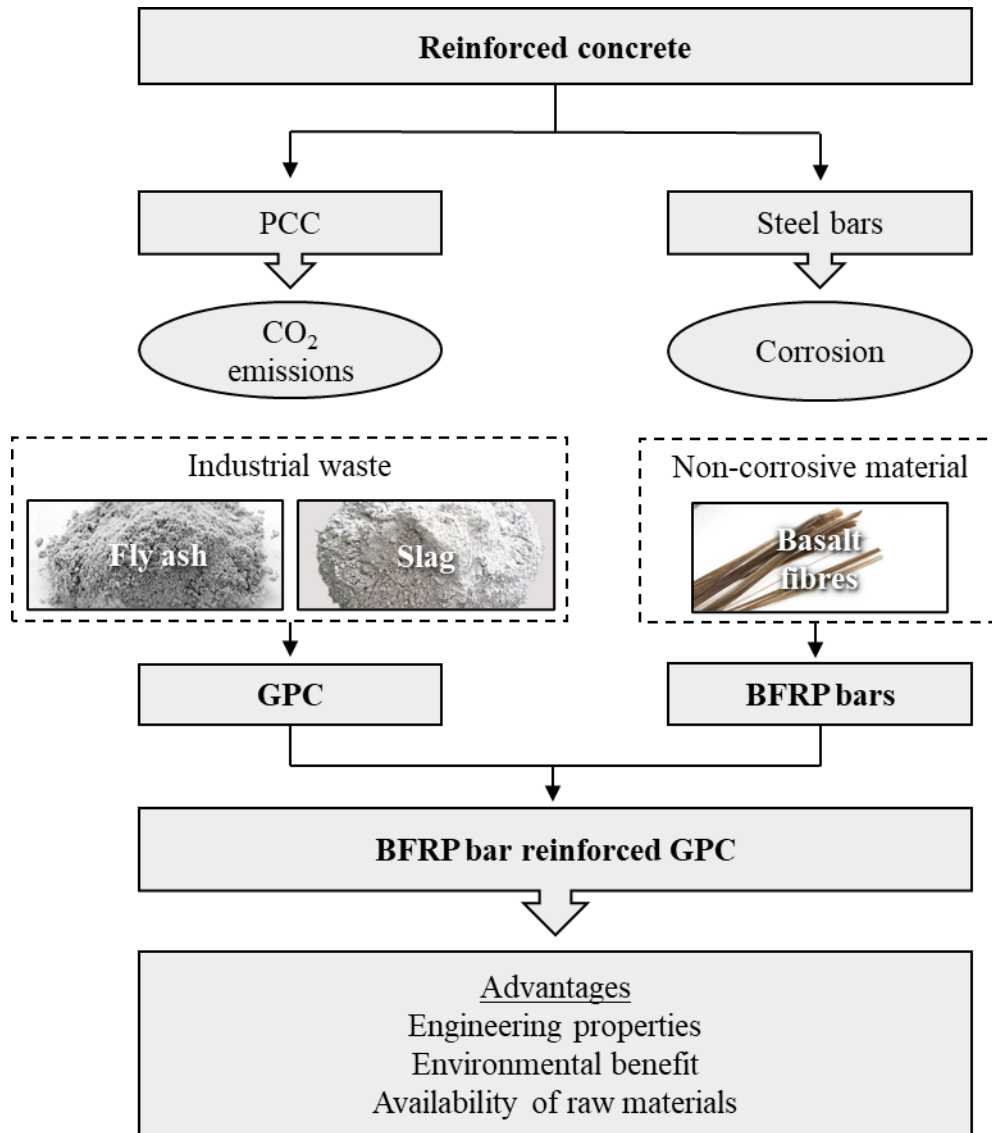
Fig. 1.1 Major motivations of this research.

1.2 Research aim and objectives

This study aims to investigate the bond behaviour of BFRP bars to GPC. As a result, this research contributes to promoting the application of these materials as a novel building system, i.e. GPC reinforced with BFRP bars, by offering guidance on predicting the bond strength, thus enriching the sustainable construction industry. The main objectives of this study are as follows:

- To experimentally characterise the physical and mechanical properties of the newly developed materials used, i.e. BFRP bars made of continuous basalt fibres embedded in vinyl-ester resin and GPC made of alkali-activated fly ash-slag cured at ambient temperature.

- To experimentally investigate the bond behaviour of BFRP bars to GPC with pull-out tests, in terms of average bond stress-slip curves and failure modes and evaluate the

effects of key influencing parameters, such as bar diameter, embedded length, bar surface configuration and concrete compressive strength on the bond behaviour.

- To develop a 3D finite element model of pull-out, based on which the tensile stress, bond stresses, slip and strain distribution along the embedded length of the bar were studied and the effects of different factors on the bond behaviour were estimated.

- To develop an algebraic bilinear model that mathematically describes the experimental bond stress-slip curve. The tensile stress and bond stress distribution over the BFRP bar embedded in GPC were analytically assessed, which have not been addressed elsewhere.

- To propose a BFRP bars to GPC bond strength prediction equation, the applicability of which is examined against experimental pull-out test results and predictions by the existing design codes for FRP reinforcement.

1.3 Methodology

To achieve the objectives mentioned above, the strategy adopted is given as follows:

- Experimental characterisation of the materials used in the research was performed. First, the engineering properties of the GPC, including workability, compressive strength, splitting tensile strength and elastic modulus, were measured using the current standard codes for PCC and the data were compared with existing prediction models. Then, the cross-section, tensile strength and modulus of elasticity of the BFRP were evaluated according to the current test methods and the results were compared with the standards available for FRP reinforcement in concrete.

- Forty-eight pull-out samples were constructed, of which thirty-six test results were presented to study the bond behaviour BFRP bars embedded in GPC cubes by considering bond stress-slip relationship, bond strength, bond ductility, failure modes and the influence factors such as bar diameter, embedment length, bar surface configuration, and concrete compressive strength. In addition, the bond performance of steel bars in GPC was tested for comparison.

- A 3D finite element model of the pull-out of BFRP bars in a GPC cube was developed using ABAQUS, which is flexible enough to include "user-defined" material properties and bond stress-slip law. A study was conducted on the bond properties that cannot be detected through experimental pull-out tests, e.g. the stress and strain distribution over the bar embedded length and the hoop splitting stress across the concrete cube section. Moreover, a parametric analysis was run on the key variables.

- An analytical bilinear model was developed to describe the bond stress-slip relationship of BFRP bars in GPC and predict the bond properties along the bonded length.
- A parametric study was run to identify the influencing variables on the bond strength. Consequently, a bond strength prediction equation was proposed based on the influencing parameters and validated with experimental data and design provisions.

1.4   Outline of this thesis

According to the objectives previously described, this thesis consists of seven chapters, as schematically shown in Fig. 1.2 and detailed as follows:

Chapter 1 introduces the research topic, providing insight on background, aim, objectives and novelty of the research program. The research strategy followed to achieve these objectives is also presented.

Chapter 2 presents a critical review of the relevant literature where the main challenges and limitations were identified. First, a summary of the properties of GPC and BFRP bars was provided. Then, the bond interaction of steel to GPC and FRP bars to PCC and GPC was discussed in terms of available experimental, analytical and numerical studies.

Chapter 3 discusses the methods and results of the experimental characterisation of the material properties. The details of test specimens and test setups are given. In addition, the results were compared with existing standards and prediction models.

Chapter 4 presents the experimental procedure, and the results of the pull-out tests carried out as part of the comprehensive investigation of the bond between BFRP bars and GPC. The results and discussions included average bond stress-slip curve, bond strength, bond ductility and failure modes, considering the effect of several parameters on the bond performance. In addition, the pull-out results of steel bars in GPC were also presented for comparison.

Chapter 5 details the development of a 3D nonlinear finite element model of the pull-out of BFRP bars in GPC cubes using ABAQUS. The model was calibrated through sensitivity analysis and validated against experimental data. Finally, the model was used to analyse the stress distributions and run a parametric study.

Chapter 6 develops an analytical bilinear bond stress-slip model for BFRP bars in GPC. The model was validated against experimental and numerical results. Thus, the bond strength influencing parameters were identified with a parametric study. Consequently, a bond strength prediction equation was proposed and discussed in comparison with experimental data and design code provisions.

Chapter 7 summarises the main contribution of this work and presents concise conclusions of the findings obtained in the thesis. In addition, the limitations of the current work were critically reviewed, and some recommendations for future research were given.
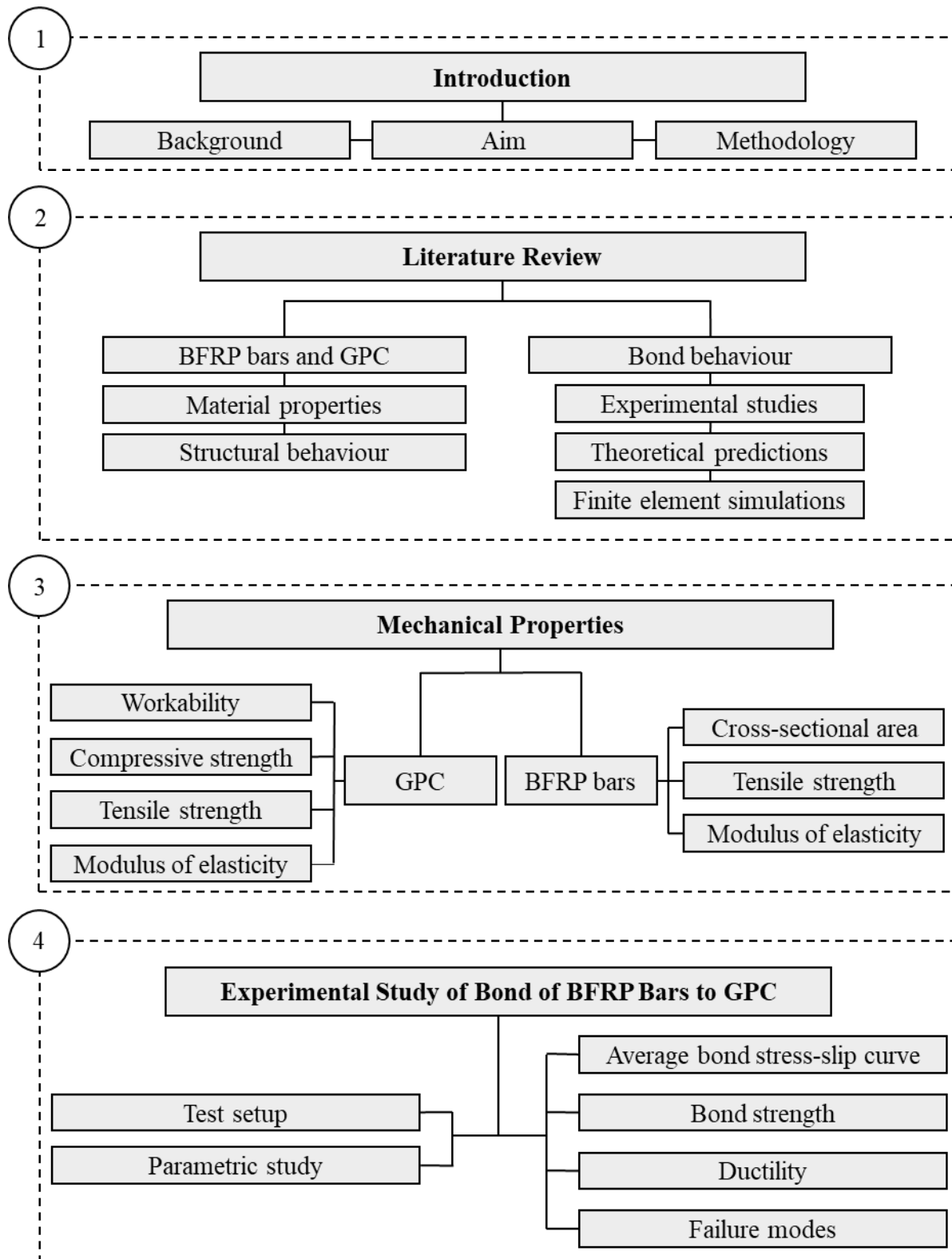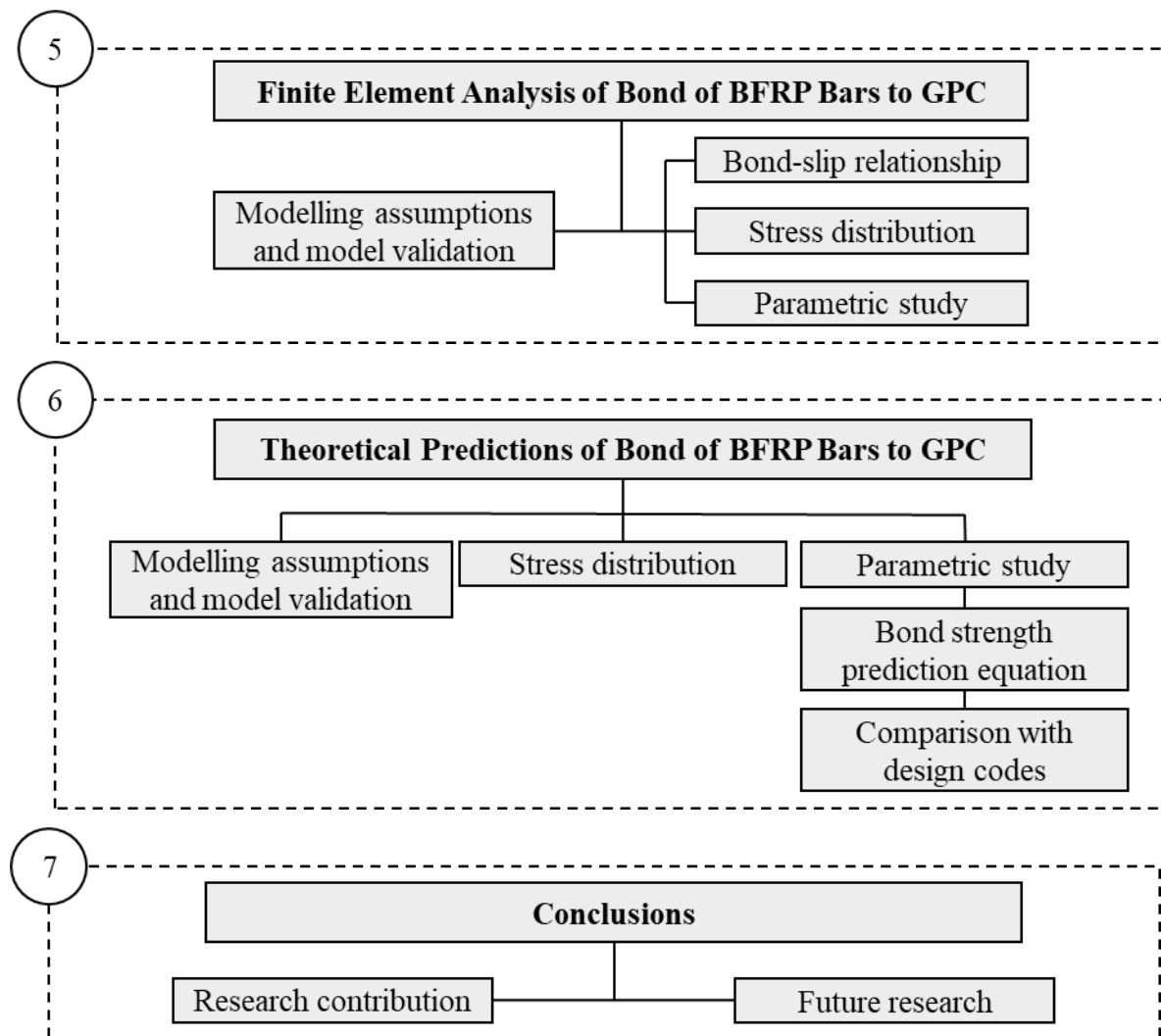
Fig. 1.2 Schematic summary of the thesis outline.

Chapter 2 Literature Review

2.1 Introduction

This chapter provides a critical review of the available studies concerning the bond of BFRP bars in GPC to summarise the recent advances and identify the research gaps and limitations in this field of research. First, a brief introduction of the motivation supporting the development of these two innovative materials is given. Afterwards, an analysis of the bond behaviour of FRP reinforcement to concrete is presented, and the available experimental studies are discussed considering the main influencing parameters. Lastly, the theoretical and numerical models currently available for studying the bond between FRP bars and concrete are reviewed.

2.2 GPC as an alternative to cement-based concrete

2.2.1 Constituents of GPC

Steel reinforced PCC is the most widely used construction material in the world. However, concerns are rising over the environmental impact of PCC, which is responsible for around 7% of global CO_2 emissions (Barcelo et al., 2014) and the use of an extensive amount of virgin materials (Rashad, 2013). Thus, it urges adopting sustainable concrete alternatives. For instance, GPC, also known as inorganic polymer concrete or alkali-activated concrete, is made from recycled industrial by-products, including FA and GGBS (Shi et al., 2011). As other aluminosilicate precursors, FA and GGBS can be used as binders when activated by alkaline liquids, obtaining a cementitious material with similar or improved features to PCC (Fernández-Jiménez and Palomo, 2003; Provis and Bernal, 2014). In addition, the use of GPC was demonstrated to reduce the CO_2 emissions by 80% compared to PCC (Davidovits, 1993).

In particular, FA is a fine powder obtained as a by-product of coal combustion in electric generation power plants. The global production of FA is about 375 million tons per year, with a disposal cost of \$20-\$40 per tonne (Dwivedi and Jain, 2014). GGBS is the slag from iron-producing blast-furnaces, rapidly quenched in water, dried and ground into a fine powder. Globally around 300-360 million tonnes of GGBS are produced annually (Rashad, 2018). Although these binders are broadly available, due to being by-product materials, some variations in their composition may be observed across different countries, given the variance in their industrial manufacturing processes. Therefore, some basic requirements must be met to ensure suitability for their use as binding material in concrete (Nath and Sarker, 2012). The precursors can be activated with alkaline solutions, including sodium hydroxide ($NaOH$) and sodium silicate (Na_2SiO_3), used individually or combined, to form the geopolymer paste,

which binds the aggregates (Hardjito et al., 2005). As per PCC, coarse and fine aggregates occupy ~ 75-80% by mass in GPC (Hardjito and Rangan, 2005). In addition, the workability could be improved by adding extra water and a superplasticiser.

2.2.2 Engineering properties of GPC

It is worth noting that several influencing factors can strongly affect the engineering properties of GPC, including constituents (e.g. binders and alkaline solutions), mix proportions (e.g. alkaline activator to binder (AL/B) ratio, fly ash to slag (FA/GGBS) ratio, sodium silicate to sodium hydroxide (SS/SH) ratio), and curing processes (e.g. ambient or heat curing) (Provis and Bernal, 2014). Fig. 2.1 displays a schematic summary of the constituents and influencing factors of GPC. For instance, FA-based concrete requires an elevated curing temperature (60 – 85 °C) because of the lower reactivity of FA, while GGBS-based concrete presents rapid setting time and low workability (Puertas et al., 2000; Palacios et al., 2008).
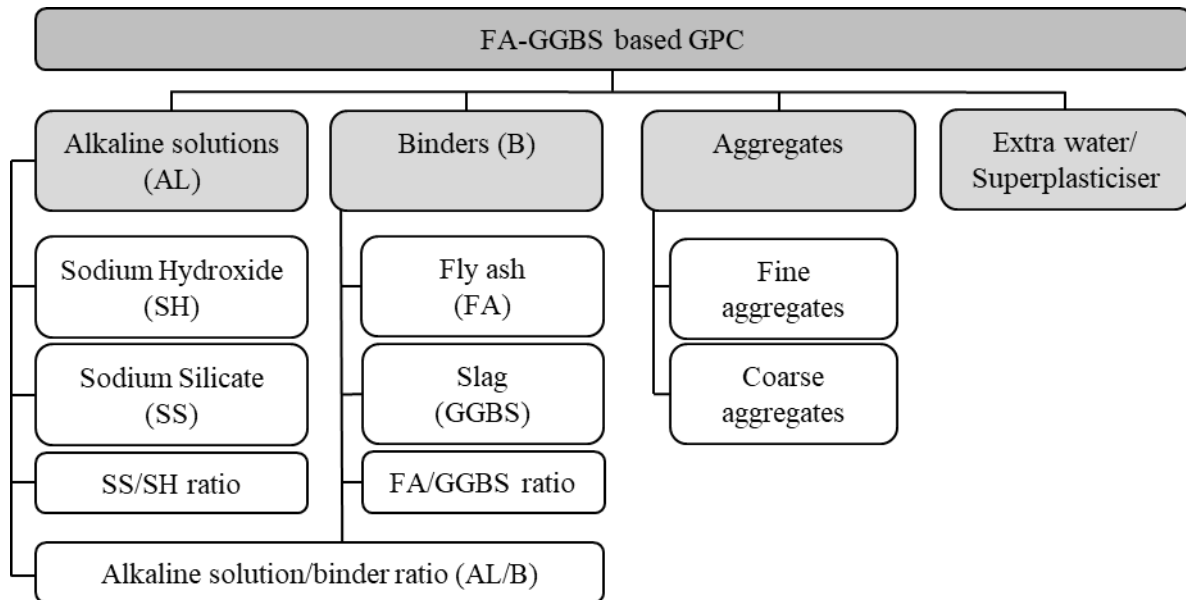
Fig. 2.1 GPC constituents and influencing factors.

Thus, previous studies were conducted on the mix proportions of FA-GGBS based GPC to achieve optimal engineering properties for infrastructure applications at ambient curing conditions. In FA-GGBS based GPC, it was found that increasing the AL/B ratio reduced the concrete compressive strength but increased workability and setting time; thus, an AL/B ratio of 0.4 was recommended for optimal fresh and hardened properties (Nath and Sarker, 2014). Considering the FA/GGBS ratio, as shown in Fig. 2.2, it was found that the 28 d compressive strength of FA-GGBS based GPC increased ~ 10 MPa with every 10% increment of slag replacement of the total binder (Nath and Sarker, 2014). However, by increasing the slag content, the workability and the setting time were reduced, as shown in Fig. 2.2a and b,

respectively (Nath and Sarker, 2012; Al-Majidi et al., 2016). To obtain setting time, workability and compressive strength suitable for casting different concrete structural members, a slag replacement of 15-20% of the total binder was suggested (Lee and Lee, 2013; Nath and Sarker, 2014). Moreover, the tensile strength of GPC was found to be superior to that of PCC with similar compressive strength (Rangan et al., 2005). It was also proved that the splitting tensile strength and the elastic modulus of GPC could be predicted from the concrete compressive strength using the existing design provisions available for PCC (Fang, 2020).

(a) (b)

(c)
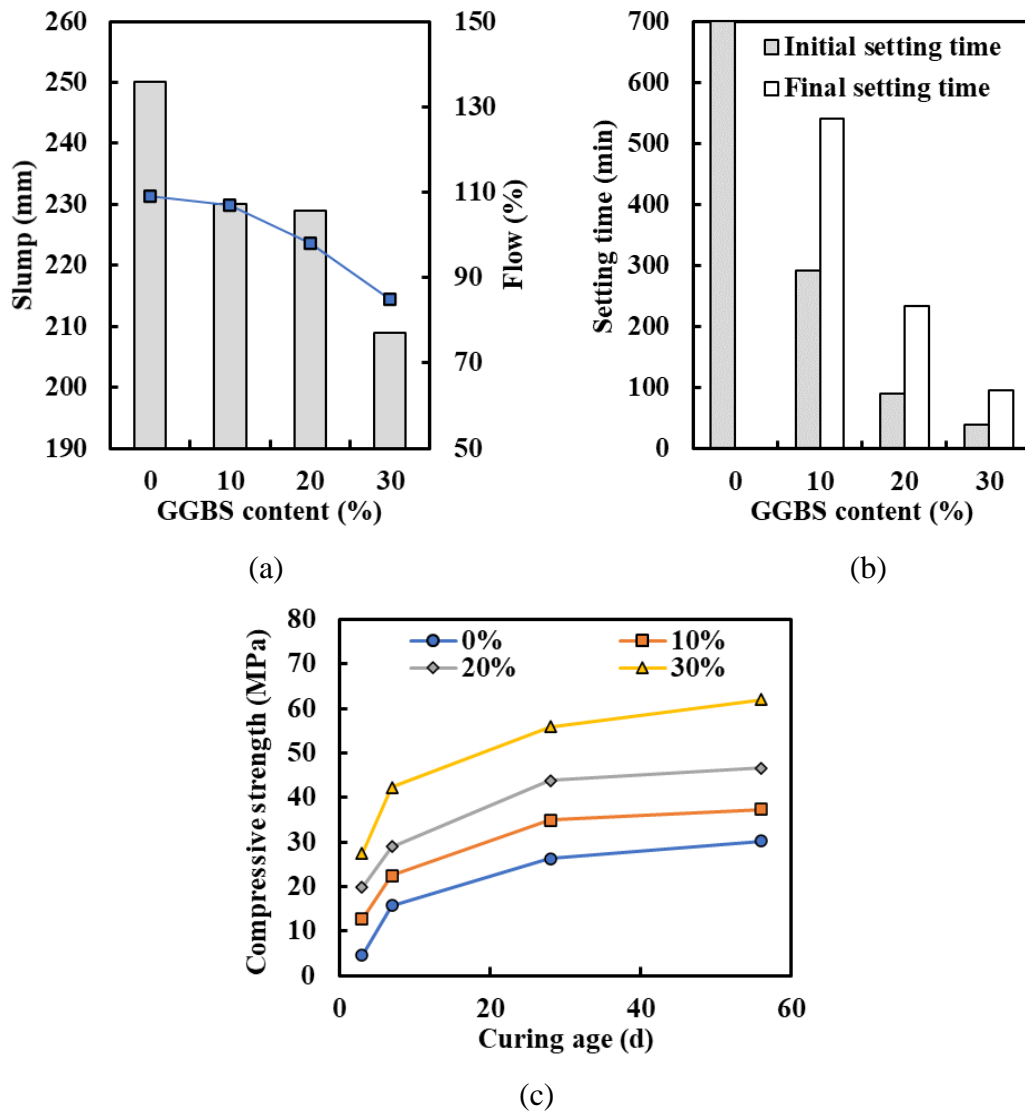
Fig. 2.2 Effect of GGBS content on GPC engineering properties (Nath and Sarker, 2014): (a) workability; (b) setting time; (c) compressive strength development.

Besides the superior engineering properties, GPC was found to be between 11% (Janardhanan et al., 2016) and 27% (Oyebisi et al., 2019) cost-effective compared to PCC. Furthermore, the use of FA-GGBS based GPC was estimated to have a global warming impact 80% lower than PCC or GPC made of other precursors (Van Deventer et al., 2010; Habert et

al., 2011; Turner and Collins, 2013). In conclusion, GPC is considered a promising alternative to PCC because of its superior engineering properties and sustainable features (e.g. low CO_2 emissions and reuse of industrial wastes). Yet, GPC presents some disadvantages. For instance, the variability of the industrial by-products used as raw materials makes it challenging to propose a standard mix design for optimal performance in terms of strength, workability and curing conditions; thus, GPC has not been included in standard design codes. Also, as the alkaline activators, i.e. sodium hydroxide and sodium silicate, are harmful to humans, their preparation and handling require special training and risk assessment.

2.2.3 Bond behaviour of steel bars to GPC

Extensive research in the last decades contributed to the knowledge of the steel to concrete bonding mechanisms and the influencing factors (CEB-FIP, 2000). In this section, a brief review of the studies on the bond of steel to GPC is presented to demonstrate that the steel bar-GPC system exhibits similar bond behaviour of steel bars to PCC. A more detailed introduction of the bond behaviour and a review of experimental studies on bond interaction of FRP bars in concrete is provided in Section 2.4.

Experimental tests revealed that, similarly to steel reinforced PCC, higher bar diameter (d_b) reduces the bond between steel bars and GPC. For instance, Sofi et al. (2007a) performed beam-end tests and direct pull-out tests on steel bars in GPC, which indicated that the normalised bond strength increased with a reduction of the bar size. Also, Kim and Park (2015), by increasing the steel bar diameter from 10 mm to 25 mm, observed a decrease in the average bond strength from 23.06 MPa to 17.26 MPa.

In regards to the mechanical properties of concrete, for steel reinforced PCC elements, the bar surface ribs are sufficiently strong, and consequently, the concrete surrounding the bar is considered the weak part of the interface (CEB-FIP, 2000). The localised pressure given by the ribs is bearded by the portion of concrete within these indentations, making the concrete compressive and shear strength fundamental properties to ensure enhanced mechanical interlock during the pull-out test. Moreover, the concrete tensile strength resists the radial component of bond forces, delaying the crack opening and avoiding the splitting failure. For both steel reinforced PCC and GPC, it was observed that increasing the concrete compressive strength (f_c) delays the pull-out and splitting failure, consequently increasing the bond strength (Sarker, 2010, 2011). However, because of the soluble silicate, GPC achieves a denser and stronger interfacial transition zone (ITZ) that increases the concrete splitting tensile strength (Topark-Ngarm et al., 2014), inducing the steel to GPC bond strength to be 10% (Castel and

Foster, 2015) to 40% (Fernández-Jiménez and Palomo, 2006) higher than PCC. Other studies attributed no considerable influence on the bond strength to the GPC compressive strength (Kim and Park, 2015; Bilek et al., 2017). As the research on the topic leads to no joint agreement, further research is needed to assess if, for the same concrete grade, GPC shows higher bond performance than OPC. Furthermore, it should be confirmed if the compressive strength has similar effects on PCC and GPC samples. It is also worth noting that heat curing affects the development of the mechanical properties of GPC and, consequently, the bond performance (Krishnaraja et al., 2014; Topark-Ngarm et al., 2014; Castel and Foster, 2015). However, this topic is irrelevant for the current study as novel mix proportions were used (Fang et al., 2018; Fang, 2020), which allowed the GPC to be cured at ambient temperature.

In regards to the confinement, as for PCC, in steel reinforced GPC, the transverse pressure offered by sufficient confinement (i.e. concrete cover and transverse confinement) delays the splitting failure and increases the frictional force on the steel to concrete interface, increasing the bond strength and reducing the slips (Chang, 2009; Sarker, 2011). A thicker concrete cover increases the confinement offered and allows higher force transfer. However, above a certain cover thickness, the increase of bond strength is limited (Rao, 2014). The cover thickness also influences the failure mode as low thickness causes splitting failure, while a thicker cover leads to bar pull-out. In addition, the confinement provided by the concrete cover could be inadequate to prevent the splitting failure, and transversal reinforcement may be necessary to prevent the propagation of splitting cracks (Ganesan and Indira, 2014).

In conclusion, the bond interaction between steel bars and GPC was demonstrated to be similar or improved compared to that of steel reinforced PCC. However, more research is required to clearly identify the effects of the influencing parameters on the bonding mechanisms.

2.3 BFRP bars as an alternative to steel rebar

2.3.1 Constituents of BFRP bars

Another issue with RC is the inadequate durability due to corrosion of the steel bars, which has an estimated global cost of $2.5 trillion (Broomfield, 1997; Bowman et al., 2016). In response to this challenge, BFRP bars, derived from natural volcanic rock, were recently introduced to replace steel reinforcement owing to their lightweight, excellent mechanical properties, together with high corrosion resistance, and a wide range of working temperatures (Serbescu et al., 2014).

To manufacture BFRP bars, the quarried basalt rocks are melted in furnaces at elevated temperatures (~1400 - 1700 °C), and continuous filaments of basalt fibres are pultruded and embedded into a polymeric matrix, such as epoxy and vinyl-ester resin, as shown in Fig. 2.3 (Militky and Kovacic, 1996; INFOMINE Research Group, 2007). Fig. 2.4 displays the microstructure of BFRP bars obtained by observing the cross-sectional area with a scanning electronic microscopy (SEM) (Ali et al., 2019). The figure shows that BFRP bars are made of three phases: the continuous basalt fibres, the resin matrix in which the fibres are embedded and the interface zone between the two. As per other FRP composites, the fibres determine the strength and stiffness of the composite along their direction while the resin binds the fibres together, transfers the stress between them and protects their surface from abrasion, impact and aggressive environments (CEB-FIP, 2007).
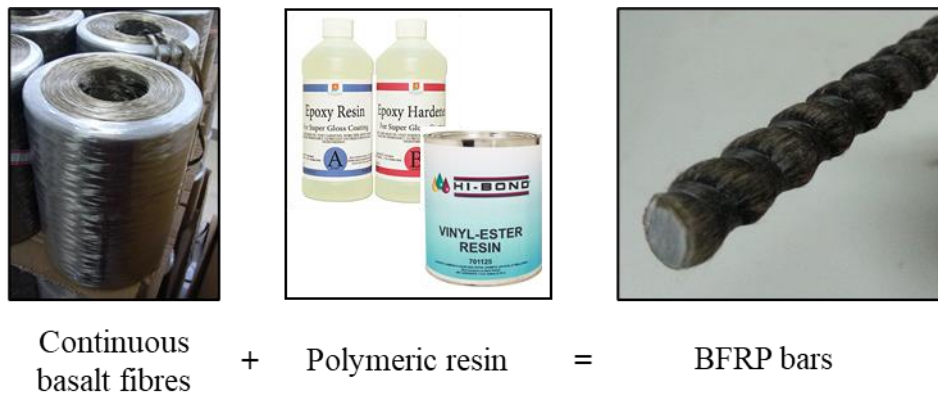
Fig. 2.3 BFRP bars constituents (adapted from Wu et al. (2015a)).
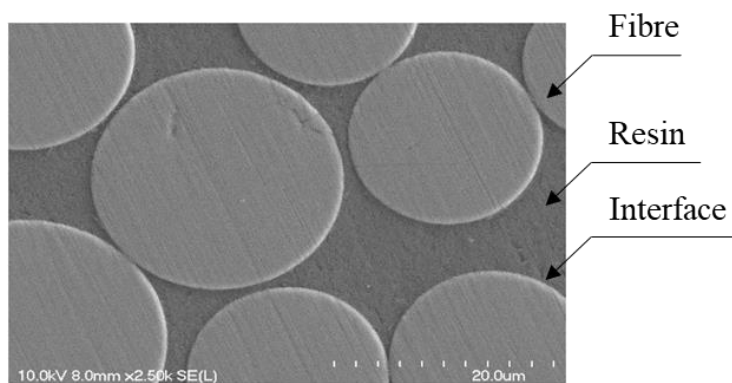
Fig. 2.4 Micrograph of BFRP bar cross-section (Ali et al., 2019).

2.3.2 Engineering properties of BFRP bars

Therefore, due to their composite nature, BFRP bars exhibit mechanical properties considerably different from traditional steel, which can vary significantly depending on the raw

materials (fibre volume fraction, resin type), geometry (bar size, external treatment) and manufacturing process (curing, possible voids and defects) (Patnaik et al., 2012; Banibayat and Patnaik, 2015). Unlike steel bars, BFRP bars display a linear elastic stress-strain relationship with an almost constant elastic modulus until the rupture point, without any yielding nor ductility before failure. The BFRP bar elastic modulus (E_b) ranges between 30 GPa and 80 GPa, considerably lower than that of steel, increasing the expected deformations for FRP RC structures (Patnaik et al., 2012; El Refai et al., 2015b; Elgabbas et al., 2015; Fan et al., 2017; Ali et al., 2019; Alnajmi and Abed, 2020; Liu et al., 2020). The literature also suggests that the BFRP bars tensile strength (f_f) is in the range of 800 and 1680 MPa, higher than that of steel reinforcement, and 20% higher than E-glass fibres composite, as shown in Fig. 2.5 (Wu et al., 2012, 2015b). The rupture strain (ε_u) was found to range between 2.63 and 3.15% (Smarter Building System, 2017; Albarrie, 2018). In addition, it was found that higher bar diameter affects the tensile strength of the bar due to several phenomena. Firstly, the number of defects increases in bigger cross-sectional areas (Bank, 2006; Sooriyaarachchi, 2006). Secondly, the non-uniform distribution of normal stress through the bar cross-section, also called shear lag effect, is more evident with higher bar sizes (CEB-FIP, 2007). Thus, only an indicative range of values, generally provided by the manufacturer, can be given to characterise the BFRP bars mechanical properties, which are summarised in Table 2.1. Furthermore, BFRP bars are anisotropic due to the fibre orientation, exhibiting a longitudinal axis stronger than the transversal one. The low shear strength, ranging between 293 MPa and 344 MPa (Elgabbas et al., 2015), is due to low interlaminar shear strength between layers, which depends on the fibre-matrix interface.
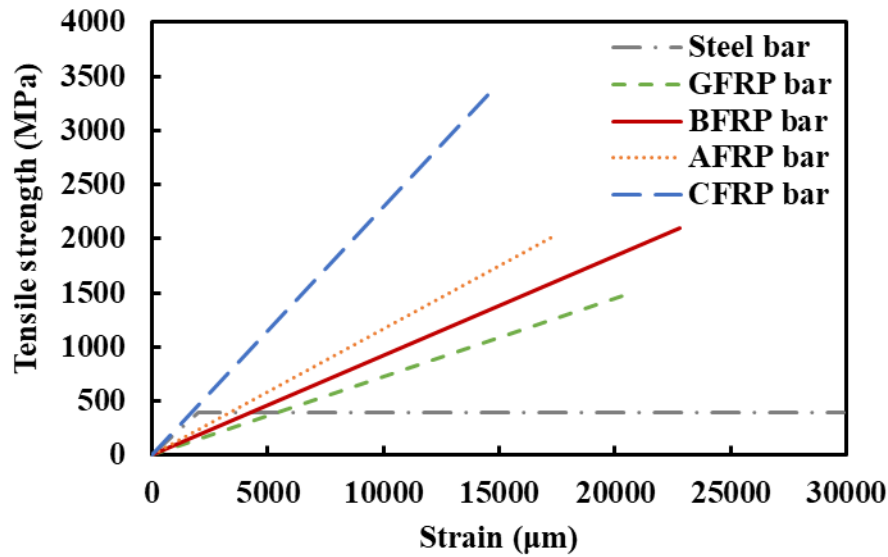
Fig. 2.5 Stress-strain relationship of different bars (Wu et al., 2012).

Given the alkaline nature of GPC, the durability properties of BFRP bars in aggressive environments are crucial aspect to be considered. A durability test of BFRP bars of 6-mm and 12-mm diameter after 9 weeks of immersion in alkaline solutions at 55°C found superior alkaline resistance of the BFRP bars compared to GFRP bars with a tensile strength retention of 60% and 51%, respectively (Wu et al., 2015b). In addition, a BFRP layer was used in a similar study to protect GFRP bars while bathed in an alkaline solution for 120 days (Li et al., 2015). This evidenced that the thicker the BFRP protective layer was, the more protection was assured to the GFRP bar, where a 5-mm protective BFRP layer drastically reduced the degradation effect of the alkaline solution on tensile properties. Even though the literature suggests improved durability of BFRP bars in an alkaline environment compared to GFRP bars, a more extensive investigation should be conducted to assess the long term effect on the mechanical properties retention of BFRP bars exposed to the GPC pore solution.

Table 2.1 Typical tensile properties of reinforcing bars of different materials (ACI 440.1R, 2006; CAN/CSA S806-12, 2012).

	f_y (MPa)	f_f (MPa)	E_b (GPa)	ε_y (%)	ε_u (%)
Steel	260 to 517	483 to 690	200	1.4 to 2.5	6.0 to 12.0
BFRP	-	800 to 1680	30.0 to 80.0	-	2.6 to 3.1
GFRP	-	483 to 1600	35.0 to 51.0	-	1.2 to 3.1
CFRP	-	600 to 3690	120.0 to 580.0	-	0.5 to 1.7
AFRP	-	1720 to 2540	41.0 to 125.0	-	1.9 to 4.4

It is also worth noting that the coefficient of thermal expansion (CET) of FRP reinforcement has different values for longitudinal and transverse directions and depends on the type and amount of fibres and the resin. The CET represents the response of a material subjected to different temperatures, describing how the heating or cooling would result in tension or compression stress in reinforced concrete members. For BFRP, the linear CET is ~ $8.0 \times 10^{-6}/℃$, similar to the GFRP bars, which CET ranges from 6.0 to $10.0 \times 10^{-6}/℃$ (Smarter Building System, 2017). Since the CET of concrete varies between 7.2 and 10.8 $\times 10^{-6}/℃$, the BFRP bars are suitable for reinforcing purposes. Furthermore, BFRP bars are dimensionally stable over a wide range of temperatures thanks to reduced thermal expansion and reduction, and thus their applicability is extended if compared to steel reinforcement or other types of FRP reinforcements (Adhikari, 2009; Aydin, 2018).

The main disadvantage of BFRP bars, and more generally of FRP reinforcement, is their brittle nature, which leads to several repercussions in their design and applications. For instance, as BFRP bars fail abruptly with no yielding nor warning before rupture, the design philosophy for flexural members differs substantially from that of steel reinforced concrete elements (ACI 440.1R, 2015). While steel-reinforced concrete sections are commonly designed to ensure tension-controlled behaviour, the non-ductile behaviour of FRP reinforcement necessitates a reconsideration of this approach, where a compression-controlled behaviour is more desirable for flexural members reinforced with FRP bars. A flexural member does exhibit some inelastic behaviour before failure by experiencing concrete crushing before tensile rupture of the FRP reinforcement. Yet, both compression-controlled and tension-controlled sections are acceptable in the design of flexural members reinforced with FRP bars, provided that strength and serviceability criteria are satisfied. To compensate for the lack of ductility, the member should possess a higher reserve of strength. For this reason, the safety coefficients should thus be higher compared to those adopted in traditional steel reinforced concrete design. Furthermore, BFRP bars cannot be bent, as usually done with steel reinforcement. Thus, for BFRP longitudinal reinforcement, some head anchors are applied at the extremities to increase the bonding (Maranan et al., 2015b), while BFRP stirrups are pultruded with their characteristic shape rather than being bent on site.

Despite the fact that the existing codes on fibre reinforced polymer (FRP) reinforcement lack the description of BFRP properties as a recent composite type, several studies (Adhikari, 2009; Lopresto et al., 2011; Elgabbas et al., 2015) confirmed that the physical and mechanical properties of the BFRP bars meet the requirements of the standard codes ACI 440 (2006) and

CSA S806 (2012) for generic structural FRP bars. Therefore, to enhance the confidence towards their use as internal reinforcement in concrete, BFRP bars should be included in the standard codes. However, to do so, further research is required to fully understand and standardise the physical, mechanical and durability properties of BFRP bars. It is worth pointing out that the bond performance of BFRP bars to PCC was discussed in Sections 2.4.3.

2.4 Experimental studies of bond behaviour of FRP bars to concrete

The bond of reinforcement to concrete is a key property that strongly influences the structural performance of RC structures, as the load-bearing depends on the shear stress generated by different mechanisms along the bar surface (CEB-FIP, 2000). The bond effectiveness guarantees serviceability, ductility, and structural capacity. Design, fabrication process, mechanical properties of the materials and environmental conditions determine the bond strength and failure; thus, several studies have been carried out to understand the impact of such factors on bond. This section introduces the bond behaviour, the test methods and the influencing factors and provides a detailed review of experimental studies on the FRP to concrete interaction.

2.4.1 Test methods

The most common tests performed for evaluating the bond include direct pull-out tests (with centric and eccentric bar in the concrete sample), beam end tests, simple beam specimen, and splice tests, which details are graphically summarised in Fig. 2.6 (CEB-FIP, 2007). Each method displays advantages and disadvantages, yet external measuring arrangements provide only an average bond stress-slip relationship, as discussed in the following sections. Furthermore, a complete investigation including different tests is necessary to characterise the bond behaviour under different stress conditions (Pecce et al., 2001).

Within the test methods, the pull-out is economical, easy to perform, and helpful in comparing the bonding efficiency of different samplings (RILEM TC, 1994). However, some limitations of this test method should be considered. Firstly, the pull-out test does not represent the actual bond stress development since, during the test, the bar is tensed, and the concrete is compressed, whereas, during the structure's life, both materials are subjected to the same stress. Secondly, the confinement provided by the compressed concrete could enhance the bond performance of the samples overestimating the bond strength. Thirdly, the thickness of the concrete cover provides further confinement, which may delay the failure due to the splitting of concrete. Thus, the results of pull-out tests should be considered as an upper bound value for the bond stress-slip performance (Focacci et al., 2000). Nevertheless, this test method

provides valuable information on the contribution offered by different parameters, and it allows to observe several types of failure.

Beam-end test (Fig. 2.6b) provides more realistic measures of the bond strength as both concrete and reinforcement are subject to tension, yet its preparation and testing is more challenging (ACI 408R, 2003). Simple beam (Fig. 2.6c) and beam splice (Fig. 2.6d) tests are also conducted to estimate the bond strength accurately and determine the splice and development length. As the main focus of this research was to conduct a parametric study assessing the influence of the dominant parameters on the bond behaviour, the centric pull-out test was identified as the most suitable method to achieve this purpose. However, different tests should be carried out for a comprehensive understanding of the bonding between BFRP bars to GPC.

(a)   (b)   (c)   (d)
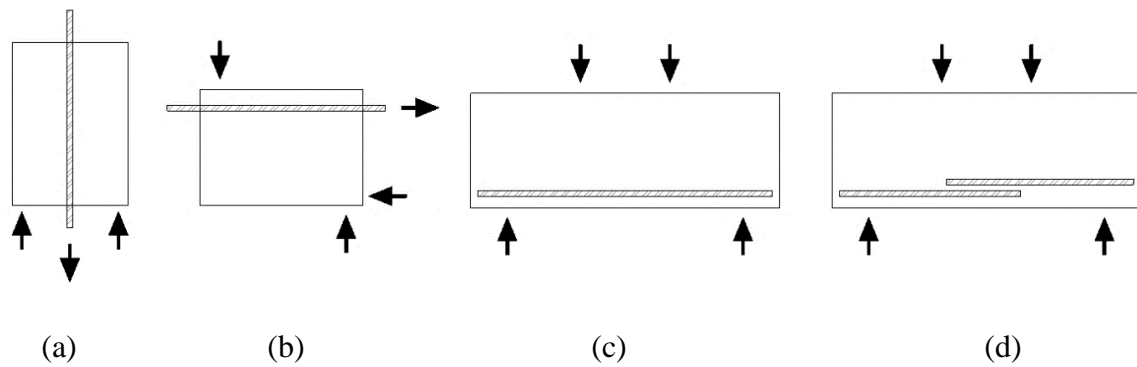
Fig. 2.6 Different bond test methods for reinforcement in concrete: (a) pull-out; (b) beam-end; (c) simple beam; (d) splice.

2.4.2   FRP-concrete interaction

During pull-out load, the longitudinal forces acting on the reinforcement are transferred to the surrounding concrete through several mechanisms defined as bond (CEB-FIP, 2000). As these forces change along the length of the bar embedded in the concrete, the difference in strains within reinforcement and concrete leads to their relative displacement, also called slip. It has also been observed that due to highly localised strains, the slips are more concentrated in the concrete layers closest to the reinforcement, called interface.

During pull-out tests, the experimental data collected are the pull-out force and the bar slips. Thus, a common way to define the bond behaviour is the bond stress-slip curve ($\tau - s$), obtained by assuming a constant distribution of bond stress along the bar embedded portion. The average bond stress of a bar in concrete under tensile force is calculated as the pull-out force over the contact surface area and may be written as follows:

$$\tau = \frac{P}{\pi\, d_b\, l_d} \tag{2.1}$$

where τ is the bond stress (MPa), P is the pull-out load (N), d_b is the nominal diameter of the bar (mm) and l_d is the embedment length (mm). The average bond strength (τ_m) is calculated by dividing the maximum pull-out load (P_m) over the bar surface area in contact with the concrete. The relative displacement of the bar is measured with reference to the undisturbed concrete, as shown in Fig. 2.7.
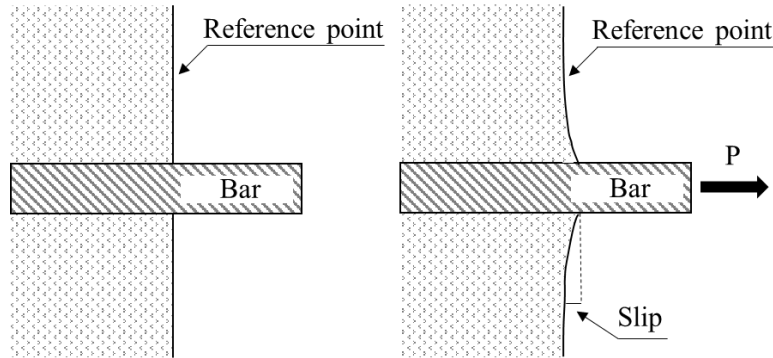
Fig. 2.7 Relative bar displacement (CEB-FIP, 2000).

While the bond of steel to concrete is well established, the bond of FRP to concrete still requires investigation. This is because FRP bars are relatively novel, exhibit anisotropic and linear elastic behaviour, and are characterised by various compositions, surface treatments, and properties. In particular, the interaction between FRP bars and concrete differs from the well-known steel to concrete due to different properties that FRP bars exhibit, including:

- Reduced modulus of elasticity;
- Reduced shear stiffness;
- Reduced shear strength of the resin matrix, which limits the strength of the surface deformations of the bar.

The ongoing research aims to understand the mechanisms involved in the bonding of FRP to concrete, including the bond failure mode and the influence of the main parameters involved. To achieve this, similarly to the steel to concrete interaction, the bond stress-slip curve obtained by pull-out tests of short embedded length samples is used for describing the FRP to concrete interaction (CEB-FIP, 2000), as shown in Fig. 2.8.

As per steel, FRP plain bars exhibit low bond strength, mainly governed by adhesion between the reinforcement and the surrounding concrete or by the interlaminar shear strength between the bar layers. Consequently, smooth bars develop slip at a very early stage after the adhesion is lost, and their bond failure is characterised by bar pull-out. For deformed surface, the stress-slip curve is distinguished as follows (CEB-FIP, 2000):

Stage I: at the beginning of the test, the force is transferred by chemical adhesion, and almost no slip is recorded even if highly localised stresses arise close to the ribs.

Stage II: by increasing the load, the adhesion is lost. The bearing stress due to the deformations of the surface against the surrounding concrete causes microcracks and enable slips, as shown in Fig. 2.9. However, as the deformations of FRP bars appear "softer" than the ribs on the steel bars, the opening of microcracks is considered delayed, suggesting a better bond behaviour at this stage.

Stage III: with a higher load, the slip increases, and so do the bearing stresses. The concrete crushed between the lugs offers interlocking. Higher load induces the longitudinal cracks to spread radially. The radial component of the bond forces is balanced against the ring of tensile stress (hoop stress) developed in the surrounding concrete. If the tensile stress exceeds the tensile strength of the concrete, longitudinal cracks appear along the reinforcement. When longitudinal cracks propagate and reach the surface, the specimen breaks suddenly because of concrete splitting, as shown in Fig. 2.10a. If more confinement is provided by a higher transverse reinforcement or thicker concrete cover, splitting is prevented, and the longitudinal cracks remain limited to a portion surrounding the bar, leading to pull-out failure.

Stage IV: if sufficient resistance is provided against splitting, for instance, in the case of short embedded length, the bond stress reaches the maximum bond strength, and the bond fails due to bar pull out, as shown in Fig. 2.10b.

Stage V: After the peak bond strength is reached, the bearing mechanism is lost, and the residual bond stress mainly depends on friction, which depends on the transverse pressure. Concrete shrinkage and bar roughness favour friction.
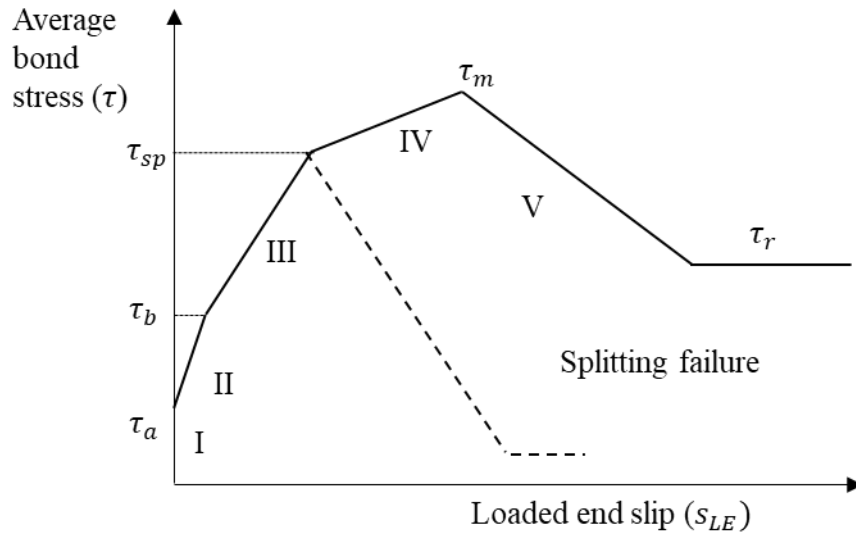
Fig. 2.8 Typical average bond stress-loaded end slip curve of an FRP bar embedded in concrete (CEB-FIP, 2000).
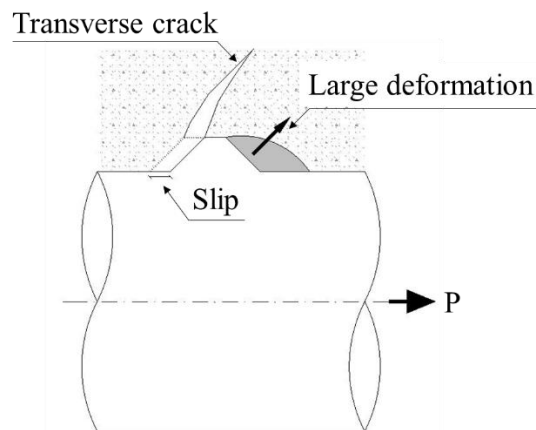
Fig. 2.9 Bar-concrete slip and wedging action of the bar (CEB-FIP, 2000).

Thus, four types of failure are possible, depending on the concrete strength and shear strength of the bar surface:

- Shearing off part or all the bar surface deformations: unlike steel bars, the bond strength is not controlled by concrete strength but by the interlaminar shear strength between layers of fibres or by the shear strength of the bar deformations;

- Concrete shear failure: the concrete is crushed in front of the bar ribs, and the bond strength depends on the shear strength of concrete;

- Combined mode: with an intermediate level of concrete strength, a combined mode is likely to occur;

- Squeeze through: due to low stiffness in the radial direction, the bar could squeeze through the concrete, transferring the force only because of friction.

If the bond strength is higher than the tensile strength of the bar, the specimen fails due to bar rupture, an example of which is given in Fig. 2.10c. In this case, the interface between bar and concrete is still intact, and the maximum bond strength has not been reached.

(a)   (b)

(c)
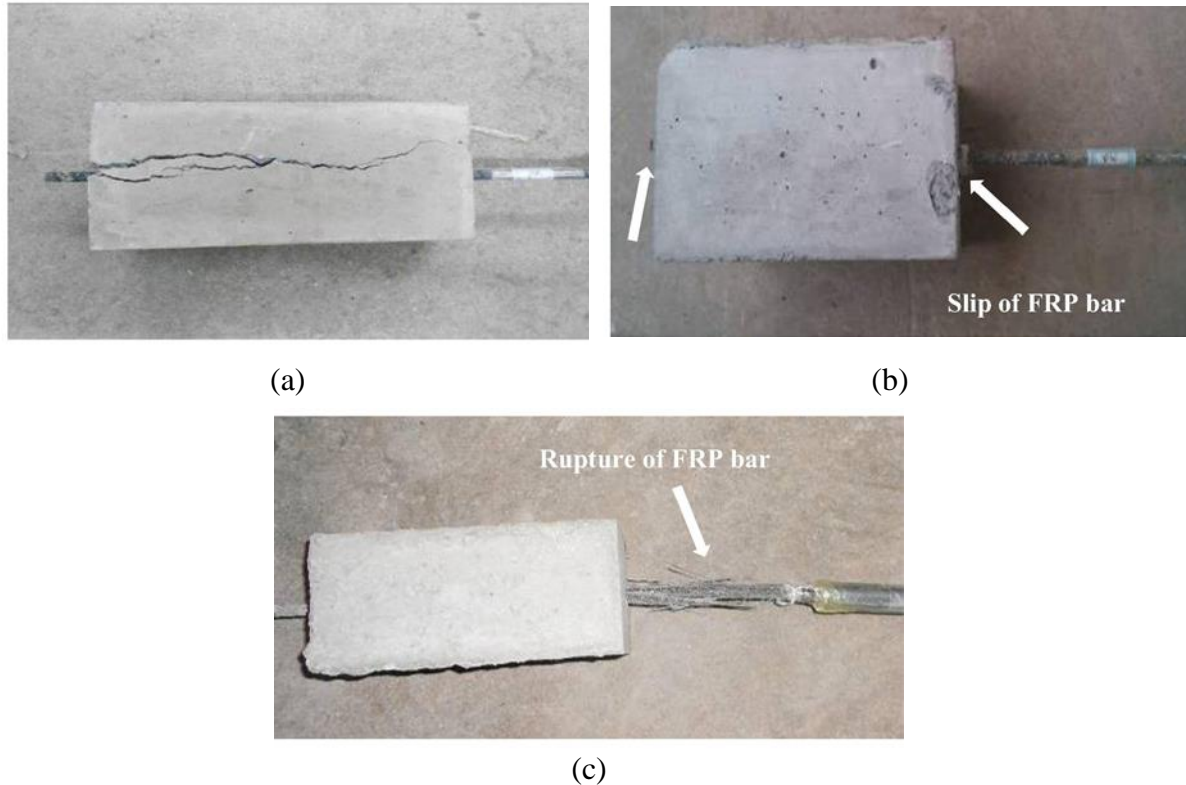
Fig. 2.10 Failure modes of specimens during pull-out test: (a) concrete splitting; (b) bar pull-out; (c) bar rupture (Li et al., 2017).

Thus, the shape of the bond stress-slip curve is related to the bond performance offered by the bar and the surrounding concrete, and three key aspects should be considered for its evaluation (Hao et al., 2009):

- Initial bond stiffness: this is the slope of the first part of the curve, defined as the secant slope at 50% of the maximum bond strength (Hamad, 1995). High stiffness express strong collaboration between bar and concrete as the bond stress transferred is high while the relative slip developed is limited;

- Peak bond strength: this point of the curve expresses the maximum load transferred by the bonding action between reinforcement and concrete. The higher this load is, the most the two components of the section are collaborating for bearing the load;

- Descending branch of the curve after the peak: the softening branch reflects the speed of bond failure. A low descending slope assures ductile failure of the bond, while higher

slopes describe a more brittle and sudden failure, exhibited, for example, by the abrupt delamination of the sand coated external layer.

2.4.3 Parameters influencing the bond of FRP reinforcement to concrete

As the load transferring mechanisms between FRP and concrete differ from those developed between steel bars in concrete, the factors influencing the bond behaviour between FRP and concrete are expected to be different or vary their impact on the bond. The available experimental studies on the bond behaviour of BFRP bars to concrete were summarised in Table 2.2, including the influencing factors investigated and the failure modes observed. However, the studies on BFRP bars to concrete are limited. Thus, this section presents more generally the influence that bar, concrete and environmental parameters have on the bond behaviour of FRP bars in PCC and GPC, assuming that similar behaviour is expected to be observed in the interaction between BFRP bars to PCC and GPC.

Table 2.2 Experimental studies on bond behaviour of BFRP bars to concrete.

Reference	Bars	Concrete	Test	Parameters	d_b	l_d	f_c	Failure mode
El Refai et al. (2015b)	BFRP GFRP	PCC	Pull-out	Fibre	8 mm	$5d_b$	50 MPa	PO, SC, BF
				Resin type (epoxy and vinyl-ester)	10 mm	$7d_b$		
				Diameter	12 mm	$10d_b$		
				Embedment length		$15d_b$		
Liu et al. (2017)	BFRP	Recycled aggregate concrete reinforced with basalt fibres	Pull-out	Concrete compressive strength	16 mm	$5d_b$	30 MPa 40 MPa 50 MPa	PO, SC
Liu et al. (2020)	BFRP Steel	PCC	Pull-out	Bar surface configuration (round rib, rectangular rib, cross-winding rib, spiral-winding rib)	12 mm	$5d_b$	30 MPa	PO, SC, FB
Michaud and Fam (2021)	BFRP	PCC	Notched beams	Concrete compressive strength Diameter Embedment length	4 mm 6 mm 8 mm	$9d$ to $108d_b$	35 MPa 55 MPa 75 MPa	
Wang et al. (2015)	BFRP	Engineered cementitious composite PCC	Pull-out	Diameter Embedment length	4 mm 10 mm 16 mm	$2.5d_b$ $5d_b$ $10d_b$ $15d_b$	46 MPa 49 MPa	PO, SC, FB

Table 2.2 Experimental studies on bond behaviour of BFRP bars to concrete. (Continued)

Reference	Bars	Concrete	Test	Parameters	d_b		l_d	f_c	Failure mode
Wang et al. (2019)	BFRP	Reinforced coral aggregate concrete	Pull-out	Concrete compressive strength Diameter Bar surface configuration	6 8 10 12 16 20	mm mm mm mm mm mm	$5d_b$ $10d_b$ $12d_b$	15 MPa 20 MPa 30 MPa	PO, SC, FB
Wei et al. (2020)	BFRP	PCC Sea sand concrete	Pull-out	Type of concrete	7.6 mm		$5d_b$	43 MPa	PO
Ovitigala (2012)	BFRP Steel	PCC	Pull-out Hinged beam	Bar diameter Embedment length	6 10 13 16 25	mm mm mm mm mm	$10d_b$ $15d_b$ $20d_b$ $30d_b$	36 MPa	PO, SC, FB
Yang et al. (2018)	BFRP CFRP Steel	Seawater coral aggregate concrete	Pull-out	Fibre Bar surface configuration (deep rib, shallow rib) Diameter	8 12 mm	mm	$2.5d_b$ $5d_b$ $7.5d_b$	36 MPa	PO, SC

Note: BFRP (basalt FRP bars); GFRP (glass FRP bars); CFRP (carbon FRP bars); PCC (Portland cement concrete); d_b (bar diameter); l_d (embedment length); f_c (concrete compressive strength); PO (pull-out failure); SC (splitting of concrete failure); FB (failure due to bar rupture).

2.4.3.1 Bar diameter

For FRP bars in concrete, larger diameters develop lower average bond strength (CEB-FIP, 2000). Four phenomena cause the negative effect that an increase of the bar diameter has on the bond strength: (1) nonlinear stress distribution along the embedded length, (2) Poisson's effect, (3) shear lag effect, and (4) bleeding.

(1) The low FRP elastic modulus generates uneven bond stress along the embedment length. The uneven stress distribution along the embedded length is more evident in bars with a larger diameter, affecting the average bond strength (Cosenza et al., 1997; Tighiouart et al., 1998; Arias et al., 2012). (2) The Poisson's effect is considered the reduction of reinforcement diameter caused by the tensile stress, ongoing, for example, during the pull-out test. Consequently, the bar lateral deformation reduces the friction and the mechanical interlock happening at the interface between bar and concrete (Achillides and Pilakoutas, 2004b). The transversal deformation is more pronounced with higher bar sizes. Furthermore, compared to steel, FRP bars exhibit lower shear stiffness, which mainly depends on the shear stiffness of the bar resin and the shear strength capacity at the resin-fibre interface. This results in the Poisson's effect being more remarked in FRP bars than in steel bars. (3) The shear lag effect, graphically displayed in Fig. 2.11, is defined as a non-uniform distribution of the normal stress within the bar's cross-section pulled in tension through the surface. As a result, the external layers are subjected to higher stress than the core layers, and the difference within the inner stress increases with the bar size, reducing the estimated average bond strength (Achillides and Pilakoutas, 2004b). For FRP bars, the shear lag effect is more remarkable than in steel bars because of low shear stiffness. (4) The bleeding of concrete could lead to defects in the interface zone between reinforcement and concrete. The bigger the bar diameter is, the bigger and more numerous are the possible voids at the interface, reducing the bond strength.

A bond strength reduction with the bar diameter increase was found for the pull-out of sand-coated GFRP bars in GPC cubes (Maranan et al., 2015a, 2015b). By increasing the bar diameter from 12.7 mm to 15.9 mm, the bond strength of a sample with a $5d_b$ embedded length reduced from 24 MPa to 22 MPa, and for an embedded length of $10d_b$, it reduced from 22 MPa to 18 MPa. Tekle et al. (2016), for sand-coated GFRP bars with fly ash-based GPC, also observed the bond strength reduction with the bar diameter increase. Referring to BFRP bars in PCC, Altalmas et al. (2015) investigated the minimum stress necessary to mobilise BFRP and GFRP bars during pull-out tests. The 8-mm BFRP bar started to slip at τ equal to 1.3 MPa (9% of the maximum stress τ_m), while, the 12-mm BFRP bar mobilised at τ equal to 0.51 MPa

(4% of the maximum stress τ_m), suggesting a lower bond performance. According to Wang et al. (2015), the bond stress between 4-mm BFRP bars and engineered cementitious composite is 5% and 23.7% higher than 10-mm bars and 16-mm bars, respectively. The same trend was confirmed by Li et al. (2017). The influence that the bar diameter has on the bond strength between BFRP bars and GPC is expected to be congruent with the results presented. However, this assumption must be verified through experimental tests.
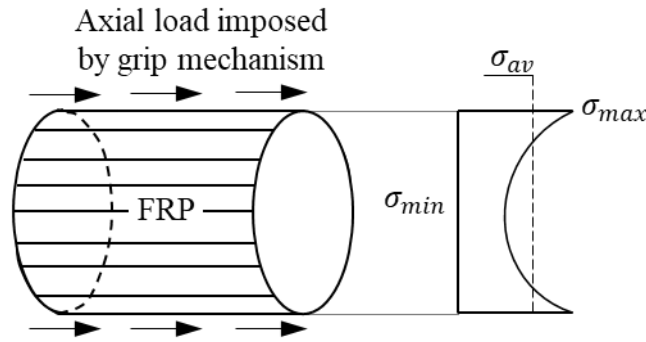
Fig. 2.11 Indicative distribution of normal stress on an FRP bar cross-section under axial load applied on the surface (shear lag effect) (Achillides, 1998).

2.4.3.2   Bar embedment length

In pull-out specimens, the embedment length (l_d) is the portion of the bar in contact with the surrounding concrete, and it is usually expressed as multiples of the bar diameter (d_b). To evaluate the effect of the embedment length on the bond performance, a portion of the bar is covered with plastic tubes or tape, preventing the bonding. Contrarily, the development length (L_d) represents the minimum length of the bar embedded in the concrete capable of developing the strength necessary to transfer the tensile force of the cross-section. In Fig. 2.12a the embedment length is longer than the development length, and thus part of the anchorage is ineffective because of slip absence. On the contrary, in Fig. 2.12b the embedment length is shorter than the development length as slips occur at any point of the bar.

For FRP bars in concrete, the average bond strength (τ_m) reduction with the increase of the embedment length is due to the nonlinear distribution of the bond forces along the bar (Achillides and Pilakoutas, 2004b). By studying the actual bond stress distribution along the bar, the peak bond stress was observed to develop near the loaded end of the specimens (Okelo and Yuan, 2005). Moreover, unlike steel reinforcing bars, FRP bars develop slips at the bar loaded end (s_{LE}) significantly higher than those measured at the bar free end (s_{FE}). The slip difference is ascribed to the low FRP bar elastic modulus causing elastic deformation along the bar embedded portion (Pecce et al., 2001). The bond behaviour of FRP bars is thus described

by two bond stress-slip curves, at the bar free and loaded ends, indicating the nonlinearity of the bond stress distribution. To obtain a more uniform distribution of the bond along the length of the bar and therefore reduce the effect of the nonlinearity on the bond stress-slip curve, short embedment lengths ($l_d \leq 5d_b$) are suggested for the test setups (CEB-FIP, 2000).

The embedment length was found to affect also the failure mode (Pecce et al., 2001). Shorter embedment length ($\sim 5d_b$) results in bar pull-out failure as the embedment length is shorter than the development length required to fully develop the necessary bond. Oppositely, the splitting tensile stress developed by longer embedded lengths ($\sim 10d_b$) is sufficient to open longitudinal cracks in the interface between reinforcement and surrounding concrete. These cracks propagate to the external surface of the concrete block and cause a brittle failure of the bond due to concrete splitting (Tepfers, 1979).

Several studies on steel and GFRP reinforced GPC samples (Maranan et al., 2014, 2015a, 2015b; Tekle et al., 2016, 2017) confirmed the influence of embedment length on the bond. For instance, Tekle et al. (2016) found that by increasing the embedment length from $3d_b$ to $6d_b$ the bond strength reduced from 18 MPa to 15.9 MPa. Concerning the BFRP bars, El Refai et al. (2015b) found an inversely proportional linear relationship between average bond strength and embedment length.

According to the author, the bond behaviour of BFRP bars to GPC could be similarly affected by the embedment length, which could cause a bond strength reduction and lead to different failure mechanisms. However, the trend should be confirmed by experimental tests.

(a)   (b)
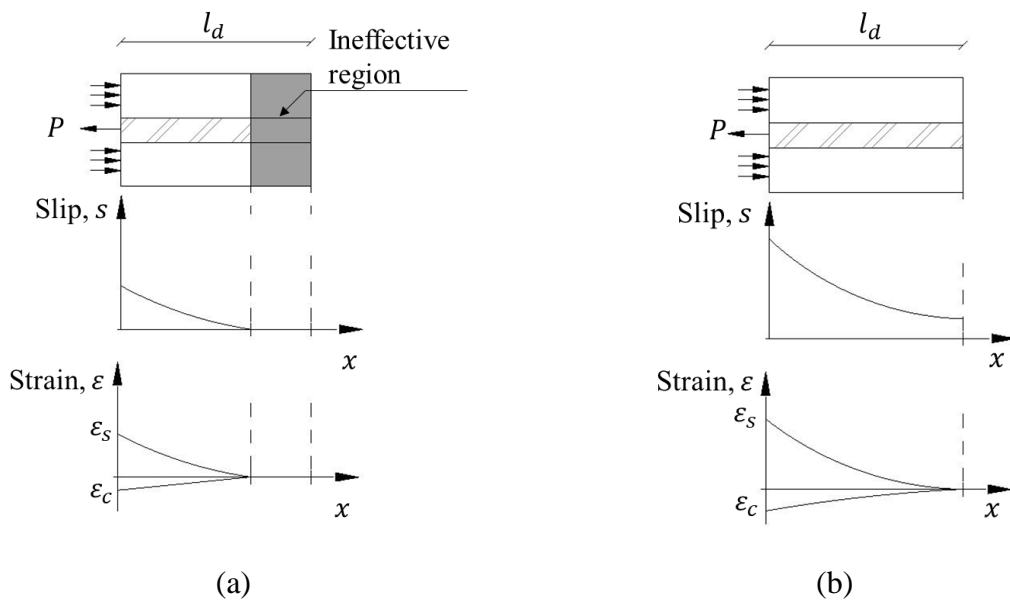
Fig. 2.12 Typical slip and strain distributions in bar pull-out with concrete in compression: (a) long embedded length; (b) short embedded length (CEB-FIP, 2000).

2.4.3.3 Bar surface

Just like in steel bars, the surface deformations play a determining role in developing the mechanical anchorage. Plain smooth bars are avoided in favour of deformed surfaces that enhance the bonding. However, oppositely to the ribbed surface of steel bars, no standard configuration has been proposed for the surface of FRP bars (CEB-FIP, 2007). The surface deformations could consist of just resin, fibre-reinforced resin or resin containing continuous longitudinal fibres. The indentations could be created by winding the rod with a separate fibre filament during the pultrusion process or machined later with specific groove geometry. Wrapped FRP rods displayed lower shear strength when compared to machined rods, highlighting the impact that the manufacturing process has on the bar performance (Tepfers and Karlsson, 1997). Another way to increase the bonding of FRP bars is to apply on the bar surface a sand coating with an epoxy resin layer. In this case, the small dense surface deformations increase the bond transfer at low load levels. However, the Poisson's effect and the splitting cracks develop at higher load levels, causing, for the small deformations offered by sand coating, a sudden loss of grip (CEB-FIP, 2000). Examples of different surface configurations are given in Fig. 2.13.

| (a) | (b) | (c) |
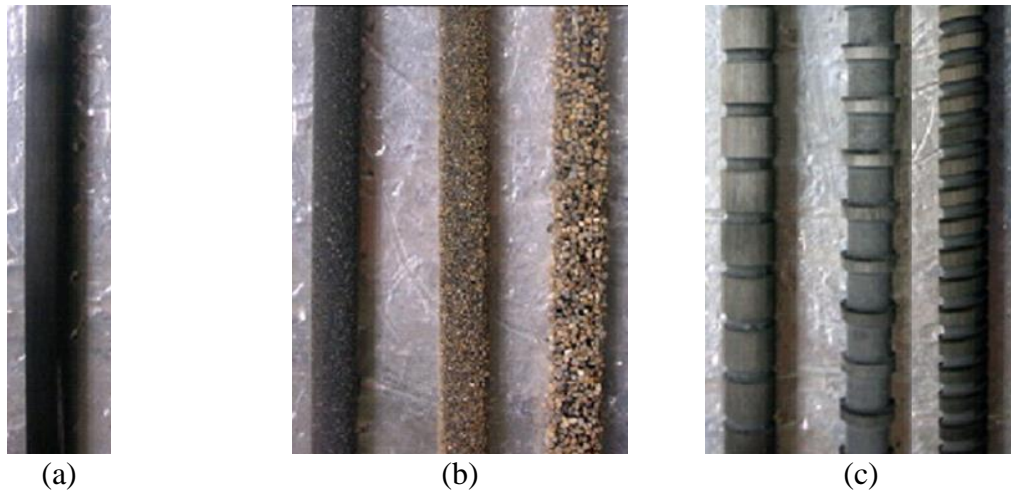
Fig. 2.13 FRP bars with different surface configurations: (a) smooth; (b) sand-coated with different sand granulometry; (c) machined with different CLR (AL-mahmoud et al., 2007).

It is worth noting that several coefficients have been proposed to define the bar surface configuration. First, the rib bearing area to rib shearing area, alternatively known as relative rib area (R_r), is calculated as follows (Hao et al., 2009):

$$R_r = \frac{projected\ rib\ area\ normal\ to\ bar\ axis}{nominal\ bar\ perimiter\ \times\ centre\text{-}to\text{-}centre\ rib\ spacing} \tag{2.2}$$

Second, the concrete lug ratio (CLR), defined as the concrete lug width in relation to the concrete and ribs width, is calculated as follows (AL-mahmoud et al., 2007):

$$Concrete\ Lug\ Ratio\ (CLR) = \frac{concrete\ width}{(concrete + FRP)\ width} = \frac{w_c}{(w_c + w_f)} \qquad (2.3)$$

Third, the ratio of the projected rib area normal to the centre-to-centre rib spacing (a_s), is calculated as follows (Baena, 2010):

$$a_s = \frac{A_r}{r_s} \qquad (2.4)$$

Thus, the bond behaviour of deformed FRP bars strongly depends on the activation of mechanical interlocking as the shear resistance offered by the surface indentation determines the bond strength. Thus, increasing the indentation depth should increase the shear resistance (CEB-FIP, 2000). Achillides et al. (2004b) suggested a surface deformation height of 5.4% d_b to provide adequate bond behaviour. Furthermore, Hao et al. (2009) varied the rib spacing from 0.5 to 3 times the bar diameter. It was found that increasing the rib spacing, i.e. reducing the R_r, had a negative effect on the bond as it reduced initial stiffness and peak bond strength, and increased the loaded end slip at the peak load. For this reason, the optimal rib spacing was suggested as equals to the bar diameter because with lower spacing ($0.5d_b$), the concrete keys within the ribs were too small to develop enough interlocking action and could be easily cracked. In addition, increasing the rib height from 4% to 6% d_b increased the initial stiffness and the peak load. This behaviour was ascribed to an increase of the bearing area of the ribs per unit length of the bar and thus a reduction of the bearing pressure of the rib. However, the beneficial effect was reduced by further increasing the rib height (7 - 9% d_b) due to reduced bar cross-sectional area. Therefore, a rib height of 6% d_b with a rib spacing equals to d_b and R_r of 0.06 was suggested as the optimal surface configuration. The optimal geometry proposed exhibited the highest bond strength, the lowest slip at maximum load and the best bond stress-slip behaviour. Furthermore, for maximising the pull-out load, the CLR could be calculated assuming a balanced failure when the shear strength of FRP lugs and concrete lugs are equal. AL-mahmoud et al. (2007) calculated an optimum CLR of 0.78. Moreover, Baena (2010) found that higher a_s developed higher bearing resistance after the loss of adhesion and the bond strength resulted increase; it also increased the radial stress, causing splitting failure.

Conversely, sand-coated FRP rebar in concrete showed good initial bond with almost linear behaviour and small free end slip, suggesting an increased chemical adhesion (Chaallal and Benmokrane, 1996; Baena, 2010). After the peak bond strength was reached, the sand coating peeled off from the rebar, and the softening branch was described by a sudden drop of

bond stress. Al-Mahmoud et al. (2007) found that the granulometry of the sand coating also affected bond strength and failure mode.

Tekle et al. (2016) compared straight non-deformed sand-coated GFRP bars with ribbed and plain steel bars in GPC. The plain steel bars failed due to bar pull-out because of poor bond strength while the ribbed and sand-coated surface configuration enhanced the bond strength causing the cracking of the concrete. The splitting failure dominated the ribbed steel bar and the sand-coated GFRP bars samples. This failure mode was considered premature as the failure was caused by the concrete while the bond was still intact. In fact, the interface between reinforcement and concrete was still undamaged, meaning that the maximum bond value was not reached. Within the specimens that failed by splitting, GFRP bars showed higher bond stress than ribbed steel bars, with an average bond strength of 15.0 MPa and 8.7 MPa, respectively, ascribed to the higher splitting stress generated by the steel ribs compared to the sand coating. Contrarily, when bar pull-out occurred, ribbed steel bars displayed better bond behaviour than sand-coated GFRP bars, because of the higher interface interlock offered by the ribs compared to the sand coating, leading to a higher pull-out load. Similarly, Maranan et al. (2015a) observed for 16-mm bar embedded for $5d_b$ in GPC a pull-out load of 85.55 kN and 94.0 kN for sand-coated GFRP bars and ribbed steel bars respectivelly.

The influence that the bar surface has on the bond was also investigated for BFRP bars in PCC. According to Li et al. (2017), the surface treatment had a higher impact on the bond behaviour than the FRP type. BFRP bars gave better results than GFRP bars, both helically wrapped, mainly because of the sand coating on the BFRP bars surface. Shen et al. (2015) confirmed the influence of the surface, especially when the concrete compressive strength was high. The outer layer of the BFRP bars detached from the inner core, and the indentations remained well connected to the concrete even after the pull-out of the bar, highlighting high adherence. El Refai et al. (2015b) observed pull-out failure of sand-coated helically wrapped BFRP bars due to delamination of the outer layer of the bar. The delamination of the interface between the sand-coated layer of the BFRP bars was more gradual and partial than that observed for GFRP bars. In addition, BFRP bars registered a smoother transition from ascending to descending branch of the bond stress-slip curve, while GFRP bars exhibited sudden failure. However, BFRP bars bond strength was lower than GFRP bars, which was ascribed to a lack of development of the mechanical interlocking that the spiral indentations on the BFRP bars should have offered.

In conclusion, bond strength, ductility and failure mode are strongly affected by the surface configuration, but no standardisation for the optimal surface treatment of FRP bars was

proposed so far. Therefore, according to the author, more research should be conducted to assess how different surface deformations or treatments influence the bond performance, aiming to improve the design provisions and the manufacturing process, to enhance the bonding.

2.4.3.4 Bar matrix

In FRP composites, the resin matrix is both a structural and a protective component. As mentioned above, its role is to include the fibres, transfer the load between them and protect them from the external environment (CEB-FIP, 2007). Since the matrix volume accounts for 30-60% of the total amount of the composite, its properties strongly influence the reinforcement mechanical properties such as bar tensile strength and resistance of the surface indentations (Baena, 2010; El Refai et al., 2015b).

The shear lag effect, already introduced in Section 2.4.3.1, is also influenced by the shear stiffness of the bar resin and the shear strength capacity at the resin-fibre interface. Furthermore, the integrity of the resin and the lack of defects, such as voids, avoid the penetration of aggressive agents from the extern, increasing the durability. Thus, the matrix should provide good chemical resistance and low moisture absorption. Nanni et al. (1995) tested glass-vinyl ester (GV), carbon-vinyl ester (CV) and carbon-epoxy (CE) bars. All the samples failed by shearing off the deformations on the surface, and the controlling factor for the bond behaviour appeared to be the resin type. The shear strength values of GV and CV bars was 60-70% of that of CE bars. CE rods also exhibited higher bond strength than GV and CV, suggesting better performance of bars made of epoxy resin than vinyl ester resin. Thus, the effect of the resin on the bond between BFRP bars in GPC is a variable that should be investigated.

2.4.3.5 Mechanical properties of concrete

In steel RC, due to the high strength of the steel bar surface ribs, the concrete is considered the weak element. However, the FRP bar surface indentations offer lower resistance to pull-out due to lower shear strength. Karlsson (1997) found that for concrete strength lower than 15 MPa, the bond strength of CFRP bars was controlled by the concrete shear strength as the concrete was crushing in front of the bar indentations. For concrete grades higher than 30 MPa, the bond failure was localised in the interface zone between the bar and the concrete. For even higher concrete strengths (>55-60 MPa), the failure was due to damage of the ribs on the bar surface, with negligible damage on the surrounding concrete. Therefore, lower concrete strength resulted in lower damage on the bar and greater damage in the concrete, and vice versa by increasing the concrete strength, the damage on the outer layers of the bar surface increased

(Achillides and Pilakoutas, 2004b). This difference in bond mechanism produces a more ductile behaviour and a higher bond strength when the failure is characterised by the shearing off of the ribs. Contrarily, a more brittle failure is registered when the bond failure is caused by the concrete failure (Pecce et al., 2001). Moreover, increasing the concrete compressive strength increases the concrete tensile strength, delaying the crack opening and improving the bond between rebar and concrete (Li et al., 2017).

In GFRP reinforced GPC, lower compressive strength caused bar pull-out, whereas specimens with higher compressive strength failed for concrete splitting (Tekle et al., 2016). In some cases, the indentations on the bar surface, relatively weak, peeled off, and the concrete remained uncrushed. It is worth noting that, unlike steel bars, the average bond strength of FRP bars in concrete cannot be considered proportional to the square root of the concrete compressive strength ($f_c^{0.5}$) (Nanni et al., 1995; Karlsson, 1997). This statement was confirmed for GFRP-reinforced GPC, but the data collected were insufficient to quantify the relationship between concrete compressive strength and bond. For BFRP reinforced PCC, low concrete compressive strength caused a bond failure that included damage on both concrete and external layer of the BFRP bars (Shen et al., 2015). Furthermore, El Refai et al. (2015b), studying the bond behaviour between BFRP bars and PCC, used high-strength concrete (50 MPa) to ensure that the damage was localised on the bar-concrete interface, not in the concrete.

The studies on steel and FRP bars in PCC and GPC suggest that the concrete compressive strength influence the bond strength and the failure mechanisms. Therefore, for BFRP reinforced GPC, the author expects that increasing the concrete compressive strength would increase the bond strength and damage the bar rather than the surrounding concrete. Thus, an experimental investigation is required.

2.4.3.6 Confinement

In steel RC, the concrete cover protects the reinforcement from aggressive environmental conditions and prevent corrosion. For non-ferrous reinforcement like BFRP bars, which exhibit non-corrosive properties, the structural role of the concrete cover appears to be the most important. As per steel bars, good confinement improves the bond behaviour of FRP reinforced members and the concrete cover design is a crucial factor to prevent bond splitting (CEB-FIP, 2000).

To examine the effect of the concrete cover on the splitting tendency, eccentric pull-out tests of GFRP bars in concrete were carried out (Tepfers and Karlsson, 1997). Compared to steel reinforced samples, FRP samples cracked at higher load delaying the splitting failure.

However, when the longitudinal crack initiated, the splitting tendency increased for FRP bars and the ultimate failure load resulted 30% lower than steel bars.

In the particular case of GFRP reinforced GPC members, the confinement influenced the failure mode. Maranan et al. (2015a) added confining stirrups and FRP jackets to the pull-out specimens to avoid splitting and obtain a pull-out failure. Tekle et al. (2016) used no transverse reinforcement and observed pull-out failure for shorter embedment length ($3d_b$), while longer embedded length ($6d_b$ and $9d_b$) caused splitting failure as the confinement provided by the concrete was not sufficient. For BFRP reinforced PCC, higher cover thickness improved the resistance to crack opening, delaying the splitting failure and enhancing the bond strength. A bond strength increase was observed by increasing the concrete cover from $3d_b$ to $6d_b$ (Li et al., 2017). However, the benefit of a thicker cover was not appreciable between $6d_b$ and $9d_b$ (Li et al., 2017), or for a concrete thicknesses above 20 mm (Wang et al., 2015).

For developing the anchorage of FRP bars, a concrete cover thickness of $4d_b$ is indicated as sufficient (CEB-FIP, 2000). However, the appropriate thickness for BFRP reinforced GPC should be investigated using eccentric pull-out or beam-end tests. Optimising the concrete cover will avoid splitting failure and offer protection from aggressive environments and external temperatures.

2.4.3.7   Exposure environments

Steel RC structures are affected by the problem of bars corrosion and, thus, the durability of the structure depends on concrete permeability, bar properties and surrounding environment. However, even if non-ferrous reinforcement exhibits non-corrosive properties, it is crucial to comprehend how FRP bars embedded in concrete behave when they undergo chemical aggression. Therefore, durability tests were performed to evaluate the influence of aggressive environments on bond behaviour. BFRP bars embedded in PCC have been exposed to different solutions such as tap water (TW), seawater (SW), acid (AC), and alkaline solutions (AK). The test settings, summarised in Table 2.3, varied to assess the bond degradation caused by different parameters, including exposure time and temperature. After the conditioning, pull-out tests were conducted in order to measure the bond degradation.

Altalmas et al. (2015) after 30-day conditioning, noticed a bond strength reduction of 25% in specimens exposed to AC and SW, while the deterioration due to AK was minor, only 14%. After 60d and 90d, the bond strength of specimens exposed to AC and SW remained stable because of the moisture absorption on the long period that dilated the reinforcement, leading to higher friction between bar and concrete. On the contrary, specimens immersed in AK

experienced further bond deterioration with a bond loss of 19% after 60 d and 25% after 90 d. Broadly, before and after the conditioning, BFRP bars bond strength was higher than GFRP bars. Contrarily, Hassan et al. (2016), after exposing the specimens to AK for 1.5 months, observed a bond strength increase of about 25% and 26% at 50 °C and 60 °C, respectively. The elevated temperatures favoured the concrete curing that enhanced the concrete compressive strength with a beneficial influence on the bond strength. After 6 months, the bond strength reduction was observed for all specimens with a loss of 16%, 7% and 5% at 40 °C, 50 °C and 60 °C, respectively. However, even after 6 months of AK exposure, the final bond strength was 12.49 MPa, above the 9.6 MPa required by the ACI standard (2006) and 8 MPa required by the CSA standard (2015). In general, higher temperatures improved the bond strength while longer exposure time slightly decreased it. Dong et al. (2016), however, found a negative effect of temperature on bond strength: after 60 days of conditioning, the degradation rate was 6%, 9.1% and 12.9% at 25 °C, 40 °C and 55 °C, respectively. They also highlighted a better resistance to aggressive settings of epoxy resin if compared to vinyl-ester resin. Furthermore, the sand coating seemed to enhance bond durability but had adverse effects on short-term bond performance.

Table 2.3 Bond durability tests of BFRP bars in concrete.

Reference	Bar type	Surface	d_b (mm)	l_d	Solution	Temperature (°C)	Duration (months)
Altalmas et al. (2015)	BFRP GFRP	sand-coated, ribbed	12	$5d_b$	AC (pH 2), SW, AK (pH 12.5)	60	1 - 3
Dong et al. (2016)	BFRP GFRP CFRP steel	ribbed	8	$6d_b$	SW	25 - 55	0.5 - 2
El Refai et al. (2015a)	BFRP GFRP	sand-coated, ribbed, helically grooved	12	$5d_b$	TW (pH 7), SW	60 - 80	3
Hassan et al. (2016)	BFRP	deformed	12	$5d_b$	AK (pH 12.9)	40 - 60	1.5 - 6

Note: BFRP (basalt FRP bars); GFRP (glass FRP bars); CFRP (carbon FRP bars); AC (acid solution); AK (alkaline solution); SW (seawater); TW (tap water).

The durability tests on the bond of BFRP bars to PCC suggests good durability properties as the bond strength after the conditioning period could still satisfy the standard requirements. Once again, the importance of the resin matrix and surface configuration in the bonding performance was observed. However, the research on the topic is still limited, and, according to the author knowledge, no investigation was published on the bond degradation of FRP bars in GPC; thus, a deeper analysis is worthwhile.

2.4.4 Summary

The bond performance of the reinforcement embedded in concrete is one of the most crucial structural aspects to investigate as it guarantees the force transfer between reinforcement and surrounding concrete. Within the tests available to investigate the bond, the pull-out test is, despite its limitations, the most economical and easy to perform, allowing to compare the effect of several influencing parameters. Nowadays, the steel-to-concrete interaction is well-known due to the numerous investigations carried out and the standardisation of the steel bar features. The research available on steel-to-GPC interaction shows a bond behaviour similar or superior to that of the traditional steel-to-PCC system. Oppositely, BFRP bars and, more generally, FRP bars display various manufacturing processes, materials employed, mechanical properties, and surface configuration. The extended assortment implies evident differences in the bond behaviour between steel and FRP bars to concrete, including bond stiffness, bond strength and failure mode. The ongoing research focuses on investigating the effects on the bond behaviour of dominant parameters, e.g. bar diameter, bar embedded length, bar surface, bar matrix, concrete mechanical properties, confinement and durability. The limited results on the study of bond between GFRP bars and GPC outline similarities with the more traditional steel to PCC interaction. Furthermore, the investigation on the bond of BFRP to PCC is increasing, highlighting similar bond performance if compared to GFRP bars in PCC. However, so far, a representative generalisation or standardisation is hard to propose. To the best of the author's knowledge, no experimental study was conducted on the bond of BFRP bars in GPC.

2.5 Theoretical predictions of bond behaviour of FRP bars to concrete

This paragraph reviews the available theoretical predictions for the bond of FRP bars to concrete, considering the existing models for describing the local bond stress-slip curve, the closed-form solution to the governing equation for calculating the interface properties over the bar length, and the current design provisions for predicting the bond strength.

2.5.1 Bond stress-slip relationship

The structural design of FRP reinforced concrete depends on understanding the local bond stress-slip curve, which controls the peak load and the development length. To date, several yet limited theoretical models were developed to analytically describe the local bond stress-slip relationship, which parameters can be calibrated from experimental pull-out test data. For instance, linear and bilinear models are the most straightforward proposed for the bond stress-slip relation of an FRP bar in concrete under a monotonic tension load. However, their precision could be limited because, as described in Section 2.4.2, the bond stress-slip law of FRP bars in concrete can be strongly nonlinear (Biscaia et al., 2013). Therefore, some nonlinear theoretical equations, calibrated on empirical data, were proposed to better approximate the experimental bond stress-slip relationship. A summary of the most well-known bond stress-slip models for FRP bars in concrete is given in Table 2.4.

2.5.1.1 Malvar model

The Malvar model (1994) was the first proposed to describe the bond behaviour between FRP bars and concrete. So far, it is the only model describing the whole curve (ascending and descending branch) with a single equation, given as follows:

$$\frac{\tau}{\tau_m} = \frac{F\left(\frac{s}{s_m}\right) + (G-1)\left(\frac{s}{s_m}\right)^2}{1 + (F-2)\left(\frac{s}{s_m}\right) + G\left(\frac{s}{s_m}\right)^2} \tag{2.5}$$

where τ is the bond stress (MPa), s is the corresponding slip at τ (mm), τ_m is the bond strength (MPa) and s_m is the slip for the bond strength (mm). F and G are curve-fitting parameters.

2.5.1.2 Modified BPE model

The Bertero-Popov-Eligehausen (BPE) model (1983) was initially proposed for the steel to concrete interaction. Cosenza et al. (1996) applied it to describe the ascending branch ($s \le s_1 = s_m$) of the local FRP to concrete bond stress-slip behaviour. The bond stress increases with the slip according to a power function, calculated as follows:

$$\frac{\tau}{\tau_m} = \left(\frac{s}{s_m}\right)^\alpha \tag{2.6}$$

where τ is the bond stress (MPa), s is the corresponding slip at τ (mm), τ_m is the bond strength (MPa) and s_m is the slip for the bond strength (mm). α is a parameter for the calibration of the curve that should be less than 1 to be physically meaningful.

The BPE model, shown in Fig. 2.14a, is described by a second branch of constant bond ($\tau = \tau_m$) until the slip $s = s_2$, then a linear descending branch from (s_2, τ_m) to (s_3, τ_m), and

a final horizontal branch $s > s_3$ with constant value of $(\tau = \tau_r)$ given by friction. For better compatibility between experimental and theoretical data in the softening branch $(s_m < s < s_u)$, an adjustment of the descending branch of the BPE model was proposed by Cosenza (1995), yielding to the modified BPE (mBPE or "double branch" model), where, in the second stage, the bond stress decreases linearly with the slip, as shown in Fig. 2.14b and expressed as follows:

$$\frac{\tau}{\tau_m} = 1 - p\left(\frac{s}{s_m} - 1\right) \tag{2.7}$$

where the parameter p is calculated from the experimental data for a better curve fitting.

The value of the parameter α is derived from the area underneath the ascending branch (Fig. 2.14), obtained from experimental data, as follow:

$$A_\tau = \frac{\tau_m s_m}{1 + \alpha} \tag{2.8}$$

The value p is also obtained from the area under the softening branch of the experimental curve.
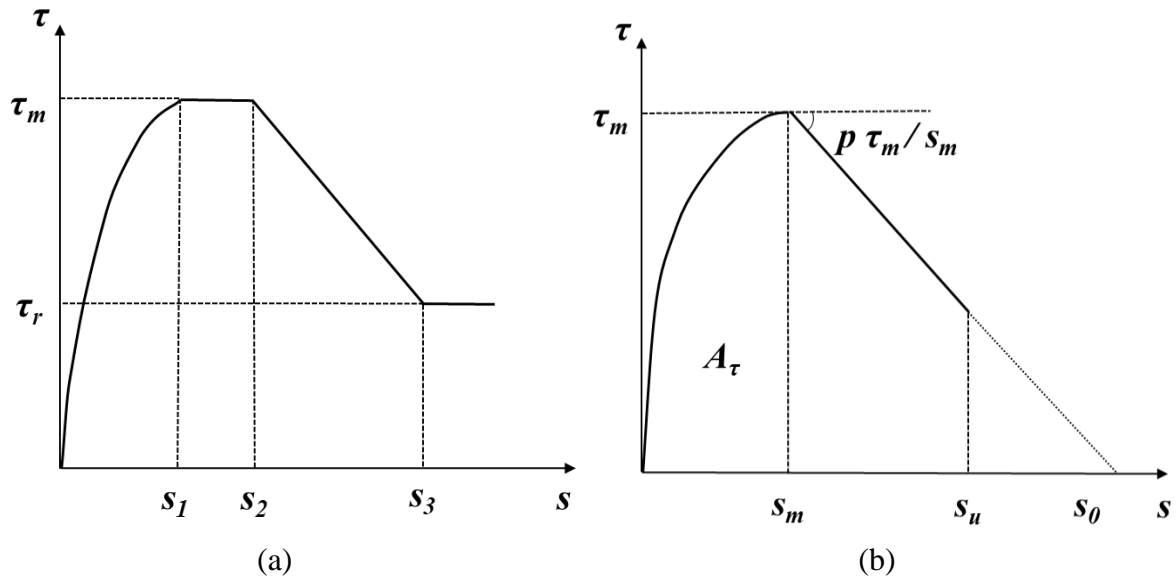
Fig. 2.14 Bond stress-slip constitutive laws: (a) BPE model (Eligehausen et al., 1983), (b) modified BPE (Cosenza et al., 1995).

2.5.1.3 CMR model

Cosenza et al. (1995) also proposed a model describing the ascending branch of the stress-slip curve using an exponential function, given as follows:

$$\frac{\tau}{\tau_m} = \left[1 - e^{\left(-\frac{s}{s_r}\right)}\right]^\beta \tag{2.9}$$

where s_r and β are parameters based on experimental data.

However, the CMR model only provides the constitutive behaviour at the serviceability state level as it lacks a definition for the descending branch.

It is worth noting that other models have been later proposed for describing the bond of FRP bars to concrete (Tighiouart et al., 1998; Baena et al., 2009; Rolland et al., 2020).

Table 2.4 Summary of theoretical models for the local bond stress-slip relationship of FRP bars in concrete.

Model	Application	Equation	Variables
Malvar	whole curve	$$\frac{\tau}{\tau_m} = \frac{F\left(\frac{s}{s_m}\right) + (G-1)\left(\frac{s}{s_m}\right)^2}{1 + (F-2)\left(\frac{s}{s_m}\right) + G\left(\frac{s}{s_m}\right)^2}$$	τ_m maximum bond stress s_m slip relative to τ_m F, G curve fitting parameters
mBPE	ascending branch	$$\frac{\tau}{\tau_m} = \left(\frac{s}{s_m}\right)^\alpha$$	τ_m maximum bond stress s_m slip relative to τ_m α curve fitting parameter
	descending branch	$$\frac{\tau}{\tau_m} = 1 - p\left(\frac{s}{s_m} - 1\right)$$	τ_m maximum bond stress s_m slip relative to τ_m p curve fitting parameter
CMR	ascending branch	$$\frac{\tau}{\tau_m} = \left[1 - e^{\left(-\frac{s}{s_r}\right)}\right]^\beta$$	τ_m maximum bond stress s_r, β curve fitting parameters

The three models were successfully applied to the experimental data of FRP in concrete (Cosenza et al., 1995, 1997), where mBPE and CMR are the most frequently used. For instance, the mBPE model was successfully applied for describing the bond stress-slip curve of the BFRP bars in PCC (El Refai et al., 2015b; Shen et al., 2015). Furthermore, the mBPE and CMR models were found suitable for describing the bond stress-slip curves of GFRP bars in GPC (Maranan et al., 2015a; Tekle et al., 2016). The CMR was more accurate between the two models, offering predictions closer to the free end curve than the loaded end. In addition, both models were adopted as constitutive behaviour for the bond interaction to perform finite element modelling. However, their formulation leads to an undefined slope (i.e. infinite slope) at the origin point, which can cause a convergency issue when the analytical law is implemented in a numerical model as the initial stiffness of the interface appears to be infinite.

Nevertheless, the application of FRP bar in construction is generally limited because of the lack of standard formulations describing their bond behaviour in concrete, which is due to several challenges, including: (1) variability of materials and geometries; (2) non-local measurements; (3) lack of standardised approach for the bond stress-slip curve definition.

Firstly, the experimental and analytical studies are generally coupled to propose empirical models that suit specific experimental data. The development of reliable and largely accepted theoretical predictions is limited by the high variability that characterises the materials (e.g. type of fibre, type of resin, concrete grade) and the geometry (bar diameter, embedded length, bar surface treatment, concrete cover, confinement), to which a high variability of the bond stress-slip parameters is ascribed (Cosenza et al., 1995; Yan et al., 2016). Furthermore, the influence of such material and geometry variables is not directly considered in the models using specific parameters. For these reasons, the average bond stress-slip curve only provides a general knowledge of the bond stress-slip performance of the considered samples (Focacci et al., 2000).

Secondly, the definition of the set of values is based on non-local measurements such as the average bond stress, which does not account for the shear stress nonlinear distribution along the bar embedded portion. It is still debated if the parameters defining the bond stress-slip constitutive law should be derived from samples with shorter ($5\,d_b$) or longer ($>5\,d_b$) embedment length. The local bond stress-slip curve can be considered a material property only when the deformation and damage of the concrete are neglectable compared to the FRP bar deformation (Mazaheripour et al., 2013b). Thus, to prevent the impact on the local bond stress-slip curve of significant deformation and damage of the concrete, it is recommended to derive the bond stress-slip constitutive law from samples with short embedded length ($5\,d_b$). Contrarily, for shorter embedment length, the local imperfections at the interface could have a higher impact on the bond stress-slip curve, resulting in scattered values of τ_m and s_m. Therefore, to minimise the effect of the local imperfections, it has been recommended to use longer embedment lengths to calibrate the bond stress-slip constitutive law (Pecce et al., 2001).

Thirdly, no specific guidelines are provided on how to identify the bond stress-slip curve parameters. For instance, some studies (Mazaheripour et al., 2013b; Rezazadeh et al., 2017) calibrated the bond stress-slip curve parameters using the measured bond stress-slip curve at the loaded end, while others (Achillides, 1998; Rolland et al., 2020) used that at the free end. In addition, given the scattering of the experimental data, in some cases, a set of parameters was provided for each sample or each set of tests (Rezazadeh et al., 2017; Rolland et al., 2020), while in other studies (El Refai et al., 2015b; Tekle et al., 2016; Yan et al., 2016), average values of different samples were considered.

2.5.2 Bond properties at the interface

The bond stress-slip curve is obtained using Eq. (2.1) based on the assumption of constant bond stress along the bar. However, if such assumption is quite accurate for steel reinforcement, for the case of FRP bars, the actual distribution of stress and slip along the embedded length cannot be neglected (Focacci et al., 2000), as already discussed in Section 2.4.3.

The actual bond stress distribution along the interface could be experimentally investigated during the pull-out test by monitoring the local strain with strain gauges, as previously done for steel bars in concrete (Lee and Mulheron, 2012). However, the surface-mounted strain gauges within the bonded region disturb the bond development, impacting the test results (Lee and Mulheron, 2015). Moreover, for FRP reinforcement, the shear lag effect could affect the recording of the strain collected using the near-surface mounted and the central-groove mounted arrangement. As an alternative to strain gauges, distributed optical fibre sensing (DOFS) technologies were recently applied to study the bond of steel and FRP reinforcement in concrete (Marchand et al., 2016; Rolland et al., 2018; Malek et al., 2019). DOFS provides accurate strain measurements with continuous recording along the optical fibre attached to the reinforcement while being less intrusive than the strain gauges (Henault et al., 2012). However, besides being an expensive instrumentation, the optical fibres could alter the pull-out response or be subject to failure (Rolland et al., 2018).

Thus, the theoretical analysis could provide helpful insight into the bond properties at the interface. The interface properties could be computed when, considering the local bond stress-slip curve and the governing equations, the analytical solutions to the differential equations are derived. Focacci et al. (2000) developed the analytical solution to calculate the slip and bond stress profiles along the bar based on the mBPE and CMR bond stress-slip laws. A closed-form solution can be determined if the embedment length is longer than the development length, i.e. if the slip at the free end of the bar is zero. When some slip is recorded at the bar free end, the differential equation must be solved numerically (Focacci et al., 2000; Pecce et al., 2001). A multilinear model was proposed for GFRP bars in high-performance steel fibre reinforced self-compacting concrete (Mazaheripour et al., 2013b). The multilinear model accounts for the rigid stiffness induced by the chemical adhesion in the initial stage of the bond stress-slip curve and the friction phase after the softening. Additionally, the stress distribution of GFRP bars in concrete was predicted using a linear model (Fava et al., 2016), which can only provide the constitutive behaviour at the serviceability state level as it lacks a definition for the descending branch.

It is worth noting that, to the best of the author's knowledge, the bond behaviour of BFRP bars in GPC has not yet been investigated analytically.

2.5.3 Bond strength design provisions

To encourage the use of FRP as reinforcement in concrete, specific guidelines were developed by extending with minor modifications those related to the steel RC, as for the case of the American and Japanese codes (JSCE, 1997; ACI 440.1R, 2015). However, the differences in material properties and interaction mechanisms make the comparison between FRP and steel reinforcement not straightforward (Cosenza et al., 2002). Therefore, over the past years, the investigations focused on examining the bond characteristics of FRP bars. From the design point of view, several national codes of practice (JSCE, 1997; CAN/CSA S806-12, 2012; ACI 440.1R, 2015; CAN/CSA-S6-14, 2017b) were formulated for evaluating the bond strength and the development length of FRP reinforcement in concrete. The equations for the bond strength prediction are summarised in Table 2.5, while Table 2.6 summarises the influencing factors considered by the existing codes in the development length evaluation. Concrete strength, bar diameter, concrete cover and bar location are contemplated in all the design provisions, while bar surface, transverse confinement and fibre type seem to play no role in some cases.

It should be noted that the bond strength predicted by ACI 440, CSA S806 and JSCE is calculated assuming a linear relationship between bond strength and the square root of the concrete compressive strength even though several studies proved that this relationship is not applicable for FRP reinforcing bars (Cosenza et al., 2002).

Table 2.5 Available design code equations for evaluating the bond strength of FRP as reinforcement in concrete.

Code	Bond strength	Eq.
JSCE (1997)	$\tau = f_{bod}/\alpha_1$	(2.10)
CSA S806 (2012)	$\tau = \dfrac{c\,\sqrt{f_c}}{1.15\,k_1 k_2 k_3 k_4 k_5\,\pi\,d_b}$	(2.11)
ACI 440.1R (2015)	$\dfrac{\tau}{0.083\sqrt{f_c}} = 4.0 + 0.3\dfrac{c}{d_b} + 100\dfrac{d_b}{l_d}$	(2.12)
CSA S6 (2017b)	$\tau = \dfrac{f_{cr}(d_{cs} + K_{tr})}{0.45\pi d_b k_1 k_6 k_7}$	(2.13)

Table 2.6 Bond influencing factors included in standard provisions for the evaluation of the development length.

Code	Concrete strength	Bar diameter	Concrete cover	Bar location	Bar surface	Transverse confinement	Fibre type
JSCE (1997)	✓	✓	✓	✓	✕	✓	✕
CSA S806 (2012)	✓	✓	✓	✓	✓	✕	✓
ACI 440.1R (2015)	✓	✓	✓	✓	✓	✕	✕
CSA S6 (2017b)	✓	✓	✓	✓	✓	✓	✓

Hossain et al. (2017) compared the bond strength provisions given by CSA S806 (2012), CSA S6 (2006), and ACI 440 (2015) with experimental data of GFRP bars reinforced beam end test. The experimental bond strength resulted higher than the theoretical predictions indicating that the design provisions provided conservative bond strength predictions, and the predicted development length was sufficient to avoid bond failure.

Additionally, for GFRP bars in high strength concrete, Saleh et al. (2018; 2019) found that CSA S806 (2012), CSA S6 (2006) and JSCE (1997) were conservative. While, in some cases, ACI (2015) was unconservative, the American code was more in agreement with the experimental data than the other guidelines considered.

Considering GFRP bars in GPC, Tekle et al. (2017) compared the experimental bond strength of spliced tests with the ACI 440.1R (2015) predictions and found that the code provision was unconservative as it overestimated the bond strength. The discrepancy was attributed to different properties displayed by GPC compared to PCC and to different geometry of the test compared to the type of samples used for deriving the ACI equation. The predicted development lengths were conservative in all the cases, especially in samples reinforced with stirrups.

2.5.4 Summary

In this section, the theoretical predictions of the bond of FRP bars to concrete were critically reviewed. Even though some models were proposed (e.g. mBPE and CMR models), a standard theoretical approach for describing the bond stress-slip constitutive law for FRP bars in concrete has not been developed yet. The lack of a widely applicable bond stress-slip model is due to several challenges, including the relatively new application of FRP bars as internal reinforcement, the high variability of FRP bars properties and parameters affecting their interaction to concrete, together with the empirical nature of the models, the nonlinearity of the

bond distribution, and the lack of a standardised approach for the identification of the bond stress-slip parameters. For these reasons, the design code provisions for evaluating the bond strength and the development length are still unfolding. The available design codes lead to unconservative or overly conservative bond strength predictions in comparison with experimental data. Some theoretical studies on the bond of BFRP bars to PCC and GFRP bars to GPC are available. However, to date, theoretical studies on BFRP bars in GPC are lacking.

2.6   Finite element simulations of bond behaviour of FRP bars to concrete

To complement the limitations of the bond experimental testing already discussed, numerical modelling based on nonlinear analysis using finite element models (FEM) is generally performed. The numerical simulation is a fundamental tool to achieve a complete understanding of the bond mechanisms which allows to appreciate more than the effects on the loaded members visible externally. With the finite element analysis, the internal performance of the cross-section can be studied, analysing the distribution of bond stress, slip and strain along the bar embedment length. Furthermore, a reliable model that accurately reproduces the empirical behaviour of the elements allows cutting down the costs related to experimental tests. This paragraph provides a detailed discussion on the available numerical studies on the bond between FRP bars and concrete, based on material models and simulation techniques.

As summarised in Table 2.7, a limited number of FE models were developed using commercial software such as ABAQUS and ANSYS to investigate the bond behaviour of FRP bars to concrete. For the FE model of pull-out of an FRP bar from a concrete block, geometry, boundary and loading conditions are straightforward. However, the available studies are still limited as the real challenge lies in the sophisticated models required to accurately simulate the nonlinear constitutive behaviours of the materials, i.e. concrete matrix and bond interaction.

Table 2.7 Summary of materials, aim and results of numerical studies of the bond between FRP bars and concrete.

Reference	Reinforcement	Concrete	Bond	Aim	Results
Fava et al. (2016)	GFRP bars Transversely isotropic elastic	PCC Isotropic linear elastic	Interfacial cracks analysed through contact using Virtual Crack Closure Technique	Compare 2D and 3D model reliability. Verify the debonding onset and propagation at the GFRP bar and concrete interface. Detect the shear stress distribution at the interface and its maximum value. Eventually identify critical zones.	• Elastic modulus of bar markedly affects bond distribution and bond strength: stiffer bar leads to more constant stress distribution. • Numerical modelling could contribute to develop reliable equations for the theoretical predictions of development length.
Gooranorimi et al. (2017)	GFRP bars Isotropic linear elastic	PCC Smeared crack model	Translator elements with prescribed stiffness	Sensitivity analysis on bond stress-slip model parameters. Investigate bond behaviour along embedded length. Parametrical study on concrete cover.	• Optimized set of value for bond stress-slip model parameters. • Smaller concrete cover change failure mode from bar pull-out to concrete splitting. • Accurate crack propagation.

Table 2.7 Summary of materials, aim and results of numerical studies of the bond between FRP bars and concrete. (Continued)

Rezazadeh et al. (2017)	GFRP bars Transversely isotropic elastic	PCC Concrete Damage Plasticity	Cohesive element Traction-separation	Present a damage-based approach for bond. FE simulation of bond stress-slip curve and strain distribution. Parametric study.	• Good accuracy of numerical strain distribution. • Higher concrete cover and concrete strength reduce splitting failure. • Increasing embedded length reduces bond strength.
Rolland et al. (2020)	AFRP, CFRP,GFRP bars Orthotropic linear elastic	PCC Isotropic linear elastic	Cohesive element Traction-separation	Describe the stress and strain gradients. Optimise bond stress-slip model parameters. Compare numerical with DOFS data.	• Good agreement between optimised numerical and experimental bond stress-slip curve. • Good agreement between local numerical strain profiles along the bar/concrete interface and DOFS measurements. • Better model accuracy at high load level.
Tekle et al. (2016)	GFRP bars Isotropic linear elastic	GPC Concrete Damage Plasticity	Surface-based cohesive behaviour Traction-separation	Investigate bond development along embedded portion of the bar.	• Nonlinear distribution of bond stress and strain along embedded length.

Table 2.7 Summary of materials, aim and results of numerical studies of the bond between FRP bars and concrete. (Continued)

Veljkovic et al. (2020)	GFRP Transversely isotropic elastic	PCC Concrete Damage Plasticity	Cohesive element Traction-separation law	Study bond influence on structural components. Compare experimental, numerical and guidelines predictions on load-deflection curves.	• Proposed bond stress-slip model led to accurate predictions. • Perfect bond was not suitable to model the problem.
Vilanova et al. (2016)	GFRP bars Isotropic linear elastic	PCC Concrete Damage Plasticity	Connector elements and contact with friction coefficient	Define bond stress-slip relationship using numerical simulation (inverse method).	• Good accuracy of predicted cracking process and tension stiffening evolution. • Good accuracy of strain distribution along the reinforcement.
Yan and Lin (2016)	GFRP bars Isotropic linear elastic	Plain (PC) and fibre-reinforced concrete (FRC) Multilinear model in compression, linear model in tension	Spring elements with prescribed stiffness	Develop a damage evolution approach for the interface. Predict bond stress-slip relations.	• Accurate bond stress-slip curve predictions. • Bar surface treatment had large impact on bond. • FRC displayed improved damage compared to PC.

Note: AFRP (aramid FRP bars); CFRP (carbon FRP bars); GFRP (glass FRP bars); GPC (geopolymer concrete); PCC (Portland cement concrete).

The FRP bars are usually modelled as solid elements with isotropic linear elastic behaviour until failure (Tekle et al., 2016; Vilanova et al., 2016; Yan and Lin, 2016; Gooranorimi et al., 2017; Elchalakani et al., 2018). However, unidirectionally-reinforced fibre composites, such as the FRP bars, could be more accurately modelled using the transversely isotropic elasticity model (Rezazadeh et al., 2017; Rolland et al., 2020).

For the concrete matrix, the simplest model used was the linear elastic behaviour (Fava et al., 2016; Rolland et al., 2020). However, the elastic behaviour is followed by a damage plastic behaviour. ABAQUS (ABAQUS 6.14 User's Manual, 2014) offers three built-in models for damage of the concrete matrix, namely concrete damage plasticity (CDP), smeared crack concrete and brittle crack concrete model. The CDP model has been extensively used in the literature (Tekle et al., 2016; Vilanova et al., 2016; Rezazadeh et al., 2017; Elchalakani et al., 2018) as its parameters can be easily defined either from experimental data or theoretical models. For instance, Rezazadeh et al. (2017) run a pull-out test of GFRP bars in PCC, adopting the digital image correlation (DIC) technique to collect strain data on the specimen front surface during the test. Fig. 2.15 shows good agreement between the concrete strain distribution at several loading stages obtained numerically with the CDP model and the experimental data obtained using the DIC. Furthermore, the simulation well represented the failure modes due to splitting for lower concrete cover and bar pull-out for higher concrete cover. The CDP was also successfully adopted for the GPC matrix where the GPC stress-strain behaviour was calculated using the modified Popovics stress-strain relationship (Popovics, 1973), based on the concrete compressive strength (f_c) and elastic modulus (E_c) obtained from experimental data (Tekle et al., 2016).
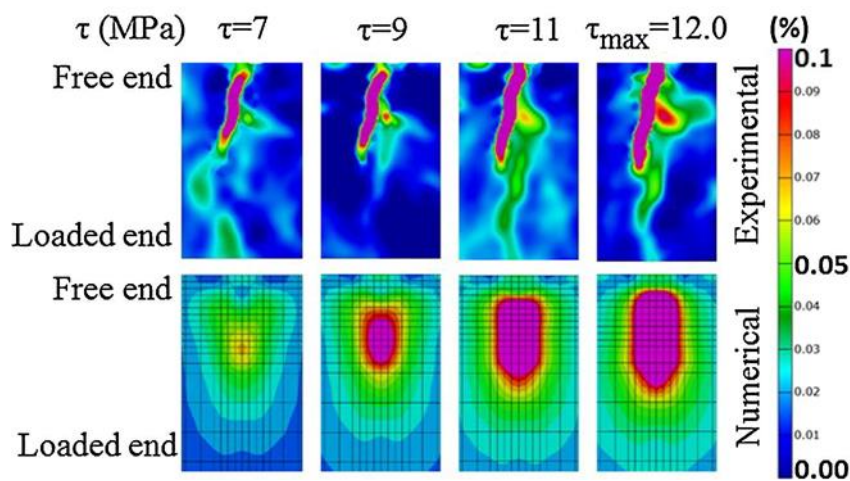
Fig. 2.15 Comparison of strain distribution obtained numerically and with DIC (Rezazadeh et al., 2017).

For modelling the bond action, several approaches were adopted. Firstly, the perfect bond approach was found inappropriate to predict the debonding process, as the relative slip between reinforcement and concrete is impeded (Yan and Lin, 2016). Alternatively, in 2D models (Gooranorimi et al., 2017) and 3D models (Yan and Lin, 2016), unidirectional connectors were used to link two nodes, one on the bar and one on the concrete surface. The experimental bond stress-slip law was assigned to the connectors as a force, being a function of displacement, providing uniform stiffness along the interface. A third approach, adopted to model bonded interfaces where the interface thickness is negligibly small and where cracks are expected to develop, consists of the linear elastic traction-separation model provided in ABAQUS. The traction-separation model can be implemented either as a surface interaction property by defining a contact with surface-based cohesive behaviour (Tekle et al., 2016) or using a cohesive element of thickness close to zero (Rezazadeh et al., 2017; Rolland et al., 2020). In the latter case, the cohesive element has two faces separated by a thickness (Fig. 2.16), connected through surface-based tie constraints to the reinforcement and the concrete, providing a continuous connection between the two materials. The traction-separation model is implemented as a property of the adhesive material. For both the surface-based cohesive behaviour and the cohesive elements, the parameters defining the traction-separation law are calibrated from experimental data or analytical models such as CMR and modified BPE models.
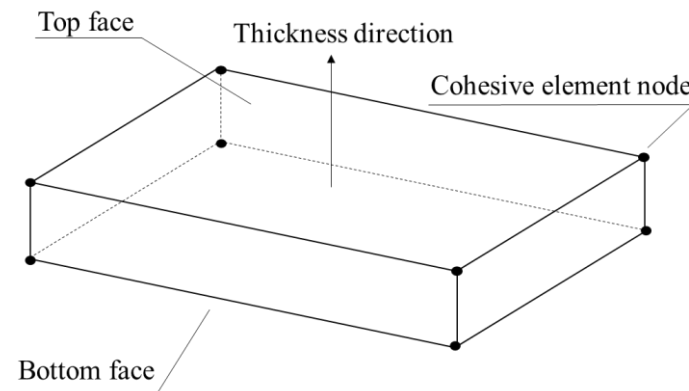
Fig. 2.16 Spatial representation of a three-dimensional cohesive element.

Tekle et al. (2016) found the traction-separation law with a cohesive surface a successful approach for simulating a pull-out test of GFRP bars in GPC. Even though power-law models (mBPE and CMR models) were found to be the most suitable to describe the experimental data, the bond behaviour was modelled using a linear behaviour up to the peak, providing a bond stiffness calculated as the ratio between the bond strength and the slip at the peak ($k = \tau_m/s_m$). This is because the mBPE and the CMR models present an undefined slope (i.e. infinite slope) at the origin point, which can cause a convergency issue during the numerical analysis as the

initial bond stiffness appears to be infinite. The FE model was successfully validated by comparing the experimental, analytical and numerical bond stress-slip curves, and it was used to investigate the distribution of the bond stress and strain along the embedded length and the debonding propagation.

Furthermore, cohesive elements were used by Rolland et al. (2018) running pull-out tests of AFRP, CFRP and GFRP bars in PCC. During the experimental test, the strain distribution along the interface between concrete and bar was measured using DOFS, which were later compared with the numerical predictions obtained using a perfect bond and a variant of the CMR model implemented with cohesive elements. In Fig. 2.17, strain profiles at different loading stages are presented, where, at a lower loading level, the perfect bond approach better represented the experimental results, while, for a higher load (81% of the pull-out load), the cohesive element better simulated the experimental strains.
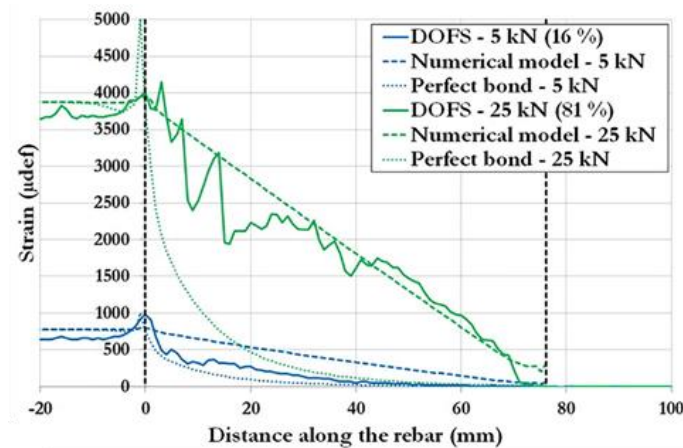
Fig. 2.17 Experimental (DOFS) and numerical strain profiles at different loading stages (Rolland et al., 2018).

It is worth mentioning that the abovementioned approaches intend to simplify a compound phenomenon happening at the interface to achieve reliable numerical simulations. The traction-separation law, for example, defines the complex bond behaviour using a reduced set of parameters. As discussed in Section 2.4.4 for the theoretical models, several considerations should be made. First, identifying the bond parameters from non-local measurements, such as the average bond stress-slip curve, reduces the precision of the simulation. Furthermore, when the parameters are calibrated from the average of the experimental results, the dispersion of the experimental data could affect the model accuracy. Additionally, several variables (e.g. materials and geometry) affect the bond behaviour, but it is still unclear how to separately account for the effect of these parameters when the bond stress-slip curve is dependent on specific experimental data.

Regarding the simulation technique, complex contact conditions, such as the bonding between reinforcement and concrete, are formulated more efficiently using an explicit dynamic method than using an implicit method (ABAQUS 6.14 User's Manual, 2014). Furthermore, the convergence of the FE method can be studied in terms of element size and loading rate. Firstly, a mesh sensitivity analysis is required to find a reasonable mesh size to represent the concrete in a reliable yet time-efficient way. Gooranorimi et al. (2017) investigated three different mesh sizes of 15 mm, 10 mm, and 7 mm square elements, where the 7 mm mesh size was finally employed since it correctly represented the concrete cracking. Tekle et al. (2016) found that a mesh size of approximately 5 mm provided acceptable results, while Vilanova et al. (2016) used an element size of 4 mm for both concrete and reinforcement. Rezazadeh et al. (2017) applied a more refined mesh in the bond zone where relatively high-strain gradients were expected to develop. Yan and Lin (2016) also used finer mesh close to the bond interface, with a mesh size of 6 mm along the axial direction and 1 mm along the radial direction of the bar. A coarser mesh size, with 12 mm along the axial direction and 6 mm along the other two orthogonal directions, was used for the further external layers of concrete. Therefore, a mesh size between 4 mm and 15 mm is recommended, with a refined mesh in the zone where more strain is expected due to load transfer. From the numerical point of view, the effect of mesh size was presented in Section 5.2.6. It is also recommended to verify the quality of the mesh by limiting the aspect ratio, i.e. the ratio between the longest and shortest edge of an element, to a maximum value of 10, as suggested by ABAQUS (ABAQUS 6.14 User's Manual, 2014). It should be mentioned that the effects of aggregate size on the material properties and the stress response were not considered as the domain size of the model and the element size in the damage region are relatively small. Secondly, the kinetic to internal energy ratio should be <10% to ensure that the effect of the loading rate does not affect the simulation results.

Therefore, according to the review, the CDP model could be efficiently used to model the GPC matrix behaviour. Considering the BFRP bars composite nature, the transversely isotropic behaviour could be the most suitable model. The bond interaction between FRP and concrete appeared to be well represented by the traction-separation law applied to cohesive element zone, to which the bond stress-slip curve could be easily input based on experimental data. Where these approaches have been successful in modelling the pull-out test of FRP bars in concrete, a FE simulation of pull-out test of BFRP bars in PCC or GPC is still lacking to date. Thus, it is fundamental to extend the research on this area with a FE model that could faithfully represent the empirical behaviour of bond of BFRP bars to GPC.

2.7 Structural performance of steel and BFRP reinforced GPC

A brief review of the structural performances of GPC reinforced with steel and BFRP bars are provided, even though beyond the scope of this research.

The study on the flexural behaviour of steel reinforced FA-based GPC beams demonstrated that load-carrying capacity and failure mode were comparable to that of steel reinforced PCC beams (Sumajouw et al., 2005a). Steel reinforced FA-GGBS based GPC beams demonstrated similar load deflection characteristics, cracking moment and service load moment of steel reinforced PCC beams (Dattatreya et al., 2011). It was also found that steel reinforced FA-GGBS based GPC beams exhibited a ductile behaviour. Also, increasing the steel reinforcement ratio increased the moment capacity and the number of cracks, and reduced the average distance between cracks (Pham et al., 2021). The study on steel reinforced FA based GPC columns proved that the load-deflection and failure behaviours were similar to those of PCC columns under biaxial bending (Rahman and Sarker, 2013). The axial load capacity increased with steel reinforcement ratio and concrete compressive strength (Sumajouw et al., 2005b). Moreover, the predictions from available standards for reinforced PCC were suitable for the design of steel reinforced GPC elements (Sumajouw et al., 2005b; Chang, 2009; Dattatreya et al., 2011; Hassan et al., 2020).

More recently, considering the environmental features and the superior engineering properties offered by GPC and BFRP bars, a new composite, i.e. FA-GGBS based GPC reinforced with BFRP bars, was proposed by Fan and Zhang (Fan and Zhang, 2016b, 2016a; Fan et al., 2021) as a sustainable and durable construction material. The studies on the structural performance of GPC reinforced with BFRP bars proved its suitability as a substitute for conventional steel RC. For instance, a comparison between BFRP reinforced GPC beams and steel reinforced PCC beams demonstrated that the development of cracking and crack patterns under flexural loading was similar within the two samples (Fan and Zhang, 2016b). Additionally, although the cracking load of steel-PCC beams was higher than the BFRP-GPC beams, the corresponding crack deflection of BFRP-GPC beams was around one time larger than the steel-PCC beams, which was ascribed to the different mechanical properties of BFRP and steel bars. Furthermore, the mechanical behaviour under eccentric compression of BFRP reinforced GPC columns and steel reinforced PCC columns was compared (Fan and Zhang, 2016a). As shown in Fig. 2.18, the load-displacement responses were similar between the two columns; however, the BFRP-GPC columns were found to have ~ 30% reduction of load-carrying capacity but improved deformation capacity compared to steel-PCC. It was also found

that compared to BFRP reinforced PCC, BFRP reinforced GPC columns displayed 5 to 19% lower peak load, but 4% to 7% increased ductility (Hadi et al., 2020).

Even though the studies on the flexural, shear and compressive behaviour of BFRP reinforced GPC support the application of BFRP reinforced GPC as a construction material, the bond of BFRP bars to GPC, which plays a critical role in the structural performance and design, has not been explored to date. It is thus vital to extensively address the bond performance of BFRP bars to GPC to encourage the application of this novel durable and sustainable composite system.
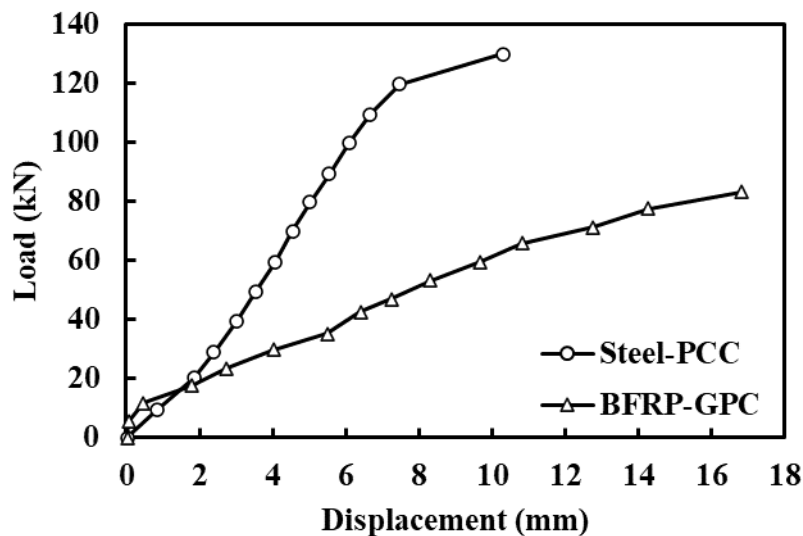
Fig. 2.18 Comparison of load-displacement behaviour between steel reinforced PCC and BFRP reinforced GPC columns (Fan and Zhang, 2016a).

2.8   Concluding remarks

In this chapter, a critical review of the research concerning the bond of BFRP bars in GPC is presented. The main challenges and limitations are summarised as follows:

- BFRP reinforced GPC was recently introduced as an alternative to steel reinforced PCC due to its environmental features and engineering properties. However, GPC and BFRP bars are still relatively novel materials characterised by a variety of constituents and manufacturing processes. The BFRP bars tensile strength is in the range of 800 and 1680 MPa and the elastic modulus varies between 30 and 80 GPa. GPC and BFRP bars have been coupled in structural studies that proved their suitability as an alternative construction system. However, the bond between GPC and BFRP bars, which plays a critical role in structural performance and design, has not been explored to date.

- Within the different bond test methods, the pull-out test is easy to perform and allows to compare the effects that different influencing parameters have on the bond behaviour. However, the stress state is different to the actual distribution in loaded members. Thus the bond strength obtained with the pull-out test should be considered as an upper bound value.

- FRP bars are characterised by reduced elastic modulus, reduced shear stiffness, reduced shear strength of the surface deformations, as well as a variety of material compositions and surface configurations. Because of these features, the bond of FRP bars to concrete strongly differs from the well-known interaction between steel bar and concrete and thus, it is challenging to standardise it.

- The bond of FRP bars to concrete is influenced by a variety of parameters, including materials (e.g. resin matrix, concrete mechanical properties), geometry (e.g. bar diameter, embedment length, surface configuration, confinement), and environment (e.g. durability). Such parameters influence the bond interaction in terms of average bond strength, bond stress-slip curve and failure mode.

- The bond stress distribution along the bar is nonlinear due to the low FRP elastic modulus. While experimental strain monitoring appears to be inefficient, theoretical and numerical analysis could provide insight into the interaction properties along the bonded length.

- The available analytical models for describing the bond stress-slip curve of FRP bars in concrete are empirical; however, no standard method is available to identify the bond stress-slip parameters. In addition, the available design code provisions are sometimes derived from the existing standards for the steel to concrete interaction, thus resulting in unconservative or too conservative predictions compared to the experimental data.

- The main challenge in developing a reliable finite element model is to accurately define the materials' behaviour, mainly because of the nonlinearity of the concrete matrix and the bond stress-slip curve, and to represent the complex interaction between FRP reinforcement and concrete.

Chapter 3 Mechanical Properties of GPC and BFRP Bars

3.1 Introduction

As mentioned in Chapter 3, GPC and BFRP bars are relatively novel materials that could be used respectively as alternatives to PCC and steel reinforcement in RC structures because of their superior engineering properties and sustainable features. However, as both materials are still under development, there exists a variation of their properties and performance. Hence, the main purpose of this chapter is to provide a thorough characterisation of the physical and mechanical properties of the materials used in this study to better understand the bond behaviour of BFRP bars in GPC.

As summarised in Fig. 3.1, the physical and mechanical properties of GPC and BFRP bars were tested according to the existing standards. First, the GPC ingredients, mix proportions, mixing procedure, sample preparation, test methods and experimental results were presented in detail. A series of crucial engineering properties of GPC including workability, compressive strength, compressive stress-strain constitutive law, splitting tensile strength and elastic modulus were tested. Then, the details about BFRP bars were presented in terms of characteristics, constituents, surface configurations, and physical and mechanical properties, with a special focus on cross-sectional area, tensile strength and modulus of elasticity.

Geopolymer concrete	BFRP bars
Workability	Cross-sectional area
ASTM C143 (2015)	ASTM D7205 (2011)
Compressive strength	Tensile strength
BS EN 12390-3:2009	ASTM D7205 (2011)
Tensile splitting strength	Modulus of elasticity
BS EN 12390-6:2009	ACI 440.3R (2004)
Modulus of elasticity	
BS EN 12390-13:2013	
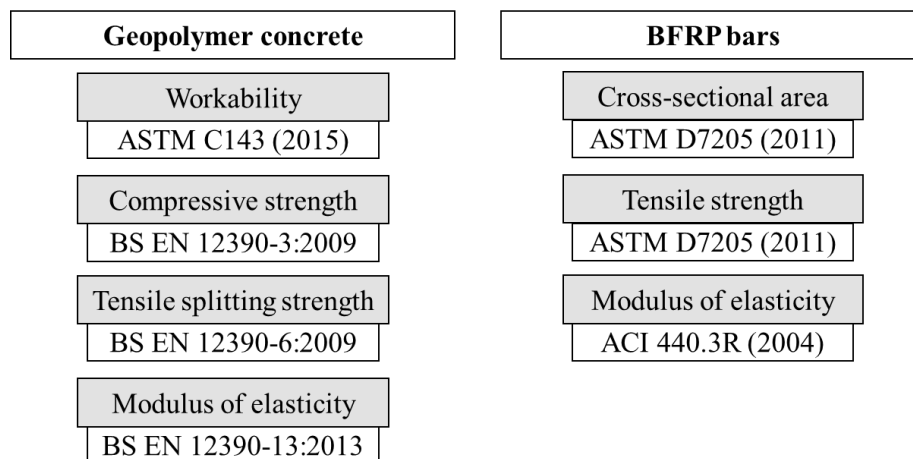
Fig. 3.1 Outline of material properties tested for GPC and BFRP bars.

3.2 GPC

3.2.1 Raw materials

In this study, low-calcium FA (equivalent to ASTM class F FA), GGBS, alkaline solution (AL), superplasticisers (SPs) and fine and coarse aggregates were used to prepare GPC. The chemical compositions and particle size distribution of FA and GGBS adopted in this study are presented

in Table 3.1 and Fig. 3.2, respectively, which play a crucial role in the strength development of GPC. As reported, the used FA and GGBS should meet a $[SiO_2]/[Al_2O_3]$ ratio of greater than 1.5 (Fernández-Jiménez and Palomo, 2003) and a $[CaO]/[SiO_2]$ ratio of greater than 1.0 (Winnefeld et al., 2014) to gain acceptable engineering properties of GPC. As finer particles contribute to higher reactivity and improved mechanical properties of GPC, 80%-90% of FA particle size should be smaller than 45 μm (Fernández-Jiménez and Palomo, 2003), while GGBS is required to have a size smaller than 40 μm (Wang et al., 2005). As indicated in Table 3.1 and Fig. 3.2, the chemical compositions of FA and GGBS adopted in this study lead to a $[SiO_2]/[Al_2O_3]$ ratio of FA and a $[CaO]/[SiO_2]$ ratio of GGBS of 1.85 and 1.25, respectively and 95% of FA was smaller than 45 μm and 92% of GGBS was smaller than 40 μm, which confirms that the used FA and GGBS can meet the above-mentioned requirements for GPC (Mostafa et al., 2001; Li et al., 2002; Fernández-Jiménez and Palomo, 2003; Wang et al., 2005; Fang and Zhang, 2020).

Table 3.1 Chemical compositions (wt%) of FA and GGBS.

Oxide	SiO_2	Al_2O_3	Fe_2O_3	CaO	K_2O	MgO	TiO_2	Na_2O	SO_3	P_2O_5
FA	55.76	30.22	3.56	2.33	0.91	0.46	1.72	0.4	0.79	0.27
GGBS	33.22	13.49	0.4	41.57	0.64	7.04	0.5	0.34	2.14	-
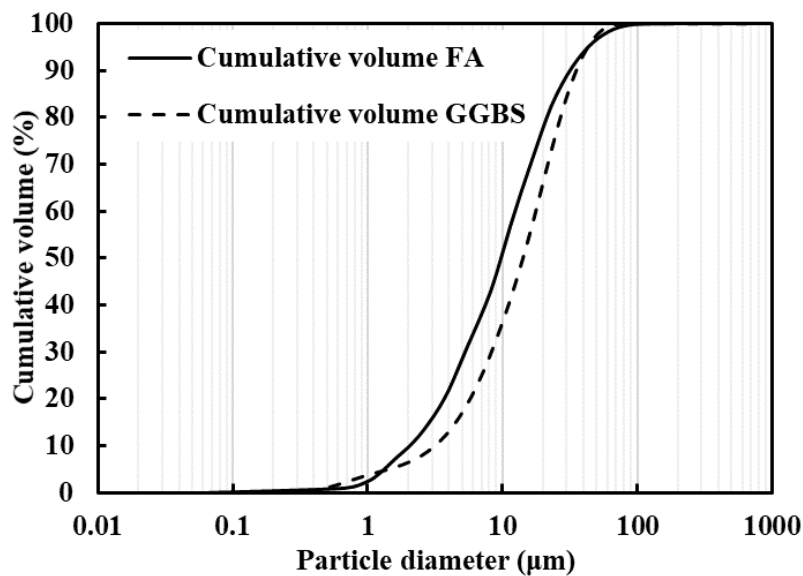
Fig. 3.2 Particle size distribution of FA and GGBS.

The alkaline activator (AL) to activate the precursors consisting of FA and GGBS was a combination of sodium hydroxide (SH) solution with a molarity of 10 M and sodium silicate (SS) (waterglass) solution. The SH solution was prepared by adding sodium hydroxide ($NaOH$)

in solid form into tap water, stirring until the solid dissolves. To obtain the desired concentration, the mass of $NaOH$ solid per litre of solution was calculated by multiplying the molar concentration with the molecular weight of $NaOH$ (40 g). To obtain a concentration of 10 M, used in this study, $10 \times 40g = 400$ g of $NaOH$ pellets were dissolved in a litre of water. The SH solution consisted of 31.40 wt% $NaOH$ and 68.60 wt% H_2O. The mixing of water and $NaOH$ is an exothermic process. Thus, the SH solution was prepared one day before the casting to allow heat release before use. The SS solution commercially available had a silicon dioxide to sodium oxide ratio (SiO_2 / Na_2O) of 2.58, which was adjusted to 2.0 by adding 46.7 g of $NaOH$ solid in 1 kg of SS solution. The SS solution was composed of 30.71 wt% SiO_2, 15.36 wt% Na_2O and 53.93 wt% H_2O.

As reported by Jang et al. (2014) and Fang et al. (2018), for FA-GGBS based GPC, the polycarboxylate-based SPs would improve the workability more effectively than the naphthalene-based SPs. Thus, to enhance the workability of GPC, 1% (by mass of the binder) polycarboxylate-based SPs was added to the mixture, which was proved to have no adverse effect on the compressive strength of GPC (Jang et al., 2014). In addition, no additional water was used in the mixtures.

Standard river sand with a nominal size of 0.03-2 mm was used as fine aggregates, while crushed limestone with a nominal maximum size of 20 mm was chosen as coarse aggregates (CA). Sieve analyses were conducted for fine and coarse aggregates and verified with the specification provided by ASTM C33 (2011). The particle size distribution for fine and coarse aggregates is displayed in Fig. 3.3, which were used in saturated surface dry (SSD) conditions according to ASTM C128 (2015) and ASTM C127 (2015), respectively.
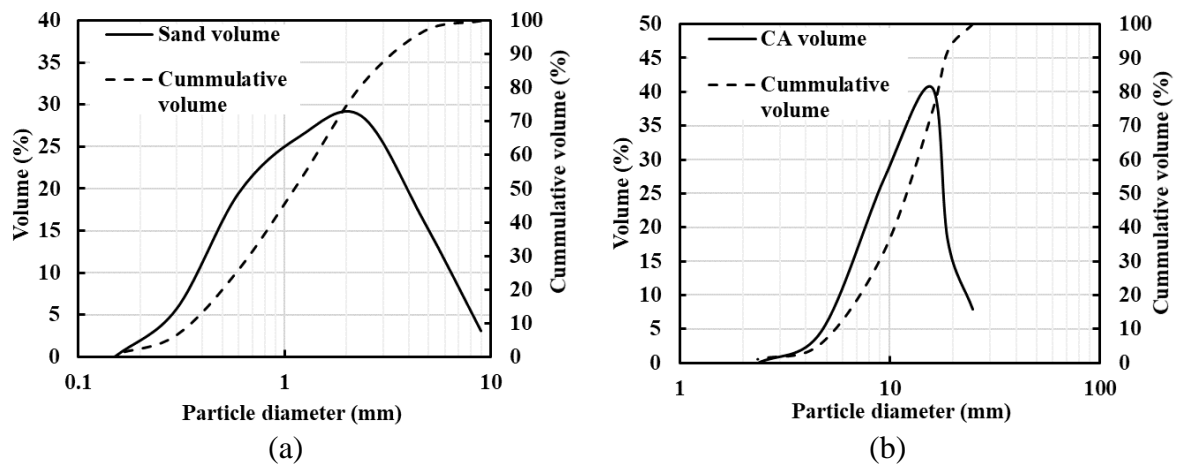
Fig. 3.3 Particle size distribution: (a) sand; (b) coarse aggregates.

3.2.2 Mix proportions

Unlike PCC, no standard guidelines are currently available in the literature for the mix design of GPC. As mentioned in Chapter 2, the choice of the concrete grade for the pull-out samples is crucial, as the concrete compressive strength strongly affects the bond performance in terms of bond strength and failure mode. For GPC cured at ambient temperature, a higher compressive strength can be obtained by reducing the FA/GGBS ratio (Nath and Sarker, 2012). However, increasing the GGBS content reduces setting time and workability and increases shrinkage (Jang et al., 2014). Therefore, according to the literature, the following factors were considered for the mix design of GPC in this study: (1) a compressive strength of GPC at 28 d of at least 30 MPa, (2) the difference in compressive strength between the two mixtures is sufficient enough (~15 MPa) to evaluate its effect of on the bond behaviour, and (3) a high enough workability of GPC to ensure the compaction and quality of samples. Some trial tests were conducted in the laboratory beforehand to obtain the optimal mixture of FA-GGBS based GPC (Fang et al., 2018; Fang and Zhang, 2020), focusing on the effects of different mixtures as well as considering the acceptable engineering properties in terms of workability, setting time and strengths. Therefore, the mixtures for the current study were obtained from the study (Fang, 2020) when still under development. Table 3.2 presents the GPC mixes, namely GPC1 and GPC2, having a slag content of 15% and 20% precursor by weight, a sodium silicate to sodium hydroxide ratio (SS/SH) of 2.0, and an alkaline activator to binder (AL/B) ratio of 0.4. According to the previous study (Fang et al., 2018), by increasing the GGBS content of the total binder by 5%, an increase of concrete compressive strength at 28 d of at least 13% was expected. The two mixes were thus selected based on the workability at the time of casting and the compressive strength at 7 d. It is worth pointing out that a third mixture having a slag content of 25% was cast as a trial to obtain samples with higher compressive strength. However, the mixture was discarded as the workability was too low to allow a good quality of pull-out samples.

Table 3.2 Mix proportions of GPC (kg/m^3).

Mix No.	FA	GGBS	SH	SS	SPs	Sand	CA
GPC1	340	60	53	107	4	632.5	1197.5
GPC2	320	80	53	107	4	634.3	1200.9

Note: FA (fly ash); GGBS (ground granulated blast-furnace slag); SH (sodium hydroxide); SS (sodium silicate); SPs (superplasticizers); CA (coarse aggregate).

3.2.3 Sample preparation

The mixing procedure for GPC is given as follows. The concrete was mixed in a pan mixer of 60 l capacity with rotating blades. The moulds were previously coated with a thin oily film to facilitate the de-moulding procedure. FA, GGBS, sand and coarse aggregates were mixed in a dry state for 3 min to ensure homogeneity of the mixture. Then, AL and SPs were added into the mixture and mixed for another 3 min. The fresh GPC was poured into the moulds up to mid-height, the specimens were compacted on a vibrating table to remove air bubbles while more concrete was poured to fill up the moulds. For the mechanical characterisation of concrete, cubic moulds of $100 \times 100 \times 100$ mm side were used for the compressive test at 1, 7, 14 and 28 d, while cylindric moulds of 100×200 mm were used for the splitting tensile test and the elastic modulus test at 28 d. Three specimens were prepared for each test to allow repeatability. The number of samples tested to obtain the mean values was selected based on a previous study on similar mixtures (Fang et al., 2018) and according to the literature. After vibrating for two more min, the specimens were covered with a plastic film to avoid moisture loss and cured for 24 h at room temperature (20 ± 2 °C). Afterwards, the specimens were de-moulded and cured in a standard curing room (20 ± 2 °C, 95% relative humidity) until the days of testing.

3.2.4 Test methods

To determine the workability of the GPC, the slump test was conducted immediately after mixing as per ASTM C143 (2015).

The compressive strength (f_c) was tested at 1, 3, 7, 28 d as per BS EN 12390-3:2009 (2009a), with a universal testing machine at a constant loading rate of 0.6 MPa/s applied monotonically until failure. The test setup is shown in Fig. 3.4a. Cubic specimens were tested, and at least three replicate samples were investigated where the mean value was obtained and used.

The splitting tensile test was conducted to indirectly measure the tensile strength of GPC. The splitting tensile strength (f_{ct}) was tested according to BS EN 12390-6:2009 (2009b), at 28 d, on cylindric concrete specimens loaded until failure at a loading rate of 1.4 MPa/min. At least three replicate samples were tested for each mixture. The test configuration is shown in Fig. 3.4b, and the splitting tensile strength was calculated as follows:

$$f_{ct} = \frac{2P}{\pi l d} \tag{3.1}$$

where P is the maximum applied force (N), l is the length of the sample (mm), and d is the diameter of the sample (mm).

The static modulus of elasticity (E_c) was tested on cylindrical specimens at 28 d according to BS EN 12390-13:2013 (2013). The elastic modulus was determined as the secant modulus measured at the stress level equal to one-third of the average compressive strength of GPC cylinders. The loading and unloading were carried out at a rate of 0.6 MPa/s. First, three preloading cycles were carried out using 10% of the ultimate load. Then, the samples were loaded with three loading cycles up to one-third of the ultimate load. Three extensometers having a gauge length of 60 mm were used to measure the longitudinal strain during the test. The extensometers were positioned vertically on the cylindric specimen at an equal distance and secured with two rubber bands to avoid any slip during the test. The test setup is shown in Fig. 3.4c. Load and strain were recorded automatically by the testing machine. At least three replicate samples were tested for each mixture. The elastic modulus can be calculated as:

$$E_c = \frac{\sigma_2 - \sigma_1}{\varepsilon_2 - \varepsilon_1}$$

(3.2)

where E_c is the modulus of elasticity (MPa), σ_2 is the stress corresponding to $f_c/3$ (MPa), σ_1 is the stress corresponding to 10% f_c (MPa), ε_2 is the longitudinal strain produced by σ_2, and ε_1 is the longitudinal strain produced by σ_1.

| (a) | (b) | (c) |
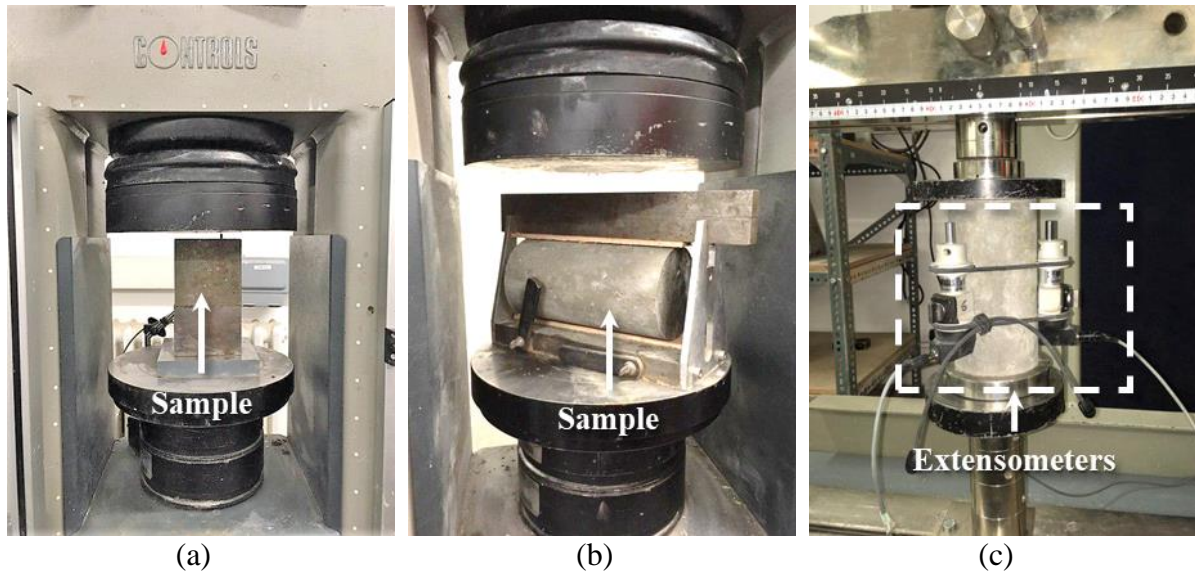
Fig. 3.4 Test setup for measuring: (a) compressive strength; (b) splitting tensile strength; and (c) elastic modulus of GPC

3.2.5 Experimental results and discussion

3.2.5.1 Workability

GPC1 and GPC2, having a slag content of 15% and 20% precursor by weight, respectively, presented a slump value of 166 mm and 154 mm. As expected (Nath and Sarker, 2014), the workability decreased 7.2% by increasing the GGBS content in the mixture. A workability

classification for GPC based on the slump value was proposed by Talha Junaid et al. (2015). The GPC can be considered highly workable with a slump value equals to 90 mm or higher. For slump values between 50 and 89 mm, the GPC is considered to have medium workability. For slump values lower than 50 mm, the workability is considered low. According to such classification, both mixtures, i.e. GPC1 and GPC2, exhibited high workability.

Conversely, due to the high reactivity provided by the high percentage of GGBS in the mixture, the setting time of the mixtures was short, and the workability rapidly reduced during the casting process. Consequently, to limit the time required to cast and assure the quality of the sample, the number of specimens prepared with a single batch of GPC was lowered.

3.2.5.2   Compressive strength

Three samples were tested for each mixture, indicating a compressive strength at 28 d of 42.34 MPa (±2.68 MPa) and 45.64 MPa (±1.04 MPa) for GPC1 and GPC2, respectively. Thus, the mixtures satisfied the required minimum concrete compressive strength at 28 d, which is 28 MPa for basic engineering application and 35 MPa for reinforced concrete (ACI 318, 2014). It is worth noting that a concrete compressive strength increase of at least 13% was expected by increasing the GGBS content of the total binder by 5% (Fang et al., 2018). However, GPC2 exhibited a compressive strength only 7% higher than GPC1. This can also be observed in Fig. 3.5, which compares the compressive strength development at different ages of the current study and the reference study used for selecting the mixtures (Fang et al., 2018). Fig. 3.5 indicates that the strength development rate of the mixture GPC2 reduced between 7 d and 28 d, achieving lower compressive strength than what could have been forecast at 7 d. It is worth noting that the minor difference between GPC1 and GPC2 strengths impacted the results of the pull-out tests, as explained in the following chapter. However, investigating why the mixture GPC2 attained a lower compressive strength than expected is beyond the scope of this work.
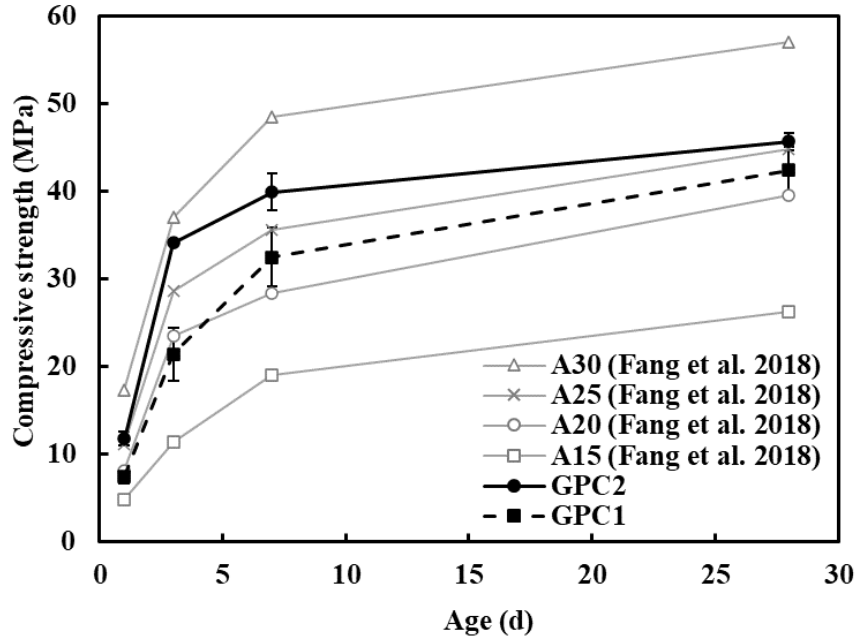
Fig. 3.5 Compressive strength of GPC at different curing ages (Fang et al., 2018).

The compressive stress-strain relationship of PCC is generally determined using the constitutive model proposed by Popovics (1973) modified by Collins et al. (1991). The Popovics model is calculated with compressive strength and elastic modulus obtained from experimental data. The complete stress-strain relationship can be obtained using Eqs. (3.3) - (3.6):

$$\sigma_c = f_c' \frac{\varepsilon_c}{\varepsilon_c'} \frac{n}{n - 1 + \left(\frac{\varepsilon_c}{\varepsilon_c'}\right)^{nh}} \tag{3.3}$$

where σ_c is the concrete compressive strength (MPa), ε_c is the strain of the concrete, f_c' is the peak concrete compressive stress (MPa), ε_c' is the strain of the concrete when σ_c is equal to f_c', and n is a curve-fitting parameter calculated as follows:

$$n = 0.8 + \left(\frac{f_c'}{17}\right) \tag{3.4}$$

The parameter h is calculated as follows:

$$h = 0.67 + \left(\frac{f_c'}{62}\right) \quad \text{when} \quad \frac{\varepsilon_c}{\varepsilon'_c} > 1$$
$$h = 1 \quad \text{when} \quad \frac{\varepsilon_c}{\varepsilon'_c} \leq 1 \tag{3.5}$$

And ε_c' is calculated as follows:

$$\varepsilon_c' = \frac{f_c'}{E_c} \cdot \frac{n}{n - 1} \tag{3.6}$$

While the constitutive law of PCC is well-known, less investigation has been carried out on the constitutive behaviour and stress-strain model of GPC. Hardjito et al. (2005) found a good correlation between the experimental stress-strain curve of a FA based GPC and the Popovics constitutive model (1973) proposed for PCC. Thomas and Peethamparan (2015) studied the engineering properties of FA-GGBS based GPC, which showed similar stress-strain behaviour to PCC up to the peak stress, and for which it is possible to determine the stress-strain relationship using the equations mentioned above. However, if compared to PCC, a brittle behaviour was observed during the post-peak softening of GPC, more pronounced for the case of GGBS based GPC. Ganesan et al. (2014) verified that the constitutive behaviour of confined GPC could be determined with the stress-strain model for confined PCC proposed by Mander et al. (1988), which is the Popovics model (1973) modified with a curve fitting factor. Furthermore, Dong et al. (2017) modified the uniaxial compressive stress-strain model presented by Desayi and Krishnan (1964) for PCC and proposed Eq. (3.7), which was more satisfactory to describe GPC:

$$\sigma_c = \frac{0.65 E_c \varepsilon}{\left(1 + \left(\frac{0.091\varepsilon}{\varepsilon'_c}\right)^4\right)^3} \tag{3.7}$$

where σ_c is the concrete compressive stress (MPa), ε_c is the strain of the concrete, f_c is the concrete compressive strength (MPa), ε'_c is the strain of the concrete when σ is equal to f_c.

It is, therefore, possible to conclude that the stress-strain behaviour of GPC can be assessed by using an analytical model based on the compressive strength (f_c), on the strain (ε_c) and on the elastic modulus (E_c).

Fig. 3.6 compares the tested stress-strain relations in compression of GPC samples and the predictions made with the Popovics model. Good agreement was found between the experimental and the modelled constitutive behaviour, allowing the use of Eq. (3.3) developed for PCC to predict the constitutive law of GPC.
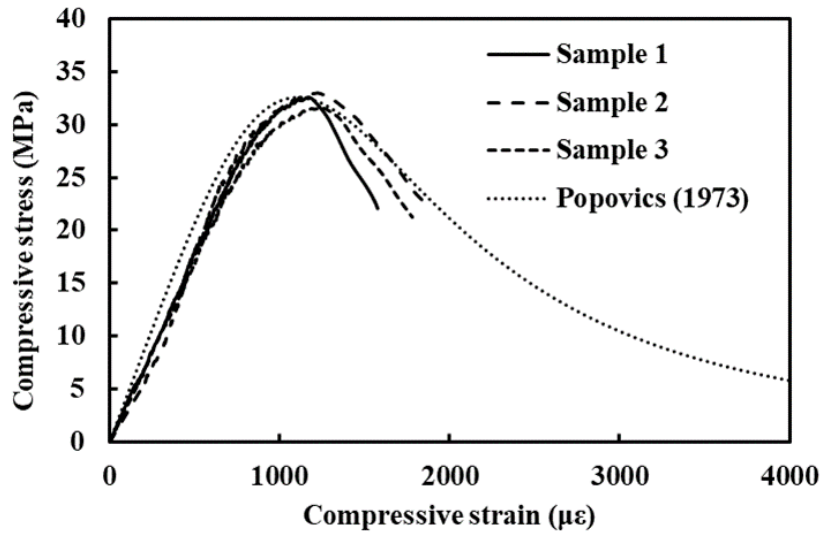
Fig. 3.6 Experimental and analytical compressive stress-strain relation for GPC.

3.2.5.3 Splitting tensile strength

The measured splitting tensile strength (f_{ct}) values were 3.57 MPa (± 0.18 MPa) for GPC1 and 3.97 MPa (± 0.07 MPa) for GPC2. In addition, Fig. 3.7 shows the experimental splitting tensile strength values compared with existing codes provisions. The splitting tensile strength can be predicted as a function of the compressive strength (f_c) as in Eq. (3.8) and Eq. (3.9), provided respectively by the standard codes ACI 318-08 (2008) and Eurocode 2 (2004). Furthermore, experimental studies highlighted that the splitting tensile strength of GPC could be calculated as proportional to the square root of the concrete compressive strength. Sofi et al. (2007b) proposed a constant of 0.48 ($f_{ct} = 0.48 \sqrt{f_c}$), Lee and Lee (2013) proposed a constant of 0.45 ($f_{ct} = 0.45 \sqrt{f_c}$). For this specific mix design, Fang (2020) proposed a constant of 0.49 ($f_{ct} = 0.49 \sqrt{f_c}$). Fig. 3.7. compares the experimental and the predicted splitting tensile strength values, indicating good agreement between experimental data and the above-mentioned models where the ACI 318-08 (2008) is the most suited for predicting the splitting tensile strength from the concrete compressive strength.

$$f_{ct} = 0.56 \, (f_c)^{\frac{1}{2}} \tag{3.8}$$

$$f_{ct} = \frac{1}{3} \, (f_c)^{\frac{2}{3}} \, for \, f_c < 50 \, MPa \tag{3.9}$$
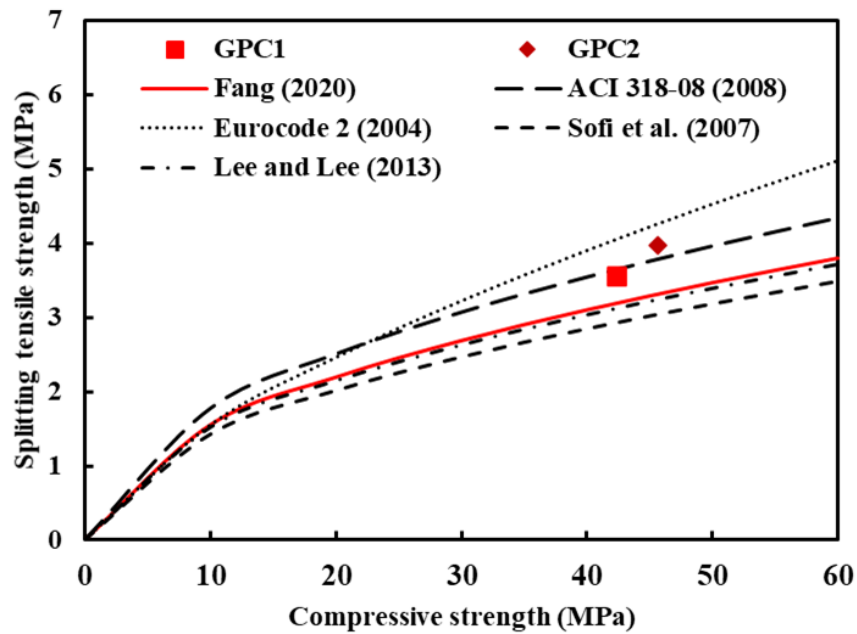
Fig. 3.7 Comparison between experimental and predicted splitting tensile strength of GPC.

3.2.5.4 Modulus of elasticity

The modulus of elasticity (E_c) is used to design the reinforced structural elements, establish the quantity of reinforcement, and determine the stress for the observed strain. The measure elastic modulus values were 30.58 GPa ($\pm$ 0.76 GPa) for GPC1 and 34.49 GPa ($\pm$ 0.48 GPa) for GPC2. Fig. 3.8 shows the measured elastic modulus of the two GPC mixtures, which, as expected, increased with concrete compressive strength.

E_c can also be modelled as a function of the compressive strength (f_c) and the density (ρ) as in the following equations provided by ACI 318-08 (2008), ACI 318-14 (2014) and AS 3600-2009 (2009), respectively.

$$E_c = 4700 \, (f_c)^{\frac{1}{2}} \tag{3.10}$$

$$E_c = 3320 \, (f_c)^{\frac{1}{2}} + 6900 \tag{3.11}$$

$$E_c = \left[0.043 \, \rho^{\frac{3}{2}} \, (f_c)^{\frac{1}{2}} \right] \pm 20\% \ \text{ for } f_{cm} \leq 40 \text{ MPa}$$

$$E_c = \left[0.043 \, \rho^{\frac{3}{2}} \, (f_c)^{\frac{1}{2}} + 0.12 \right] \pm 20\% \ \text{ for } f_{cm} > 40 \text{ MPa} \tag{3.12}$$

Fig. 3.8 compares the experimental data and the model predictions, suggesting good agreement between the measured values and the models, being the ACI 318-08 (2008) the best fit. Previous studies also compared the experimental elastic modulus of GPC with the predictions made with the abovementioned equations. For example, Thomas and Peethamparan (2015) proposed to use ACI 318-08 (2008), Dong et al. (2017) found that ACI 318-14 (2014) was the most suitable, while Sofi et al. (2007b) confirmed that the elastic modulus of GPC fits

within limits provided by AS 3600-2009 (2009). The models could thus be used to predict the elastic modulus of GPC.
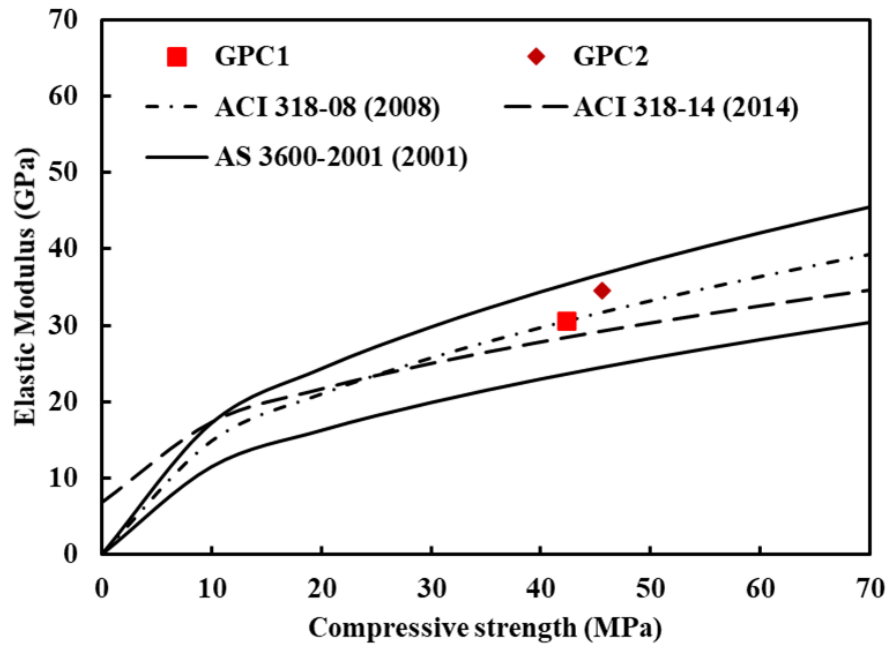
Fig. 3.8 Comparison between experimental and predicted elastic modulus of GPC.

A summary of the compressive strength, splitting tensile strength, and elastic modulus of the mixes GPC1 and GPC2 is provided in Table 3.3. The analytical models identified as the best fitting were used in the numerical simulation presented in Chapter 5 for determining the mechanical properties for a given concrete compressive strength.

Table 3.3 Mechanical properties of GPC.

Mix No.	f_c (MPa)	f_{ct} (MPa)	E_c (GPa)
GPC1	42.34 ± 2.68	3.57 ± 0.18	30.58 ± 0.76
GPC2	45.64 ± 1.04	3.97 ± 0.07	34.49 ± 0.48

3.3   BFRP bars

3.3.1   Sample preparation

Fig. 3.9 shows the ribbed BFRP bars used in this study, produced by pultrusion of continuous basalt fibres embedded in vinyl-ester with a minimum fibre volume ratio of 75% (per unit weight). Three nominal diameters of 6 mm, 8 mm and 10 mm were tested. The ribs with a smooth and round surface, as displayed in Fig. 3.10, were obtained during pultrusion with a nylon laminate helically wrapped around the outside diameter to improve the bar-concrete bonding. The rib depth was 6% of the diameter, which provides adequate bonding to concrete

(Achillides, 1998). In addition, 8-mm steel bars and 8-mm BFRP bars with a ribbed profile and sand-coated surface treatment were tested for comparison.

Fig. 3.9 Characteristics of bars used in this study: (a) 6-mm ribbed BFRP bar; (b) 8-mm ribbed BFRP bar; (c) 10-mm ribbed BFRP bar; (d) 8-mm sand-coated BFRP bar; (e) 8-mm steel bar.

Fig. 3.10 Surface configuration of BFRP bar.

3.3.2   Test methods

3.3.2.1   Cross-sectional area measurements

The nominal cross-sectional areas of BFRP bars were calculated as a circle based on the nominal diameter, while the average cross-sectional areas were determined following the Archimedes principle as per ASTM D7205 (2011). The measured diameter was calculated as an average of five representative specimens obtained from the same bar stock used for the tests. A BFRP bar sample of 100-mm length was immersed in a graduated cylinder filled with water, as shown in Fig. 3.11. The bar volume was calculated indirectly by the difference in water level before and after the immersion. The volume was then divided by the length of the sample to determine the cross-sectional area (A_b) and the diameter (d_b) as follows:

$$A_b = 1000 \, (V_1 - V_0)/L \tag{3.13}$$

$$d_b = 2\sqrt{A_b/\pi} \tag{3.14}$$

where V_0 is the initial volume of water (ml), V_1 is the volume of water with BFRP bars (ml), and L is the length of the sample (100 mm).

It is worth noting that the cross-sectional area of BFRP bars can also be measured using a 3D laser scanning technique.
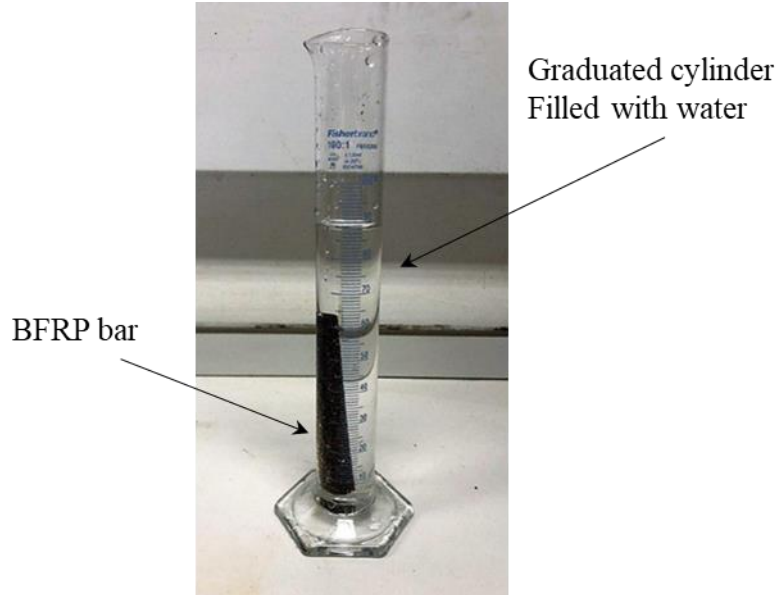
Fig. 3.11 Measurement of the cross-sectional area of BFRP bars using Archimedes principle.

3.3.2.2 Uniaxial tension test

FRP bars in different sizes could contain slightly different fibre volume fractions. As the strength of FRP bars depends on the content of fibre rather than resin (CEB-FIP, 2007), the different fibre content in FRP bars with varying size would lead to variation in macroscopic mechanical properties (Sooriyaarachchi, 2006). Therefore, the mechanical properties of different BFRP bars including tensile stress-strain curve, tensile strength and elastic modulus were determined by conducting uniaxial tension tests according to ASTM D7205 (2011). For data reliability, five samples for each BFRP bar diameter were tested until failure. Due to their composite nature, BFRP bars are anisotropic, presenting a low transverse strength compared to longitudinal strength. To prevent the damage induced by the machine grips applying the load, an anchorage system was placed at the bar extremity between the bar and the grip, as recommended in ASTM D7205 (2011). The anchorage consisted of a steel tube of prescribed length and diameter to ensure sufficient tensile strength of the steel tube, which was filled with cement grout to ensure sufficient bond between the anchor and the bar. The length of the steel tube was 300 mm for all bar diameters, while the external diameter of steel tube was 35 mm

for the 6-mm and 8-mm bar diameters and 42 mm for the 10-mm bar diameter. The detail of the protective anchorage is illustrated in Fig. 3.12. The longitudinal detail of a typical specimen for tensile tests is shown in Fig. 3.13, where the free length of the BFRP bar was 400 mm. It should be mentioned that misalignment should also be avoided to prevent bending, which could cause premature failures of BFRP.
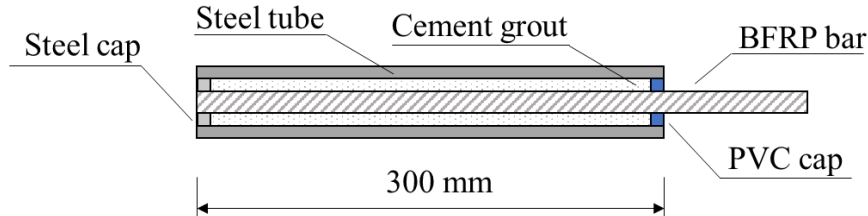
Fig. 3.12 Detail of anchorage system for BFRP bars tensile test protection.
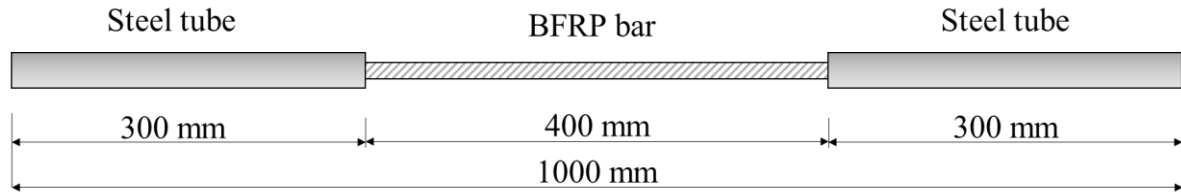
Fig. 3.13 Longitudinal detail of tensile test specimen.

More details about the tensile test on BFRP bars are presented in Fig. 3.14. The BFRP bar, fitted with anchors at both extremities, was mounted in a universal testing machine so that the anchorage tubes would be positioned in correspondence with the grips of the testing machine, as shown in Fig. 3.14b. The bar was monotonically loaded in tension under displacement control at a constant rate of 1 mm/min until failure. The applied force and longitudinal displacements were recorded automatically by the testing machine. The longitudinal strain was also measured by an electronic extensometer positioned at the mid-length of the bar, as displayed in Fig. 3.14b. During the test, the load and strain data were recorded using an automated data acquisition system, based on which the mechanical properties can be calculated with the nominal cross-sectional area. Among them, the ultimate tensile strength can be calculated as follows:

$$f_f = \frac{P_m}{A_b} \tag{3.15}$$

where f_f is the ultimate tensile strength (MPa), P_m is the maximum force prior failure (N), and A_b is the nominal cross-sectional area of the bar (mm^2).

According to ACI 440.3R (2004), the modulus of elasticity was calculated as a linear regression of the data points from 20% to 50% of the bar tensile strength:

$$E_f = \frac{F_1 - F_2}{(\varepsilon_1 - \varepsilon_2) A_b} \tag{3.16}$$

where E_f is the longitudinal modulus of elasticity (MPa), F_1 and ε_1 represent the load (N) and strain corresponding to 50% of the ultimate tensile capacity, and F_2 and ε_2 denote the load (N) and strain corresponding to 20% of the ultimate tensile capacity.

For comparison, the bond behaviour of 8-mm diameter ribbed steel bars was also estimated, and thus the tensile tests were also conducted on steel bars, the details of which are illustrated in Fig. 3.15.

(a)   (b)   (c)
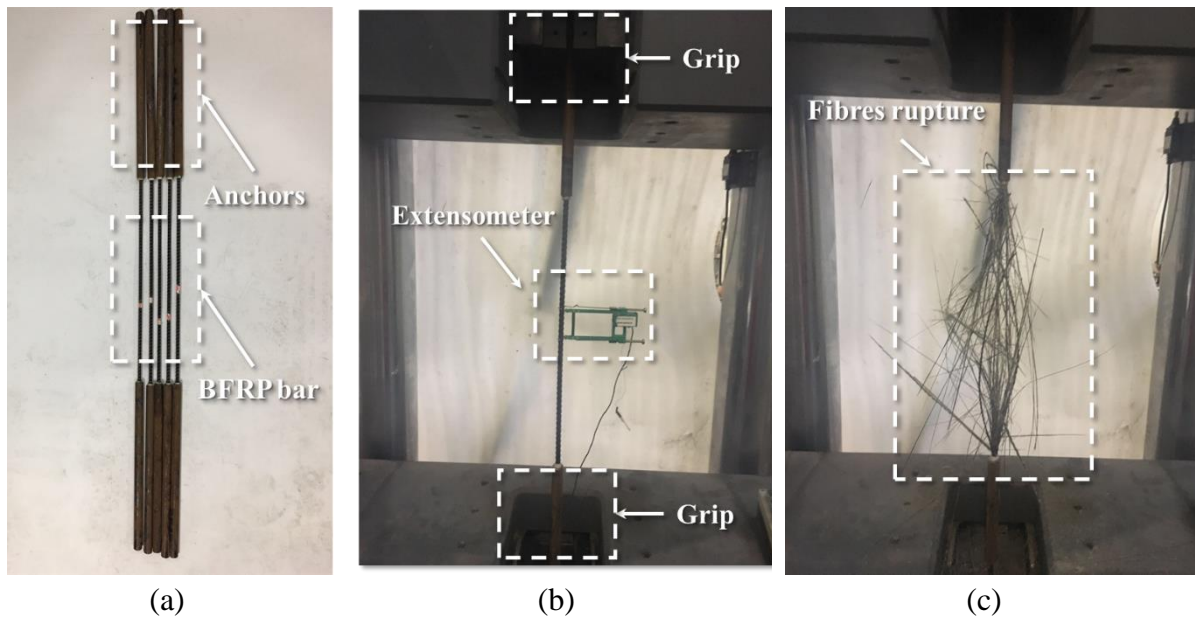
Fig. 3.14 Tensile test of BFRP bars: (a) BFRP bar specimens and steel anchors; (b) tensile test setup; (c) BFRP bar after failure.
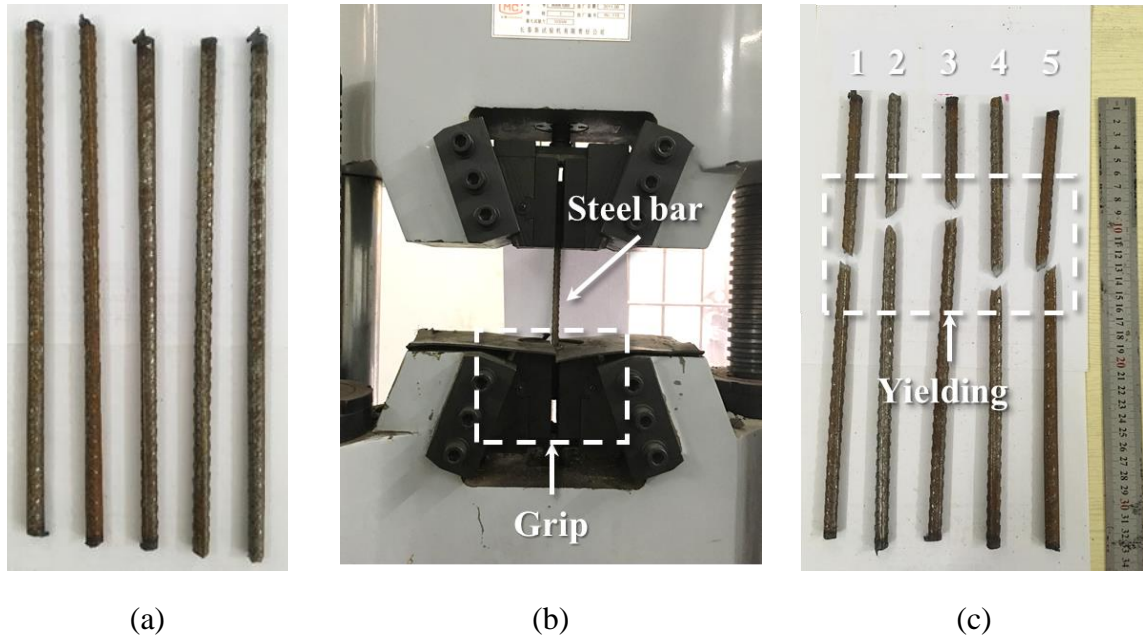
Fig. 3.15 Tensile test of steel bars: (a) steel bar specimens; (b) tensile test setup; (c) steel bars after failure.

3.3.3　Experimental results and discussion

The tensile properties of the bar are among the most important for the structural design, as the bar tensile strength affects the structural elements' capacity while the elastic modulus influences their serviceability. Thus, the physical and mechanical properties of BFRP bars and steel bars were tested and are listed in Table 3.4.

3.3.3.1　Tensile stress-strain curve

Fig. 3.16 shows the tensile stress-strain curves of BFRP bars, which exhibited a linear behaviour without any yielding point until an abrupt and brittle failure was attained, as expected from FRP bars. A high variability in the stress-strain behaviour of different 6-mm BFRP bar samples at high stress levels can be observed. Such unexpected mechanical behaviour may be ascribed to the manufacturing method of BFRP bars, which could have led to some degree of inhomogeneous properties, as discussed below. Lower mechanical properties of BFRP bars could have affected the pull-out test results, as discussed in Section 4.3.

3.3.3.2　Tensile strength

Fig. 3.14c displays the failure of BFRP bars due to fibres rupture, while the steel bars failed due to yielding with some visible necking, as shown in Fig. 3.15c. Compared to steel, BFRP bars exhibited a higher tensile strength and a lower elastic modulus. As expected, the tensile strength of 10-mm BFRP bar (876 MPa) was 21% lower than that of 8-mm BFRP bar (1117 MPa) due to the potentially increased voids and defects with the increase of bar diameter (Bank,

2006; Adhikari, 2009). However, unexpectedly, the tensile strength of the 6-mm BFRP bar was 899 MPa, approximately 19% lower than that of the 8-mm BFRP bar, which, as already discussed, can be ascribed to the manufacturing process.

As no standard code is available for BFRP bars, the current standards for GFRP bars were applied for comparison, as GFRP bars are the most similar FRP bars to BFRP bars compared to those included in the standard codes. It can be found that all the BFRP bars met the requirements for GFRP bars, according to CSA S807 (2015), corresponding to a grade II classification for GFRP bars that requires a tensile strength of 703 MPa and an elastic modulus of 50 GPa. The Poisson's ratio of BFRP bars was 0.2-0.3, as provided by the manufacturer.

Table 3.4 Physical and mechanical properties of BFRP and steel bars.

Nominal diameter (mm)	Effective diameter (mm)	Ultimate tensile strength f_f (MPa)	Elastic modulus E_b (GPa)
6	5.15	899.89	55.4
8	7.20	1117.58	58.2
10	8.00	876.37	57.5
ST	-	515.68	210.0

Note: 6 (6-mm diameter ribbed BFRP bar); 8 (8-mm diameter ribbed BFRP bar); 10 (10-mm diameter ribbed BFRP bar); ST (8-mm diameter steel bar).
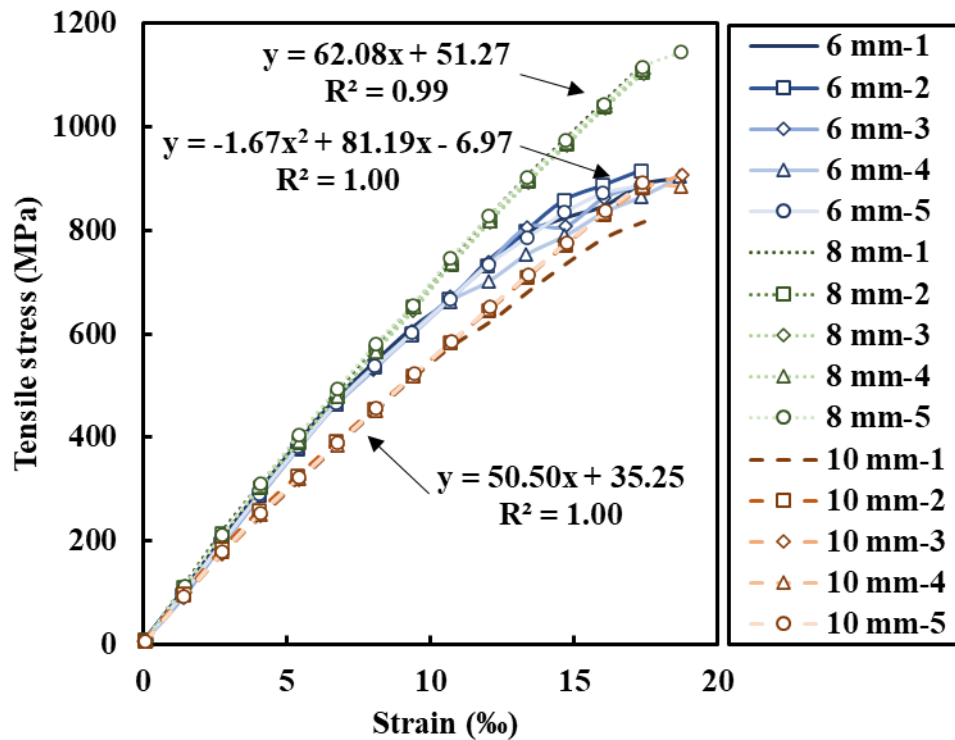
Fig. 3.16 Uniaxial tensile behaviour of BFRP bars with various diameters.

3.4   Concluding remarks

This chapter presents an experimental study on the mechanical properties of the materials adopted in this study, i.e. GPC and the BFRP bars. Based on the experimental results, the main conclusions can be drawn as follows:

- The two mixtures (i.e. GPC1 and GPC2) exhibited high workability, which was indicated by slump values of 166 and 154, respectively. The workability reduced by increasing the GGBS/FA ratio.

- The two mixtures, GPC1 and GPC2, exhibited a compressive strength at 28 d of 42.34 MPa and 45.64 MPa, respectively. A 5% increase in GGBS content of the total binder increased the compressive strength only by 7%, not as effectively as anticipated, affecting the pull-out test performance discussed in Chapter 4. The splitting tensile strength at 28 d of GPC1 and GPC2 was 3.57 MPa and 3.97 MPa, respectively, and the elastic modulus at 28 d of GPC1 and GPC2 was 30.58 GPa and 34.49 GPa, respectively.

- The available equations for PCC could be adopted to predict the mechanical properties of GPC, as confirmed by a comparison with experimental data. In particular, the GPC compressive stress-strain relation could be predicted using the analytical model proposed by Popovics (1973), while the splitting tensile strength and the elastic modulus could be predicted from the concrete compressive strength using the ACI 318-08 (2008) for PCC. The prediction equations were used in Chapter 5 to identify the material property parameters adopted in the finite element simulation.

- The tensile strength of the BFRP bars ranged between 876 MPa and 1117 MPa, being higher than that measured for the steel bars. Unexpectedly, the 6-mm BFRP bar exhibited high variability in the stress-strain behaviour of different 6-mm BFRP bar samples and a tensile strength 19% lower than the 8-mm BFRP bars, which could have affected the pull-out test performance presented in Chapter 4. In addition, the BFRP bars elastic modulus varied from 55 GPa to 58 GPa.

Chapter 4 Experimental Study of Bond of BFRP Bars to GPC

4.1 Introduction

The properties of BFRP bars and GPC have been extensively characterised in the previous chapter. However, the reinforcement-to-concrete bond is another key property that strongly influences the structural performance of reinforced concrete structures. The load transfer between reinforcement and concrete is characterised by the local bond stress-slip curve, which is determined from pull-out or beam-end tests (Sturm and Visintin, 2019). Recently, several experimental studies assessed the interaction between steel reinforcement and GPC (Sofi et al., 2007a; Castel and Foster, 2015) and between BFRP bars in concrete (El Refai et al., 2015b; Dong et al., 2016) using pull-out and beam-end tests. On the contrary, the bond interaction between these two innovative materials, namely BFRP bars and GPC, is still completely unknown.

In this chapter, the bond behaviour between BFRP bars and GPC is experimentally investigated through pull-out tests. The pull-out specimen preparation, test setup and testing procedure are detailed according to ACI 440.3R (2004). The most important results on the experimental series, including bond stress-slip relationship, failure modes and average bond strength, are discussed together with the influence of several parameters on the bond performance such as bar diameter, embedment length, surface configuration, and concrete compressive strength. Furthermore, a comparison with samples reinforced with deformed steel bars provides an insight into the difference between the two bonding performances.

4.2 Experimental program

4.2.1 Sample preparation

The pull-out samples, graphically represented in Fig. 4.1, consisted of BFRP bars embedded at various depths in GPC cubes, the mechanical properties of which were presented in Chapter 3. The GPC was cast on a 150-mm cubic mould, an example of which is shown in Fig. 4.2. Five timber faces were cut and assembled, while the sixth face was left open to allow the casting. In addition, two faces had a central hole to allow the BFRP bar to pass through. The BFRP bar, 700-mm long, was placed horizontally, aligned transverse to the concrete casting direction. A support was inserted underneath the bar to keep it aligned in a horizontal position. An anchorage was fitted at the bar loaded extremity to prevent grip induced damage, as discussed

for the tensile test in Section 3.3.2.2. Bond-breaker PVC tubes of different lengths were applied to prevent bonding along a portion of the bar to obtain embedment lengths of $5d_b$, $10d_b$, $15d_b$. A thin film of oil was applied on the mould faces to allow ease of demoulding. The samples were mixed, cast, and cured as discussed in Section 3.2. A total of forty-eight pull-out samples were prepared, where four nominally identical specimens were cast for each studied parameter to ensure data reliability. The samples for the characterisation of the mechanical properties of concrete presented in Section 3.2.5 were cast at the same time as the pull-out samples.
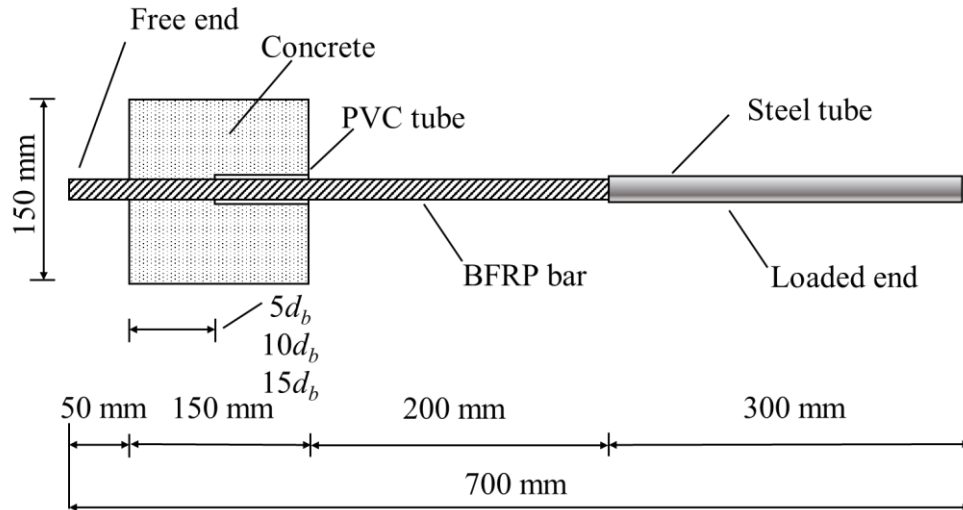
Fig. 4.1 Longitudinal detail of pull-out test specimen.
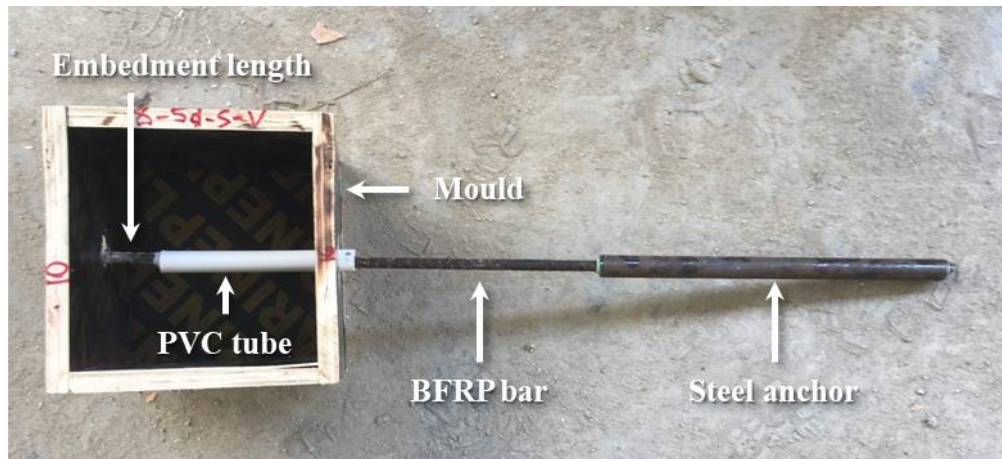
Fig. 4.2 Pull-out mould before casting, containing BFRP bar and PVC tube.

The influence of key parameters on the bonding strength and failure mode was tested. The primary variables were chosen according to the literature review provided in Chapter 2. The parameters investigated i.e. bar diameter, embedded length, bar surface, and concrete compressive strength, were chosen considering to the following:

- Bar diameter and embedment length: according to the literature, the bond strength is expected to reduce with the increase of bar diameter and embedment length. Three bar diameters and three embedment lengths were chosen between those most commonly studied in the literature to observe this trend for BFRP bars in GPC.

- Bar surface treatment: compared to smooth bars, the deformations on the bar surface enhance the mechanical interlocking, thus developing higher bond strength (Achillides and Pilakoutas, 2004a). To improve the bond connection, different bar surface treatments are available, yet no standardisation was proposed as it is still debated which surface treatment provides higher bond strength. For instance, the sand coating appeared to enhance the chemical adhesion, consequently reducing the slips at the beginning of the test (Chaallal and Benmokrane, 1996; Baena, 2010). However, after the peak, the descending branch of the bond stress-slip curve was characterised by an abrupt failure due to peeling off of the sand-coated layer. Therefore, in this study, two surface configurations, i.e. ribbed and sand-coated, were adopted, considering their influence on bond stiffness and strength. Even though the depth of the indentations and the size of the grains are important features that have been previously investigated in detail (AL-mahmoud et al., 2007; Baena, 2010; Solyom and Balázs, 2020), in this study, no quantification was carried out, and thus the discussion is only qualitative.

- Concrete compressive strength: according to the literature (Okelo and Yuan, 2005; Baena et al., 2009), an increase of concrete compressive strength (f_c) results in higher bond strength, up to a certain f_c limit beyond which the concrete grade no longer influences the bond (Karlsson, 1997; Achillides, 1998). Higher concrete strength leads to higher adhesion and higher concrete tensile strength, delaying the internal cracking of concrete. Moreover, the interface of rupture also appears to be affected by the concrete compressive strength, i.e. for lower f_c (~30 MPa) the failure is generally more evident in the concrete while for higher f_c (~50 MPa) the damage is concentrated on the bar external layers (Karlsson, 1997; Baena, 2010). Thus, to investigate the influence of the concrete compressive strength on the bond between BFRP bars and GPC, two concrete mixes were selected based on the concrete compressive strength at 7 d and the workability during the casting, as detailed in Section 3.2. As previously shown in Fig. 3.5, the compressive strengths at 7 d measured for GPC1 and GPC2 were noticeably different. However, the strength development of GPC2 reduced its slope between 7 d and 28 d of curing, resulting in two strengths not significantly detached, being 42.34

MPa for GPC1 and 45.64 MPa for GPC2. The impact that such a result had on the pull-out test was discussed in Section 4.3.2.4.

For comparison purposes, steel-reinforced specimens were also tested. Each specimen was identified using a code that summarises the bar diameter (6 mm, 8 mm, 10 mm), the embedment length ($5d_b$, $10d_b$, $15d_b$), the surface configuration (S = sand-coated), the type of concrete (GPC2), the material when different from FRP (ST = steel), and the tested sample. For instance, the code **8-15d-1** represents a bar of 8-mm diameter and $15d_b$ embedment length and the first sample tested. Most of the bars presented a ribbed surface, and most of the specimens were cast with GPC1; thus, these specifications were included only when necessary. A summary of the pull-out test specimens is provided in Table 4.1, including sample identification, bar diameter (d_b), bar embedded length (l_d), length of the bond-breaker PVC tube, surface configuration of the bar, and concrete compressive strength (f_c).

Table 4.1 Summary of details of pull-out test specimens.

Specimen	d_b	l_d		PVC	Surface	Type	f_c
	(mm)		(mm)	(mm)			(MPa)
6-5d	6	5db	30	120	ribbed	BFRP	42.34
6-10d	6	10db	60	90	ribbed	BFRP	42.34
6-15d	6	15db	90	60	ribbed	BFRP	42.34
8-5d	8	5db	40	110	ribbed	BFRP	42.34
8-10d	8	10db	80	70	ribbed	BFRP	42.34
8-15d	8	15db	120	30	ribbed	BFRP	42.34
10-5d	10	5db	50	100	ribbed	BFRP	42.34
10-10d	10	10db	100	50	ribbed	BFRP	42.34
10-15d	10	15db	150	0	ribbed	BFRP	42.34
8-5d-S	8	5db	40	110	sand-coated	BFRP	42.34
8-5d-GPC2	8	5db	40	110	ribbed	BFRP	45.64
ST-8-5d	8	5db	40	110	ribbed	steel	42.34

4.2.2 Test setup and testing procedure

Fig. 4.3 shows the pull-out test configuration. During testing, the samples were held by a frame made of two steel plates connected by four rods. The lower plate had a central hole to allow the bar to pass through. The upper plate had a pin on the top to be gripped by the upper jaw of the testing machine. The relative slips between bar and concrete were recorded using linear variable displacement transducers (LVDT), one at the free end and three at the loaded end. A

universal testing machine with a capacity of 1000 kN was arranged to apply the load to the bar under displacement control at 1.3 mm/min, as per ACI 440.3R standard (2004). Conducting the test in displacement control instead of force control allowed better reading of the stress-slip curve. At the end of pull-out tests, some samples were cut open to investigate the surface between concrete and bar, while others split open during the test. For each configuration, four samples were constructed, three of which were tested. If some anomaly was detected, the corresponding data were discarded, and the test was repeated on the fourth sample.

1. Machine top jaw
2. Bar free end
3. LVDTs
4. Concrete cube
5. Bond breaker PVC tube
6. Steel frame
7. Bar loaded end
8. BFRP bar
9. Steel tube
10. Machine loading jaw
11. Data aquisition system

(a)   (b)
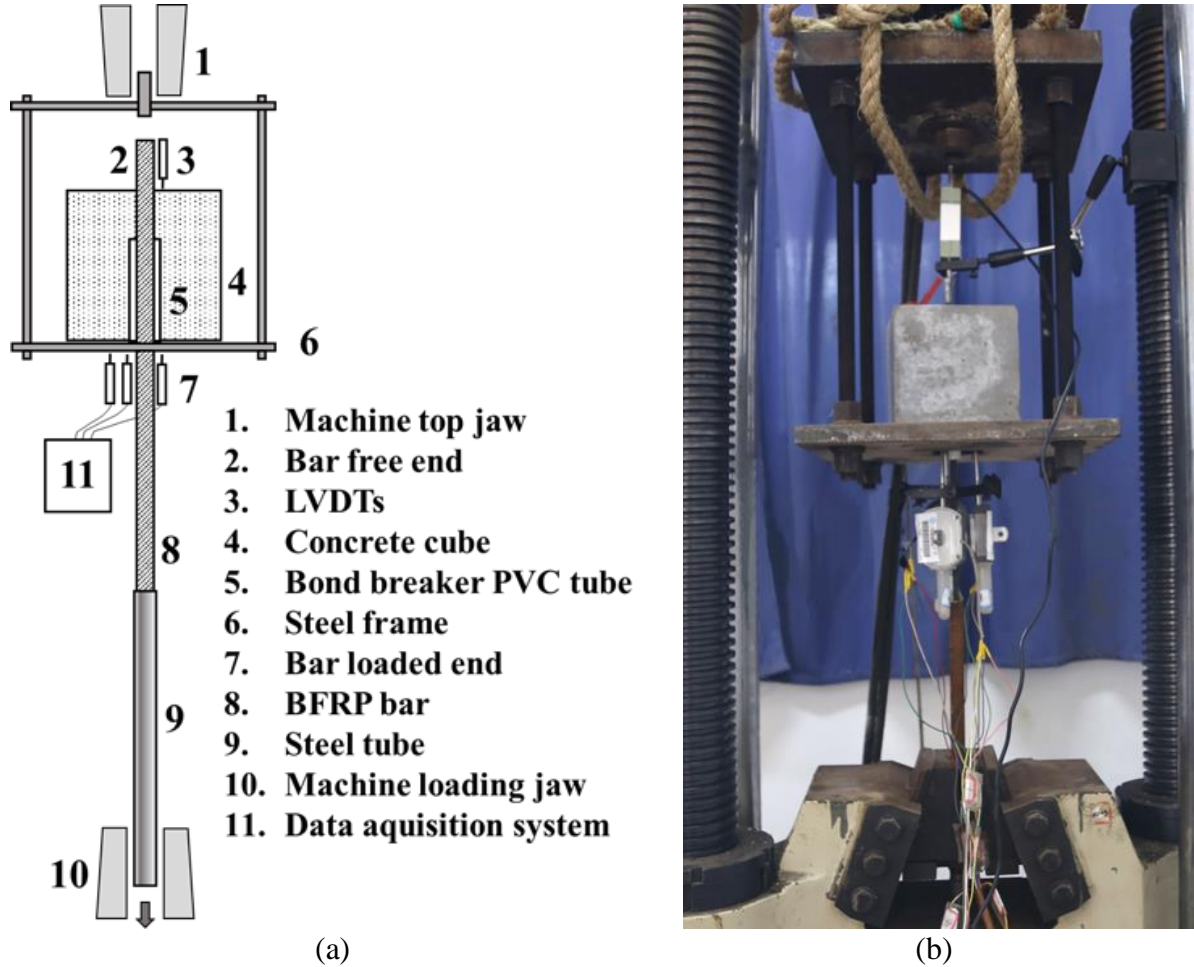
Fig. 4.3 Pull-out test configuration: (a) graphical detail; (b) photo.

4.3   Results and discussion

4.3.1   Bond stress-slip relationship

The experimental data of the pull-out tests consist of tensile load applied and slips at the free end and loaded end. The average bond stress is defined as the shear force per surface area of the bar-concrete interface, which can be calculated from the measured pull-out load as follows:

$$\tau = \frac{P}{\pi d_b l_d}$$

(4.1)

where τ is the average bond stress (MPa), P is the tensile load (N), d_b is the nominal bar diameter (mm) as per common practice (Baena et al., 2009), and l_d is the embedment length (mm).

The average bond strength (τ_m) can be calculated by dividing the peak load (P_m) by the contact surface area.

The slips at the loaded end were recorded with LVDTs connected to the bar. Hence, the readings account for the slip and the elastic elongation of the bar between the actual loaded end, at the beginning of the embedded portion, and the LVDTs attachment point. As the elastic modulus of BFRP is low, the elongation should not be neglected as for steel rebars. Hence, a correction that considers the elastic elongation should be applied to the measured slip, according to:

$$s_{m,LE} = s_e - s_c \tag{4.2}$$

$$s_c = \frac{Pl_c}{A_b E_b} \tag{4.3}$$

where $s_{m,LE}$ is the loaded end slip (mm), s_e is the slip measured at the loaded end (mm), s_c is the slip correction due to the bar elongation (mm), P is the tensile load (N), l_c is the length between the embedded portion inside the concrete cube and the point of reading (mm), A_b is the nominal cross-sectional area of the bar (mm^2), and E_b is the elastic modulus of the bar (MPa).

The length to be considered for the calculation of the slip correction s_c is given by the free length of the bar between the LVDTs attachment and the concrete cube, and the length of the bond-breaker PVC tube used to study different embedded lengths. The PVC tube length changed for different samples, depending on the bar diameter and embedded length, according to Table 4.1.

The pull-out test results are summarised in Table 4.2, which includes the mode of failure (PO = pull-out of the bar, BF = bar failure, SC = splitting of concrete), the failure load (P_m), the bond strength (τ_m), the slip at the free end ($s_{m,FE}$) for the maximum load, the slip at the loaded end ($s_{m,LE}$) for the maximum load, and the respective standard deviation (SD) and coefficient of variation (COV), together with the bond stress at the onset of slip at the loaded ($\tau_{ons,LE}$) and free ($\tau_{ons,FE}$) ends.

Table 4.2 Pull-out test results.

Sample ID	Failure	P_m (kN)	τ_m (MPa)	Average			COV (%)	$s_{m,LE}$ (mm)	Average (mm)			COV (%)	$s_{m,FE}$ (mm)	Average (mm)			COV (%)	$\tau_{ons,LE}$ (MPa)	$\tau_{ons,FE}$ (MPa)
6-5d-1	BF	8.20	14.50					0.13					0.07					0.71	2.12
6-5d-2	BF	9.80	17.33	15.21	±	1.87	12.3%	0.18	0.14	±	0.04	26%	0.09	0.08	±	0.007	9%	0.35	3.18
6-5d-3	BF	7.80	13.79					0.11					0.08					1.06	2.83
6-10d-1	BF	15.60	13.79					0.34					0.08					0.18	1.59
6-10d-2	BF	18.40	16.27	13.91	±	2.3	16.5%	0.40	0.35	±	0.05	14%	0.08	0.08	±	0.003	4%	0.18	2.30
6-10d-3	BF	13.20	11.67					0.30					0.08					0.35	0.71
6-15d-1	BF	24.80	14.62					0.34					0.11					0.35	2.59
6-15d-2	BF	24.20	14.26	14.49	±	0.18	1.2%	0.38	0.37	±	0.02	6%	0.11	0.14	±	0.059	41%	0.35	0.71
6-15d-3	BF	24.60	14.50					0.38					0.21					0.35	3.18
8-5d-1	PO	41.50	41.28					0.57					0.33					0.50	1.49
8-5d-2	PO	41.00	40.78	42.11	±	1.88	4.5%	0.59	0.57	±	0.02	4%	0.34	0.32	±	0.033	11%	0.50	1.49
8-5d-3	PO	44.50	44.26					0.55					0.28					0.50	2.49
8-10d-1	BF	83.00	41.28					1.41					0.30					0.25	1.49
8-10d-2	BF	82.00	40.78	41.19	±	0.38	0.9%	1.34	1.37	±	0.04	3%	0.28	0.27	±	0.032	12%	0.25	1.49
8-10d-3	BF	83.50	41.53					1.36					0.24					0.25	6.71
8-15d-1	PO	57.00	18.90					1.25					0.13					0.17	1.16
8-15d-3	PO	56.60	18.77	18.81	±	0.08	0.4%	1.35	1.32	±	0.06	5%	0.20	0.17	±	0.042	24%	0.07	0.93
8-15d-4	PO	56.60	18.77					1.35					0.20					0.13	0.86
10-5d-2	PO	39.00	24.83					0.49					0.26					0.38	0.51
10-5d-3	PO	44.60	28.39	25.85	±	2.22	8.6%	0.60	0.54	±	0.06	10%	0.34	0.30	±	0.042	14%	0.38	2.55
10-5d-4	PO	38.20	24.32					0.54					0.30					0.25	1.02

Table 4.2 Pull-out test results. (Continued)

Sample ID	Failure	P_m (kN)	τ_m (MPa)	Average			COV (%)	$s_{m,LE}$ (mm)	Average			COV (%)	$s_{m,FE}$ (mm)	Average			COV (%)	$\tau_{ons,LE}$ (MPa)	$\tau_{ons,FE}$ (MPa)
10-10d-1	BF	72.80	23.17					1.14					0.30					0.13	0.25
10-10d-2	BF	70.80	22.54	22.41	±	0.83	3.7%	0.98	1.05	±	0.08	8%	0.22	0.25	±	0.040	16%	0.13	0.19
10-10d-3	BF	67.60	21.52					1.04					0.24					0.13	0.38
10-15d-1	SC	50.40	10.70					0.95					0.14					0.08	0.64
10-15d-2	SC	61.40	13.03	12.34	±	1.43	11.6%	1.18	1.12	±	0.14	13%	0.18	0.17	±	0.03	15%	0.08	1.15
10-15d-3	SC	62.60	13.28					1.21					0.19					0.17	0.93
ST-8-5d-1	Y	22.60	22.48					2.09										0.20	
ST-8-5d-2	Y	22.20	22.08	22.68	±	0.72	3.2%	2.02	2.07	±	0.04	2%	-	-	±	-	-	0.09	-
ST-8-5d-3	Y	23.60	23.48					2.09										0.20	
8-5d-S-1	PO	22.00	21.88					0.33					0.21					0.20	2.19
8-5d-S-2	PO	22.40	22.28	22.08	±	0.20	0.9%	0.38	0.39	±	0.07	18%	0.24	0.27	±	0.07	28%	0.20	0.80
8-5d-S-3	PO	22.20	22.08					0.47					0.35					0.20	0.60
GPC2-8-5d-1	PO	29.60	29.44					0.64					0.45					0.20	1.39
GPC2-8-5d-2	PO	26.00	25.86	27.59	±	1.79	6.5%	0.57	0.57	±	0.07	12%	0.40	0.40	±	0.06	15%	0.20	1.39
GPC2-8-5d-3	PO	27.60	27.45					0.50					0.33					0.20	0.80

Note: BF (bar failure); PO (pull-out); SC (splitting of concrete); P_m (maximum pull-out load); τ_m (bond strength); $s_{m,LE}$ (slip corresponding to maximum pull-out load at the loaded end); $s_{m,FE}$ (slip corresponding to maximum pull-out load at the free end).

The bond-stress slip curve of FRP bars in concrete generally consists of three regions: ascending branch, peak point and, according to the type of failure, a softening branch. The initial linear ascending stage is characterised by a high initial stiffness attributed to the chemical adhesion between the concrete and the bar. When the adhesion is lost, the slip increases more rapidly as the bond is provided by mechanical interlock and friction until the maximum bond stress (τ_m) is reached. After the peak, the softening branch is registered, defined by a bond stress reduction and an increase of the bar slip.

Figs. 4-4 to 4-6 show the average bond stress-slip curves of BFRP bars in GPC at both free (FE) and loaded ends (LE) for the three identical samples having bar diameter 6 mm, 8 mm and 10 mm, with different embedded length, respectively. As expected, three typical stages can be identified. The chemical adhesion was lost almost immediately, as suggested by the low level of bond stress at the onset of the slip at the loaded end ($\tau_{ons,LE}$), given in Table 4.2, ranging from 0.07 to 1.06 MPa. The early loss of chemical adhesion implies that the bond is mainly dependent on the mechanical interlock offered by the bar ribs and the concrete (Achillides and Pilakoutas, 2004a). In the ascending branch, the stress increase was accompanied by a slip increase following a linear behaviour until the peak point. The linear ascending branch of BFRP bars in GPC is consistent with that observed for pull-out studies of similar materials such as GFRP bars in PCC (Baena, 2010; Rezazadeh et al., 2017).

After the peak point, the bond stress dropped sharply, followed by minor slippage for all the samples, except the sample *6-15d* that exhibited a small region of constant stress level as shown in Fig. 4.4c. The softening branches of the samples that failed due to bar rupture displayed a sharp reduction of the stress with limited slips, indicating the brittle failure along with a significant energy release. A pronounced reduction in bond stress was also observed for the sample *8-5d*, which failed due to bar pull-out with a sudden loss of bond stress after the peak point. The sample *10-5d* also failed due to bar pull-out but exhibited a more extended softening branch with a sharp falling slope. A similar bond loss along with small slips was illustrated during pull-out tests of BFRP bars in PCC cubes (El Refai et al., 2015a). It is worth noting that the softening branch for the sample *10-15d* was not recorded as the concrete cube split abruptly into two parts during the test.

Due to the low longitudinal elastic modulus of BFRP bars, there existed a difference between the slips measured at the bar ends, where the free end slipped at the maximum bond stress between 0.07 and 0.34 mm, and the loaded end slipped between 0.11 and 1.41 mm. Hence, the bond behaviour of BFRP bars was characterised by two curves, i.e. the bond stress-

slip response at both the free and loaded ends. As soon as the pull-out test began, after the chemical adhesion between the bar and surrounding concrete was lost, the loaded end slip could be observed, and it increased rapidly. On the other hand, the onset of the slip at the free end happened at a higher level of stress, as seen in Fig. 4.4 and Fig. 4.5a and b, and it developed at a slower pace than that at the loaded end. The difference between the slips at the free and loaded ends implies the nonlinear distribution of shear bond stress along the BFRP bar embedded portion, which can be attributed to the peak bond stress moving progressively towards the bar free end as the load increases (Benmokrane et al., 1996).

(a)

(b)

(c)
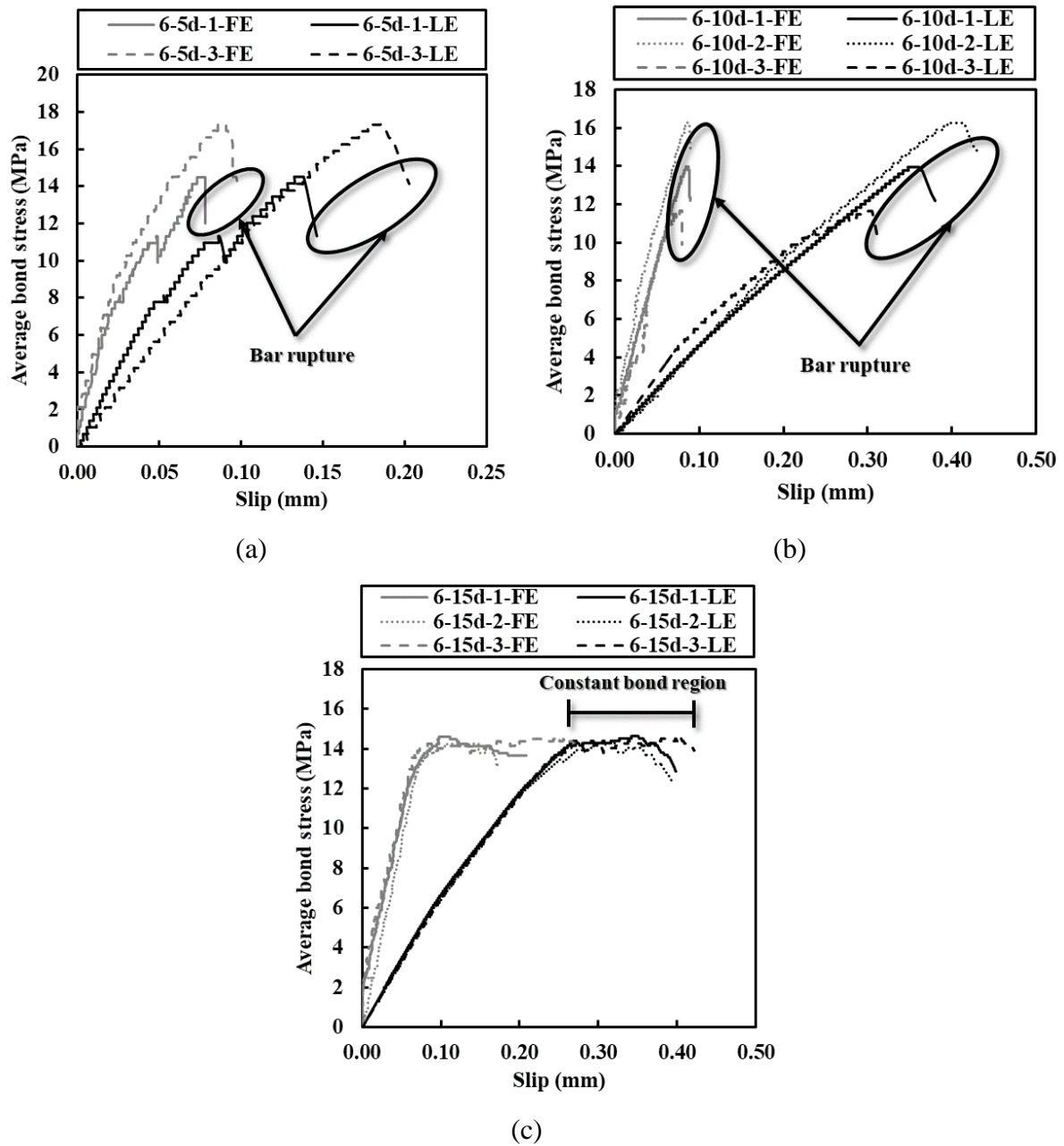
Fig. 4.4 Average bond-stress slip curves at the free end (FE) and loaded end (LE) of samples 6 mm bar diameter, all failed due to bar rupture: (a) *6-5d*, (b) *6-10d*, (c) *6-15d*.

(a)

(b)

(c)
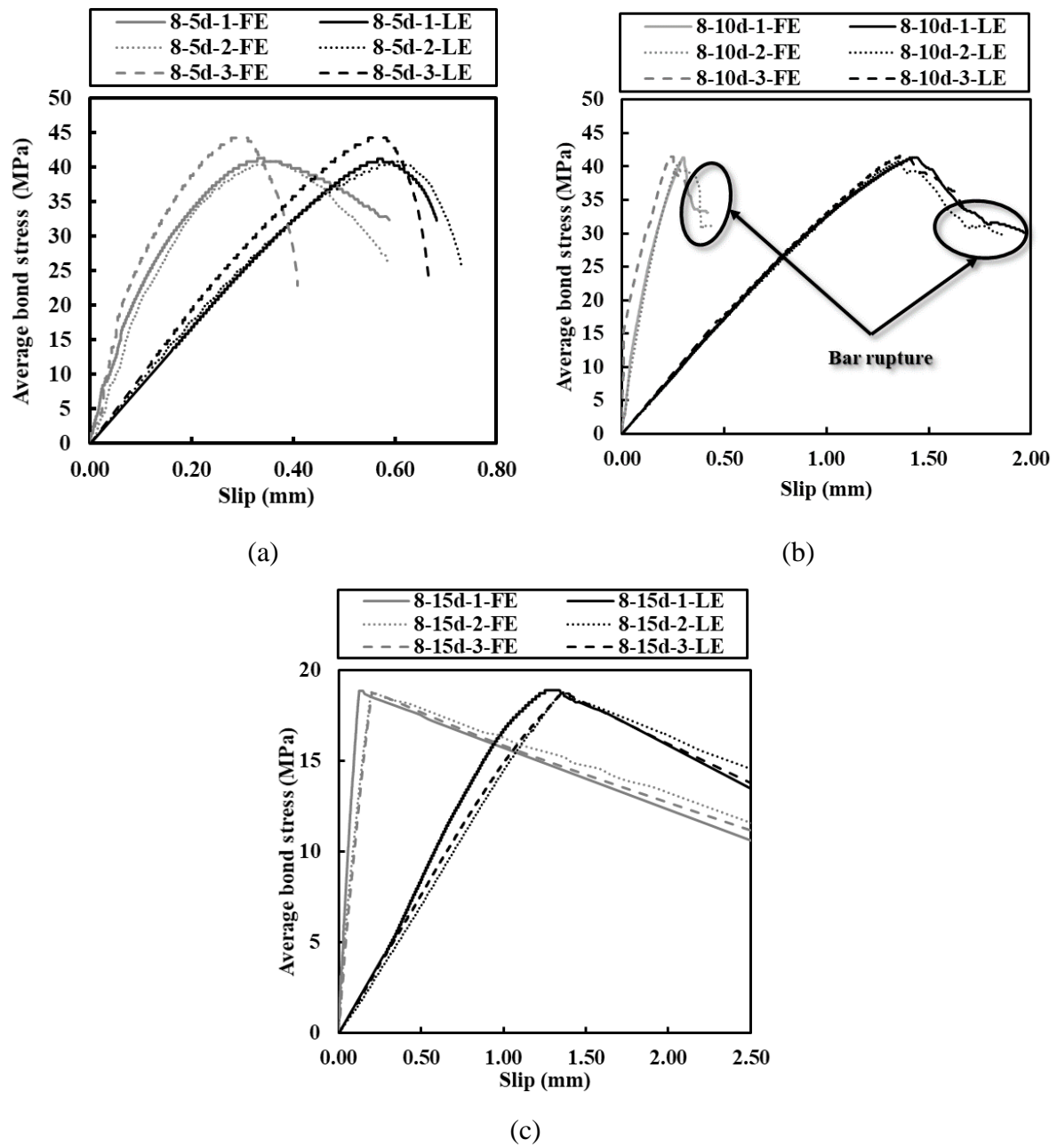
Fig. 4.5 Average bond-stress slip curves at the free end (FE) and loaded end (LE) of samples 8 mm bar diameter: (a) *8-5d* failed due to pull-out, (b) *8-10d* failed due to bar rupture, (c) *8-15d* failed due to pull-out.

(a)

(b)

(c)
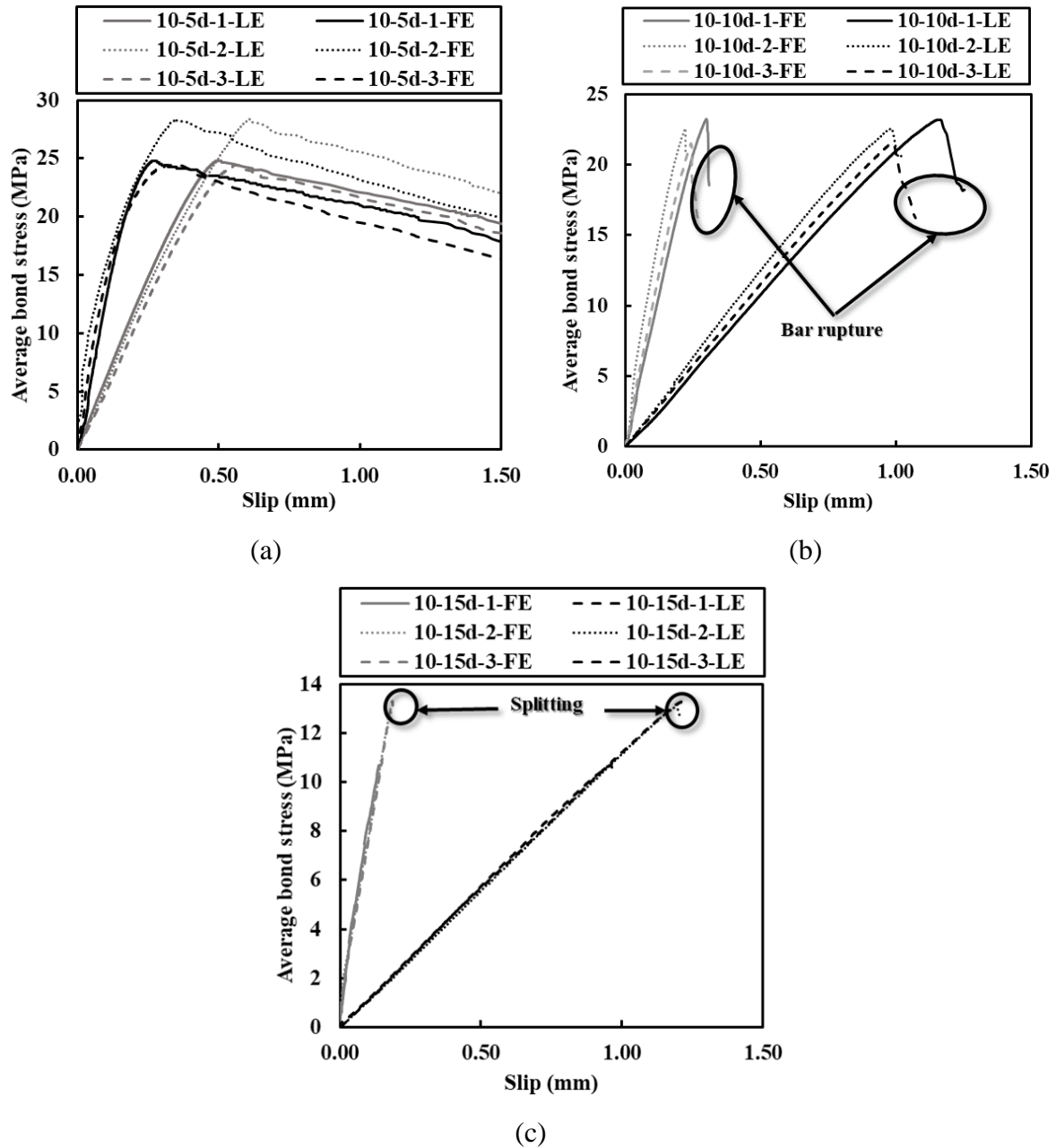
Fig. 4.6 Average bond-stress slip curves at the free end (FE) and loaded end (LE) of samples 10 mm bar diameter: (a) *10-5d* failed due to pull-out; (b) *10-10d* failed due to bar rupture; (c) *10-15d* failed due to concrete splitting.

4.3.2   Bond strength

The bond strengths of different pull-out samples are displayed in Table 4.2. It is worth noting that the samples *8-5d* and *8-10d* recorded particularly high bond strength values. Such result can be discussed considering Table 4.3, which summarises the different configurations (sets) tested, the sample repetitions, the total number of tests and the bond strength coefficient of variation (COV) of the present study in comparison with those of available studies of pull-out

tests of steel and FRP bars in concrete blocks (Ahmed et al., 2008; Baena, 2010; El Refai et al., 2015b; Tekle et al., 2016). In this study, three to four samples were tested for each set, similarly to the reference studies. The bond strength COV was found to be between 0.4% and 16.5%, suggesting a good estimate of the failure load for BFRP bars in GPC, also in agreement with those reported in the reference studies. The preliminary results of the statistical analysis based on three to four repetitions should be confirmed in the future on a broader number of samples. Therefore, as good repeatability of the bond strength values of the samples *8-5d* and *8-10d* were observed in this study, further experimental tests should be run to support such findings. The effects of different factors on the bond strength of BFRP bars in GPC are analysed and discussed in detail below.

Table 4.3 Comparison of COV of maximum bond stress with existing studies.

Author	Material	Concrete	Sets	Repetitions	Total number of tests	COV
Present work	B, S	GPC	14	3 or 4	48	0-17%
El Refai et al. (2015)	B, G	PCC	16	3	48	2-30%
Baena (2010)	C, G, S	PCC	23	2 or 3	88	1-41%
Tekle et al. (2016)	G	GPC	9	3	27	4-16%
Ahmed et al. (2008)	C, G, S	PCC	8	5	40	2-21%

Note: B (basalt FRP); G (glass FRP); C (carbon FRP); S (steel); PCC (Portland cement concrete); GPC (geopolymer concrete).

4.3.2.1 Effect of embedment length

Fig. 4.7 shows the effect of BFRP bar embedment length in GPC on bond strength, which indicates that the increase of bar embedment length from $5d_b$ to $15d_b$ resulted in a reduction of the bond strength of 52% for 8-mm bars and 55% for 10-mm bars, respectively, while only a 5% reduction of bond strength can be observed for 6-mm bars. The graph indicates that the 6-mm bar samples exhibited lower bond performance than expected since the bond strength was supposed to exceed that of higher bar diameters, as discussed in the next paragraph.

The reduction in bond strength with the increase of embedment length can be attributed to (1) the nonlinear distribution of bond stress along the bar-concrete interface and (2) a more extensive surface area of contact between bar and concrete, which lowers the bond strength. The changing trend observed for BFRP bars in GPC agrees with the findings of pull-out studies on similar materials such as BFRP bars in PCC (El Refai et al., 2015b), where a bond strength reduction of up to 29% was reported, and different FRP bars in PCC (Benmokrane et al., 1996; Achillides and Pilakoutas, 2004a). The embedded length also influenced the failure mode,

where shorter embedded length ($5d_b$) led to a pull-out failure such as in samples **8-5d** and **10-5d**, while higher embedded length ($15d_b$) caused the splitting of concrete, such as in samples **10-15d**, as discussed in detailed in Section 4.3.4.
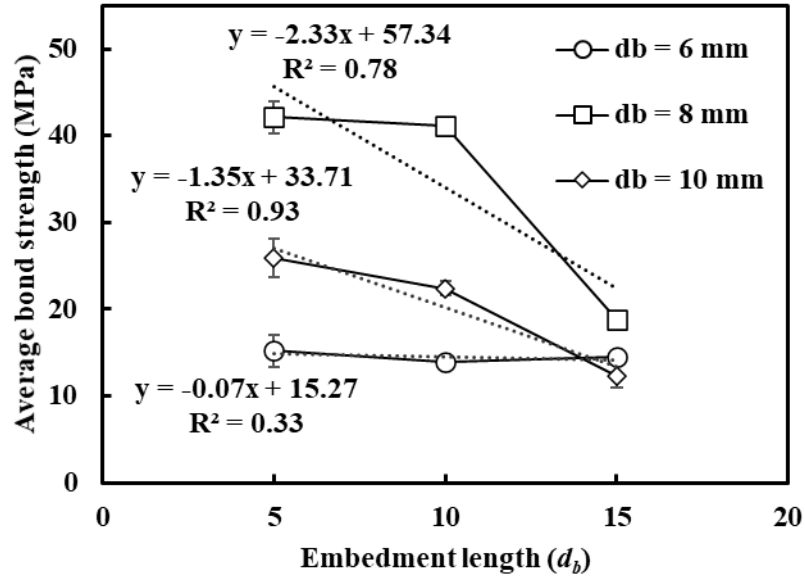
Fig. 4.7 Average bond strength between BFRP bar and geopolymer concrete against embedment length.

Fig. 4.8 displays the slips at the bar loaded and free ends for different bar diameters and embedment lengths, and Fig. 4.9 shows the bond stress-slip curves at the loaded end of samples having 8-mm bar diameter and different embedment lengths. Fig. 4.8 suggests that higher embedment length resulted in higher loaded end slip at the peak bond stress while it led to no significant variation for the free end slip at peak bond stress. A similar outcome was found in studies investigating GFRP bars in PCC and GPC (Mazaheripour et al., 2013a; Tekle et al., 2016; Saleh, 2018). Consequently, Fig. 4.9 reflects that the initial stiffness reduced with the increase of the embedment length, as reported by other studies (Achillides and Pilakoutas, 2004a; Saleh, 2018).
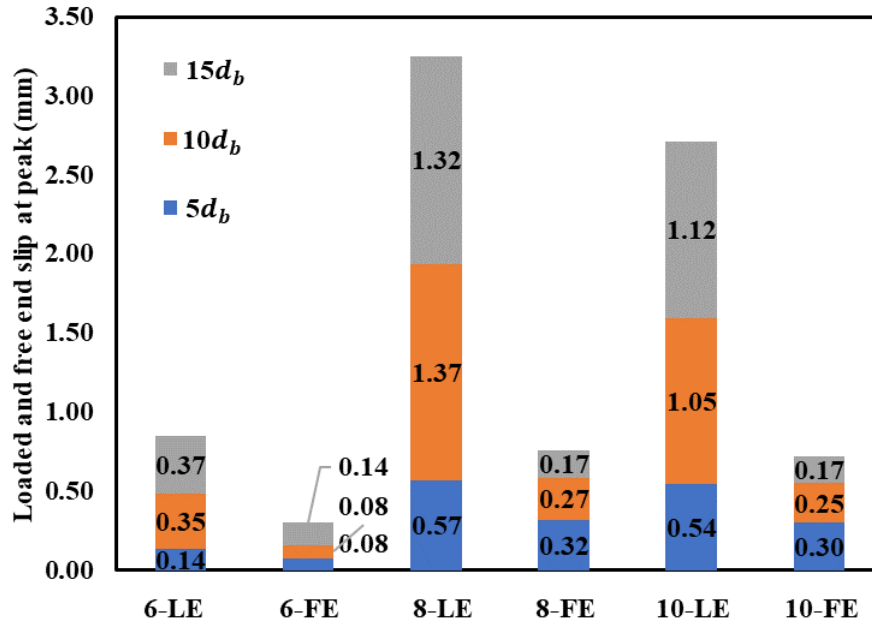
Fig. 4.8 Bar slip at loaded and free end for different bar diameter and embedment length.
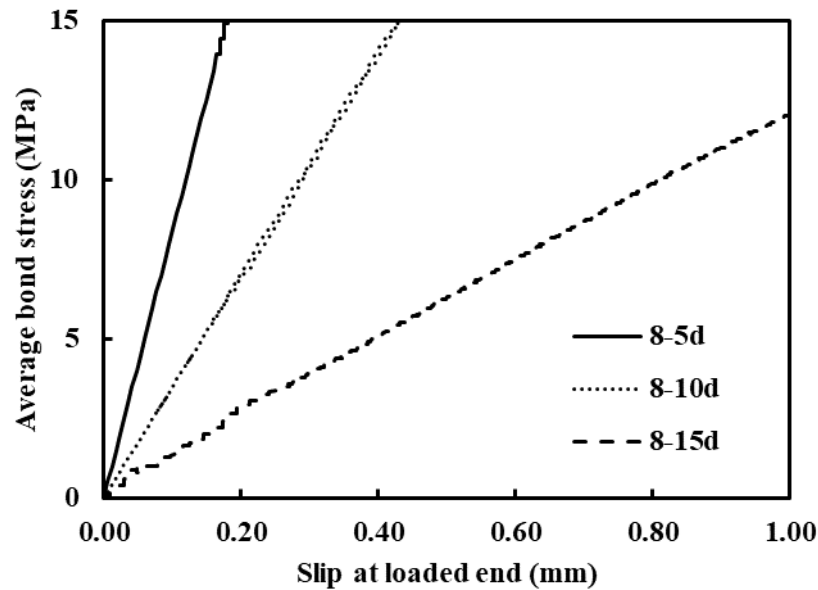
Fig. 4.9 Bond stress-slip at loaded end curve of 8-mm bar diameter embedded for different lengths.

4.3.2.2   Effect of bar diameter

Fig. 4.10 shows the effect of BFRP bar diameter on bond strength, indicating a reduction of bond strength with increasing diameter, which is consistent with the findings on BFRP bars in PCC (Li et al., 2017), CFRP bars in PCC (Achillides and Pilakoutas, 2004a), and GFRP bars in GPC (Tekle et al., 2016). The bond strengths for 10-mm bars were about 34% to 46% lower

than those for 8-mm bars with the same embedded length. The bond strength drop with increasing diameter can be ascribed to three phenomena that increase with the size of the bar: (1) nonlinear distribution of stress along the concrete-bar interface; (2) shear lag effect; (3) Poisson's effect. First, for longer embedment lengths, the nonlinear bond stress distribution negatively affects the average bond stress. Second, for a bar subject to a tensile load applied to the surface, the shear lag effect can be described as a non-uniform distribution of the normal stress through the cross-section of the bar, where the maximum stress (σ_{max}) is found at the bar surface and the minimum stress at the bar core. Thus, it exists a difference between σ_m and the average stress over the whole cross-section of the bar (σ_{av}). Increasing the bar diameter increases the difference between σ_m and σ_{av}, especially due to relatively low axial shear stiffness of FRP bars (Achillides and Pilakoutas, 2004a). Third, the Poisson's effect causes a slight reduction of the diameter of the bar under tension, reducing the friction and mechanical interlocking.

Nevertheless, the 6-mm bars unexpectedly exhibited an average bond strength of about 23% to 66% lower than 8-mm bars, which can be attributed to the premature failure caused by bar rupture. As discussed in Section 3.3.3, the 6-mm bars had relatively lower mechanical properties, adversely affecting their bond performance.
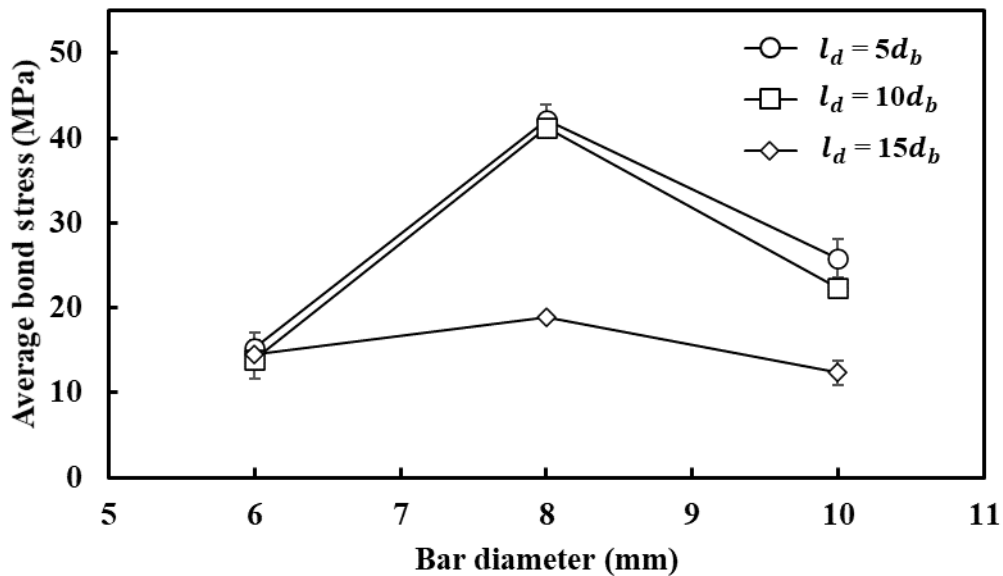
Fig. 4.10 Average bond strength between BFRP bar and geopolymer concrete against bar diameter.

4.3.2.3   Effect of bar surface treatment

As shown in Fig. 4.11a, the ribbed bar developed an average bond strength 47% higher than the sand-coated bar, with a bond strength of 42.11 MPa and 22.08 MPa, respectively. The bond stress-slip curves, shown in Fig. 4.11b, suggest similar initial stiffness between the ribbed and sand-coated bars, especially for the samples *8-5d-S-1* and *8-5d-S-2*. However, at a bond stress level of around 13 MPa, the bond stiffness of the sand-coated bar changed, leading to a pull-out failure at a lower stress than the ribbed bars. Similar behaviour was observed by Aiello et al. (2007) as ribbed GFRP bars exhibited high bond strength with low slip compared to other surface types such as sand coating.

These results only offer a preliminary indication of the effect of the surface treatment on the bond between BFRP bars and GPC as the comparison is based on limited data, i.e. one set of samples for each surface configuration. The result should be confirmed by a more extensive data set, including different bar diameters and embedment lengths.

(a)   (b)
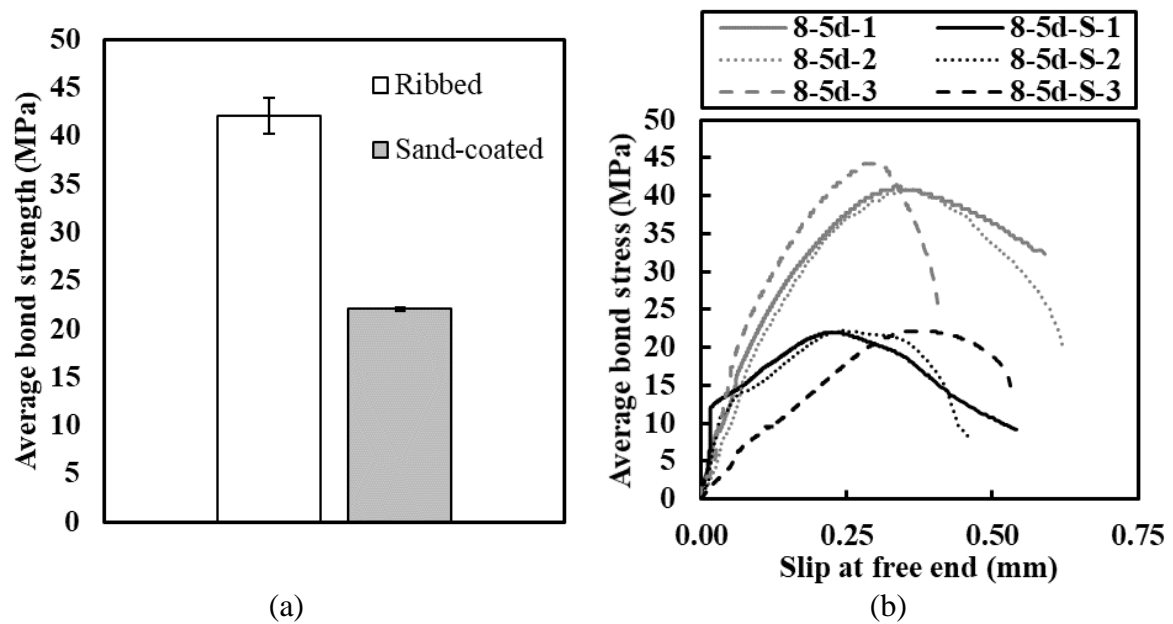
Fig. 4.11 Comparison between ribbed and sand-coated *8-5d* bars: (a) average bond strength; (b) bond stress-slip curve at the free end.

4.3.2.4   Effect of concrete compressive strength

Fig. 4.12 shows that the average bond strength of the GPC2 samples, which failed due to bar pull-out, was 27.58 MPa, 34% lower than that of the GPC1. The unexpected result was thus ascribed to the minor difference observed within the two concrete compressive strengths at 28 d. Furthermore, the lower workability and the rapid setting time of GPC2 at the time of casting could have produced bubbles and defects, reducing the quality of the bar-concrete interface. Inconclusive results were also found by Saleh (2018), studying GFRP bars in high strength

concrete where significant bond strength variations led to no clear conclusion on the effect of the concrete strength.

The author advises further investigating the phenomenon by increasing the concrete compressive strength range to appreciate different bond strengths and damage patterns at the bar-concrete interface. Furthermore, it is recommended to consider different bar diameters and embedment lengths to obtain sufficient data to draw solid conclusions.
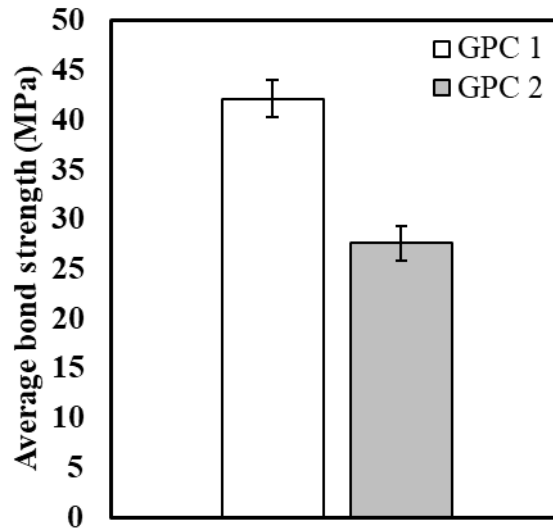
Fig. 4.12 Influence of compressive strength of GPC on the average bond strength.

4.3.3 Bond ductility

Good material mechanical properties at the local scale allow the bond action to establish the collaboration between reinforcement and concrete, ensuring an adequate level of safety. On the other hand, the bond also controls the structural behaviour by providing an adequate level of ductility. The bond ductility is considered the ability to develop large reinforcement slips while withstanding the load, allowing the formation of secondary cracks between two main contiguous cracks (CEB-FIP, 2000). To evaluate the ductility of the test results, a slip-ductility ratio was calculated from the bond stress-slip curve according to Fig. 4.13 (Cohn and Bartlett, 1982) and the following:

$$r = \frac{\Delta_{0.85}}{\Delta_C} \tag{4.4}$$

where $\Delta_{0.85}$ is the slip corresponding to 85% of the maximum bond stress (τ_m) and Δ_C is obtained at the intersection of the tangent to the bond stress-slip curve at the origin, with the slip corresponding to the maximum bond stress (τ_m).
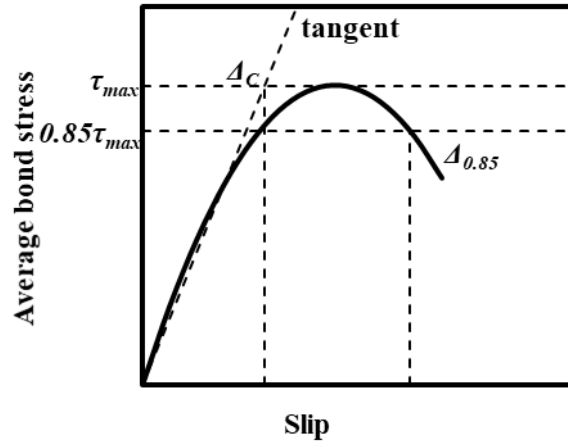
Fig. 4.13 Definition of slip-ductility ratio to evaluate the bond ductility.

A ratio equal to 1 implies a brittle and sudden failure, while higher ratio values indicate increased ductility. The slip-ductility ratio for the samples *6-15d*, *8-15d* and *10-10d* are graphically displayed in Fig. 4.14. For the *6-15d* samples, the slip-ductility ratio (r) was 1.89, for the *8-15d* sample r ranged from 1.47 to 1.60, and for the *10-10d* sample r was between 1.10 and 1.17. Thus, the figures and the ratio values suggest that the *10-10d* samples exhibited limited ductility. On the other hand, the *6-15d* samples offered higher ductility, as evidenced by the plateau observed in the bond stress-slip curve (Fig. 4.14a).

In addition, even though the concrete cover was 70 mm, the *10-15d* samples failed in a very brittle and violent way due to splitting, indicating a total lack of ductility. Splitting is considered a premature type of failure that prevents the full development of the bond capacity. Therefore, for future studies, transverse reinforcement should be adopted to avoid a sudden failure, thus increasing the sample ductility and allowing the softening branch measurement. On the other hand, compared to the pull-out test, the concrete cover splitting tendency could be better estimated considering the eccentric pull-out test and the ring pull-out test.

(a)

(b)

(c)
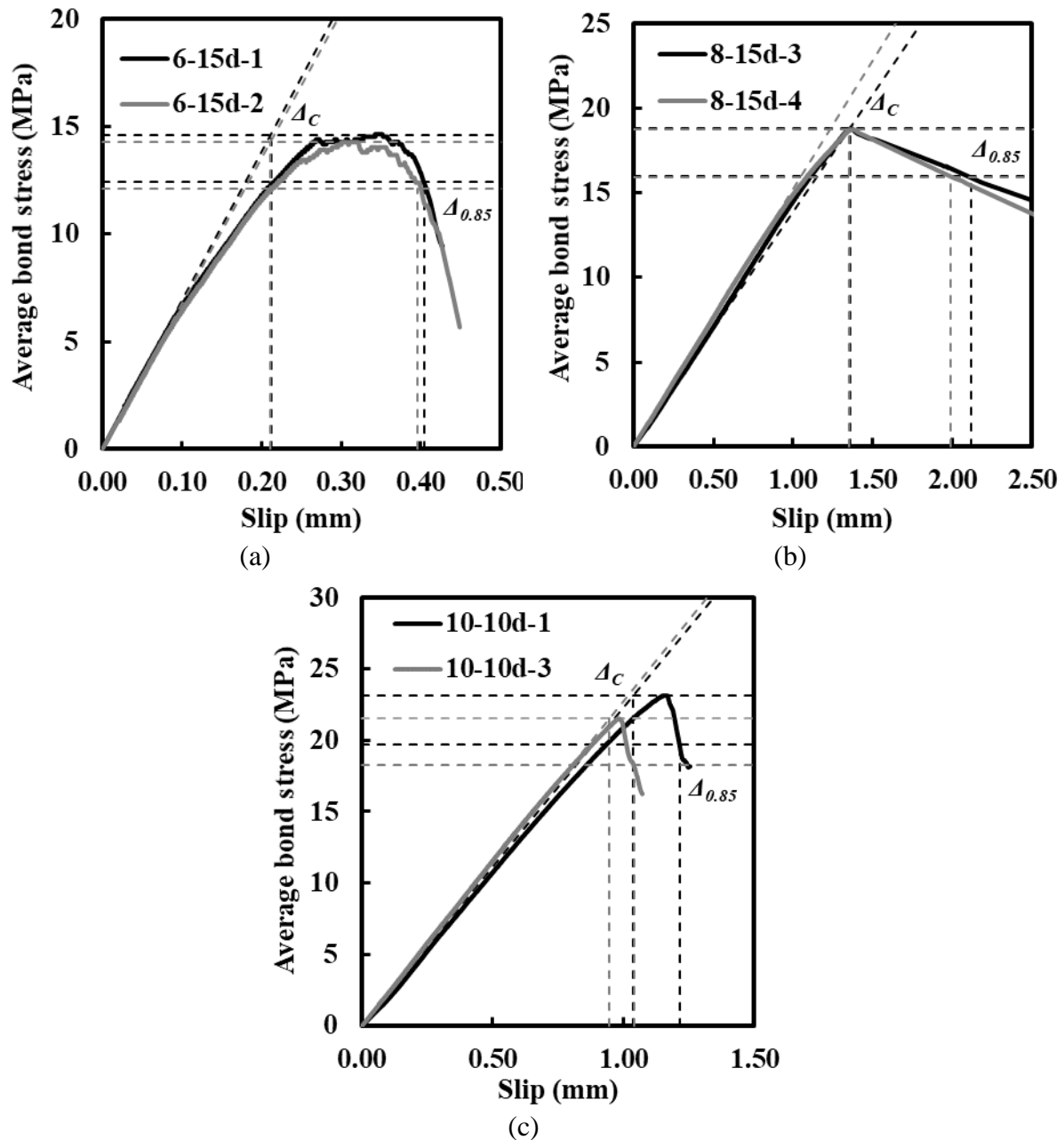
Fig. 4.14 Ductility of the bond for different samples: (a) *6-15d*; (b) *8-15d*; (c) *10-10d*.

The bond ductility can also be discussed considering the measurement variability of the bond stress-slip curve. Fig. 4.15 shows the average bond stress-slip curves of the three samples *10-5d*. In Fig. 4.15a, the standard deviation (SD) of the average bond stress is plotted. In the ascending branch, the data were consistent, with a minimal SD, but the SD increased significantly after the peak, suggesting higher measurement variability. A similar tendency was also observed for the slip measurements in Fig. 4.15b. The higher variability after the peak could be ascribed to the type of failure, i.e. the crushing of the concrete lugs. In samples characterised by short embedment length and high bond strength, high stresses are localised at

the bond interface, emphasising the concrete crushing and causing excessive brittle failure (Fava et al., 2016).

Fig. 4.16 displays a comparison of the free and loaded end slips of the samples **8-5d** and **8-10d** with literature pull-out tests data of 8-mm BFRP embedded in a PCC block for a length of $5d_b$ and $10d_b$ (El Refai et al., 2015b; Dong et al., 2018a; Yang et al., 2018). It is worth noting that, given the novelty of the research topic, no data are currently available in the literature to directly compare the bond performance of BFRP bars in GPC obtained with the current study. Moreover, while the SD calculated on three measurements can only provide a qualitative assessment, a statistical analysis on a higher number of samples could confirm the reliability of the measurements more robustly. Nevertheless, the comparison suggests that the SD of the slips at the peak was remarkable for most of the studies, being the SD of the current work the smallest one. Thus, while the ascending branch could be considered stable, the peak and softening were characterised by higher uncertainty. Hence, for a conservative design, the standard provisions should be formulated considering the ascending portion of the bond stress-slip curve, related to the serviceability condition, and neglecting the contribution of bond after-peak (Cosenza et al., 2002).

(a)   (b)
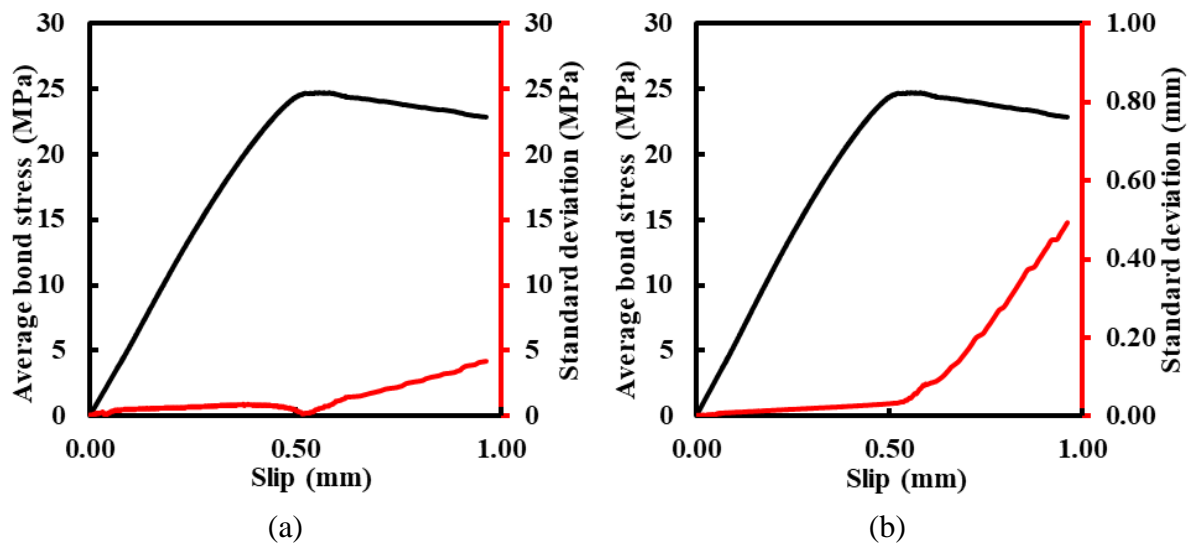
Fig. 4.15 Average bond stress-slip curve (**10-5d**) and standard deviation: (a) SD of the bond stress; (b) SD of the slip.
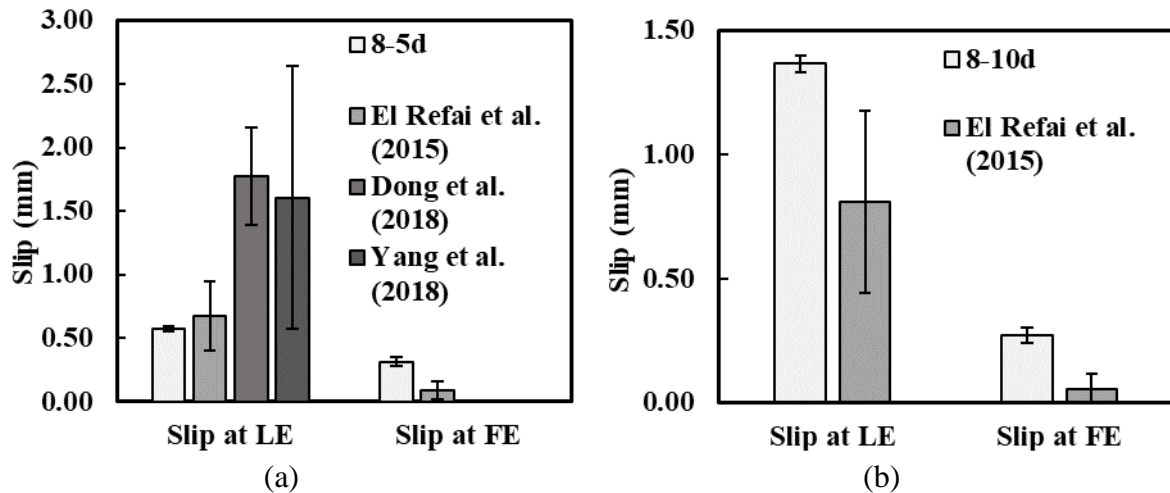
Fig. 4.16 Comparison between experimental and literature data of slips at loaded (LE) and free (FE) ends: (a) $5d_b$ embedment length; (b) $10d_b$ embedment length.

4.3.4 Failure modes

Fig. 4.17 shows the typical failure modes of BFRP bar pull-out tests, including bar pull-out (PO), concrete splitting (SC), and bar rupture (BF). The failure mode was affected by the embedment length. Shorter embedment length ($5d_b$), e.g. in samples **8-5d** and **10-5d**, provided insufficient interaction area between BFRP bars and GPC, leading to pull-out failure. Bar pull-out is experienced when the embedded length is shorter than the development length (Pecce et al., 2001), representing the minimum length of the bar embedded in the concrete capable of developing the strength necessary to transfer the tensile force from the reinforcement to the concrete.

Fig. 4.17a illustrates the sample **8-5d** cut open to inspect the interface zone between the bar and the concrete, indicating that the pull-out failure was due to concrete lugs shearing off, causing the embedded concrete surface to become smooth, while the bar ribs were intact, implying a high rib shear strength and good integrity between the ribs and the successive bar layers. The pull-out failure usually occurs at the interface when the shear bond strength between the bar and surrounding concrete is exceeded. When the concrete provides an adequate amount of confinement to prevent splitting, the cracks remain limited to the portion surrounding the bar, leading to a pull-out failure (CEB-FIP, 2000). Bar pull-out is the preferred type of failure during pull-out tests, as it provides an estimation of the bonding between bar and concrete. On the other hand, concrete splitting and bar rupture are considered premature failures as the interface between bar and concrete is still intact after the sample failure (Tekle, 2017).

It is worth noting that, according to the literature (Achillides and Pilakoutas, 2004a), for concrete strength higher than 30 MPa, the bond failure is expected to occur due to the peel-off

of the bar surface layers. However, in this study, the damage was found in the concrete lugs rather than on the bar layers. The rapid setting time of the fresh GPC could have impeded proper compaction of the concrete along the embedded length, resulting in local imperfections that weakened the concrete in contact with the reinforcement. On the other hand, the bar surface deformations exhibited high shear strength as no delamination was found.

(a)

(b)

(c)   (d)
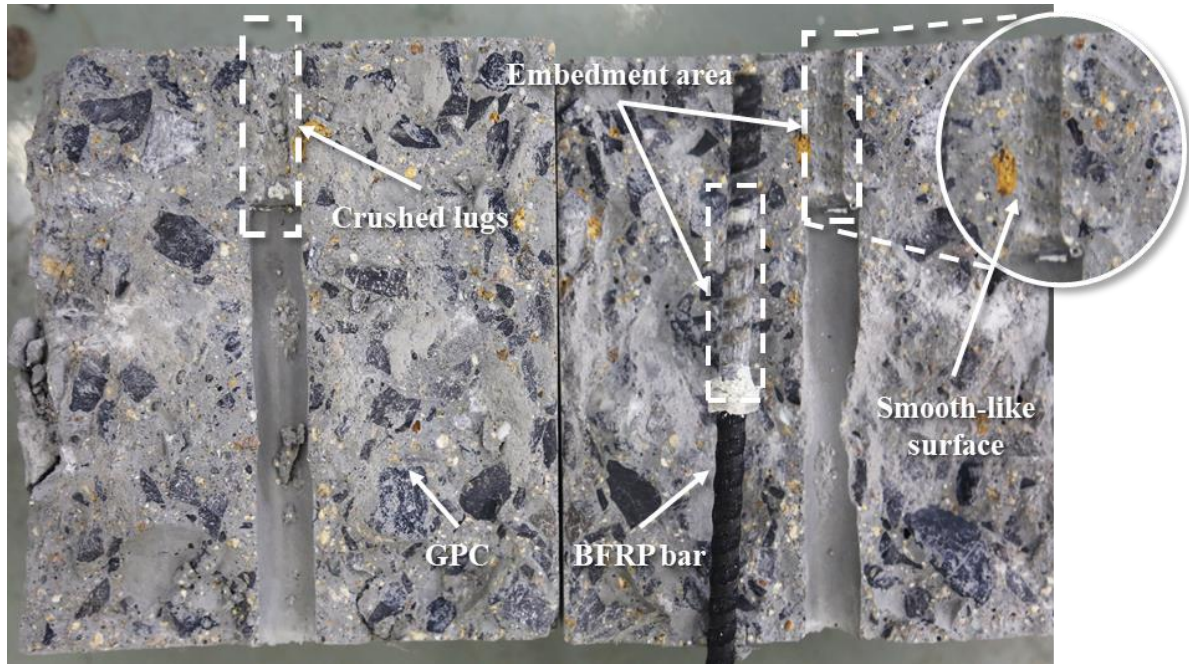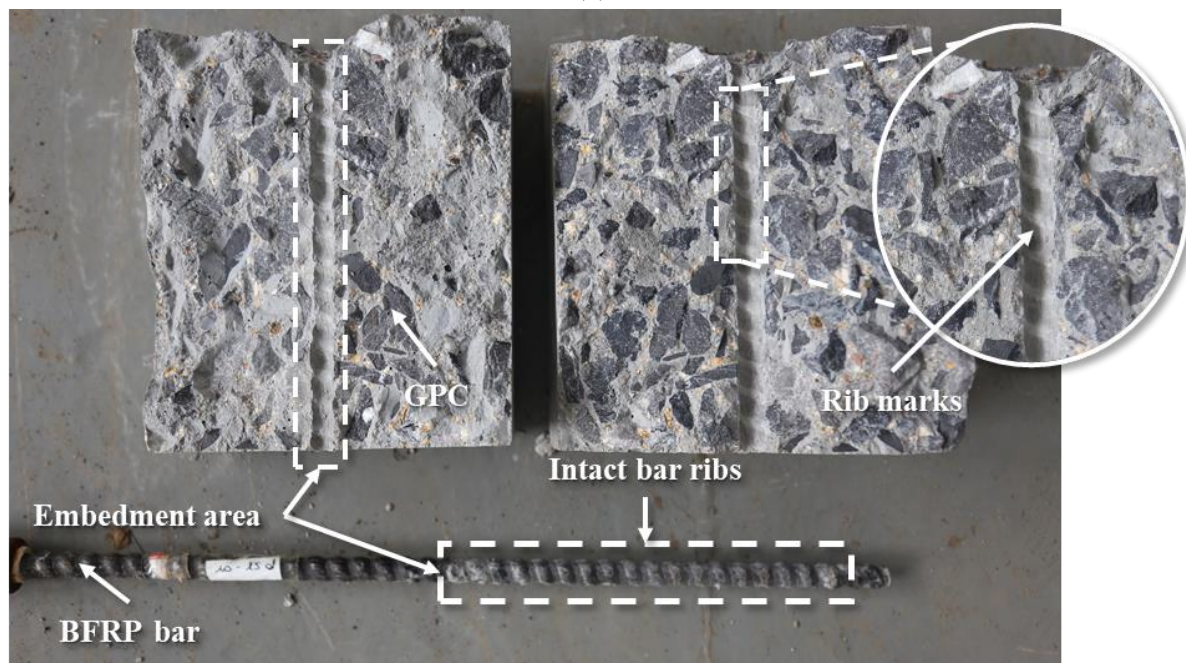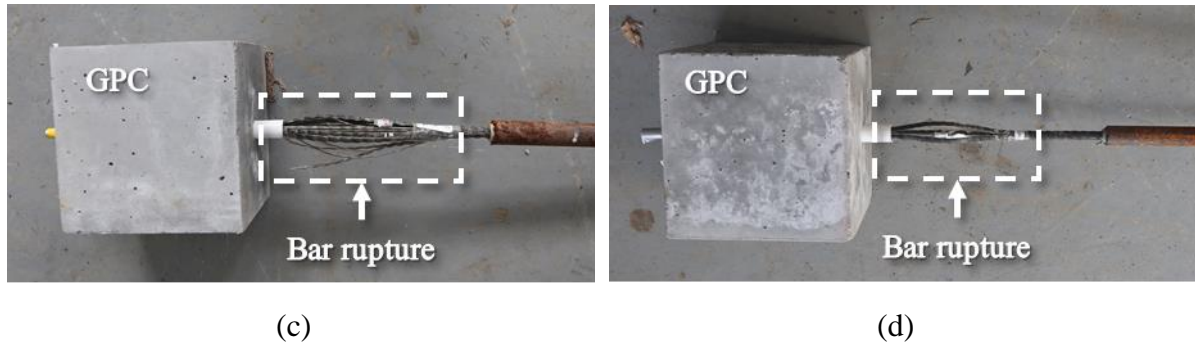
Fig. 4.17 Typical failure modes under pull-out tests due to: (a) pull-out of the bar for sample **8-5d**; (b) splitting of concrete for sample **10-15d**; (c) bar rupture in tension for sample **6-5d**; d) bar rupture in tension for sample **8-10d**.

Fig. 4.17b shows the sample **10-15d** that split open during the test, suggesting that the longer embedment length ($15d_b$) would cause concrete splitting. Only a thin layer of concrete can be found on the bar surface while the bar surface and the concrete at the interface were still intact, indicating that the maximum bond strength was not attained. Furthermore, the splitting failure is generally associated with poor confinement. The radial stress originated by the tensile pull-out load generates some cracks at the interface between the rebar and the surrounding concrete. When the concrete confinement is not sufficient to bear the radial stress and the concrete tensile strength is reached, the cracks propagate towards the concrete surface, resulting in splitting failure while the interface zone with the reinforcement remains intact. The present findings are consistent with the behaviour observed for GFRP bars in PCC (Pecce et al., 2001; Yan et al., 2016) and GFRP bars in GPC (Maranan et al., 2015b; Tekle, 2017).

The splitting failure can be better understood considering the schematic representation of the bond force given in Fig. 4.18. The bond force develops at an angle (α) with the bar axis, which depends on the bar elastic modulus, the concrete shear strength at the location of the microcracks, and the bar surface (CEB-FIP, 2000). The bond force can be therefore divided into a tangential component (τ), developing along the bar interface, and a radial component (σ_r), in the normal direction to the bar axis. The radial component is balanced by a tensile stress ring (σ_t) generated in the concrete around the reinforcement. At this stage, the splitting resistance of the concrete surrounding the reinforcement plays a critical role as if the value of the tensile hoop exceeds the concrete tensile strength, splitting cracks may develop longitudinally along the reinforcement, causing the splitting failure of the sample. Increasing the angle (α), increases the radial component (σ_r) leading to earlier splitting failure. As above-mentioned, α depends on the bar surface deformations. Steel bars display strong surface ribs, which generate higher radial bond stress, thus inducing earlier splitting failure. On the other

hand, the lower shear strength of the resin matrix reduces the strength of the FRP bars surface deformations compared to steel. Therefore, softer bar ribs generate lower radial stress (CEB-FIP, 2000).
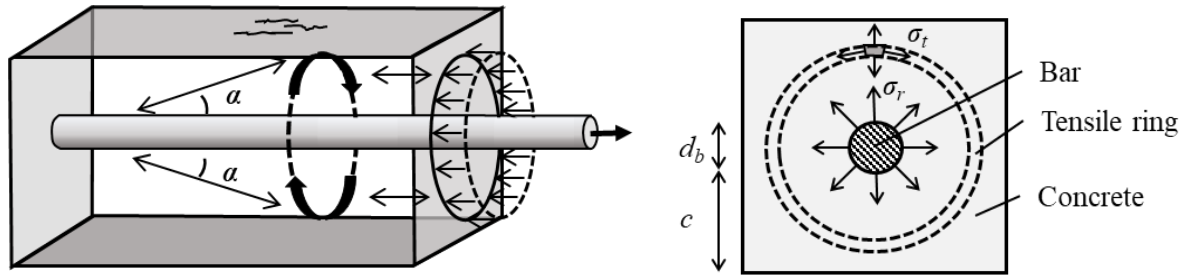
Fig. 4.18 Schematic representation of radial components of the bond force balanced against tensile stress rings in the concrete in the anchorage zone.

The splitting tendency was investigated by Tepfers (1973), who proposed three predictive models to calculate the bond stress (τ) causing splitting. The models, which consider the concrete in the elastic stage, partly cracked elastic stage and plastic stage, are given in Eqs. (4.5) - (4.7) and shown in Fig. 4.19a, b and c, respectively.

$$\frac{\tau}{f_{ct}} = \frac{1}{\tan \alpha} \frac{\left(c + \frac{d_b}{2}\right)^2 - \left(\frac{d_b}{2}\right)^2}{\left(c + \frac{d_b}{2}\right)^2 + \left(\frac{d_b}{2}\right)^2} \tag{4.5}$$

$$\frac{\tau}{f_{ct}} = \frac{\left(c + \frac{d_b}{2}\right)}{1.664 \, d_b \tan \alpha} \tag{4.6}$$

$$\frac{\tau}{f_{ct}} = \frac{2c}{d_b \tan \alpha} \tag{4.7}$$

where τ is the bond stress (MPa), f_{ct} is the tensile strength of concrete (MPa), c is the concrete cover (mm), d_b is the bar diameter (mm), and the angle of the reaction force is $\alpha = 45°$.

The results of the samples *10-15d*, failed due to splitting, are plotted in Fig. 4.20 against the elastic, partly cracked elastic and plastic stages defined above. In addition, the experimental data are compared with results of pull-out tests run on CFRP, GFRP and steel bars placed centrally in a concrete sample (Tepfers, 1973). It was found that the samples *10-15d* data lie between the elastic and the partly cracked elastic range, suggesting a high splitting tendency, comparable to that of steel, that can be ascribed to the deep and strong ribs of the bar surface, visible in Fig. 4.17b. The result was supported by the experimental evidence as an abrupt failure was observed during the test, giving almost no warning before the cover splitting. As discussed

above, the interlaminar shear between bar layers appeared to be strong as no delamination was observed, and the failure was governed by the concrete strength.

The results found by Tepfers (1973) for sand-coated GFRP bars can be compared against those of the current study. The data obtained with sand-coated GFRP bars were better aligned on a plastic stage defined by a smaller angle, i.e. $\alpha = 30°$, suggesting that the sand coating provided lower lateral splitting pressure against the surrounding concrete than bars with large indentations, such as steel bars and the **10-15d** BFRP bars. The current study also observed such a trend as the radial bond stress developed by the sand-coated BFRP bars was not high enough to lead to splitting failure. To confirm the results, different diameters and embedment lengths of sand-coated bars should be tested.
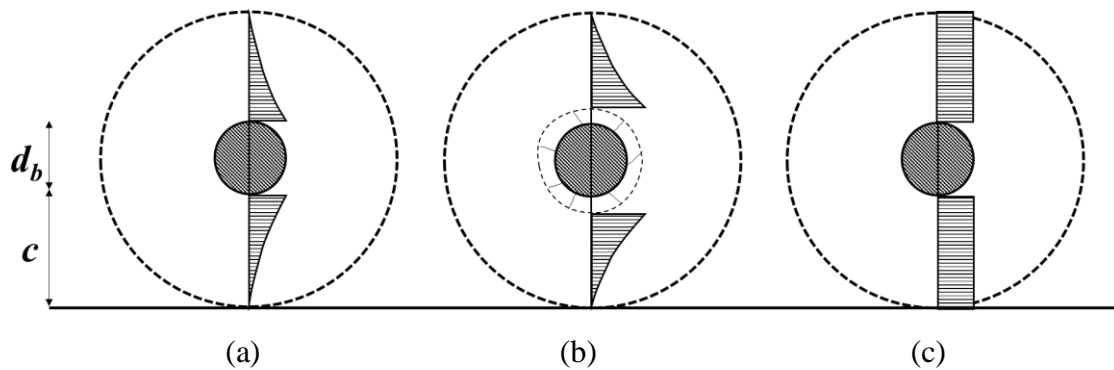
Fig. 4.19 Tensile stress distribution: (a) elastic; (b) partly cracked elastic; (c) plastic stage.
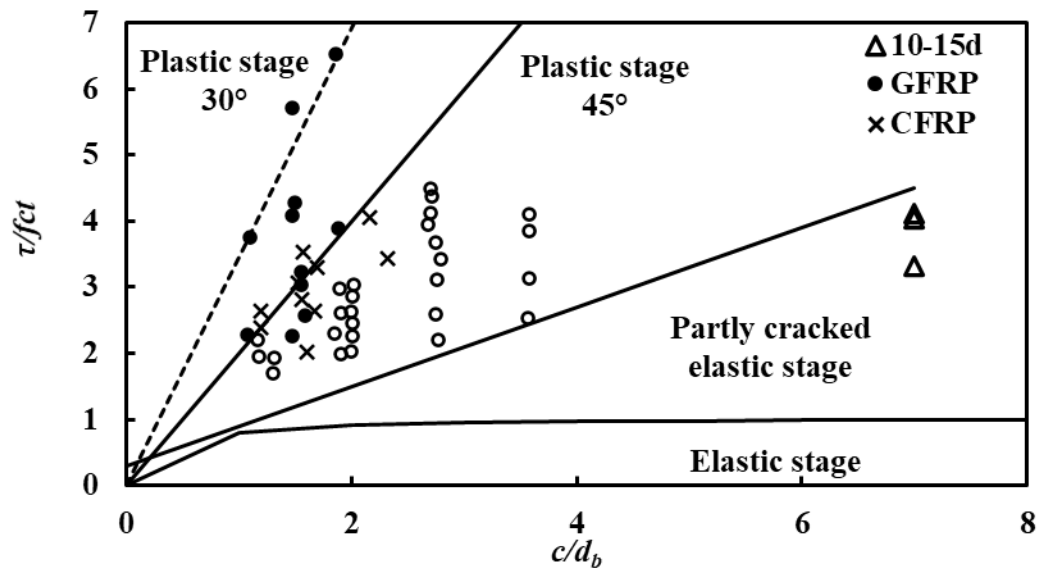
Fig. 4.20 Effect of thickness of concrete cover on bond capacity of pull-out specimens on the occurrence of concrete cover cracking along the bar.

Fig. 4.17c and d display the failure of specimens induced by bar rupture, which occurs when the bond is adequate, and the pull-out load reaches the bar tensile strength leading to its failure in tension. As for concrete splitting, the bar rupture is considered a premature type of failure as the interface between the bar and surrounding concrete is still intact (Tekle, 2017).

Table 4.4 compares the bar nominal tensile strength, the experimental maximum pull-out load and the failure mode observed during the tests. Some samples (*6-15* and *10-10*) failed due to bar rupture at the expected tensile stress, while others underperformed or exceeded the tensile strength. For instance, the samples *6-5d* and *6-10d* failed respectively at a load of 66% and 38% lower than the expected one, while the samples *8-10* overperformed and failed at a load level 46% higher than the expected one. Overall, all 6-mm BFRP bars failed due to bar rupture, regardless of the embedment length. The variability of bond performance can be ascribed to the variations of tensile stress-strain behaviour for 6-mm bars discussed in Section 3.3.3.

It is worth noting that the variation in the material properties is generally considered by the design codes, which recommend the use of safety factors for the material resistance. Given the higher variability characterising the FRP reinforcement compared to steel, the material safety coefficients are usually greater than those used for traditional steel reinforcement to assure the reliability of the section. However, given the different types of failure mechanisms attained by the FRP reinforced sections and the size-effect issue that can be encountered in FRP bars, further work is needed to assess the reliability of the safety coefficients (Iervolino and Galasso, 2012; ACI 440.1R, 2015; CAN/CSA-S6-14, 2017a).

Table 4.4 Comparison between tensile strength of BFRP bars of different diameters and maximum pull-out load and failure mode of the samples.

d_b (mm)	A_b (mm^2)	f_f (MPa)			P_f (kN)			P_m (kN)		
								5d	10d	15d
6	28.27	899.89	±	13.62	25.44	±	0.39	8.60[BF]	15.73[BF]	24.53[BF]
8	50.27	1117.6	±	16.70	56.18	±	0.84	42.33[PO]	82.83[BF]	56.73[PO]
10	78.54	876.37	±	34.97	68.83	±	2.75	40.60[PO]	70.40[BF]	58.13[SC]

Note: d_b (bar diameter); A_b (bar cross-sectional area); f_f (bar tensile strength); P_f (tensile load causing bar failure); P_m (average maximum pull-out load); BF (bar failure); SC (splitting of concrete); PO (pull-out).

4.3.5 Comparison of the bond of steel bars and BFRP bars to GPC

The bond behaviour of an 8-mm diameter steel bar embedded for $5d_b$ in GPC was investigated through pull-out tests for comparison purposes. As expected, the bond stress-slip relationship (see Fig. 4.21a), showed a linear ascending branch followed by a region of constant bond stress around the peak pull-out load. After the peak point, the samples failed due to bar rupture after yielding as the bond strength exceeded the bar tensile strength. The constant bond stress region represents one of the main differences between the bond performance of steel and BFRP bars. Consequently, the analytical BPE model (Eligehausen et al., 1983) developed for the steel-to-concrete interaction was later modified into the mBPE model (Cosenza et al., 1997) with no constant bond region to better represent the FRP-to-concrete interface behaviour. The constant bond region, together with the slip-ductility ratio ranging from 3.70 to 4.52, shown in Fig. 4.21b, suggests the higher ductility offered by the steel reinforcement compared to the BFRP reinforced samples.

Fig. 4.22 and Table 4.5 summarise the results of the current study and other references from the literature (Baena, 2010; Maranan et al., 2015a; Tekle, 2017) investigating the average bond strength of different bars (steel, BFRP, GFRP and CFRP bars) embedded in PCC and GPC. The comparison is based on the average bond strength normalised with the square root of concrete compressive strength. The studies led to conflicting conclusions on whether FRP bars offer improved bond strength than steel bars. As shown in Fig. 4.22, in the current study, the steel reinforced samples exhibited an average bond strength 46% lower than the BFRP reinforced samples. However, the comparison was based on one set of samples for each reinforcement type, considering one bar diameter and embedment length. Therefore, more robust conclusions could only be drawn from a broader data set with different bar diameters and embedment lengths.
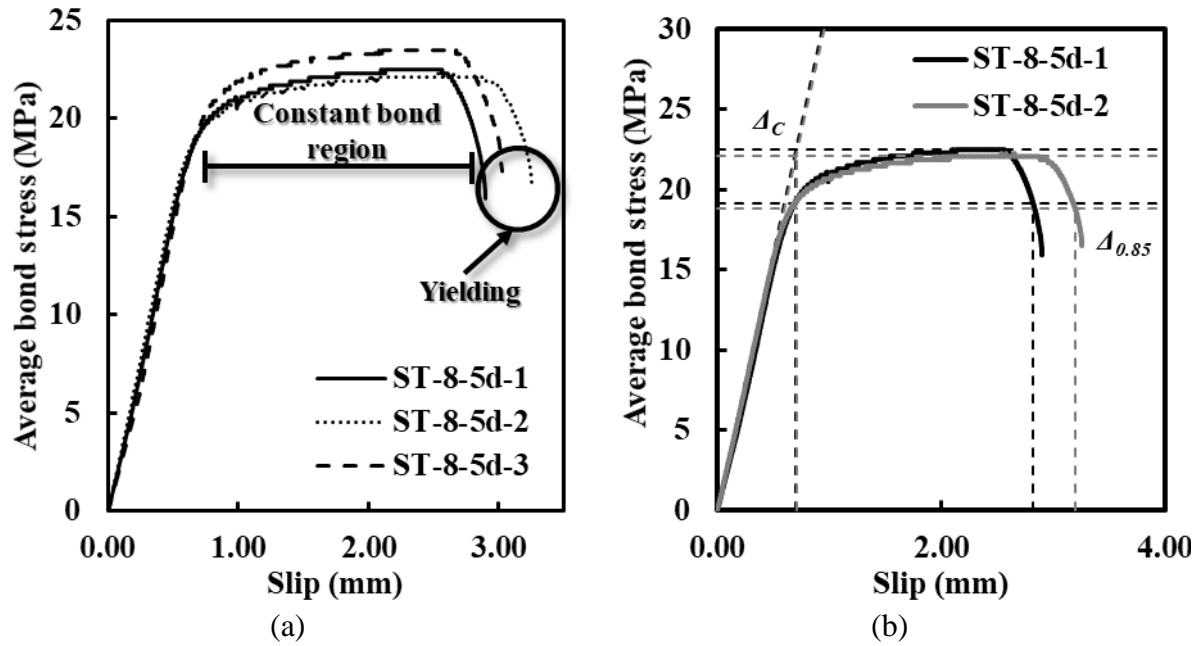
Fig. 4.21 8-mm steel bar diameter with $5d_b$ embedment length: (a) bond stress-slip curves; (b) slip-ductility ratio.
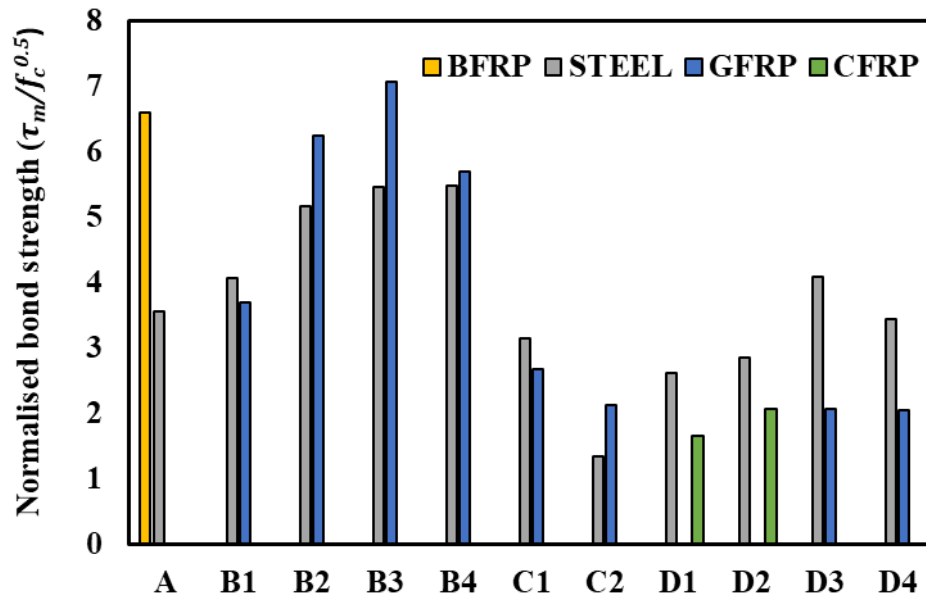
Fig. 4.22 Comparison between BFRP, steel, GFRP and CFRP bars bond performance based on the average bond strength normalised by the concrete compressive strength square root (Baena, 2010; Maranan et al., 2015b; Tekle, 2017).

Table 4.5 Comparison between BFRP, steel, GFRP and CFRP bars bond performance based on the average bond strength normalised by the concrete compressive strength square root.

Sample	Study	d_b	l_d	Concrete	FRP Fibre	FRP τ_m (MPa)	FRP f_c (MPa)	FRP $\tau_m/f_c^{0.5}$	STEEL τ_m (MPa)	STEEL f_c (MPa)	STEEL $\tau_m/f_c^{0.5}$
A	Current study	8	$5d_b$	GPC	B	42.11	40.67	6.60	22.68	40.67	3.56
B1	Maranan et al. (2016)	16	$5d_b$	GPC	G	21.27	33.00	3.70	23.43	33.00	4.08
B2		16	$5d_b$		G	35.93	33.00	6.25	29.67	33.00	5.16
B3		16	$5d_b$		G	40.61	33.00	7.07	31.43	33.00	5.47
B4		16	300 mm		G	32.79	33.00	5.71	31.50	33.00	5.48
C1	Tekle (2017)	16	$3d_b$	GPC	G	18.84	49.30	2.68	22.53	50.80	3.16
C2		16	$9d_b$		G	15.00	49.30	2.14	9.57	50.80	1.34
D1	Baena (2010)	12	$5d_b$	PCC	C	8.79	28.25	1.65	14.07	28.60	2.63
D2		16	$5d_b$		C	10.77	26.92	2.08	15.23	28.41	2.86
D3		12	$5d_b$		G	15.15	53.40	2.07	28.99	49.99	4.10
D4		16	$5d_b$		G	15.56	57.25	2.06	25.40	54.35	3.45

Note: B (basalt FRP); G (glass FRP); C (carbon FRP), GPC (geopolymer concrete); PCC (Portland cement concrete).

4.4 Concluding remarks

This chapter presented a series of pull-out tests carried out to investigate the bond behaviour of BFRP bars in GPC. The effect of key parameters such as bar diameter, embedment length, surface treatment and concrete compressive strength on bond behaviour were investigated. Each sample provided information about failure mode, average bond strength, slip at the free and loaded ends, and bond stress-slip curve. The main conclusions can be drawn as follows:

- For the majority of the samples, the bond stress-slip curve consisted of a linear ascending branch followed by a sudden bond stress loss and minor slippage. Low $\tau_{ons,LE}$ indicated low chemical adhesion; thus, the bond of BFRP bars in GPC was mainly offered by the mechanical interlocking of the bar ribs. The difference in slips at the bar free and loaded ends suggested a nonlinear distribution of bond stress along the BFRP bar.

- The failure bond stress COV ranged between 0.4% and 16.5%, suggesting consistency in the failure load and indicating good agreement with pull-out test studies available in the literature.

- The bar diameter and embedment length significantly influenced the bond behaviour in terms of average bond strength and failure patterns. As the bar diameter increased from 8 to 10 mm, the average bond strength was reduced by 34 - 46%. Increasing the bar embedment length from $5d_b$ to $15d_b$ reduced the average bond strength by 5%, 52% and 55% for the 6-mm, 8-mm and 10-mm bars, respectively.

- The samples reinforced with ribbed and sand-coated bars exhibited similar initial stiffness and failure mode (i.e. bar pull-out). However, the ribbed bars achieved a bond strength 47% higher than the sand-coated bars.

- The bond strength of the samples prepared with GPC2 was 34% lower than that of GPC1. This unexpected result can be ascribed to the minor difference between the two concrete compressive strengths (~3 MPa) and possible concrete defects at the interface caused by the rapid setting time of GPC2 at the time of casting.

- The steel-reinforced samples achieved a bond strength 46% lower than the samples reinforced with BFRP bars. The comparison also suggested that steel-to-concrete interaction significantly differs from that of FRP bars as yielding of the bar led to a more ductile bond behaviour.

- The observed failure modes included bar pull-out, concrete splitting, and bar rupture. Shorter embedment lengths $(5d_b)$ led to pull-out failure due to insufficient contact area

between BFRP bars and GPC, while longer embedment lengths ($15d_b$) caused concrete splitting. The pull-out failure can be ascribed to the crushing of the concrete lugs while no damage could be found on the reinforcement surface, suggesting high shear strength of the BFRP bar ribs. All samples containing 6-mm BFRP bars failed due to bar rupture, regardless of the embedment length, which could be attributed to the reduced mechanical properties of the 6-mm BFRP bars.

Chapter 5 Finite Element Analysis of Bond of BFRP Bars to GPC

5.1 Introduction

The experimental pull-out tests provide crucial data for understanding the bond behaviour between reinforcement and concrete via slip and load measurements and different failure modes. However, as discussed in Chapter 2, experimentally measuring the spatial distribution of interfacial shear stress and longitudinal tensile stress during the pull-out test is challenging due to the strain gauges disturbing effect on the bond performance and the optical fibre failure. To address this difficulty, the finite element (FE) model as a cost-effective tool can be used to investigate stress field and bond properties. As discussed in Chapter 2, the simulation of the pull-out process has been extensively used for steel and other FRP bars in PCC. However, to the best of the author's knowledge, there was no numerical analysis for BFRP bars embedded in GPC. Thus, in this chapter, a three-dimensional (3D) explicit quasi-static FE analysis is conducted using ABAQUS (ABAQUS 6.14 User's Manual, 2014) to simulate the pull-out test of BFRP bars embedded in GPC. The FE analysis is used first to support the interpretation of the experimental results discussing the stress distribution along the bar embedded portion, second to conduct a parametric study expanding the number of case studies investigated.

First, the FE method was described. To obtain the modelling parameters, the experimental results presented in Chapter 3 were used for the GPC matrix and the BFRP bar, and the experimental pull-out test results presented in Chapter 4 were used for the bond stress-slip relationship. The CDP model was adopted for the nonlinear behaviour of the GPC matrix, while the BFRP bar was modelled using the transversely isotropic behaviour. In addition, the cohesive elements with a traction-separation response were used for the interaction between the bars and the concrete. Second, the method to calibrate the model against the mesh size, the loading rate and the mass scale factor was explained. The bond stress-slip curve and the failure modes obtained from the numerical analysis were compared with the experimental data for validation. Third, the numerical results were reported in terms of the distribution of shear bond stress and axial tensile stress at the interface. Finally, a parametric study discussed the effects of bond stress-slip curve parameters, bar diameter, embedment length, bar elastic modulus, and concrete compressive strength on the predicted bond strength.

5.2 Finite element model

5.2.1 Geometry and boundary conditions

The 3D FE models were established in ABAQUS to simulate the pull-out process. A schematic diagram of the geometry model is shown in Fig. 5.1a, consisting of a cubic GPC block with a side length (l_s) of 150 mm and an embedded longitudinal bar with a diameter d_b. The concrete cover (c) was defined as the distance between the bar and the free surface. Despite the ribbed surface of the actual bar specimen, the bar was modelled as a perfect cylinder with a smooth surface, as commonly adopted in the literature (Achillides and Pilakoutas, 2006; Vilanova et al., 2016; Rezazadeh et al., 2017). Thus, the effect of rib geometry on the bond properties was implicitly considered through cohesion strength. The bar was in contact with the concrete for an embedded length of l_d. According to the experimental setup, d_b were equal to 6 mm, 8 mm and 10 mm, and l_d ranged between $5d_b$, $10d_b$ and $15d_b$, depending on the sample represented. Furthermore, the boundary conditions were set to be consistent with the experimental pull-out test, as displayed in Fig. 5.1b. The bottom surface of the concrete block was fixed. The pull-out load parallel with the bar axis was applied at the end of the bar using a displacement-control method. The loading rate is detailed in the following section. By taking advantage of the symmetrical conditions, only a quarter of the sample was used, to reduce the computational cost.

(a)   (b)
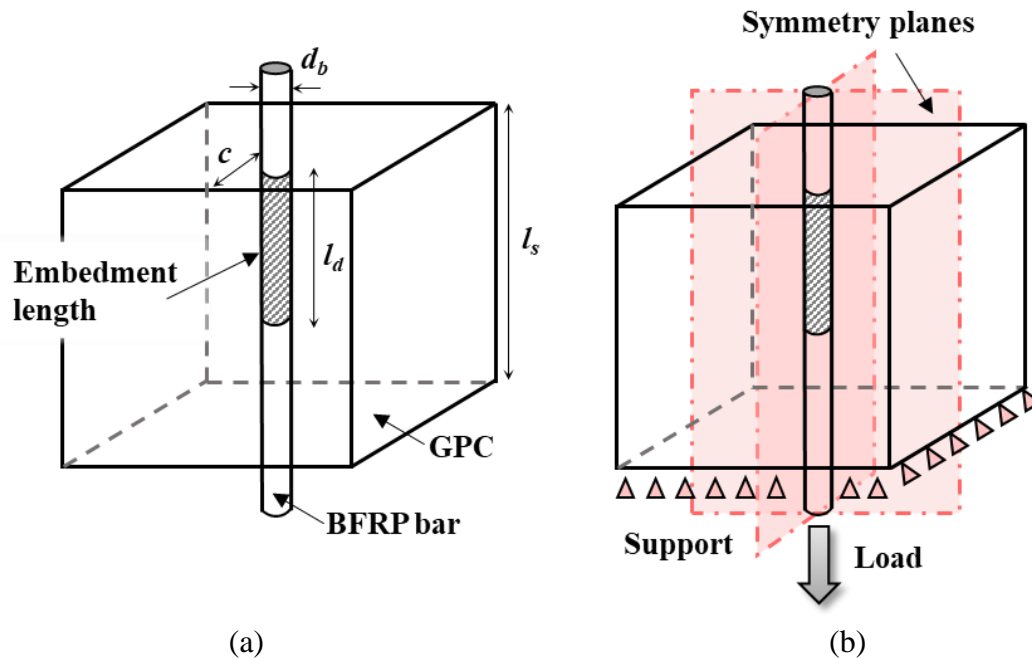
Fig. 5.1 Finite element model: (a) schematic of the specimen composed of the cubic GPC block with side length of l_s and cover of c; and the cylindrical BFRP bar with embedded length of l_d and diameter of d_b; (b) boundary conditions.

5.2.2 Loading condition

The explicit solution method was adopted to solve the quasi-static analysis considering its advantages for the simulation of complex contact behaviours and nonlinear problems (ABAQUS 6.14 User's Manual, 2014; Ziari and Kianoush, 2014; Vilanova et al., 2016). As described in Section 4.2.2, a loading rate of 1.3 mm/min (i.e. 0.022 mm/s) was adopted in the experimental pull-out tests. However, for simulations, a higher loading rate can be adopted for computational efficiency. To find the maximum possible loading rate, the effect of the loading time on the simulation results is investigated. Fig. 5.2 illustrates the bond stress-slip curves obtained for different loading rates ranging from 0.022 mm/s to 75 mm/s, considering the sample *10-5d* as a reference. The discrepancy of the curves can be mainly observed for loading rates higher than 35 mm/s, which is chosen as a threshold loading rate for this study. To further speed up the simulation, the mass scaling is non-uniformly applied to the smallest elements, which control the stable time increment. For this, the minimum stable time increment is set to 10^{-7} (*FIXED MASS SCALING, DT=1e-07, TYPE=SET EQUAL DT). As seen in Fig. 5.3, the ratio of kinetic energy to internal energy (KE/IE) is below 10% for the entire simulation, which guaranteed the accuracy of the quasi-static process (ABAQUS 6.14 User's Manual, 2014).

Regarding the computational convergence in solving a non-linear problem, it should be noted that an explicit dynamic analysis was adopted in ABAQUS, the procedure of which performs a large number of small-time increments efficiently. An explicit central-difference time integration rule is used, the operator of which is conditionally stable (ABAQUS 6.14 User's Manual, 2014). Therefore, this feature ensures convergence.
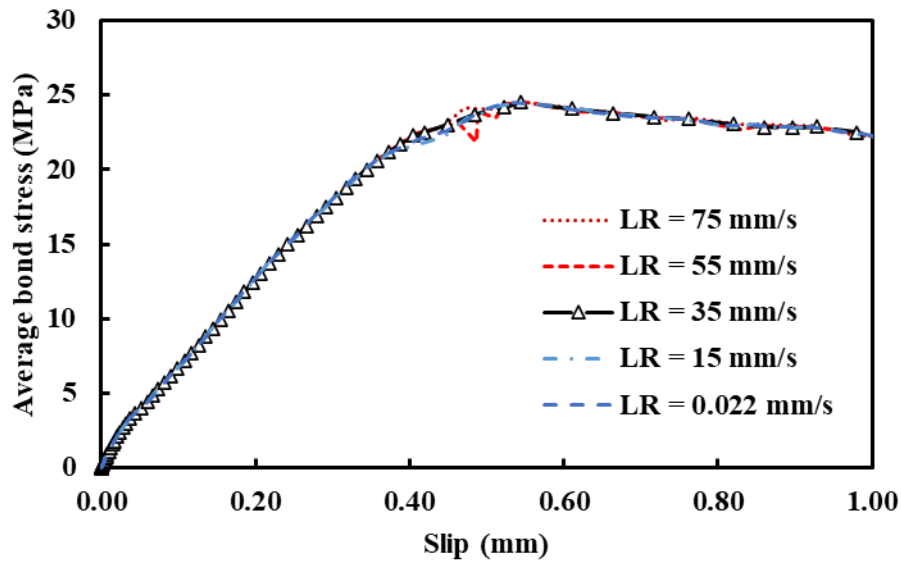
Fig. 5.2 Effect of loading rate (LR) on bond stress-slip curve.

(a)   (b)
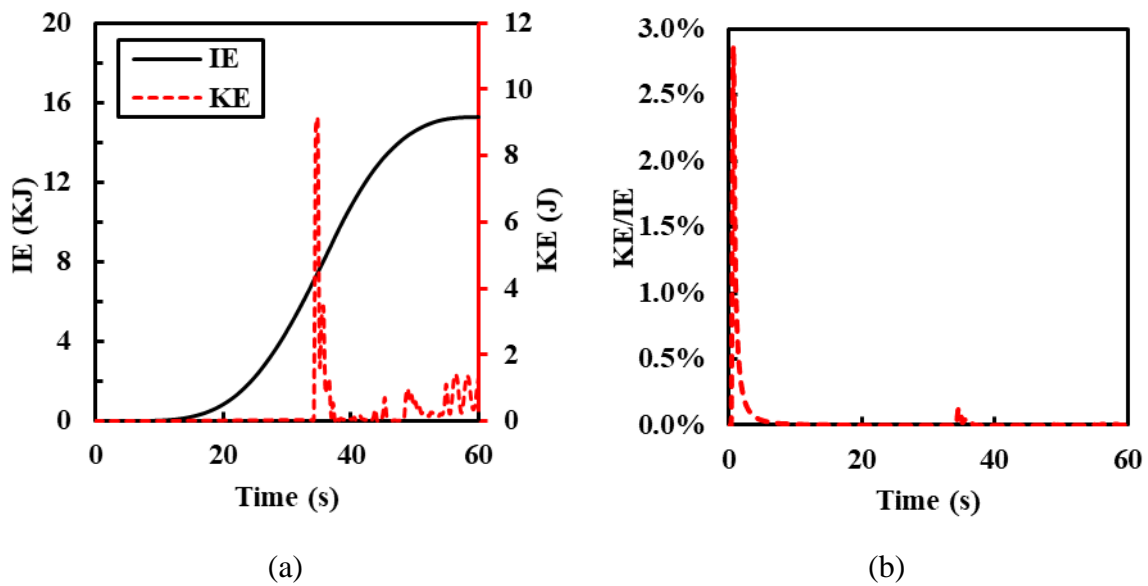
Fig. 5.3 Energy-time relationship with loading rate of 35 mm/s and minimum stable time increment of 10^{-7}: (a) internal energy (IE) and kinetic energy (KE); (b) KE/IE ratio.

5.2.3   Concrete damage plasticity

The CDP constitutive model has been widely adopted to simulate tensile cracking and compressive crushing in concrete-like materials (Vilanova et al., 2016; Rezazadeh et al., 2017; Tekle, 2017; Veljkovic et al., 2017; Elchalakani et al., 2018), and it was used in this study for modelling GPC. As the constitutive behaviour is fully documented in the ABAQUS user's manual (ABAQUS 6.14 User's Manual, 2014), only some key details are described here.

In Fig. 5.4 it is shown the uniaxial compressive and tensile behaviour of concrete. The elastic behaviour is linear until the value of initial yield (σ_{c0}), which is assumed to be equal to 0.3 of the compressive strength f_c (Jankowiak and Lodygowski, 2005). In the plastic regime, the response is typically characterised by stress hardening followed by strain-softening. As discussed in Section 3.2.5.2, the compressive stress-strain relationship of GPC was defined using the constitutive model proposed by Popovics (1973) and modified by Collins et al. (1991), given in Eqs. (3.3)-(3.6). In ABAQUS, the compressive stress-strain data is defined with the compressive stress versus inelastic strain data, being the inelastic hardening strain ($\varepsilon_c^{in,h}$) defined as:

$$\varepsilon_c^{in,h} = \varepsilon_c - \frac{\sigma_c}{E_c} \tag{5.1}$$

where ε_c is the total strain and σ_c/E_c equals to the elastic strain. Then, ABAQUS converts the inelastic strain values to plastic strain values using the following relationship:

$$\varepsilon_c^{pl} = \varepsilon_c^{in} - \frac{d_c}{1 - d_c} \frac{\sigma_c}{E_c} \tag{5.2}$$

(a)　　　　　　　　　　　　　　　　　(b)
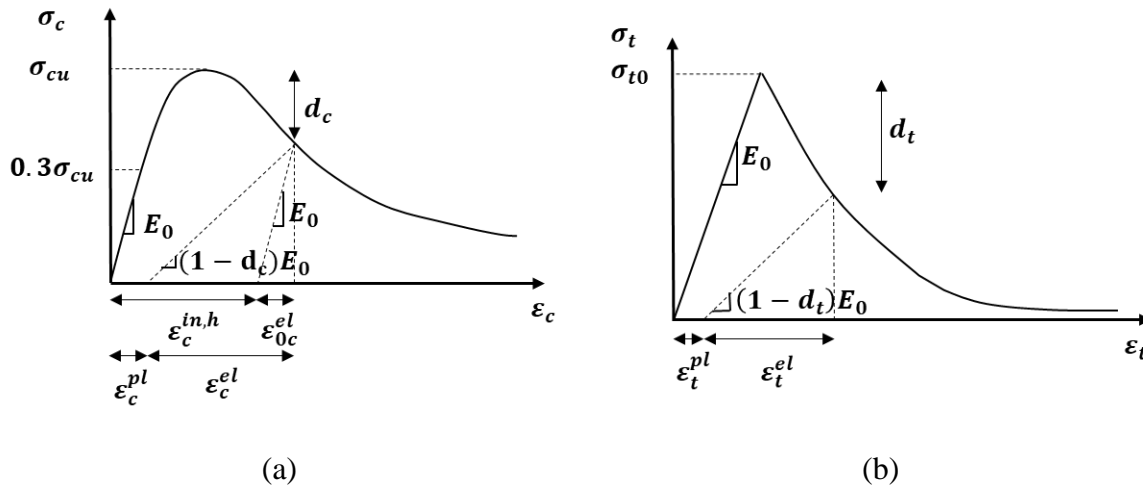
Fig. 5.4 Concrete response to uniaxial loading: (a) in compression; (b) in tension. (Jankowiak and Lodygowski, 2005; ABAQUS 6.14 User's Manual, 2014)

Under uniaxial tension, the stress-strain response follows a linear elastic relationship until the failure stress (σ_{t0}) is reached. For PCC, σ_{t0} is usually assumed to be 70% of the splitting tensile strength, obtained either from experimental data or analytical models, as discussed in Section 3.2.5. The tensile softening behaviour is approximated by the linear fracture energy-based criterion to avoid unreasonable mesh sensitivity results (Hillerborg et al., 1976). The

energy required to open a unit area of crack (G_f) is defined as a material parameter that can be calculated according to the most recent CEB-FIP model code (2010) as follows:

$$G_f = 73 f_{cm}^{0.18} \tag{5.3}$$

where f_{cm} is the mean compressive strength (MPa) expressed as:

$$f_{cm} = f_c + 8 \tag{5.4}$$

As shown in Fig. 5.5, the strength loss after cracking is presumably linear, and the complete loss takes place at a displacement of $u_{t0} = 2G_f/\sigma_{t0}$.

The damage indices of d_c for compression (DAMAGEC), d_t for tension (DAMAGET) and scalar stiffness degradation variables d (SDEG), are used to represent the spatial evolution of cracks. These variables range from 0, when the material is undamaged, to 1, when a total loss of strength is reached. However, excessive damage may compromise the convergence rate, and it is recommended to avoid adopting values of the damage parameters above 0.99, corresponding to a 99% reduction of stiffness (ABAQUS 6.14 User's Manual, 2014).

The scalar stiffness degradation variables have been calculated based on the simplified damage plasticity model for concrete proposed by Esfahani et al. (1998). d_c is defined as a function of the inelastic (crushing) strain and is calculated as follows:

$$d_c = 1 - \sigma_c/f_c \tag{5.5}$$

where σ_c is the stress in compression and f_c is the concrete compressive strength.

d_t is provided as a function of the displacement (u_t), and is calculated as follows:

$$d_t = 1 - \sigma_t/\sigma_{t0} \tag{5.6}$$

where σ_t is the stress in tension and σ_{t0} is the concrete tensile strength.
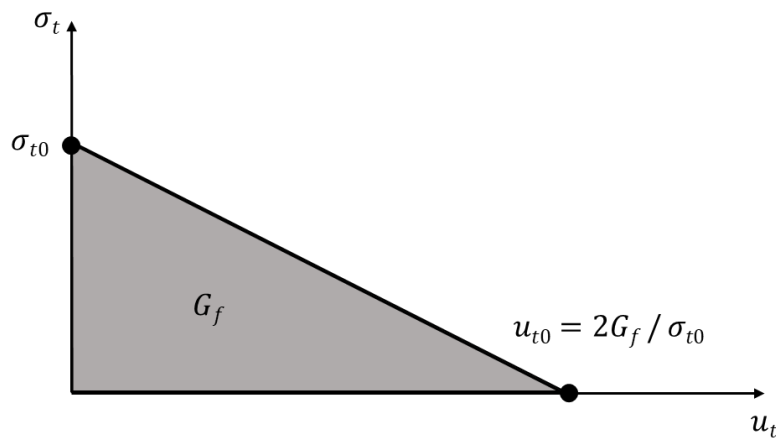
Fig. 5.5 Post failure stress-fracture energy curve (ABAQUS 6.14 User's Manual, 2014)

Other material parameters for the elastic behaviour include the Poisson's ratio (v) and the concrete elastic modulus (E_c). A Poisson's ratio of 0.2 was used for this study, according to that suggested by Fang (2020). As discussed in Section 3.2.5.4, the elastic modulus of GPC was measured experimentally. For the concrete grades not evaluated experimentally, the elastic modulus was estimated as a function of the compressive strength (f_c) following the recommendations of ACI 318-08 (2008).

Furthermore, the CDP model requires dilatation angle measured in the p–q plane at high confining pressure (ψ), flow potential eccentricity that defines the rate at which the function approaches the asymptote (e), ratio of initial equibiaxial compressive yield stress to initial uniaxial compressive yield stress (σ_{b0}/σ_{c0}), ratio of the second stress invariant in tension to that in compression (K_c), and viscosity parameter representing the relaxation time of the viscoplastic system (μ). The values of the flow potential function could be identified experimentally; however, no standard guidelines are available for their calculation. As this is beyond the scope of this study, the default values suggested by Jankowiak and Lodygowski (2005) were adopted. A summary of the values assigned to these parameters for the CDP model is given in Table 5.1.

Table 5.1 Values of parameters used in CDP model for GPC in this study.

Elasticity (ACI 318, 2008; Fang, 2020)				Plasticity (Jankowiak and Lodygowski, 2005)			
E_c (GPa)	ν	ψ	e	σ_{b0}/σ_{c0}	K_c	μ	f_c (MPa)
30.58	0.20	38°	0.1	1.16	0.67	0.0005	42

Compressive behaviour (Popovics, 1973)		Compression damage (Esfahani and Rangan, 1998)	
Yield stress σ_c (MPa)	Inelastic strain ε_c^{in}	Damage parameter d_c	Inelastic strain ε_c^{in}
12.67	0.00000	0.00	0.00000
27.07	0.00003	0.00	0.00003
33.15	0.00008	0.00	0.00008
37.89	0.00018	0.00	0.00018
40.96	0.00033	0.00	0.00033
41.69	0.00040	0.00	0.00040
42.15	0.00049	0.00	0.00049
42.33	0.00058	0.00	0.00058
41.65	0.00070	0.02	0.00070
40.44	0.00084	0.04	0.00084
38.94	0.00099	0.08	0.00099
37.20	0.00115	0.12	0.00115
35.30	0.00131	0.17	0.00131
25.30	0.00214	0.40	0.00214
11.64	0.00358	0.73	0.00358
8.04	0.00420	0.81	0.00420
5.70	0.00478	0.87	0.00478
4.15	0.00533	0.89	0.00533

Tensile behaviour (CEB - FIP, 2010)		Tensile damage (Esfahani and Rangan, 1998)	
Yield stress σ_{t0} (MPa)	Fracture energy G_f (N/mm)	Damage parameter d_t	Displacement u_{t0} (mm)
2.50	0.08	0	0
		0.99	0.043

5.2.4   BFRP bar

FRP bars are usually modelled as solid with isotropic linear elastic behaviour (Tekle et al., 2016; Vilanova et al., 2016; Yan and Lin, 2016; Gooranorimi et al., 2017; Elchalakani et al., 2018). However, as shown in Fig. 5.6, BFRP bar is a unidirectionally-reinforced fibre composite with transversely isotropic elastic behaviour. The elastic modulus (E) in the

longitudinal direction (indicated by subscript 3), parallel to the fibres, is higher than those in the transverse directions (indicated by subscript 1 and 2), behaviour that can be expressed as follows:

$$E_L = E_3 > E_1 = E_2 = E_T \tag{5.7}$$

where the subscript L stands for "longitudinal" and T for "transverse".
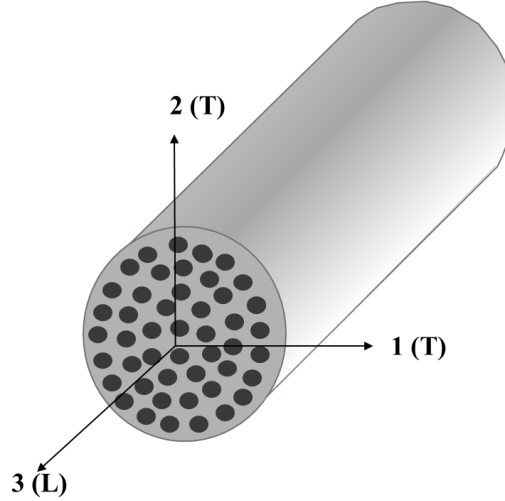
Fig. 5.6 Example of transversely isotropic material.

The transverse isotropic elasticity has been used by Rezazadeh et al. (2017) to model GFRP bars. The elastic constants for the definition of the transversely isotropic elasticity were derived from the Chamis formulae (1984) and the rule of mixtures, i.e. a weighted mean used to predict various properties of a composite material made of continuous and unidirectional fibres. The parameters were identified according to the following equations.

The equivalent elastic modulus (E_b^{eq}) and shear modulus (S^{eq}) can be calculated as follows:

$$E_{b,L}^{eq} = V_f E^f + (1 - V_f) E^m \tag{5.8}$$

$$E_{b,T}^{eq} = \frac{E^m}{1 - \sqrt{V_f}\left(1 - \frac{E^m}{E^f}\right)} \tag{5.9}$$

$$S_L^{eq} = S_T^{eq} = \frac{S^m}{1 - \sqrt{V_f}\left(1 - \frac{S^m}{S^f}\right)} \tag{5.10}$$

where superscript f and m denote fibre and matrix, respectively and V_f is the fibre volume fraction equals to $v^f / (v^f + v^m)$. The equivalent Poisson's ratios (v_b^{eq}) along longitudinal and transversal directions are given as:

$$v_{b,T}^{eq} = V_f v^f + (1 - V_f)v^m \tag{5.11}$$

$$v_{b,L}^{eq} = \frac{E_T^{eq}}{2S^{eq}} - 1 \tag{5.12}$$

Both fibres and matrix in BFRP bars can be regarded as isotropic materials. The values of elastic modulus (E) and Poisson's ratio (v) of basalt fibres and vinyl-ester resin (matrix) were obtained from Golla and Prasanthi (2016) and CEB-FIP (2007), respectively, based on which the shear modulus (S) can be calculated as:

$$S = \frac{E}{2\,(1 + v)} \tag{5.13}$$

Table 5.2 summarises the properties of basalt fibre and matrix and the equivalent elastic constants of BFRP bars with fibre volume fraction of 75% calculated using Eqs. (5.8)-(5.13), assigned to all bar diameters. It is worth noting that the equivalent longitudinal elastic modulus of BFRP bars agrees with the experimental data presented in Section 3.3.3.

Table 5.2 Material properties of BFRP bar.

	Basalt fibre	Vinyl-ester resin	BFRP bar	
			$E_{b,L}^{eq}$	$E_{b,T}^{eq}$
Elastic modulus E (GPa)	79.30	3.25	19.18	60.29
			S^{eq}	
Shear modulus S (GPa)	31.47	1.18	7.09	
			$v_{b,T}^{eq}$	$v_{b,T}^{eq}$
Poisson's ratio v	0.26	0.38	0.29	0.35

Note: eq (equivalent); L (longitudinal); T (transversal).

5.2.5   BFRP bar-concrete interaction

The cohesive model with uncoupled bilinear traction-separation law was used to simulate the interfacial behaviour between BFRP bars and GPC. As shown in Fig. 5.7, for the ascending branch, an initial linear elastic behaviour is assumed until the peak point, where the cohesive bond failure initiates. The peak bond stress is followed by the progressive degradation of the bond stiffness governed by a damaging process, leading to the separation between the two surfaces.
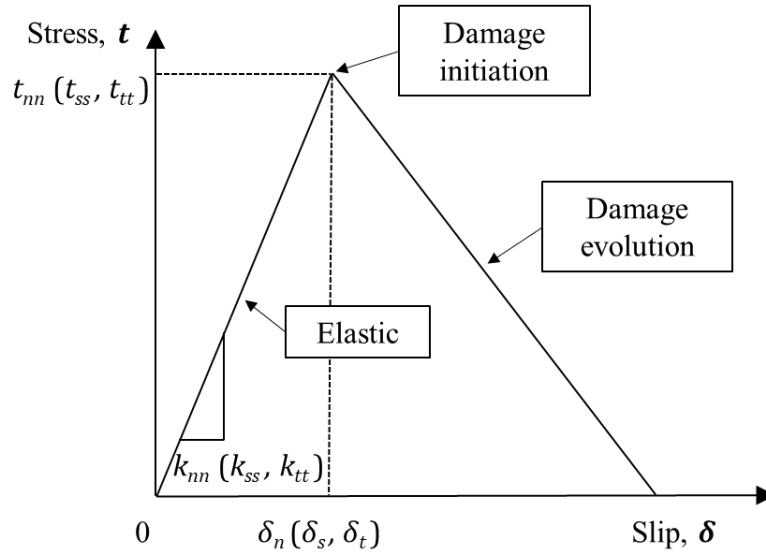
Fig. 5.7 ABAQUS typical traction-separation response.

The elastic behaviour can be described using Eq. (5.14) in terms of an elastic constitutive matrix (k) relating the nominal stress (t) to the nominal strains across the interface (ε).

$$t = k\varepsilon \tag{5.14}$$

The elastic behaviour can be described as:

$$t = \begin{bmatrix} t_n \\ t_s \\ t_t \end{bmatrix} = \begin{bmatrix} k_{nn} & 0 & 0 \\ 0 & k_{ss} & 0 \\ 0 & 0 & k_{tt} \end{bmatrix} \begin{bmatrix} \delta_n \\ \delta_s \\ \delta_t \end{bmatrix} = k\delta \tag{5.15}$$

where t represents the nominal stress (i.e., traction vector) and δ is the relative displacement between bar and concrete (i.e., separation). The subscripts denote the normal direction (n) and two shear directions (s and t). The stiffness matrix k relates the nominal stress to the displacement. The off-diagonal terms were set to zero to simulate an uncoupled behaviour between the three components, normal (k_{nn}) and shear (k_{ss} and k_{tt}). For stability, the uncoupled behaviour requires positive values of the stiffness i.e. $k_{nn} > 0$, $k_{ss} > 0$ and $k_{tt} > 0$. The elastic bond shear stiffness k_{ss} and k_{tt} can be obtained as:

$$k_{ss} = k_{tt} = \frac{\tau_m}{s_{m,FE}} \tag{5.16}$$

where τ_m stands for the maximum bond stress and $s_{m,FE}$ denotes the corresponding slip, obtained from experiments.

Due to lack of experimental data, the normal stiffness (k_{nn}) can be derived from the tangential stiffnesses as follows (Henriques et al., 2013):

$$k_{nn} = 100 \, k_{ss} = 100 \, k_{tt} \tag{5.17}$$

The damage initiation was modelled using the quadratic nominal stress criterion, which considers the damage to initiate when the maximum nominal stress ratio reaches 1.

$$\left(\frac{\langle t_n \rangle}{t_n^0}\right)^2 + \left(\frac{t_s}{t_s^0}\right)^2 + \left(\frac{t_t}{t_t^0}\right)^2 = 1 \tag{5.18}$$

where t_n^0, t_s^0, and t_t^0 represent the critical values of the nominal stress when the deformation is either purely normal to the interface or purely in the first or second shear direction, respectively. The Macaulay bracket symbol $\langle\ \rangle$ is used to signify that pure compressive stress does not initiate the damage.

During the pull-out process, the damage mainly initiates and evolves in the tangential directions since the shear stress is significantly greater than normal stress. It suggests that the critical normal strength has a negligible effect on the mechanical response. Therefore, for FE modelling, a large enough value of t_n^0 can be used to ensure the possible damage occurrence only along the shear direction. The shear critical tractions are assumed to be equal to the measured bond strength (τ_m) from pull-out experiments in terms of bond stress-slip curve, as follows:

$$t_s^0 = t_t^0 = \tau_m \tag{5.19}$$

To describe the tabular softening evolution, the scalar damage (D) is used, which changes monotonically from 0 (no damage) to 1 (fully damage). D is described as a function of the effective displacement for the effective displacement at initiation, as follows:

$$\delta_{mi} = s - s_{m,FE} \tag{5.20}$$

$$D = 1 - \frac{\tau}{ks} \tag{5.21}$$

where δ_{mi} is the effective relative displacement, τ and s are the bond stress and corresponding slip curve of the actual bond stress-slip curve, and $s_{m,FE}$ is the slip at the free end corresponding to the maximum bond stress and k is the bond stiffness calculated as $\tau_m/s_{m,FE}$.

The stress components of the traction-separation law are influenced by the damage as follows:

$$t_n = \begin{cases} (1-D)t_n^0, & t_n^0 \geq 0 \\ t_n^0, & t_n^0 < 0 \end{cases} \quad \text{(no damage to compressive stiffness)} \tag{5.22}$$

$$t_s = (1-D)t_s^0, t_t = (1-D)t_t^0$$

where t_n^0, t_s^0 and t_t^0 are the traction components predicted by the elastic traction-displacement behaviour for the current separation without damage. To set these, the keywords with the

keywords *DAMAGE INITIATION, CRITERION=QUADS and *DAMAGE EVOLUTION, TYPE=DISPLACEMENT, SOFTENING = TABULAR were used. The tabular values were identified considering Eqs. (5.20) and (5.21), and Table 5.3 which lists the corresponding material properties defined in the cohesive model, based on the experimental data presented in Chapter 4. Further details on the choice of the values are provided in Section 6.4. As output variables, the indices of SDEG, DAMAGEC and DAMAGET are selected to determine the overall damage.

It is worth noting that the experimental data consider the bond behaviour macroscopically rather than the individual material and structural properties. Therefore, the bond stress-slip values represent specific experimental conditions, limiting the analysis of different influencing parameters (Achillides, 1998).

Table 5.3 Bond stress-slip parameters used for the cohesive elements' properties.

Model	k_{nn} (MPa/mm)	k_{ss}, k_{tt} (MPa/mm)	t_n^0 (MPa)	t_s^0, t_t^0 (MPa)	$s_{m,FE}$ (mm)	s_u (mm)
8-5d-1	12509.34	125.09	100.00	41.28	0.33	0.95
8-5d-2	11995.13	119.95	100.00	40.78	0.34	0.95
8-5d-3	15922.65	159.23	100.00	44.26	0.28	0.94
8-10d-1	13899.26	138.99	100.00	41.28	0.30	9.20
8-10d-2	14462.22	144.62	100.00	40.78	0.28	8.80
8-10d-3	17672.12	176.72	100.00	41.53	0.24	9.20
8-15d-1	14999.72	150.00	100.00	18.90	0.13	5.00
8-15d-2	9575.01	95.75	100.00	18.77	0.20	6.20
8-15d-3	9383.51	93.84	100.00	18.77	0.20	6.20
10-5d-1	9512.71	95.13	100.00	24.83	0.26	5.00
10-5d-2	8253.85	82.54	100.00	28.39	0.34	4.00
10-5d-3	8243.69	82.44	100.00	24.32	0.30	4.00
10-10d-1	7802.34	78.02	100.00	23.17	0.30	5.00
10-10d-2	10243.79	102.44	100.00	22.54	0.22	6.00
10-10d-3	8891.63	88.92	100.00	21.52	0.24	6.00

5.2.6 Finite element mesh

The GPC block and the BFRP bar were meshed using eight-node 3D solid hexahedral elements (C3D8). The interaction between BFRP bar and GPC was simulated by eight-node 3D cohesive elements (COH3D8) with an initial thickness of 0.001 mm, considering the material model described in Section 5.2.5. A mesh sensitivity analysis was conducted to estimate the effect of element size at the interface between the bar and the concrete, where a higher strain gradient is expected. As an example, the numerical results of the sample *10-5d* are reported for six

different mesh sizes corresponding to 3180, 4240, 5820, 7020, 8400 and 10555 elements, which is achieved by changing the average element size at the interface ranging from 10 mm to 2.5 mm, chosen according to the literature review provided in Chapter 2. Fig. 5.8a shows the average bond stress-slip curves for the models with different element numbers (mesh sizes). The bond stress is calculated based on the sum of the nodal values of the reaction force at the bar end, while the slips are obtained from the nodal value of the slip at the loaded ends. The figure determines an insignificant difference (<2%) among the bond stress-slip curves for the models with different element numbers. As depicted in Fig. 5.8b, the simulated bond strength became approximately constant at 24.51 MPa that is close to the experimental data (24.83 MPa) when further increasing the number of elements from 7020 to 10555. Therefore, the mesh with 5820 elements (Fig. 5.9) was adopted, where the size of elements varies almost between 5 to 10 mm from the bar-concrete interface to the free surface of concrete.

(a)   (b)
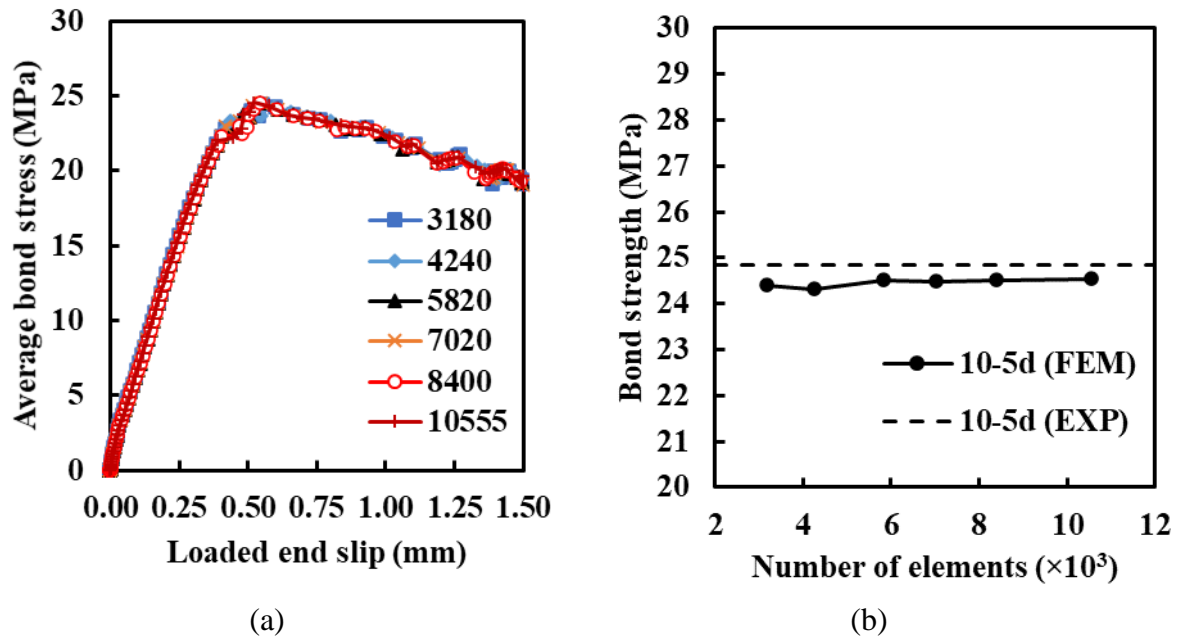
Fig. 5.8 Comparison between model *10-5d* with different element numbers: (a) bond stress-slip curves; (b) bond strength.

Here, the effects of aggregate size on the material properties and the stress response were not considered as the domain size of the model and the element size in the damage region are relatively small. A meso-scale model of concrete matrix may be used to study the influence of coarse aggregates on the failure pattern.
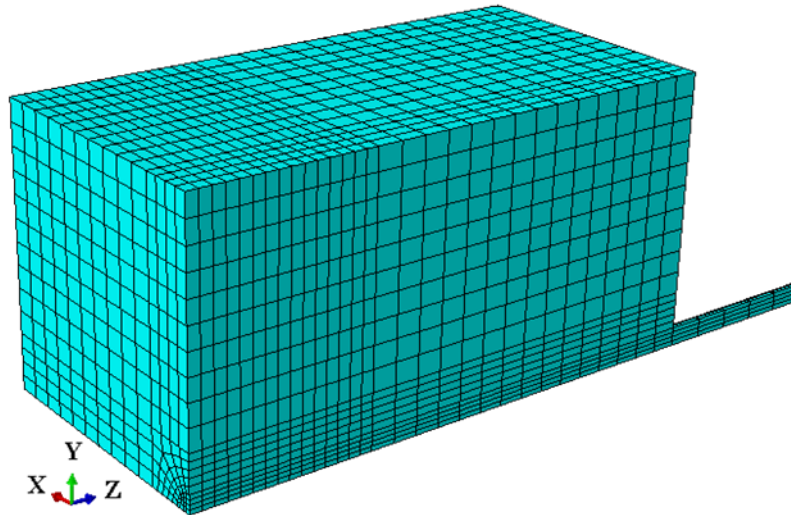
Fig. 5.9 Finite element mesh of BFRP bar and GPC for pull-out simulations.

5.3 Model validation

To validate the FE model with experiments, *10-5d*, *10-15d* and *10-10d* samples were selected, to compare the results in different failure modes, including the complete bar pull-out, the splitting of concrete and the bar rupture, respectively.

5.3.1 Bond stress-slip relationship

A comparison between the simulated and measured average bond stress-slip curves at the bar free and loaded ends is shown in Fig. 5.10 which indicates a generally good agreement between them in terms of curve shape, maximum stress values and stiffness. Some discrepancies can be mainly observed between the results for *10-10d* at the loaded end, which can be ascribed to the complexity of the rupture failure mechanism due to splitting of fibre bundles rather than tensile fracture, making the pull-out process less predictable. The current FE model can allow the bar tensile failure, while for an accurate estimation of the failure mechanisms and bond stress-slip response, different failure criteria can be considered.

It is worth noting that, as schematically shown in Fig. 5.11, the splitting failure is considered premature as the maximum bond capacity is not developed. The experimental bond stress-slip curves recorded for the samples *10-15d* provided only the ascending branch of the $\tau - s$ behaviour as the concrete cubes split open in a brittle way before reaching the peak and the descending branch. Therefore, to predict the bond behaviour of the *10-15d* sample, the bond stress-slip curve obtained from the sample *10-5d* was adopted as the interface behaviour for the FE simulation. As a result, good agreement was found between experimental and numerical results since the sample *10-15d* failed, as expected, due to splitting at a bond strength of 12.34 MPa, close to the experimental value of 13.03 MPa.

(a)

(b)

(c)
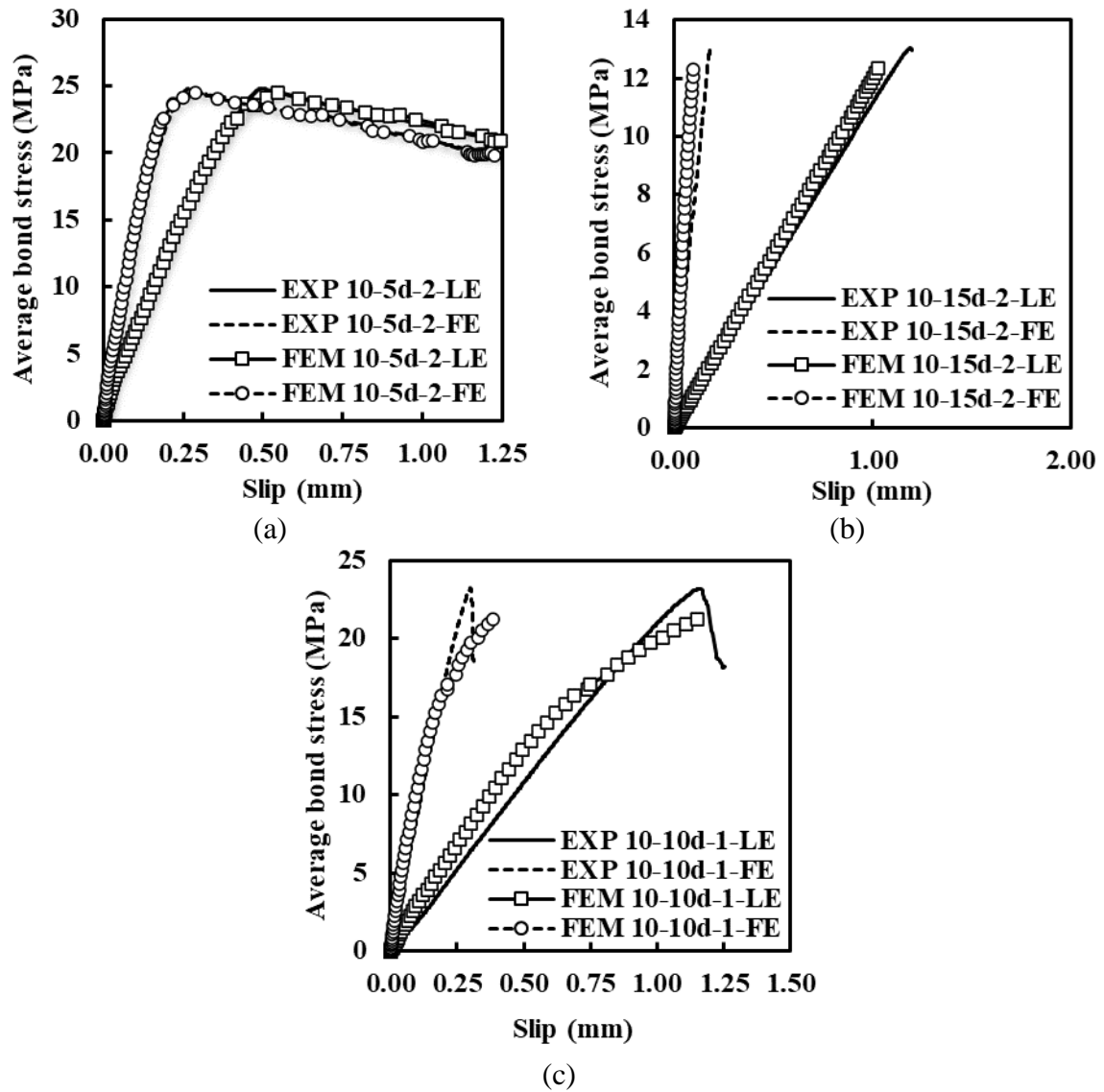
Fig. 5.10 Comparison of numerical and experimental results in terms of bond stress-slip curves at the free end (FE) and loaded end (LE) of samples: (a) *10-5d*; (b) *10-15d*; (c) *10-10d*.
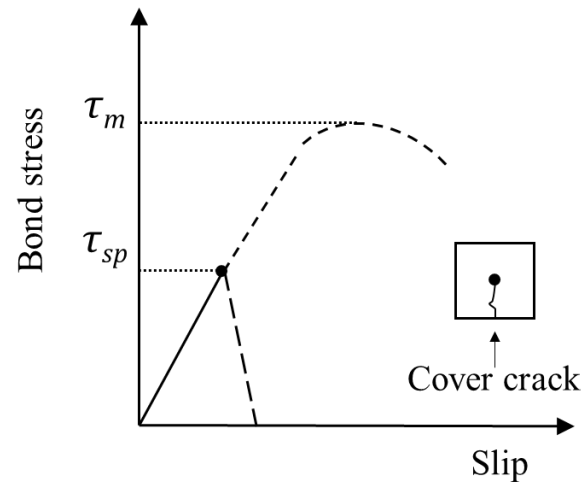
Fig. 5.11 Splitting failure induced by cover crack (CEB-FIP, 2007).

5.3.2 Failure modes

The FE model was further validated by comparing the failure patterns observed in the experiments, considering that the failure patterns in the concrete model can be represented by the failed elements with an SDEG value greater than ~0.8 (Naderi et al., 2021). According to the experimental observations, in the case of complete bar pull-out, the damage was mainly localised in the concrete around the interface, where the mechanical interlocking caused microcracking and consequent shearing off of the concrete between the bar ribs, generating at the interface a smooth-like surface with no ribs marks, (Fig. 5.12a). As illustrated in Fig. 5.12b, the local damage distribution in the model was consistent with the experiments as the cohesive elements and tetrahedron elements around the bar are failed. Fig. 5.12c suggests that the dominant failure can be attributed to the concrete damage in compression. For the concrete splitting failure, longitudinal cracks propagated radially from the interface to the surface of the concrete cube. Such failure was caused by the long embedded length (i.e. $15d_b$), which intensifies the interlocking force and local stress in a relatively larger area. Two split pieces of the concrete specimen are shown in Fig. 5.13a. It can be appreciated the difference with the bar pull-out failure as with concrete splitting failure the ribs marks can be observed on the bar-concrete interface because of the limited slip of the bar. Fig. 5.13b proves that the simulated failure had the same pattern as the longitudinal cracks observed experimentally, while Fig. 5.13c demonstrates that the dominant failure can be ascribed to the concrete damage in tension. Similar results were found for the pull-out modelling of FRP bars in PCC (Zanuy et al., 2013; Gooranorimi et al., 2017; Rezazadeh et al., 2017). The bar rupture mainly occurred due to the strong bond between the bar and concrete, which allowed the pull-out stress to reach the bar

tensile strength (Fig. 5.14a). In the simulation, this failure can be represented by the longitudinal stress distribution along the free length of the bar. Fig. 5.14b indicates that the bar tensile stress (876 MPa) was reached, causing the failure of the BFRP bar in tension.

Thus, it can be proved that the models developed here can provide reliable predictions of the pull-out of BFRP bars in GPC. Thus, the model allows further investigation of the stress distributions along the bar, which are difficult to be experimentally studied.

(a)

(b)

(c)
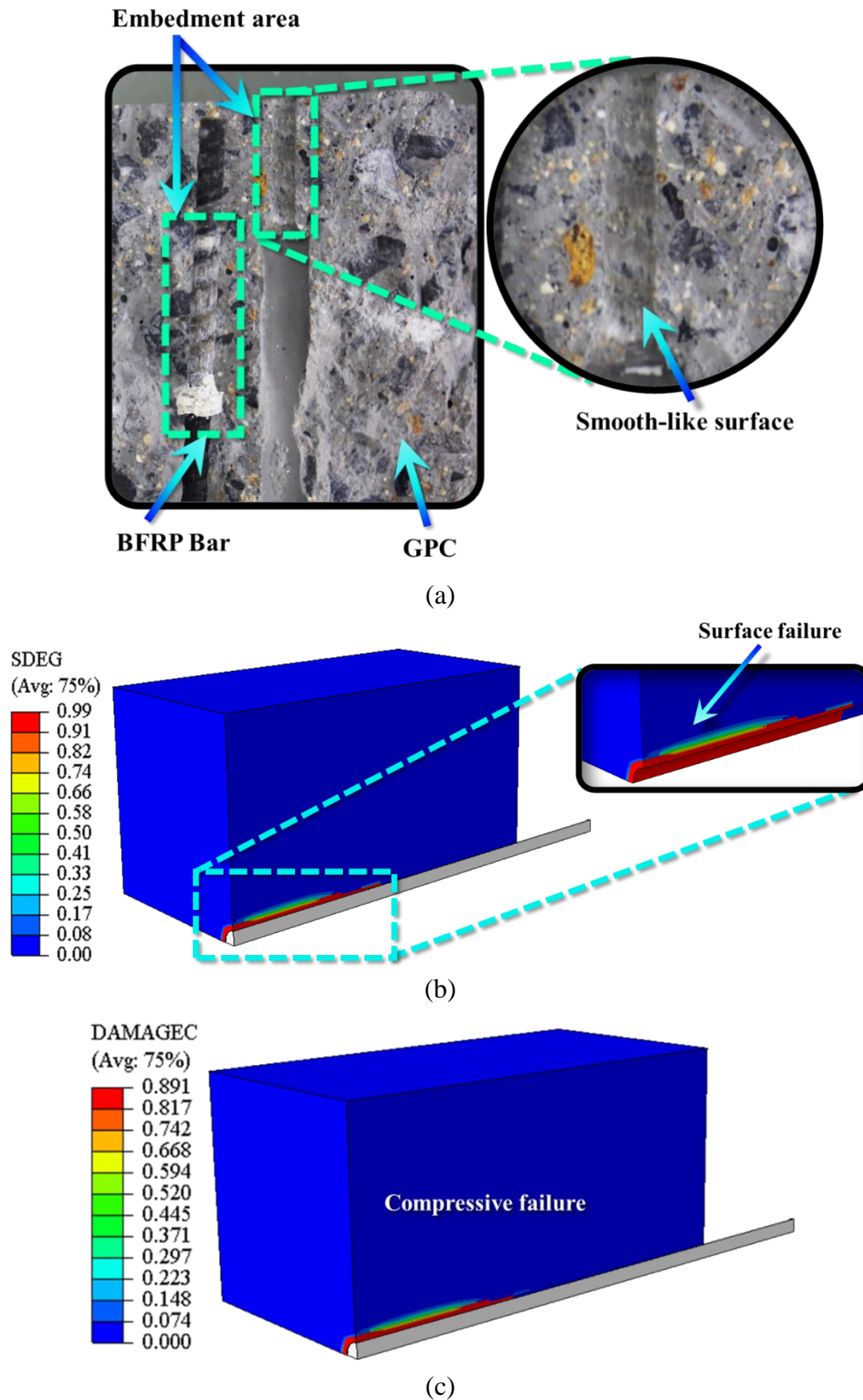
Fig. 5.12 Damage and failure patterns due to bar pull-out of sample *10-5d*: (a) experimental observation; (b) simulated overall damage; (c) simulated concrete damage in compression.

127

(a)

(b)   (c)
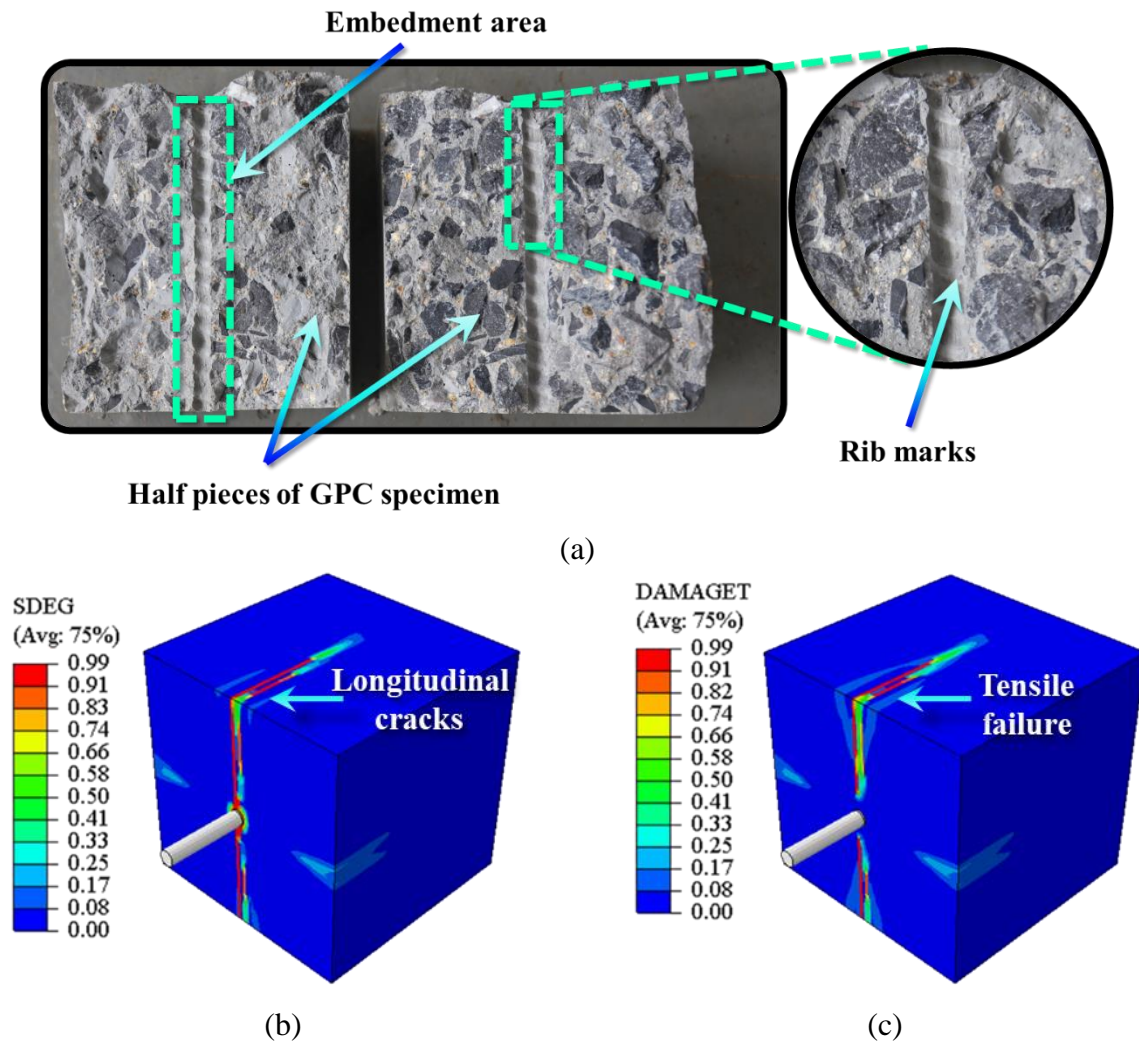
Fig. 5.13 Damage and failure patterns due to splitting of sample *10-15d*: (a) experimental observation; (b) simulated overall damage; (c) simulated concrete damage in tension.

(a)

(b)
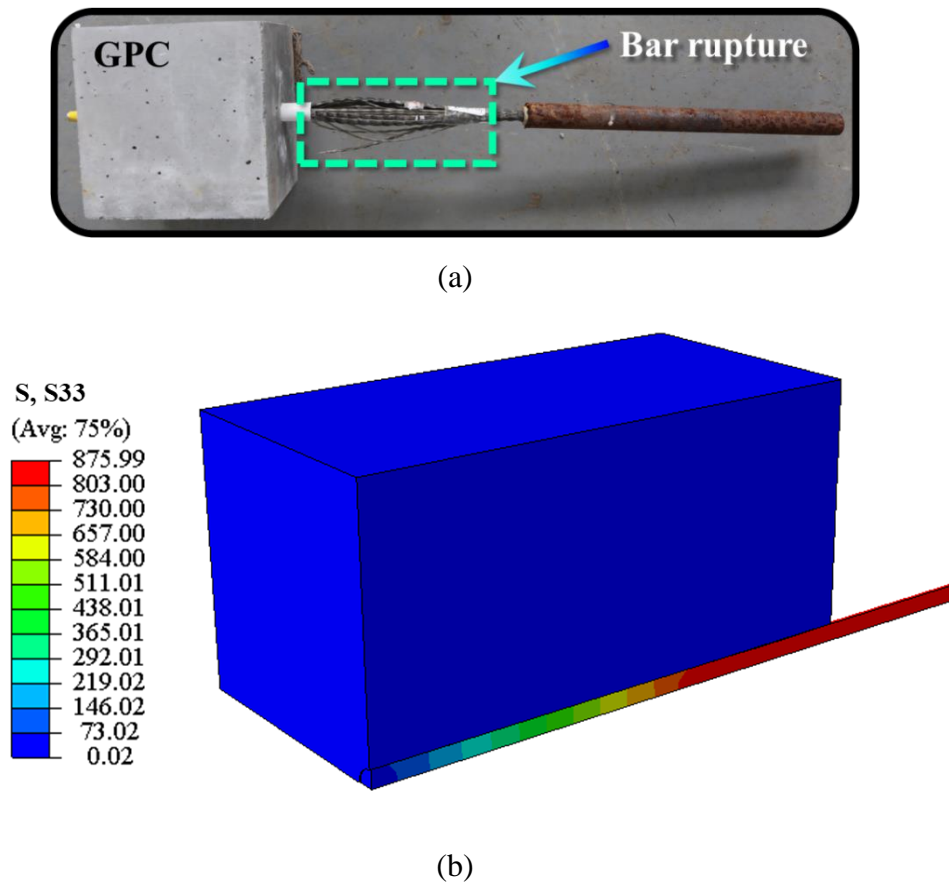
Fig. 5.14 Failure due to bar rupture of sample *10-10d*: (a) experimental observation; (b) simulated longitudinal stress distribution along the bar.

5.4   Results and discussion

5.4.1   Distribution of tensile and bond stresses

The relatively low stiffness of BFRP bars induces a non-uniform displacement along the embedded portion of the bar (Achillides and Pilakoutas, 2006). Hence, besides the average bond stress, it is vital to explore the local stress/strain distribution at the interface to fully understand the load transfer mechanism between GPC and BFRP bars. However, as discussed in Chapter 2, the experimental measurement of the strains would not be accurate given that the measuring tools (e.g. strain gauges and distributed optical fibre sensors) would either negatively affect the test performance or easily get damaged (Henault et al., 2012; Lee and Mulheron, 2012, 2015; Marchand et al., 2016; Rolland et al., 2018; Malek et al., 2019). Thus, numerical simulation can be carried out to study the distribution of different stress components during the bar pull-out process as well as the failure mechanisms.

5.4.1.1   Shear bond stress and longitudinal tensile stress distribution

Fig. 5.15 shows the shear bond stress and the longitudinal tensile stress at different distances from the free end (DF) for the samples *8-15d* and *10-10d*. The shear bond stress can be

calculated using the elemental data at the interface along the embedded length, while the tensile stress can be obtained using the nodal data on the bar surface. Each curve was plotted at a different percentage of the maximum pull-out load (P_m), i.e. 20 %, 40%, 60%, 80%, 90% and 100%. Also, the shear bond stress can be analytically obtained based on the axial equilibrium of an infinitesimal segment of the bar, as illustrated in Fig. 5.16:

$$\tau(s_b(x)) = \frac{d_b}{4}\frac{d\sigma}{dx} \tag{5.23}$$

where $\tau(s_b(x))$ is the shear stress along dx. More details were provided in Chapter 6.

In the FE simulations, $d\sigma/dx$ can be approximated by the gradient of axial stress between two consecutive nodes. As seen in Fig. 5.15, a comparison between the simulation results of shear stress and the calculated data using Eq. (5.23) confirms that the simulation results satisfy the equilibrium condition.

(a)

(b)
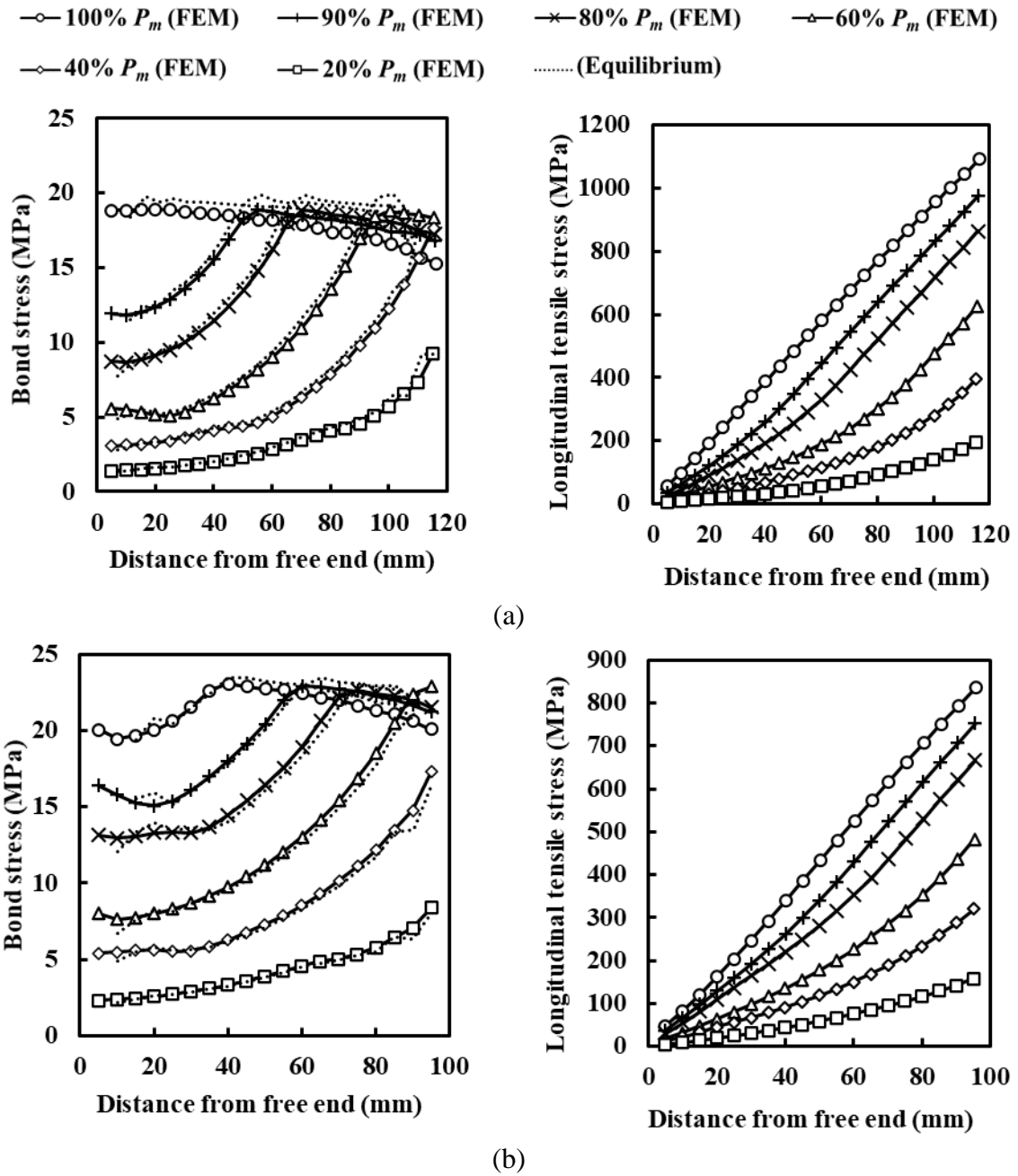
Fig. 5.15 Simulation results of stress distribution along distance from free end (DF): (a) model **8-15d** failed due to bar pull out; (b) model **10-10d** failed due to bar rupture.

Generally, Fig. 5.15a indicates that by increasing the pull-out load, the bond stress increased and the peak bond stress migrated from the loaded end towards the free end of the bar. When the pull-out load was less than 40% of P_m, the bond stress increased by moving through the embedded section from the loaded end to the free end. In other words, in the elastic regime, the peak stress occurred in the region close to the maximum distance from the free end (i.e. 120 mm for **8-15d** and 100 mm for **10-10d**). By further increasing the load, the bond stress increased through the whole bar until the stress reached the maximum bond strength ($\sim 60\% P_m$)

at DF_{max}. When the load exceeded the threshold value, a bond stress redistribution took place and then no more increase of shear stress was seen in that portion. It can be observed that the stress redistribution developed by increasing the load from $80\% P_m$ to $90\% P_m$. When the bar was completely pulled out (the sample **8-15d**) at $100\% P_m$, the bond stress over the embedment length exhibited an almost constant bond stress profile. It is worth noting that, in the sample **8-15d**, the portion of embedment length with constant bond stress increased from 20% at $60P_m$ to 100% at $100P_m$. Conversely, for the sample **10-10d** at $100\% P_m$, the local shear stress level around the free end (DF of 0 to 40 mm) did not reach the bond strength after the bar rupture occurred due to exceeding the tensile strength of the bar at a point out of the embedded part. Regarding the sample **10-10d**, the length portion with constant bond stress increased from 5% at $60P_m$ to 60% at $100P_m$. Thus, in this state, the premature rupture of the bar prevented the section from attaining the maximum bond strength capacity. A similar bond stress distribution was found for GFRP bars in PCC (Benmokrane et al., 1996; Achillides and Pilakoutas, 2006; Rezazadeh et al., 2017; Saleh, 2018) and for GFRP bars in GPC (Tekle et al., 2016). On the other hand, during the pull-out of steel bars in GPC, the peak bond stress was located at the bar loaded end for the entire duration of the test (Cui et al., 2020), which suggested that the peak bond stress migration is to be attributed to the BFRP reinforcement rather than the type of concrete (e.g. PCC and GPC).
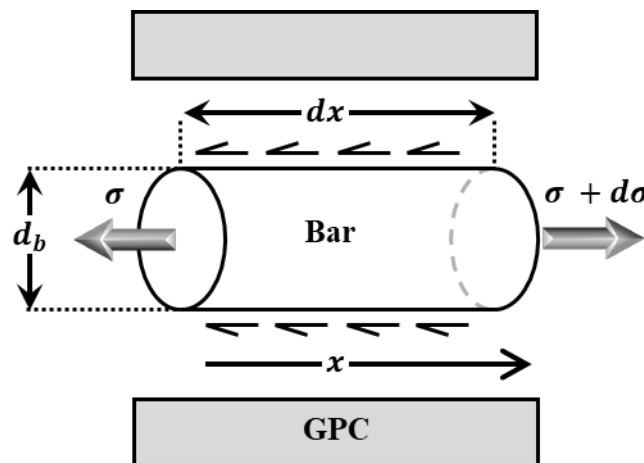
Fig. 5.16 Infinitesimal segment of BFRP bar in concrete subject to tension and bond stress.

To quantitatively analyse the variability of the bond stress along the bar embedment length, the coefficient of variation (COV) was obtained as the ratio of the standard deviation to the average value. For the sample **8-15d**, the value of COV decreased from 66% at $20\% P_m$ to 7% at $100\% P_m$, while for the sample **10-10d**, the COV reduced from 46% at $20\% P_m$ to 6% at $100\% P_m$. Furthermore, it can be observed that the bond stress distribution was more uneven

for longer embedment lengths, leading to lower average bond strength, as found in the experimental results discussed in Section 4.3.2.1.

As seen in Fig. 5.15b, during the whole loading process (i.e. 0-100% P_m), the longitudinal tensile stress increased with the increasing distance from the free end, and the change of longitudinal tensile stress against distance from the free end tends to be linear with the increase of applied pull-out load.

5.4.1.2   Radial bond stress

As discussed in Chapter 4, during pull-out, the radial bond stress (σ_r) induced at the bar-concrete interface may lead to radial cracking (i.e. splitting) of the concrete cover along the bar longitudinal axis (Tepfers, 1979). Fig. 5.17 shows the variations of the splitting tensile stress normalised to the concrete tensile strength along the radial distance from the centre of the bar at different loading stages. A comparison between the simulation results for the samples *10-5d* and *10-15d*, which failed due to bar pull-out and concrete splitting, respectively, indicates that the splitting tensile stress increased with the pull-out load and when the embedment length was relatively long ($15d_b$), the splitting stress level reached the concrete tensile strength, leading to the failure of the concrete elements, which agrees well with the experimental observations.
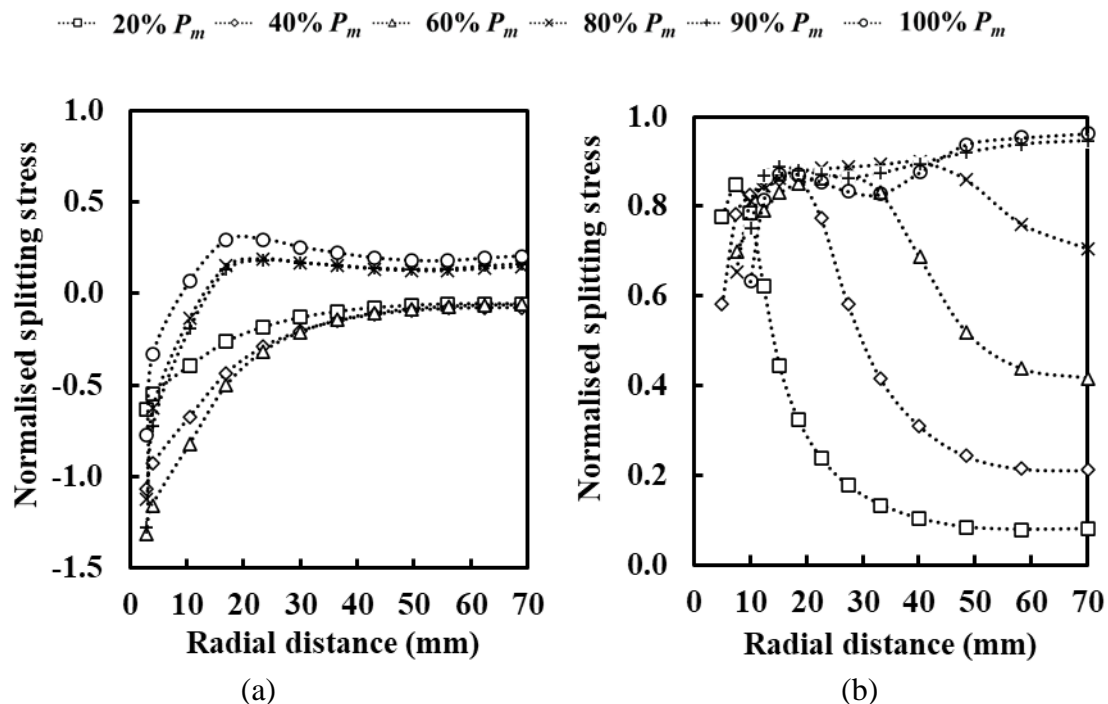
Fig. 5.17 Simulation results of splitting tensile stress distribution normalised to concrete tensile strength along radial distance from bar centre at different loading stages: (a) model *10-5d* failed due to bar pull-out; (b) model *10-15d* failed due to concrete splitting.

5.4.2 Parametric study on bond strength

In this section, a parametric study was performed to investigate the effects of different factors on bond behaviour of BFRP bars in GPC, including bond stress-slip properties (i.e. bond strength (τ_m), slip at peak (s_m) and ultimate slip (s_u)), bar characteristics (i.e. bar diameter (d_b), bar embedment length (l_d), and bar elastic modulus in the longitudinal direction (E_b)), and compressive strength of concrete (f_c). The sample ***10-5d*** was taken as an example for study since a complete bar pull-out failure can be observed in the experiments, and thus the maximum bond strength can be obtained. While the value of each parameter varied, the others remained unchanged with respect to the reference case. Table 5.4 summarises the values of the parameters assigned for the reference model and the corresponding ranges, which were studied. In the following, the effect of each parameter on the bond strength (i.e. average bond stress at $100\% P_m$) is discussed.

It is worth noting that the bond is generally affected by several mechanical and structural parameters, and the parametric study assumes that the effect of each parameter can be studied independently. However, as mentioned in Section 5.2.5, the input bond stress-slip curve depends on the specific experimental setup from which it was calibrated, and it is not possible to decouple the effect of one parameter from the others.

Table 5.4 Selected parameters and their values for parametric study of sample ***10-5d***.

	τ_m (MPa)	s_m (mm)	s_u (mm)	d_b (mm)	l_d (d_b)	E_b (GPa)	f_c (MPa)
Reference value	24	0.26	5	10	5	60	42
Studied range	20-30	0.1-0.5	5-9	6-20	5-20	30-80	20-70

5.4.2.1 Effect of bond stress-slip parameters

The bond stress-slip parameters change in a range from slightly smaller to greater than the reference values, which values were chosen based on the results of pull-out of BFRP bars in concrete (El Refai et al., 2015b). Fig. 5.18 shows the influences of τ_m, s_m and s_u on the bond strength of BFRP bars in GPC. As seen in Fig. 5.18a, the bond strength increased linearly with the slope of ~1 by increasing τ_m from 20 MPa to 30 MPa. Fig. 5.19 shows that, along the embedment length, the bond stress reached a constant value at the τ_m stress level. On the other hand, the changes of slip parameters (s_m and s_u) had an insignificant effect (Fig. 5.18b and c). The simulated bond strength remained almost constant (~24 MPa) as s_m (0.1-0.5 mm) and s_u (5-9 mm) changed with standard deviations of only about 0.19 and 0.24 MPa, respectively,

implying that the FE simulation was more sensitive to the bond strength compared to the slips. No changes on the failure mode were observed as all samples failed due to bar pull-out.
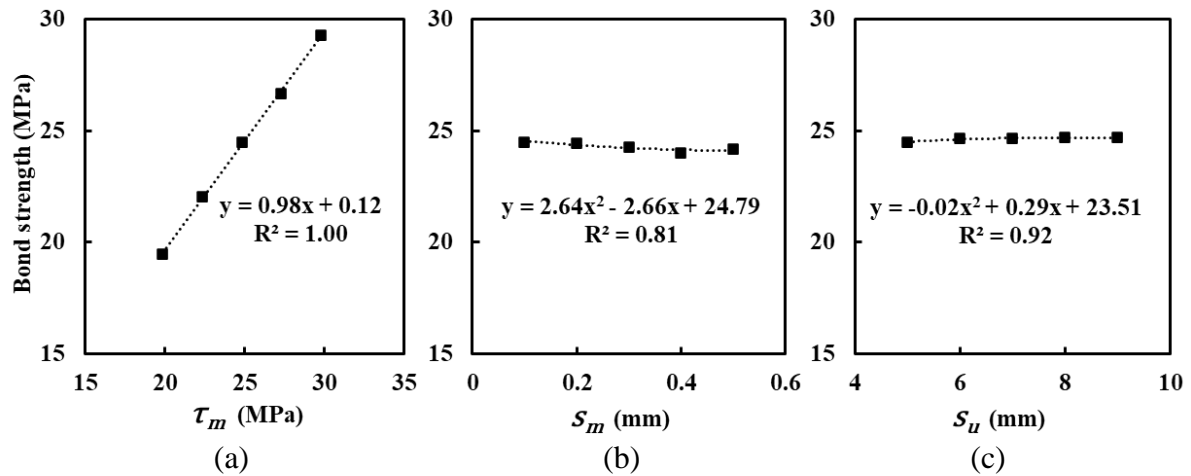
Fig. 5.18 Effect of bond stress-slip properties on average bond strength: (a) bond strength; (b) slip at peak; (c) ultimate slip.
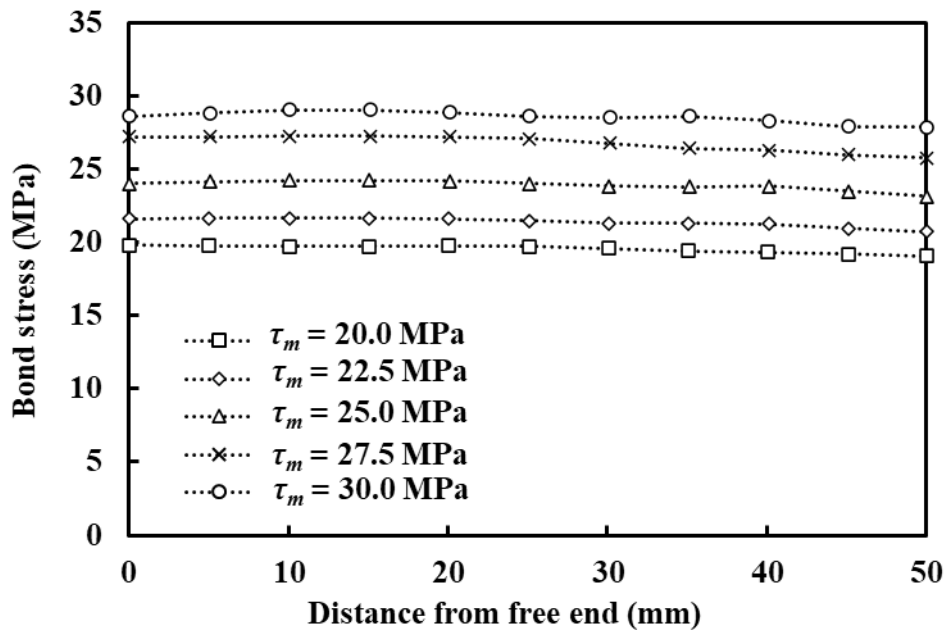
Fig. 5.19 Bond stress distribution at peak pull-out load for different values of τ_m.

5.4.2.2 Effect of bar characteristics

The range of BFRP bar diameters for this study was selected considering the most common BFRP bar diameters investigated in literature (El Refai et al., 2015b; Li et al., 2017; Wang et al., 2019). Fig. 5.20 shows the simulated bond strength as a function of the BFRP bar diameter, indicating an approximately 34% decrease in bond strength with the increase of bar diameter

from 6 mm to 20 mm, due to a combined effect of three factors. (1) A larger contact area corresponding to the larger diameter at the BFRP bar-concrete interface reduces the average bond stress level. (2) There exists a non-uniform distribution of the axial tensile stress across the cross-section of the BFRP bar between the surface and the centre, due to the so-called shear lag effect that is more pronounced for the BFRP bar with a larger diameter, as demonstrated in Fig. 5.21.
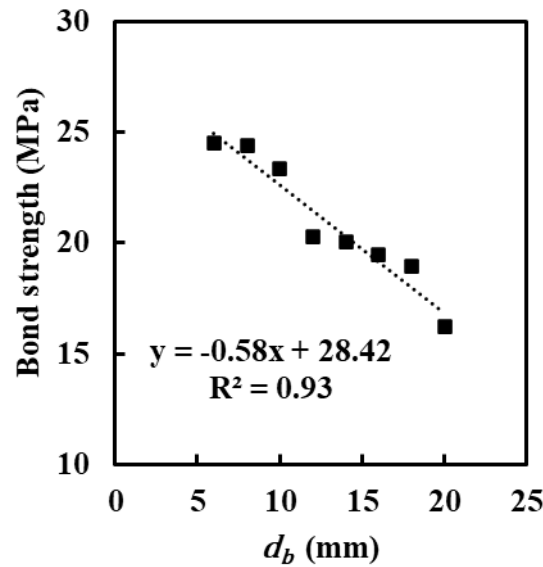
Fig. 5.20 Influence of bar diameter on bond strength.

Fig. 5.21a shows the tensile stress at the bar loaded end normalised to that on the bar surface (σ/σ_m) against the distance from the bar surface normalised to the bar radius at the end of the loading process. Fig. 5.21b illustrates the simulated axial stress contours at the cross-section of the BFRP bars with various diameters. It should be considered that the colourful contour plot does not directly represent the elemental values. This is a common way to visualise the spatial/cross-sectional stress distribution with respect to the elements through the model. Fig. 5.21 indicates that the shear lag effect was insignificant, and the stress distribution was almost uniform when the bar diameter was smaller than 10 mm. With the increase of bar diameter from 10 mm to 20 mm, the maximum stress difference across the bar cross-section increased and reached $20\%\sigma_m$. (3) The longitudinal tensile stress can lead to a reduction in bar diameter, i.e. the so-called Poisson's effect (Achillides and Pilakoutas, 2004a), which becomes more significant with increasing bar diameter as the lateral deformation increases with the bar size. Consequently, the mechanical interlocking and the friction at the bar surface are reduced, resulting in reduced bond strength. Regarding the failure mode, the specimens with BFRP bar diameters smaller than 18 mm failed due to bar pull-out, while those with larger bars (18 mm

and 20 mm) failed in the form of concrete splitting due to reduced concrete cover thickness and reduced confinement accordingly.

(a)

(b)
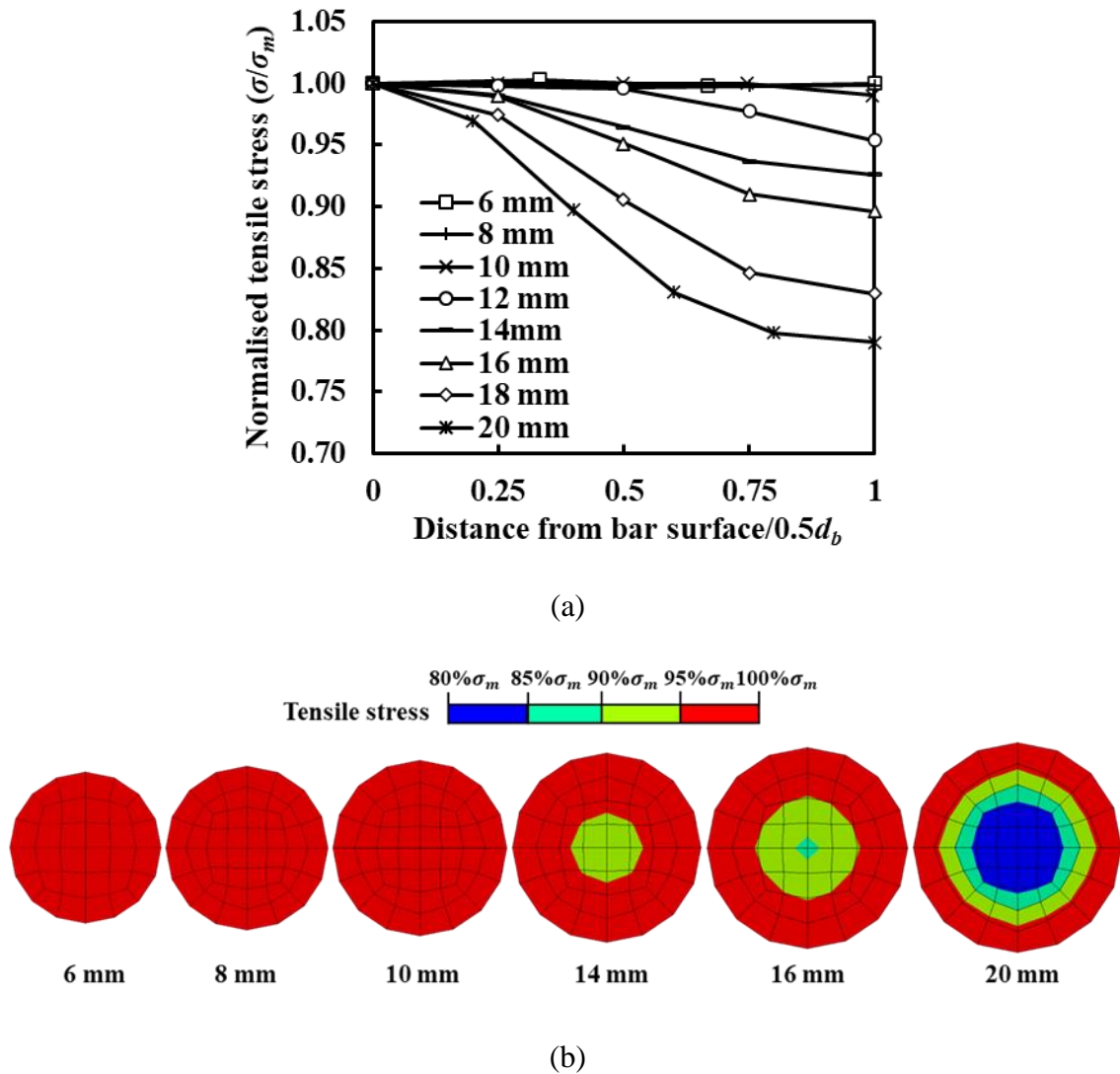
Fig. 5.21 Shear lag effect at the loaded end for different bar diameters: (a) axial stress normalised to stress on bar surface (σ/σ_m); (b) examples of tensile stress distribution at the bar cross-section at maximum pull-out load.

Fig. 5.22a shows the effect of the embedment length ranging from $5d_b$ to $20d_b$ with an increment of $2.5d_b$ on the bond strength of BFRP bars to GPC, being these values the most used to investigate the bond of BFRP bars in concrete (El Refai et al., 2015b; Li et al., 2017; Yang et al., 2018). It should be mentioned that to allow longer embedment lengths and avoid concrete splitting failure, the geometry of the sample was slightly adjusted by doubling the size of the concrete block side parallel to the bar axis to 300 mm. Furthermore, for comparison purposes, two cases were investigated: (1) the bar failure was neglected in the model (Case 1), and (2) it is assumed that the bar fails at a tensile stress level of 876 MPa (Case 2). Fig. 5.22a

presents the bond strength against varying l_d for Cases 1 and 2, and the calculated bond strength (τ_m) according to ACI 440.1R (2015) for structural concrete reinforced with FRP bars as a function of the embedment length, given as follows:

$$\frac{\tau_m}{0.083\sqrt{f_c}} = 4.0 + 0.3\frac{c}{d_b} + 100\frac{d_b}{l_d} \tag{5.24}$$

In Case 1, all samples failed due to pull-out of the bar. The bond strength was reduced by about 21% by increasing l_d from $5d_b$ to $20d_b$. In Case 2, the sample with shorter embedment lengths ($5d_b$ to $10d_b$) followed a failure mode of bar pull-out and experienced a 23% reduction in bond strength like that for Case 1. However, for the samples with longer embedment lengths ($12.5d_b$ to $20d_b$), the failure mode changed to bar rupture along with an approximately 42% drop in bond strength with increasing l_d. The variation of bond strength against the embedment length of BFRP bar for different failure modes follows different trends, as illustrated in Fig. 5.22, which also indicates that the predictions by the ACI code underestimate the bond strength for the BFRP-GPC system while not reflecting the effect of failure mode. This result was consistent with the findings of studies investigating BFRP bars in PCC (El Refai et al., 2015b) and GFRP bars in GPC (Tekle, 2017), in which the bond strength values excided the ACI provisions. A similar result was also found by Yan et al. (2016) and Rezazadeh et al. (2017) for GFRP in PCC, a different system from BFRP in GPC, which still presents similarities between BFRP and GFRP bars.

Fig. 5.22b displays the simulated bond strength of BFRP bar in GPC as a function of the elastic modulus of BFRP bar ranging from 30 GPa to 80 GPa, which are commonly reported for BFRP bars (Patnaik et al., 2012; El Refai et al., 2015b; Elgabbas et al., 2015; Fan et al., 2017; Ali et al., 2019; Alnajmi and Abed, 2020; Liu et al., 2020). It can be found that the elastic modulus of the bar in the longitudinal direction had no significant influence on both the bond strength (with a standard deviation of only 0.13 MPa) and the failure mode. It is worth noting that a uniform axial stress can be observed along the embedded portion of the BFRP bar at $100\%P_m$ for the bar elastic moduli of 30 GPa and 80 GPa. The elastic modulus of GFRP bars was also found to have no significant effect on the bond strength between GFRP bars and GPC (Tekle, 2017).
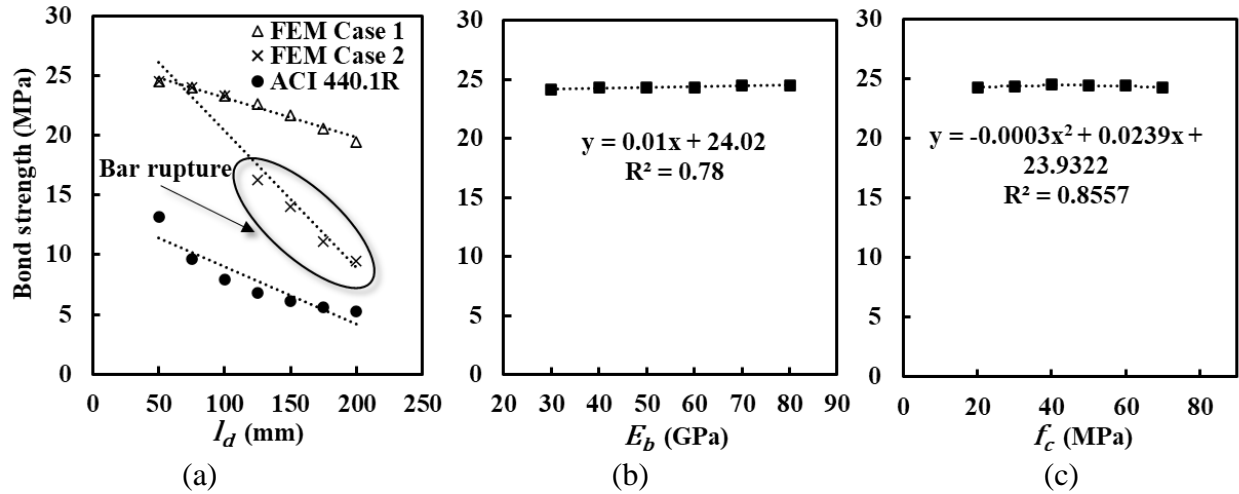
Fig. 5.22 Bond strength as a function of: (a) embedment length; (b) elastic modulus of the bar; (c) concrete compressive strength. Dotted lines are guides to the eye.

5.4.2.3 Effect of concrete compressive strength

The influence of the concrete compressive strength on the simulated bond strength of BFRP bar in GPC was assessed considering a concrete compressive strength varying from 20 MPa to 70 MPa, values usually investigated for the BFRP-to-concrete interaction (Altalmas et al., 2015; El Refai et al., 2015b; Dong et al., 2018a; Liu et al., 2020; Michaud and Fam, 2021). Fig. 5.22c indicates that the compressive strength of GPC had a negligible influence on the simulated bond strength (standard deviation was only equal to 0.08 MPa) and the failure mode. As discussed in Chapter 2, some previous studies (Tepfers and Karlsson, 1997; Achillides, 1998; Achillides and Pilakoutas, 2004a; Baena, 2010) reported that there exists an obvious influence of the concrete compressive strength on bond strength and failure mode of FRP bars embedded in PCC, while some others (Tighiouart et al., 1998; Esfahani et al., 2013) demonstrated the negligible influence of concrete compressive strength on bond. The discrepancy can be explained by the fact that mix proportions, preparation and geometry of the concrete samples (e.g., constituents, curing conditions, and size/shape) can differ between studies. Moreover, the bond strength is affected by the interaction of several mechanical and structural parameters, which effects cannot be decoupled.

5.5 Concluding remarks

In this chapter, the bond behaviour of BFRP bars to GPC during the quasi-static pull-out process was systematically investigated using an integrated 3D finite element model. Based on the material properties and the bond stress-slip curve experimental characterisation, the bond behaviour was evaluated using the elastic transversely isotropic model for the BFRP bars, the CDP model for the GPC matrix, and the cohesive model with traction-separation law for the

BFRP bar-GPC interface. Mesh, loading time and mass scaling sensitivity analysis were run to identify a suitable combination for a quick yet reliable analysis. First, the model was validated against the experimental data. Then, the stress analysis and the parametric studies were carried out. Based on the simulation results, the main conclusions can be drawn as follows:

- A nonlinear distribution can be observed for the tensile and bond stress along the BFRP bar length, as suggested by the COV of the bond stress that reached up to 66% at lower load levels ($20\% P_m$). With the increase of pull-out load (P_m), the peak bond stress moved gradually from the loaded end towards the free end, leading to a more constant bond stress level, with a COV of 6% at $100\% P_m$. The BFRP-GPC samples with long bar embedment lengths failed due to concrete splitting due to the hoop stress on the concrete induced by the interaction between bar and concrete. The simulation results show a good agreement with experimental data.

- From the parametric study emerged that the bond stress-slip parameters influenced the bond strength. In particular, the bond strength increased linearly with the slope of ~1 by increasing τ_m from 20 to 30 MPa. The slip at peak s_m and ultimate slip s_u did not influence the bond strength nor the failure mode.

- The bar diameter has a significant influence on the bond behaviour of BFRP bar in GPC. The bond strength was reduced by 34% with the increase of the bar diameter from 6 mm to 20 mm, which can be attributed to a combined effect of the larger contact area corresponding to the larger diameter, the shear lag effect (i.e. the existence of a non-uniform distribution of the axial tensile stress across the cross-section of the BFRP bar between the surface and the centre) and the Poisson's effect.

- The bond behaviour of BFRP bars in GPC in terms of bond strength and failure mode is strongly influenced by the bar embedment length. As the embedment length increases from $5d_b$ to $20d_b$, the bond strength is decreased by approximately 20% and 40% for the samples with failure modes of bar pull-out and bar rupture, respectively. Moreover, the predictions of bond strength by the ACI equation for FRP bar reinforced normal concrete seemed to be conservative for the BFRP-GPC system where the different failure modes were not be considered.

- Both the elastic modulus of the BFRP bar and the compressive strength of GPC had no significant influence on the bond behaviour of the BFRP bar in GPC in terms of bond strength and failure mode.

Chapter 6 Theoretical Study of Bond of BFRP Bars to GPC

6.1 Introduction

In Chapter 4, the bond behaviour of BFRP bars in GPC was experimentally investigated through pull-out tests. The local bond stress-slip curves were then obtained from experimental data, assuming an even shear stress distribution along the bonded portion, even though the low longitudinal elastic modulus of FRP bars causes bond stress nonlinearity as suggested by the difference in slips observed at the bar free and loaded ends. However, as discussed in Section 2.4.2, the experimental study of the bond distribution through strain monitoring can negatively impact the pull-out test results (Henault et al., 2012; Lee and Mulheron, 2015; Rolland et al., 2018). To overcome the experimental limitations, numerical modelling based on nonlinear analysis using finite element models (FEM) was performed in Chapter 5. However, analytical modelling is a time-effective alternative to numerical modelling to investigate the bond interface properties. Several yet limited local relationships between bond stress and slip ($\tau(s)$) were proposed for FRP bars in concrete, and closed-form solutions for the exact computation of the bond stress, slip and strain distribution along the FRP in concrete were developed. However, to the best author's knowledge, the bond behaviour of BFRP bars in GPC has not yet been investigated analytically. Thus, in this chapter, an analytical procedure for studying the bond properties of BFRP bars in GPC was proposed.

In this chapter, a bilinear model was proposed to theoretically describe the local bond stress-slip relationship of BFRP bars in GPC, and closed-form solutions of the governing equations were developed to predict the interface properties. The bilinear model was validated against experimental data from Chapter 4 and numerical results from Chapter 5 and then used to predict the tensile stress and bond stress distribution along the bar embedded portion. A parametric study was then carried out to estimate the influences of the involved bond stress-slip curve variables and the bar properties on the maximum pull-out load, based on which the underlying mechanisms of BFRP-GPC interaction were explored and discussed in depth.

6.2 Analytical model

6.2.1 Governing equations

In Section 5.4.1.1, the equilibrium relationship between shear bond stress and bar's axial stress was briefly introduced to verify the FE simulation results. In the following, the governing equation of a reinforcing bar embedded in a concrete prism under a tensile load is introduced in more detail (Russo et al., 1990).

Fig. 6.1 shows a schematic illustration of an infinitesimal segment of a bar embedded in concrete during the pull-out process under a tensile load. The bond stress acting on the contact surface between bar and concrete is $\tau = \tau(s)$, where $s = s(x)$ represents the relative displacement (slip) between bar and concrete at a location x, and $\sigma = \sigma(x)$ denotes the tensile stress at the location x, being x a reference axis along the bar. Thus, the tensile stress acting on the bar cross-sectional area and the shear stress acting on the contact surface between the bar and the concrete were considered. The equilibrium of a small length dx of a bar with diameter d_b and the slip can be described, respectively, as follows:

$$\tau(s_b(x))\pi d_b dx = \frac{\pi d_b^2}{4} d\sigma(x) \tag{6.1}$$

$$\varepsilon_b - \varepsilon_c = \frac{ds(x)}{dx} \tag{6.2}$$

where $\varepsilon_b = \varepsilon_b(x)$ is the strain of the bar and $\varepsilon_c = \varepsilon_c(x)$ is the strain of the concrete at the location x.

Based on Eq. (6.1), the following equation can be derived:

$$\tau(s_b(x)) = \frac{d_b}{4} \frac{d\sigma(x)}{dx} \tag{6.3}$$

As per previous studies (Yankelevsky, 1985; Focacci et al., 2000; Yuan et al., 2004), two assumptions are made herein: (1) the BFRP bar along the longitudinal direction is considered to be linear elastic; (2) the deformation of concrete is ignored as the displacement of concrete at the bar-concrete interface is negligible compared to the displacement of the points of the bar.

Based on the first assumption, the BFRP bar linear elastic behaviour is expressed as follows:

$$\sigma(x) = E_b \varepsilon_b(x) \tag{6.4}$$

where E_b is the elastic modulus of the bar.

Based on the second assumption, the slip $s(x)$ at the interface between concrete and reinforcement is equal to the displacement of the cross-section of the bar $s_b(x)$ at the location x, and is defined as:

$$s(x) = s_b(x) \tag{6.5}$$

Considering Eq. (6.5), Eq. (6.2) can be written as:

$$\frac{ds(x)}{dx} = \frac{ds_b(x)}{dx} = \varepsilon_b \tag{6.6}$$

The governing differential equation can therefore be expressed as:

$$\tau(s_b(x)) = \frac{E_b d_b}{4} \frac{d\varepsilon_b(x)}{dx} \tag{6.7}$$

As discussed in Chapter 5, the bond stress in Eq. (6.7) is directly proportional to the strain gradient along the length of the bar, providing a critical equilibrium condition to be verified.

Rearranging Eq. (6.6) and Eq. (6.7), it is possible to obtain the following:

$$\frac{d^2 s_b(x)}{dx^2} = \frac{4}{E_b d_b} \tau(s_b(x)) \tag{6.8}$$

Introducing the constant a_1 defined as:

$$a_1 = \frac{4}{E_b d_b} \tag{6.9}$$

Eq. (6.8) can be written as:

$$\frac{d^2 s_b(x)}{dx^2} = a_1 \tau(s_b(x)) \tag{6.10}$$

From this point of the text onwards, the bar slip and bar strain will be referred to as $s(x)$ and $\varepsilon(x)$, omitting the bar subscript to ease the formulation.

The experimental bond stress-slip curves $\tau(s)$ can be analytically described by different models (Biscaia et al., 2013). Linear, quadratic, or parabolic equations relate the slip with the bond stress through parameters calibrated from experimental data. Once the bond stress-slip model is defined, a closed-form solution of the governing differential equation for the given bond stress-slip model is required to theoretically study the distribution of stresses, strain and slip along the bond length, properties that define the bond behaviour. In the following paragraph, the closed-form solution based on a bilinear bond stress-slip model is proposed.
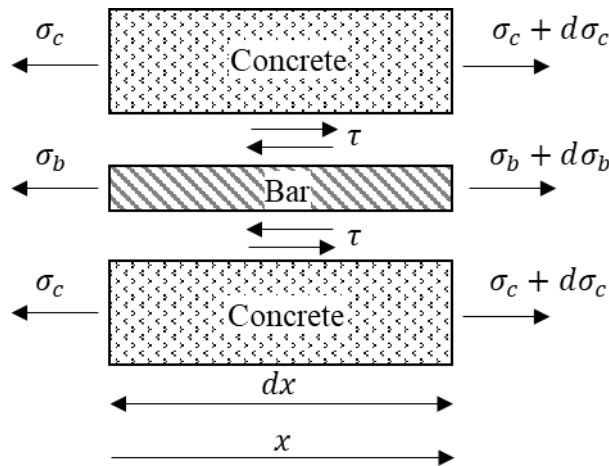
Fig. 6.1 Equilibrium in a bar embedded in a concrete block under axial tensile force.

6.2.2 Local bilinear bond stress-slip relationship

Fig. 6.2 illustrates the bilinear model proposed to describe the local bond stress-slip relationship for BFRP bars in GPC, which was investigated experimentally in Chapter 4. The bond stress-slip curve can be expressed as:

$$\tau(s) = \begin{cases} ks & 0 \leq s \leq s_m \\ \dfrac{\tau_m}{s_d}(s_m + s_d - s) & s_m \leq s \leq s_u \end{cases} \qquad (6.11)$$

where $s_d = s_u - s_m$ being s_u the ultimate slip (mm).

In the ascending branch, the bond stress increases linearly with the slip up to the peak bond stress τ_m which indicates the bond damage initiation. The debonding process evolves with the increment of the slip while the bond stress also decreases linearly.

The local bond stress-slip parameters analytically describing the bond behaviour between FRP bars and concrete are generally calibrated from experimental data. However, several approaches have been used in the literature. For instance, some studies (Achillides and Pilakoutas, 2006; Rolland et al., 2020) calibrated the parameters on the bond stress-slip curve measured at the bar free end, while others (Rezazadeh et al., 2017) used the loaded end bond stress-slip curve. In other cases, the bond stress-slip parameters were not obtained directly from experimental data; instead, the optimal set of values was calibrated starting from a set of assumed tentative values with an iterative process that minimises an error function between theoretical and experimental curves (Focacci et al., 2000; Pecce et al., 2001; Tekle et al., 2016). According to Cosenza et al. (1997), the slip (s_m) is generally evaluated at the free end of the bar. In this study, the latter approach was adopted for both the analytical and numerical modelling, as according to the FE simulation results, this method provided the best fit with the experimental data. Thus, the peak bond stress (τ_m) and the free end slip at maximum pull-out load (s_m) were adopted according to the experimental pull-out data provided in Table 4.2. As the ultimate slip (s_u) was not available experimentally, it was calibrated with an iterative procedure, to optimise its value by minimising the error between analytical and experimental maximum pull-out load, according to:

$$Error(P_m) = \frac{\left| P_{m,EXP} - P_{m,AN} \right|}{P_{m,EXP}} \qquad (6.12)$$

In the following sections, closed-form solutions for each phase of the bilinear relationship are developed to predict the normal tensile stress, shear bond stress, slip and strain along the bar. Thus, a good approximation of the interface properties can be obtained from only two significant points of the experimental bond-stress slip curve, i.e. the bond peak (τ_m, s_m) and the ultimate slip (s_u).
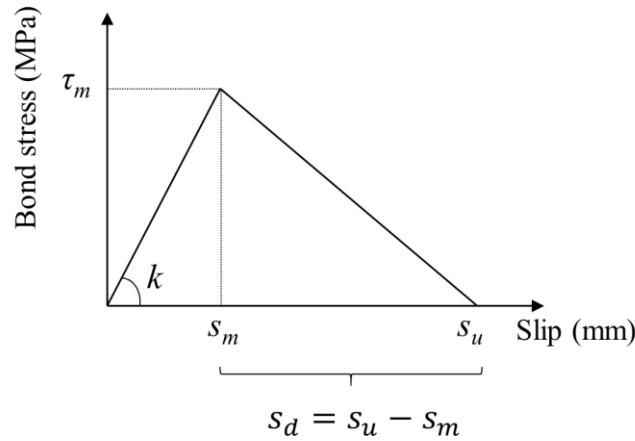
Fig. 6.2 Bilinear bond stress-slip relationship.

6.2.3   Solution for linear ascending bond phase

The bond stress-slip equation for a linear ascending bond stress-slip curve up to the peak bond stress can be written as:

$$\tau = ks \tag{6.13}$$

where k is calculated as in Eq. (5.16).

The differential governing equation given in Eq. (6.10) is solved with the interfacial bond stress-slip characteristics $\tau(s)$, along with the boundary conditions for this specific pull-out problem.

Substituting Eq. (6.13) into the governing equation of Eq. (6.10) yields:

$$\frac{d^2 s(x)}{dx^2} = a_1 ks \tag{6.14}$$

By solving the differential equation in Eq. (6.14), the slip variation is obtained:

$$s(x) = c_1 \cosh(\lambda_1 x) + c_2 \sinh(\lambda_1 x) \tag{6.15}$$

Differentiating Eq. (6.15) yields:

$$\frac{ds(x)}{dx} = \lambda_1 c_1 \sinh(\lambda_1 x) + \lambda_1 c_2 \cosh(\lambda_1 x) \tag{6.16}$$

Substituting Eq. (6.15) into the linear ascending bond stress-slip of Eq. (6.13) results in:

$$\tau(x) = k[c_1 \cosh(\lambda_1 x) + c_2 \sinh(\lambda_1 x)] \tag{6.17}$$

Considering Eq. (6.4), the normal stress acting along the bar is calculated as:

$$\sigma(x) = E_b[\lambda_1 c_1 \sinh(\lambda_1 x) + \lambda_1 c_2 \cosh(\lambda_1 x)] \tag{6.18}$$

in which the constant $\lambda_1 = \sqrt{a_1 k}$ and the constants c_1 and c_2 can be calculated using the following boundary conditions.

145

Fig. 6.3 shows the case of a bar embedded in a concrete block for an embedded length (l_d) with a pull-out load (P) applied at the extremity. A reference axis x is defined staring at the free end. For this case, two boundary conditions can be determined at each loading stage, i.e. at the free end $(x = 0)$ the strain is null, as given in Eq. (6.19), and at the loaded end $(x = l_d)$ the strain is known and given as in Eq. (6.20):

$$x = 0; \quad \left.\frac{ds_b}{dx}\right|_{x=0} = \varepsilon_b(0) = 0 \tag{6.19}$$

$$x = l_d; \quad \left.\frac{ds_b}{dx}\right|_{x=l_d} = \varepsilon_b(l_d) = \frac{P}{E_b A_b} \tag{6.20}$$

Eq. (6.16) can be solved using the boundary conditions given in Eq. (6.19) and Eq. (6.20), and the two constants of integration c_1 and c_2 are obtained as follows:

$$c_1 = \frac{P}{E_b A_b} \frac{1}{\lambda_1 \sinh(\lambda_1 l_d)} \qquad c_2 = 0 \tag{6.21}$$

Hence, slip $s(x)$, strain $\varepsilon(x)$ and bond stress $\tau(x)$ and tensile stress $\sigma(x)$ can be calculated at each position x along the bar according to Eq. (6.22), (6.23), (6.24) and (6.25), respectively.

$$s(x) = \frac{P}{E_b A_b \lambda_1} \frac{\cosh(\lambda_1 x)}{\sinh(\lambda_1 l_d)} \tag{6.22}$$

$$\frac{ds(x)}{dx} = \frac{P}{E_b A_b} \frac{\sinh(\lambda_1 x)}{\sinh(\lambda_1 l_d)} \tag{6.23}$$

$$\tau(x) = \frac{Pk}{E_b A_b \lambda_1} \frac{\cosh(\lambda_1 x)}{\sinh(\lambda_1 l_d)} \tag{6.24}$$

$$\sigma(x) = \frac{P}{A_b} \frac{\sinh(\lambda_1 x)}{\sinh(\lambda_1 l_d)} \tag{6.25}$$
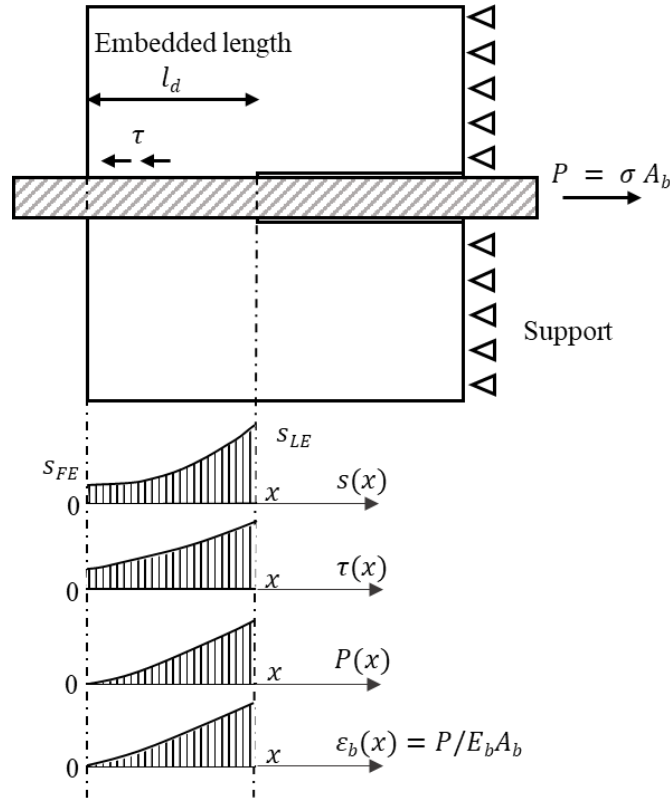
Fig. 6.3 Functions defining a bar embedded in a concrete block, adapted from Focacci et al. (2000).

6.2.4 Solution for linear descending bond phase

The bond stress-slip relationship for a linear descending behaviour can be expressed as:

$$\tau = \frac{\tau_m}{s_d}(s_m + s_d - s) \tag{6.26}$$

Substituting Eq. (6.26) into the governing Eq. (6.10) leads to:

$$\frac{d^2 s(x)}{dx^2} = \lambda_2^2(s_m + s_d - s) \tag{6.27}$$

Solving the differential equation of Eq. (6.27) gives the slip variation:

$$s(x) = c_3 \sin(\lambda_2 x) + c_4 \cos(\lambda_2 x) + s_m + s_d \tag{6.28}$$

Differentiating Eq. (6.28) yields the slip strain variation:

$$\frac{ds(x)}{dx} = \lambda_2 c_3 \cos(\lambda_2 x) - \lambda_2 c_4 \sin(\lambda_2 x) \tag{6.29}$$

Substituting Eq. (6.28) into Eq. (6.26) results in the shear bond stress variation:

$$\tau(x) = -\frac{\tau_m}{s_d}[c_3 \sin(\lambda_2 x) + c_4 \cos(\lambda_2 x)] \tag{6.30}$$

The normal stress distribution is given as:

$$\sigma(x) = E_b[\lambda_2 c_3 \cos(\lambda_2 x) - \lambda_2 c_4 \sin(\lambda_2 x)] \tag{6.31}$$

where the constant $\lambda_2 = \sqrt{\frac{\tau_m}{s_d}} a_1$ and the constants c_3 and c_4 can be solved through substitution of the boundary conditions given in Eq. (6.19) and Eq. (6.20), as per the ascending bond behaviour, yielding to the following:

$$c_3 = 0 \qquad\qquad c_4 = -\frac{P}{E_b A_b \lambda_2} \frac{1}{\sin(\lambda_2 l_d)} \qquad (6.32)$$

The slip, strain, bond stress and tensile stress distribution along the bar embedded length are finally given as follows:

$$s(x) = -\frac{P}{E_b A_b \lambda_2} \frac{\cos(\lambda_2 x)}{\sin(\lambda_2 l_d)} + s_m + s_d \qquad (6.33)$$

$$\frac{ds(x)}{dx} = \frac{P}{E_b A_b} \frac{\sin(\lambda_2 x)}{\sin(\lambda_2 l_d)} \qquad (6.34)$$

$$\tau(x) = \frac{\tau_m}{s_d} \frac{P}{E_b A_b \lambda_2} \frac{\cos(\lambda_2 x)}{\sin(\lambda_2 l_d)} \qquad (6.35)$$

$$\sigma(x) = \frac{P}{A_b} \frac{\sin(\lambda_2 x)}{\sin(\lambda_2 l_d)} \qquad (6.36)$$

6.2.5 Solution for transition between ascending and descending bond phases

During the pull-out test, at low stress levels, the ascending phase conditions exist along the entire length of the bar. Then, the peak bond stress migrates from the loading point towards the bar free end by increasing the pull-out load. Thus, at higher loading levels, the position of the peak stress (x_p) is found in the embedment length (l_d), and two bond phases act over the bonded length. The ascending bond phase conditions exist along part of the bar towards the free end $(0 < x < x_p)$, while the descending bond phase conditions exist on the part of the bar towards the loaded end $(x_p < x < l_d)$ that already reached the peak bond stress. Therefore, to obtain the interface properties for the transition phase, it is necessary to consider two boundary conditions and three conditions of continuity (slip, strain, and stress), given as follows:

- Strain at the free end according to the ascending phase (Eq. (6.16)), to be null;
- Strain at the loaded end according to the descending phase (Eq. (6.29)), to be equal to $P/E_b A_b$;
- Slip according to ascending phase (Eq. (6.15)) and descending phase (Eq. (6.28)), to be equal;
- Strain according to ascending phase (Eq. (6.16)) and descending phase (Eq. (6.29)), to be equal;

- Bond stress according to ascending phase (Eq. (6.17)) and descending phase (Eq. (6.30)) to be equal;

which can be summarised in an equation system describing the bond behaviour in the transition phase:

$$
\begin{cases}
\left.\dfrac{ds(x)}{dx}\right|_{x=0} = \lambda_1 c_1 \, sinh(\lambda_1 x) + \lambda_1 c_2 cos\, h(\lambda_1 x) = 0 \\[2mm]
\left.\dfrac{ds(x)}{dx}\right|_{x=l_d} = \lambda_2 c_3 \, cos(\lambda_2 x) - \lambda_2 c_4 \, sin(\lambda_2 x) = \dfrac{P}{E_b A_b} \\[2mm]
c_1 \, cosh(\lambda_1 x) + c_2 sin\, h(\lambda_1 x) = c_3 \, sin(\lambda_2 x) + c_4 \, cos(\lambda_2 x) + s_m + s_d \\[1mm]
\lambda_1 c_1 \, sinh(\lambda_1 x) + \lambda_1 c_2 cos\, h(\lambda_1 x) = \lambda_2 c_3 \, cos(\lambda_2 x) - \lambda_2 c_4 \, sin(\lambda_2 x) \\[1mm]
k[c_1 \, cosh(\lambda_1 x) + c_2 \, sinh(\lambda_1 x)] = -\dfrac{\tau_m}{s_d}[c_3 \, sin(\lambda_2 x) + c_4 \, cos(\lambda_2 x)]
\end{cases}
\tag{6.37}
$$

Once the value of the constants c_1, c_2, c_3, c_4 and the position of the peak stress x_p are known, the interface properties for the bar portion in the ascending phase are obtained using Eqs. (6.15) - (6.18) while the interface properties for the portion following the softening behaviour can be calculated using Eqs. (6.28) - (6.31).

The solution for the differential equations based on a bilinear bond stress-slip model that govern the response of a bar under axial pull-out load were proposed. Fig. 6.4 graphically summarises the flowchart of the algorithm used to calculate the bond properties at each loading stage. The analysis uses an incremental loading procedure run with the software MATLAB (The MathWorks, 2018).
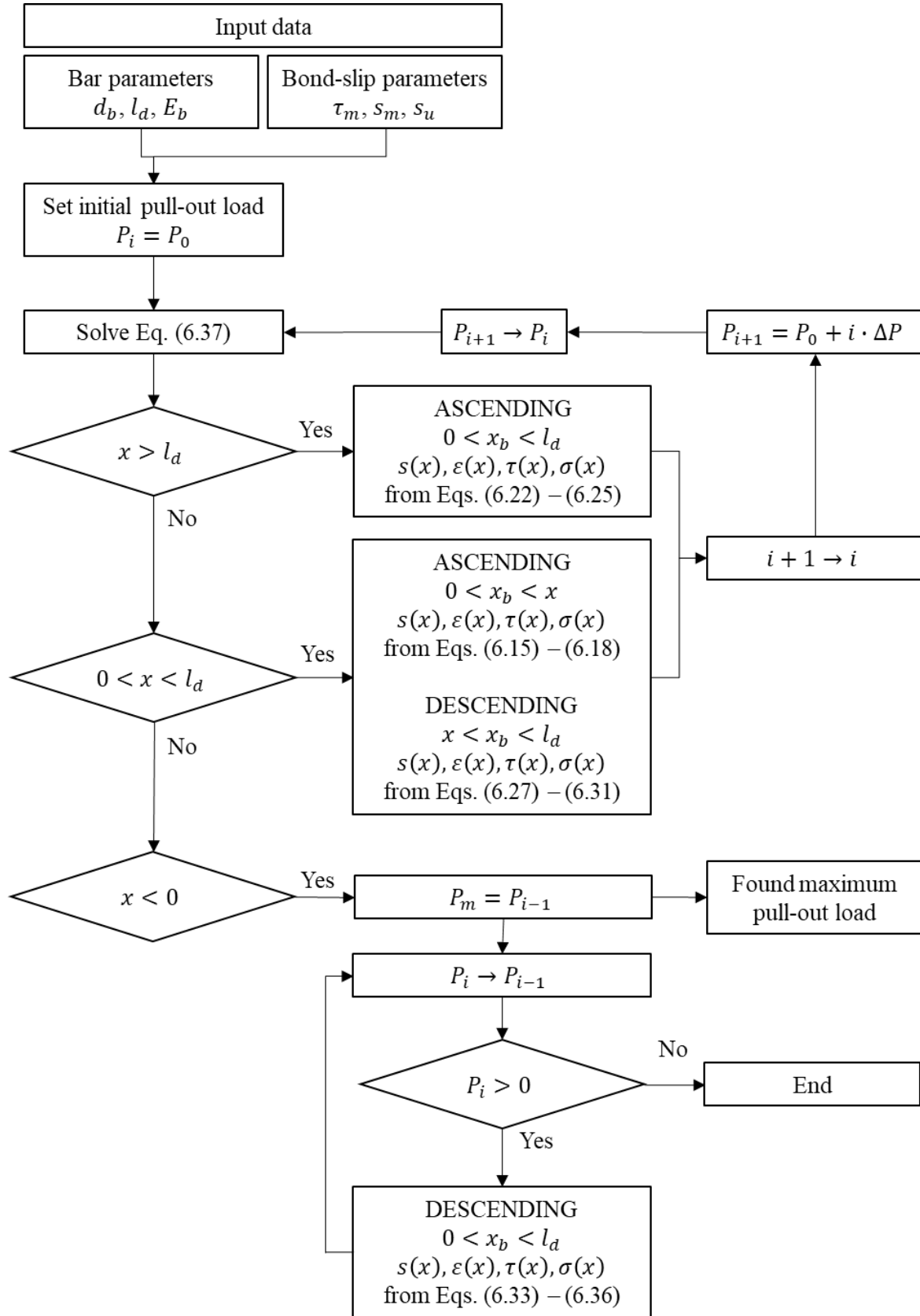
Fig. 6.4 Flowchart of the proposed model.

6.3   Comparison between analytical and finite element analyses

The proposed theoretical model and the FE model are valuable tools to investigate analytically and numerically the bond interaction along the embedded length in terms of bond and tensile stress, slip and strain distribution. Similarities and differences between the analytical and numerical methods are therefore compared and discussed.

Both the theoretical and the FE models require the definition of the bond behaviour and the BFRP bar behaviour. First, for the bond stress-slip property, a bilinear constitutive law is assigned in both models. Second, regarding the BFRP bar constitutive behaviour, the analytical model assumes a linear elastic behaviour on the bar longitudinal axis, parallel to the fibre direction. On the other hand, the FE model uses the transversely isotropic constitutive law, a more complex model that better represents the actual behaviour of the BFRP bars. Nonetheless, in the FE model, the BFRP bar behaviour is isotropic in the transverse direction yet linear elastic along the longitudinal axis, thus similar to that adopted in the analytical model. However, it is worth noting that while the tensile strength of the BFRP bar is taken into account in the FE model, the analytical model does not allow to consider the bar rupture.

Considering the differences, while the FE model includes a detailed concrete matrix constitutive law, the analytical model is instead developed based on the assumption that the concrete strains at the interface are negligible. Thus, the contribution of concrete is neglected in the analytical formulation. This assumption could cause discrepancies between the predictions obtained with the two models if the concrete strains calculated numerically results to be not negligible. Furthermore, the FE analysis is carried out under displacement control, as in the experimental pull-out test. The algebraic analysis, on the other hand, is performed under force control. This difference is expected to have no significant impact on the results, yet a slight discrepancy between the maximum predicted pull-out load and the experimental data or the numerical prediction could be observed. Finally, while the FE model allows investigating also the radial bond stress profile, as presented in Section 5.4.1.2, the analytical model can only predict the shear bond stress distribution.

In the following, the theoretical predictions are compared with the FE simulation results to validate the analytical model and assess if the differences highlighted affect the models' performance.

6.4   Model validation using the bond stress-slip relationship

The proposed model was applied to the experimental results of the pull-out of BFRP bars in GPC. The validity of the theoretical predictions was assessed by comparing the analytical

predictions with the experimental data and the FE simulation results in terms of bond stress-slip curves. Further validation was carried out also considering the tensile stress and bond stress distribution.
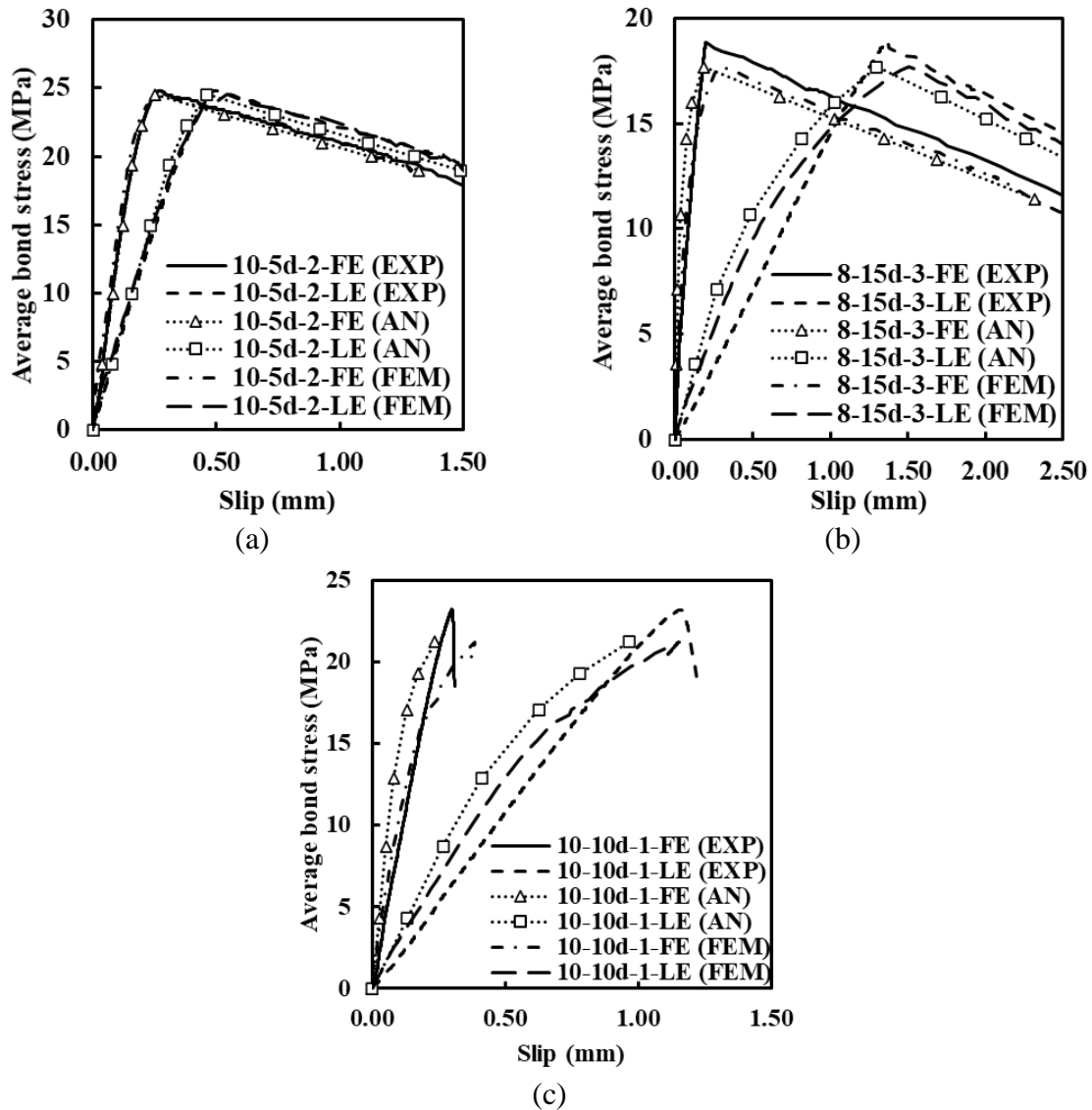
Fig. 6.5 Comparison between experimental, algebraic and FEM bond stress-slip curves for sample: (a) *10-5d-2*, failed due to bar pull-out; (b) *8-15d-3*, failed due to bar pull-out; (c) *10-10d-1*, failed due to bar rupture.

The comparison between experimental data, FEM and algebraic predictions of the average bond stress-slip curve at both free and loaded end of the samples *10-5d-2*, *8-15d-3*, and *10-10d-1* are displayed in Fig. 6.5. Thus, it can be seen that the proposed model offered the predictions of the bond stress-slip curve with satisfactory accuracy in terms of values and shape compared to the experimental data. The goodness of the bond stress-slip curve predictions was determined considering the ratio of experimental data to analytical predictions. Table 6.1 presents the values of mean, standard deviation (SD), coefficient of variation (COV), lower 95%

confidence level (95% LCL) and upper 95% confidence level (95% UCL) for the mean and extreme values (Min and Max). Fig. 6.6 displays the ratio between experimental data and analytic predictions for bond strength, slip at the free end and slip at the loaded end, together with mean and confidence limits. In general, the predictions showed a good fit with the experimental results, with a COV ranging from 5% to 16%. Only limited outliers were observed. Due to the limited data set used for the statistical analysis, the goodness of the fit should be considered a preliminary indication of the theoretical model performance, which should be further confirmed with a broader set of results.

A comparison between numerical and analytical bond stress-slip curves was also carried out considering the root mean square percentage error calculated as $RMSPE = \sqrt{\frac{\sum_{i=1}^{n}\left(P_{m,FEM}-P_{m,AN}\right)^2}{n}}$. The sample *10-5d-2* exhibited an error of 5% at the free end slip curve and 7% at the loaded end slip curve. For *8-15d-3*, an RMSPE of 8% was observed at the free end and 16% at the loaded end. For *10-10d-1*, an error of 9% was calculated at the free end and 12% at the loaded end. The comparison indicates that regardless of the differences between numerical and analytical models discussed in Section 6.3, the two methods led to similar bond stress-slip curves.

The comparison of the bond stress-slip curves and the statistical analysis suggest that the theoretical model is a valid tool for predicting the bond stress-slip curve of BFRP bars in GPC. After such validation, the theoretical formulation was used to predict bond and tensile stress distribution along the bar embedded portion presented below.

Table 6.1 Summary of descriptive statistics.

	EXP/AN		
	τ_m	$s_{m,FE}$	$s_{m,LE}$
Mean	1.09	1.17	1.04
SD	0.08	0.19	0.05
COV	8%	16%	5%
95% LCL	1.06	1.09	1.02
95% UCL	1.13	1.26	1.06
Min	1.02	0.98	0.95
Max	1.44	1.83	1.22

Note: SD (standard deviation); COV (coefficient of variation); 95% LCL (lower 95% confidence limit for the mean); 95% UCL (upper 95% confidence limit for the mean).

(a)

(b)

(c)
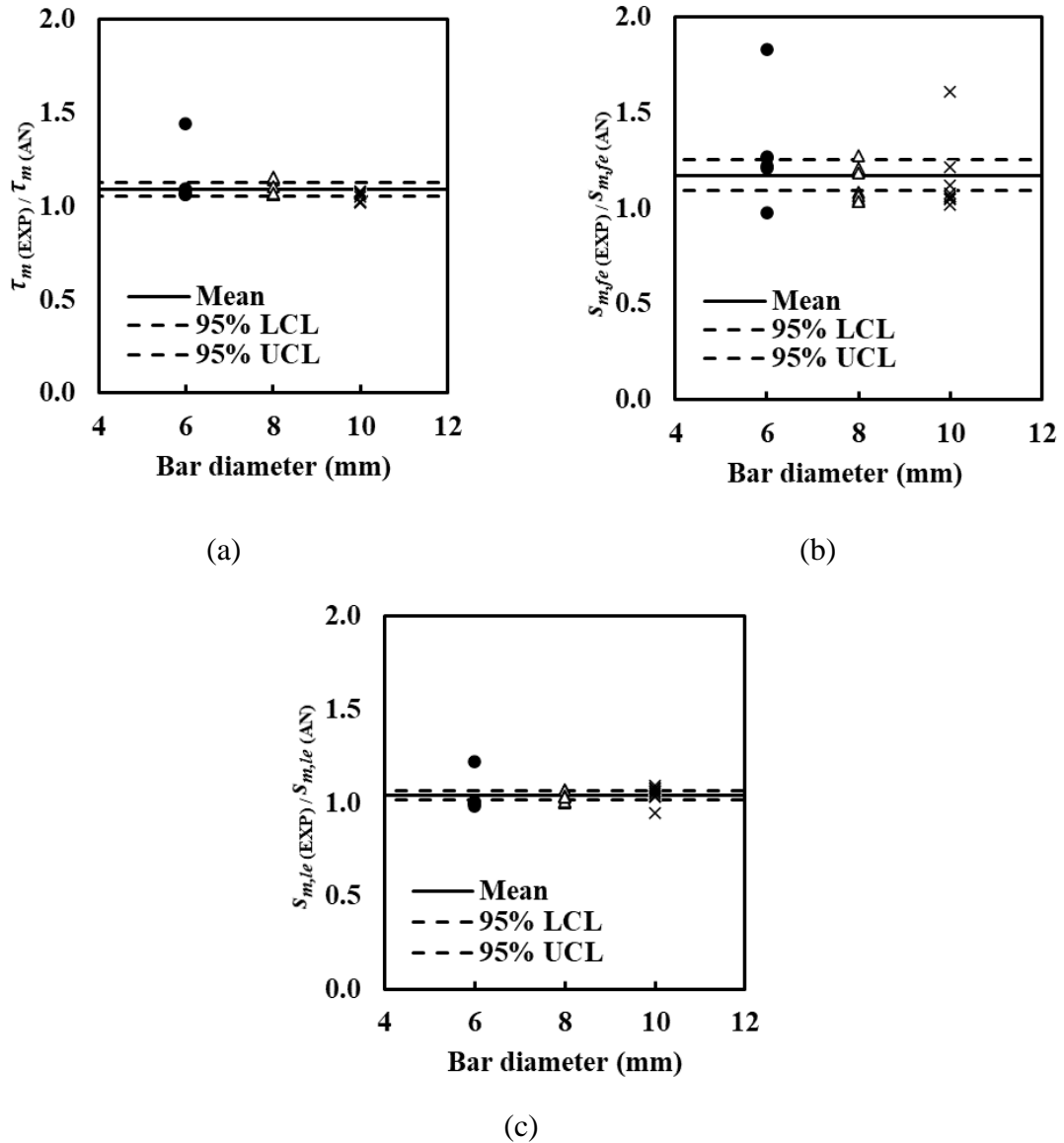
Fig. 6.6 Ratio of experimental to analytical results: (a) bond strength; (b) slip at the free end; (c) slip at the loaded end.

6.5 Results and discussion

6.5.1 Distribution of tensile and bond stresses

As already mentioned, one of the main aims of the analytical model is to provide an insight into the interface stress distribution during the pull-out, which is otherwise difficult to access experimentally.

Fig. 6.7, Fig. 6.8 and Fig. 6.9 display the distribution of the bar longitudinal tensile stress and the shear bond stress at the interface for the samples *10-5d-2*, *8-15d-3*, *10-10d-1*, respectively, comparing the theoretical predictions and the FE simulation results already validated in the previous chapter. Generally, good agreement was found between the algebraic and the FE simulation results.

154

Fig. 6.7a, Fig. 6.8a and Fig. 6.9a display the bar longitudinal tensile stress, which increased with the load level and decreased from the loaded end towards the free end. The tensile stress tended to be nonlinear for lower pull-out loads but linear for higher pull-out loads.

As shown in Fig. 6.7b, Fig. 6.8b, and Fig. 6.9b, the bond stress along the bar increased with increasing pull-out load until the maximum bond stress was reached. For lower pull-out loads (20% - 60%P_m), the peak bond stress was found at the bar loaded end, and by increasing the load level, the peak bond stress reached the maximum bond stress and progressively migrated towards the bar free end. Thus, as discussed for the experimental data and the FE simulation results, the nonlinear distribution of the bond stress along the bar embedment length can vary compared to the average bond stress, even more remarkably for longer embedment lengths. Conversely, as observed in the literature (Mazaheripour et al., 2013b; Ling et al., 2019; Lu et al., 2021), for shorter embedment length ($5\,d_b$) a relatively uniform bond stress distribution can be obtained, an example of which is displayed in Fig. 6.7b for the sample ***10-5d-2***, which bond stress was close to the experimental bond strength value (24.83 MPa) provided in Table 4.2.

Fig. 6.10 shows the bond stress concentration factor (K_b), defined as the ratio of the predicted peak bond stress to the average bond stress, at different load levels. A parametric study was run to estimate the variation of K_b for different bar diameters (8 and 10 mm) and embedment lengths ($5d_b$, $10d_b$, $15d_b$) whilst maintaining the bond stress-slip parameters. K_b increased with increasing bar diameter and embedment length and reduced with increasing load. High values of K_b, ranging from 1.50 to 3.93, were found at low load levels (20%P_m), while increasing the pull-out load, the K_b value was ~1.0. This trend indicated a strong nonlinearity of the bond stress profile at lower load levels and a more even distribution at higher loads, consistent with that illustrated in Fig. 6.7b, Fig. 6.8b, and Fig. 6.9b. Furthermore, the variation of K_b with bar diameter and embedment length can be observed at lower loading stages, while for higher load levels (80% - 100%P_m) all samples displayed a similar K_b.
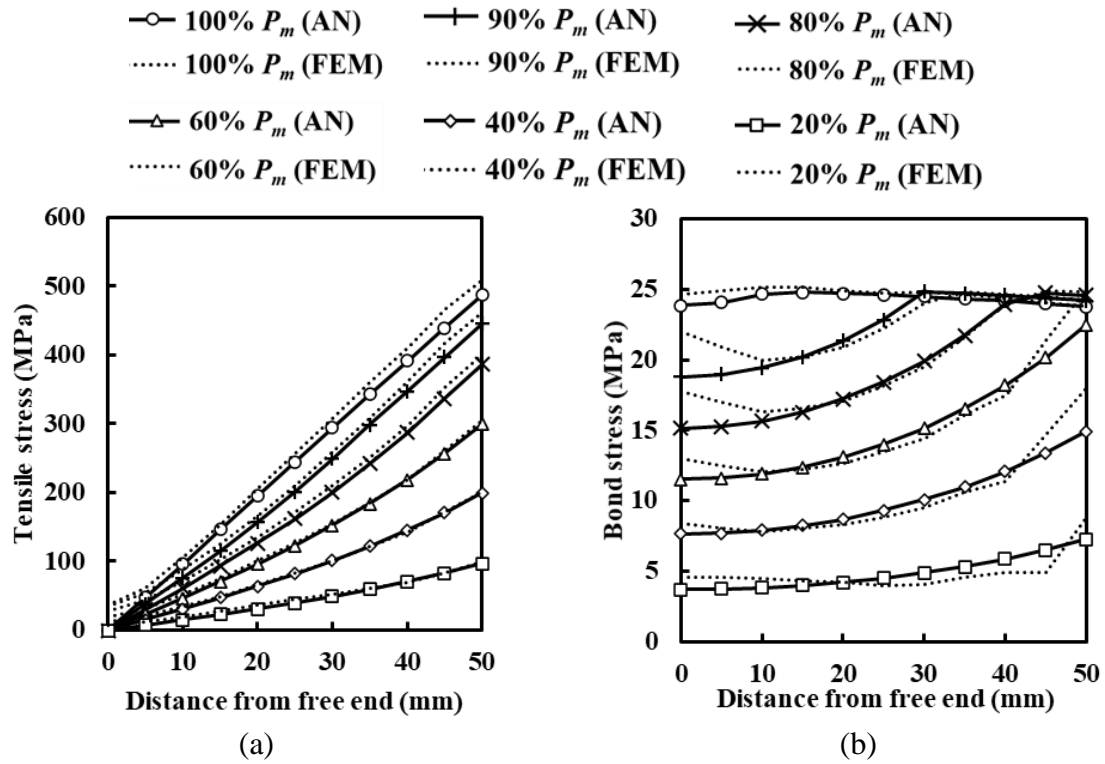
Fig. 6.7 Comparison between algebraic and FE results for sample *10-5d-2*: (a) tensile stress; (b) bond stress.
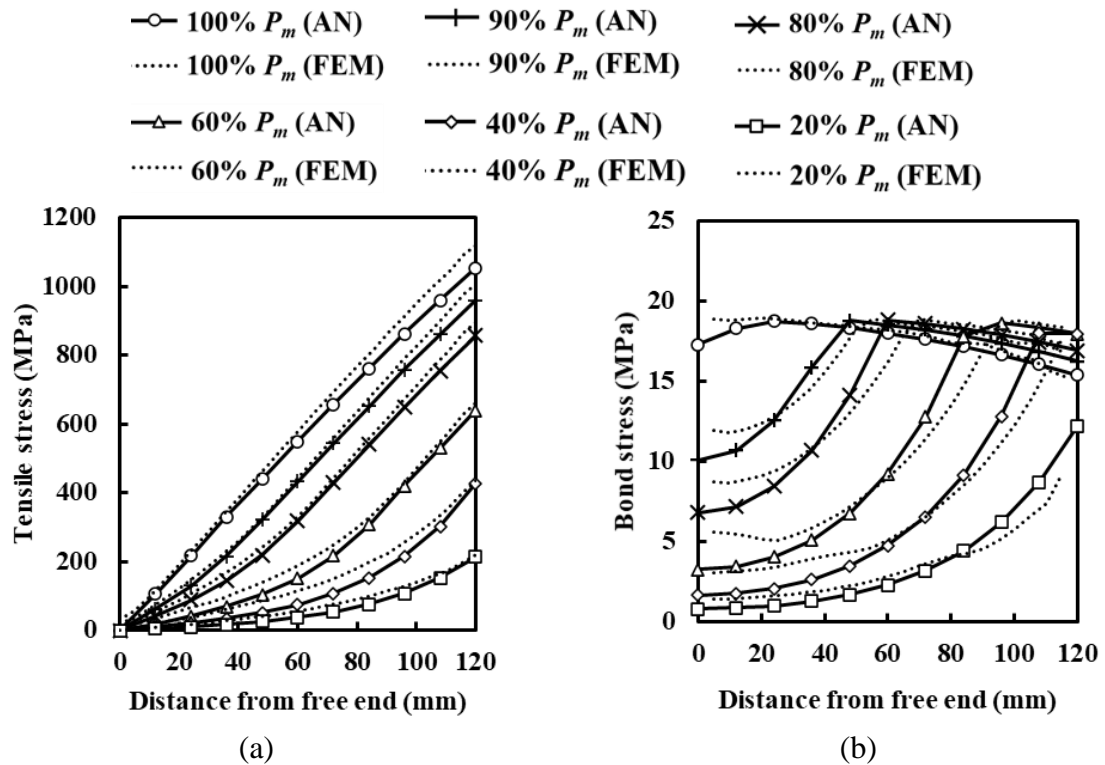
Fig. 6.8 Comparison between algebraic and FE results for sample *8-15d-3*: (a) tensile stress; (b) bond stress.
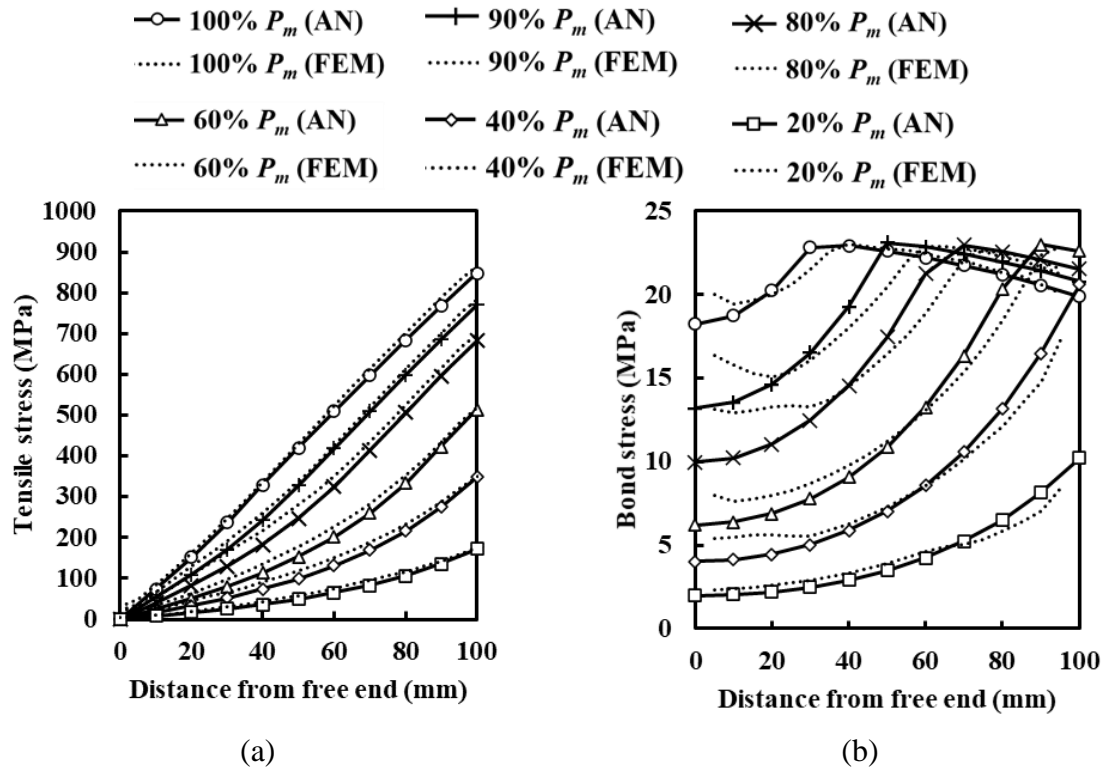
Fig. 6.9 Comparison between algebraic and FE results for sample *10-10d-1*: (a) tensile stress; (b) bond stress.
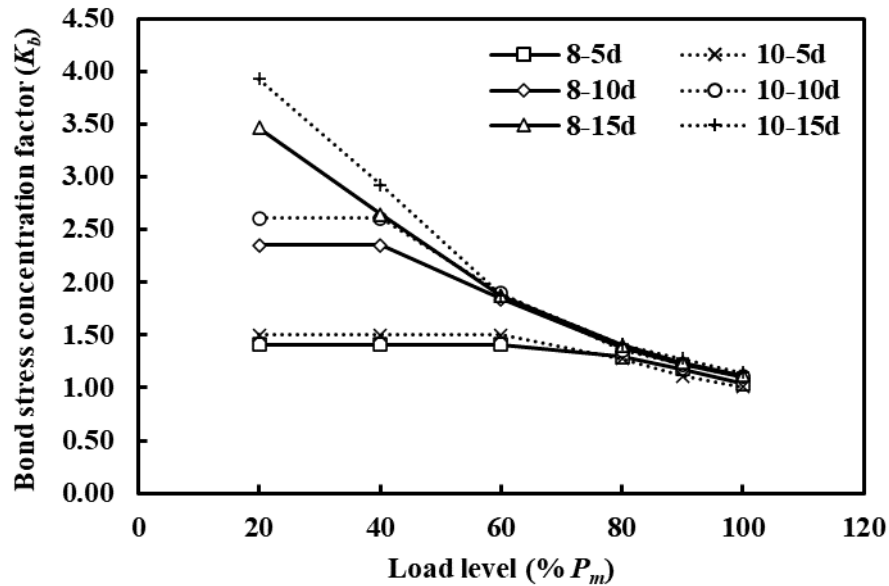
Fig. 6.10 Variation of bond stress concentration factor with load level for different bar diameters and embedment lengths.

6.5.2 Parametric study on bond strength

In this section, a parametric study was carried out to estimate the influence on the bond strength of different parameters considered in the theoretical equations, including the parameters characterising the bond stress-slip curve, namely, slip at peak (s_m), ultimate slip (s_u) and bond strength (τ_m), as well as bar characteristics including diameter (d_b), embedment length (l_d), and elastic modulus of BFRP bar (E_b). For the parametric study, the value of each parameter varied while the other parameters remained unchanged. As a reference, the sample **10-5d-2** was chosen within those that failed due to bar pull-out, as this failure mode provide a close estimation of the bond strength. Table 6.2 summarises the values adopted in the parametric study. Numerical results were also reported for comparison purposes. The study was run considering the maximum pull-out load which is proportional to the bond strength according to the Eq. (4.1).

Table 6.2 Summary of ranges of values for the studied parameters.

Parameter	s_m (mm)	s_u (mm)	τ_m (MPa)	d_b (mm)	l_d (d_b)	E_b (GPa)
Reference value	0.26	5	24	10	5-15	60
Studied range	0.1-0.5	5-9	20-30	6-20	5-20	30-80

6.5.2.1 Effect of bond stress-slip parameters

First, the sensitivity of the theoretical predictions to the bond stress-slip parameters was evaluated. As seen in Fig. 6.11, the bond strength (τ_m) was in the range of 20 and 30 MPa, the value of the slip at peak (s_m) varied between 0.1 and 0.5 mm, and the value of the ultimate slip (s_u) changed from 5 to 9 mm, which have been chosen based on the study on pull-out of BFRP bars in PCC (El Refai et al., 2015b). As indicated in Fig. 6.11a, the maximum pull-out load increased linearly with the bond strength. Nevertheless, the slip at peak and the ultimate slip had no significant influence on the maximum pull-out load (see Fig. 6.11b and c). Thus, the theoretical predictions seemed to be sensitive to the bond strength of the bond stress-slip curve.

Fig. 6.11 also indicates that the theoretical predictions match those obtained with the FE study run for a 10-mm bar with an embedment length of $5d_b$.
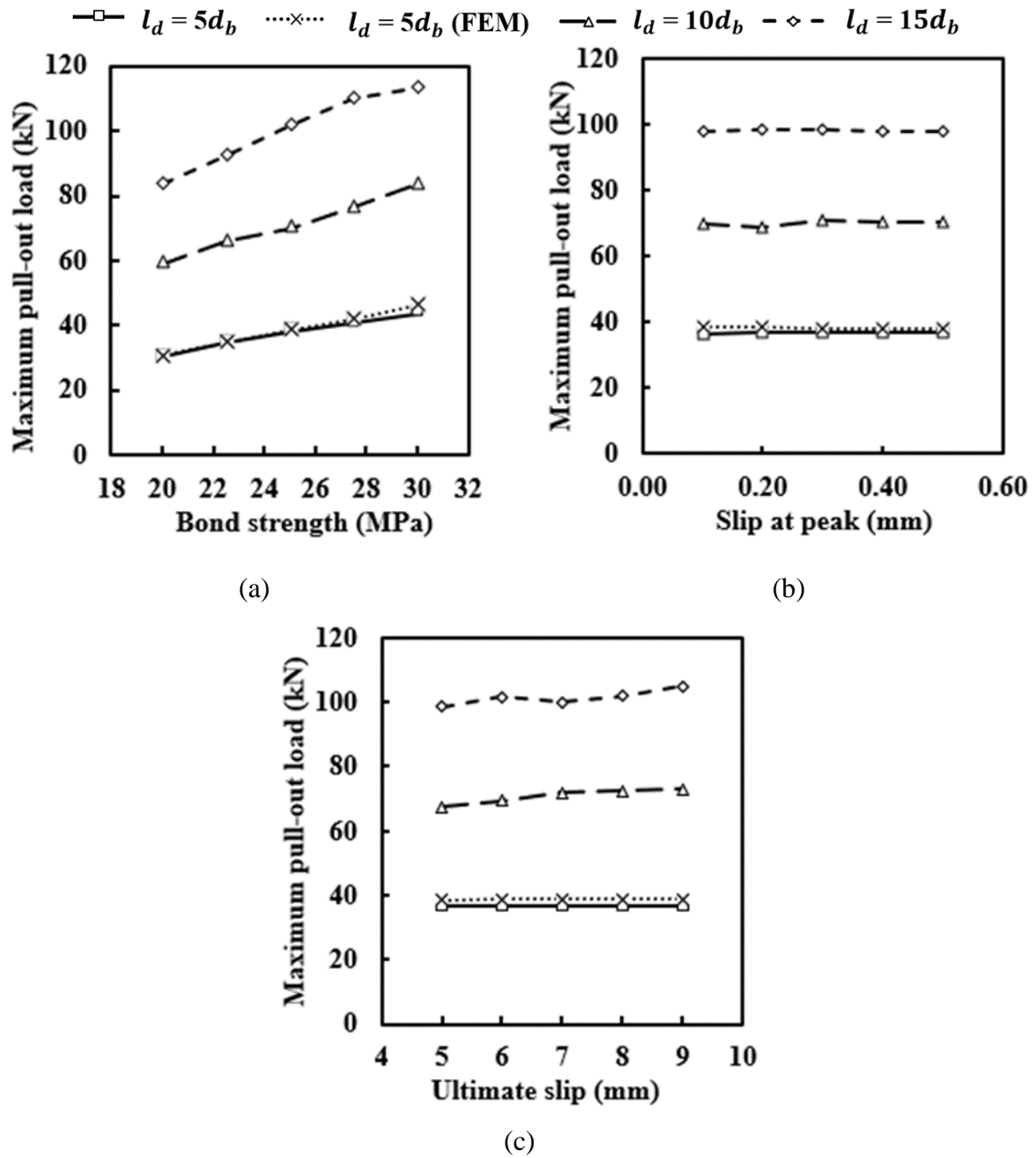
Fig. 6.11 Variation of maximum pull-out load with: (a) bond strength; (b) slip at peak; (c) ultimate slip.

6.5.2.2 Effect of bar characteristics

Different bar diameters ranging from 6 to 20 mm with an increment of 2 mm, and embedment lengths in the range of 5 - $20d_b$ with an increment of $2.5d_b$ were adopted to estimate the effects of bar diameter and embedment length on maximum pull-out load, which are the most commonly used ranges to investigate the bond between BFRP bars and concrete (El Refai et al., 2015b; Li et al., 2017; Yang et al., 2018; Wang et al., 2019). The results shown in Fig. 6.12a and b indicate that both bar diameter and embedment length significantly influenced the maximum pull-out load, which remarkably increased with bar diameter and embedment length.

The predicted bond strength reduced less significantly compared to the experimental data: it was reduced by ~5% with the increase of bar diameter from 6 to 10 mm and by ~11% as the embedment length increased from $5d_b$ to $15d_b$. Compared to the experimental data, the lower reduction in bond strength with increasing bar diameter and embedment length obtained from theoretical predictions can be attributed to the sensitivity of theoretical predictions to the bond stress-slip parameters, as discussed above.

In addition, in Fig. 6.12, the FE simulation results, already discussed in Chapter 5, are compared with the analytical predictions. In Fig. 6.12a, the influence of the bar diameter on the maximum pull-out load was explored using an embedment length of $5d_b$, while, in Fig. 6.12b, different embedment lengths were investigated with a 10 mm bar diameter and a bond strength of 24 MPa. It is worth noting that the FE simulation data given in Fig. 6.12b were obtained neglecting the BFRP bar tensile strength to be compared with the analytical results which were based on a similar assumption. In both cases, the analytical predictions were consistent with the numerical results, further validating the proposed analytical method.

(a)
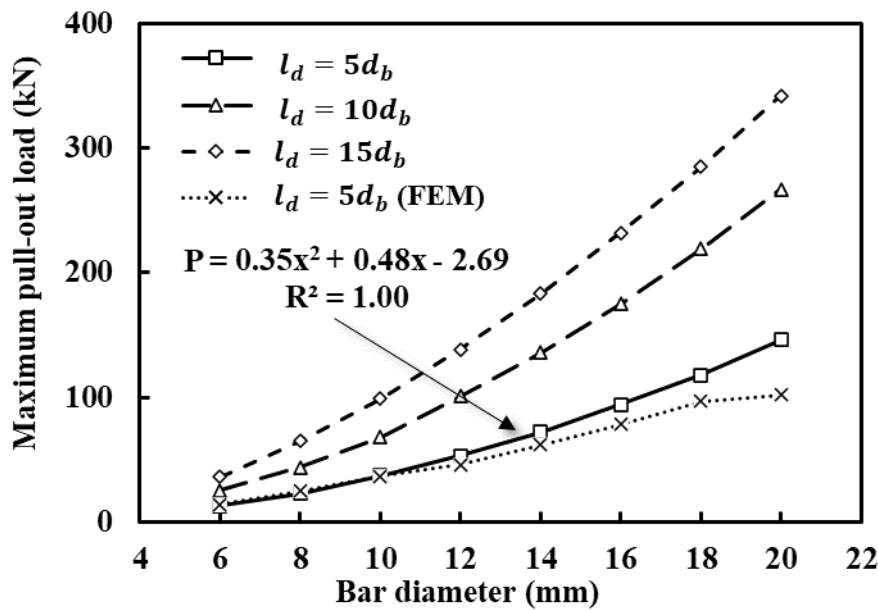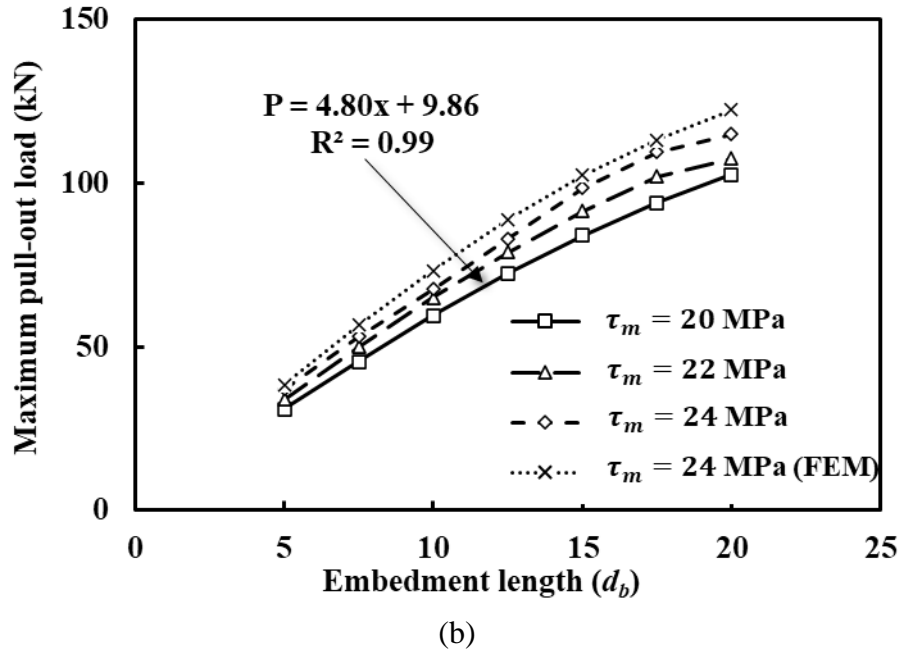
(b)
Fig. 6.12 Variation of pull-out load with: (a) bar diameter; (b) embedment length.

Fig. 6.13 shows the variation of maximum pull-out load with the elastic modulus of BFRP bar ranging from 30 to 80 GPa, which are commonly reported in the literature on BFRP bars (Patnaik et al., 2012; El Refai et al., 2015b; Elgabbas et al., 2015; Fan et al., 2017; Ali et al., 2019; Alnajmi and Abed, 2020; Liu et al., 2020). For BFRP bars in GPC, the predicted maximum pull-out load remained relatively constant, regardless of the bar elastic modulus, implying that the BFRP bar elastic modulus had no significant influence on the maximum pull-out load. A similar conclusion was drawn in literature for materials comparable to those investigated here where the changes in elastic moduli of GFRP bars from 30 to 65 GPa (Mazaheripour et al., 2013b) and 42 to 50 GPa (Tekle, 2017) had a negligible influence on the maximum pull-out load of GFRP bars in PCC and GPC, respectively. In addition, Fig. 6.13 indicates good agreement between the analytical results and the numerical parametric study run for a 10-mm bar and $5d_b$ embedment length.

It is worth mentioning that BFRP bars have a lower elastic modulus than conventional steel rebars (CEB-FIP, 2000). Fig. 6.14 shows a comparison of the bond stress distribution of the 10-mm BFRP bar with an elastic modulus of 57.5 GPa for the samples *10-5d-2* and *10-10d-1* with that of steel rebar, which has an elastic modulus of 210 GPa but the same configurations. The bar elastic modulus remarkably influenced the distribution of bond stress along the bar embedded in GPC. The stiffer steel rebar provided a more constant bond stress distribution along the embedded length than the more uneven distribution exhibited by the BFRP bar with a relatively lower elastic modulus. The effect of the nonlinearity is even more

evident for longer embedment lengths (Fig. 6.14b), as previously suggested by the bond stress concentration factor (K_b). Therefore, the nonlinearity of the bond stress between BFRP bars and GPC can be attributed to the bar elastic modulus, similarly to the findings for GFRP bars in PCC (Fava et al., 2016).
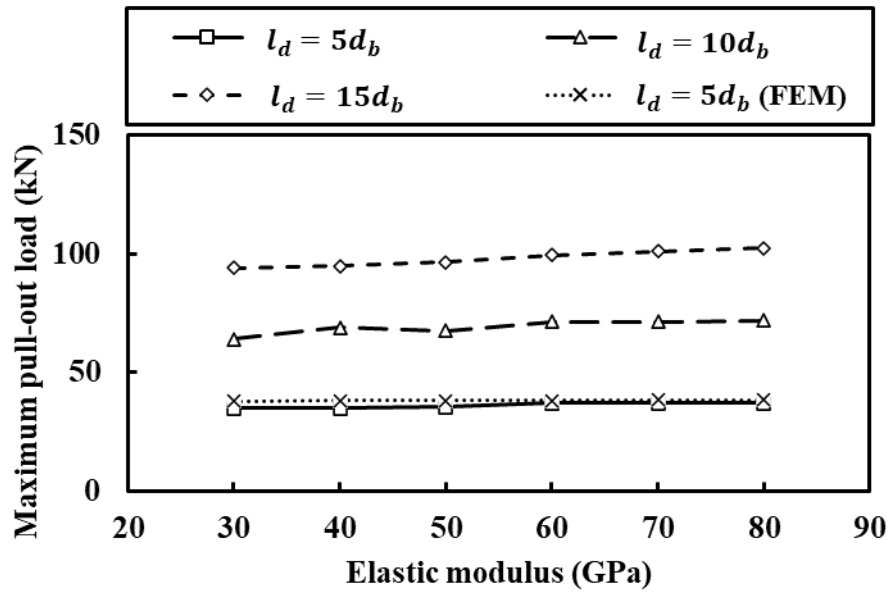
Fig. 6.13 Variation of pull-out load with BFRP bar elastic modulus.

(a)

(b)
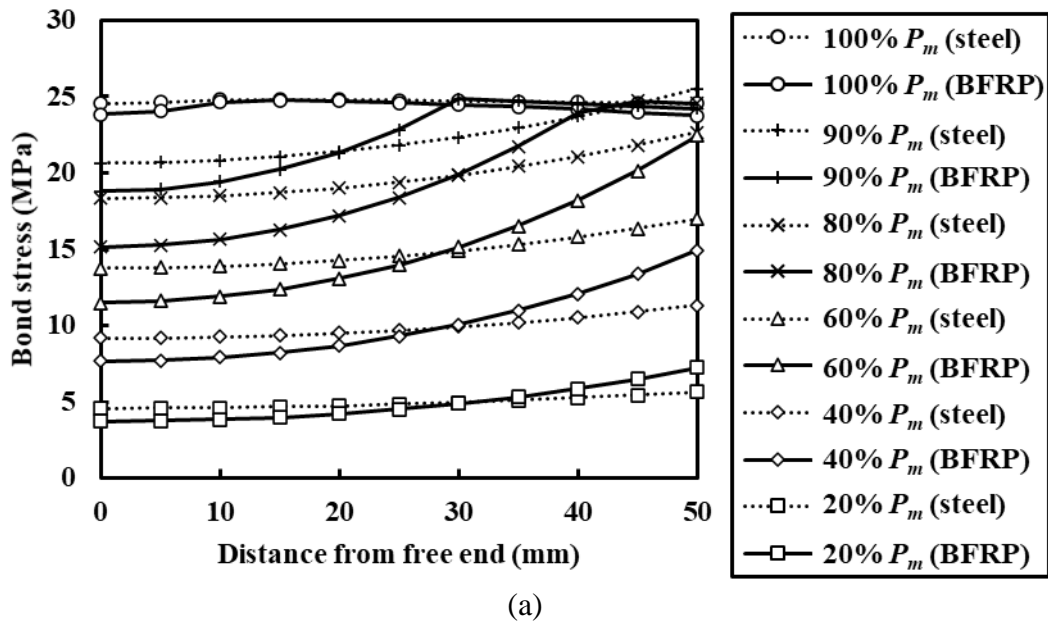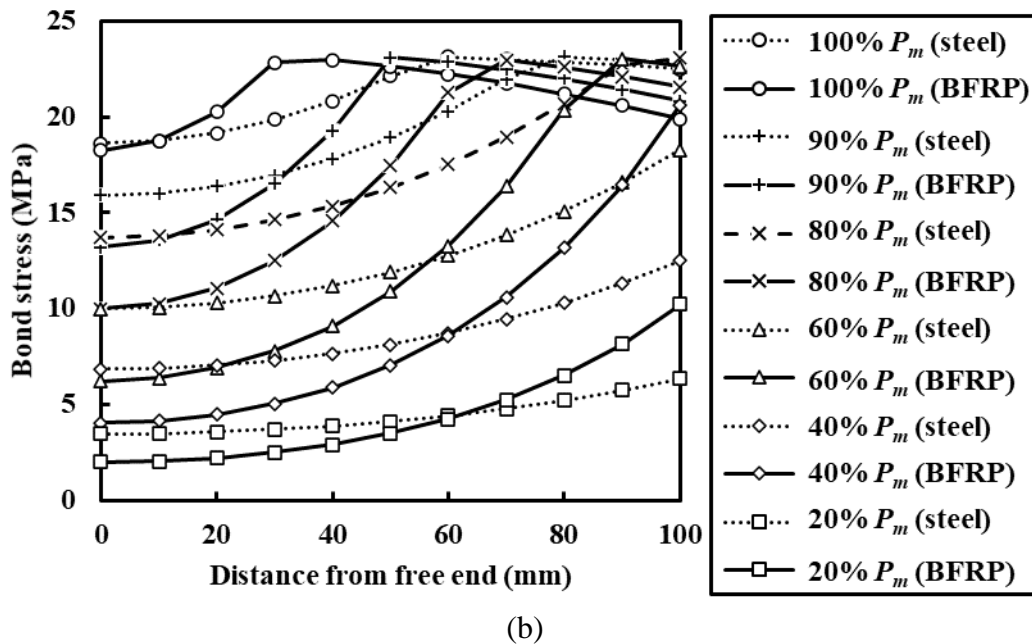
Fig. 6.14 Comparison between bond stress distribution of BFRP bar and steel bar: (a) sample *10-5d-2*; (b) sample *10-10d-1*.

6.5.3 Theoretical predictions of bond strength

According to the paramedic study above, among the parameters evaluated, only bar diameter and embedment length significantly influenced the maximum pull-out load and consequently the bond strength. Therefore, the bond strength of BFRP bars in GPC was expressed as a function of bar diameter (d_b) and embedment length (l_d) by fitting the obtained data shown in Fig. 6.12 as follows:

$$\tau_m = -0.0162d_b^2 + 0.41793d_b - 0.42526l_d + 23.2037 \tag{6.38}$$

It is worth noting that in the existing bond strength predictions (Eqs. (6.39) - (6.42)), the concrete compressive strength is included as an influencing parameter. Yet, in Eq. (6.38), such a variable was not considered as the parametric studies in Section 5.4.2.3 suggested no effects on the bond strength between BFRP bars and GPC. In Table 6.3, the experimental bond strengths of BFRP bars in GPC are compared with the predictions obtained from available standard codes for FRP bars and Eq. (6.38). The relevant recommendations of ACI 440 (2015), CSA S806-12 (2012), CSA S6-14 (2017b), and JSCE (1997) for predictions are given in Eqs. (6.39) - (6.42), respectively:

$$\frac{\tau_m}{0.083\sqrt{f_c}} = 4.0 + 0.3\frac{c}{d_b} + 100\frac{d_b}{l_d} \tag{6.39}$$

$$\tau_m = \frac{d_{cs}\sqrt{f_c}}{1.15\,k_1k_2k_3k_4k_5\,\pi\,d_b} \tag{6.40}$$

163

$$\tau_m = \frac{f_{cr} d_{cs}}{0.45 \pi d_b k_1 k_6 k_7} \tag{6.41}$$

$$\tau_m = f_{bod}/\alpha_1 \tag{6.42}$$

where τ_m is the bond strength developed (MPa), c is the concrete cover dimension (mm), f_c is the concrete compressive strength (MPa), k_1 is the bar location factor equal to 1.0, k_2 is the concrete density factor equal to 1.0, k_3 is the bar size factor equal to 0.8, k_4 is the bar fibre factor assumed equal to 1.0, k_5 is the bar surface profile equal to 1.05, d_{cs} is the smallest of the distance from the closest concrete surface to the centre of the bar being developed which shall not be taken greater than $2.5 d_b$, k_6 is the coating factor equal to 1.0, k_7 is the bar size factor equal to 0.8, f_{cr} is the tensile strength of the concrete and equal to $0.4\sqrt{f_c}$ where the value of $\sqrt{f_c}$ shall not exceed 8.0 MPa. For the JSCE code, α_1 is the modification factor equal to 0.6, f_{bod} is the design bond strength of concrete (MPa) calculated as $f_{bod} = \alpha_2 \left(0.28 \frac{f_{ck}^{2/3}}{\gamma_c} \right)$ where the value of f_{bod} shall not exceed 3.2 MPa, α_2 is the modification factor equal to 1.0, f_{ck} is the characteristic value for concrete compressive strength (MPa), and γ_c is the safety factor for concrete equal to 1.3. The CSA S6 and JSCE codes consider the confining effect offered by the transverse reinforcement, which was neglected in this study since no stirrups were used in the tested samples.

As indicated in Table 6.3, the CSA S806, CSA S6 and JSCE codes provided similar values of predicted bond strength, regardless of the variations of bar diameter and embedded length, which is due to the limitations imposed on the concrete cover (c) for the Canadian standards (CSA S806 and CSA S6) and α_1 for the Japanese standard (JSCE). Furthermore, the influence of embedment length on bond strength was neglected in both CSA S806 and JSCE. On the contrary, the prediction by ACI 440 considered the effect of the embedment length and thus, a reduction in predicted bond strength with the increase of embedment length can be observed. However, as per the other design codes, no difference was found between different bar diameters as the effect of bar diameter was not considered due to the limitation imposed on the ratio c/d_b. It is also worth noting that the design codes offers no indication in regards to the FRP bar tensile strength.

In addition, Fig. 6.15 graphically displays the comparison between experimental data and the bond strength predicted with the abovementioned standard codes. Table 6.3 and Fig. 6.15 suggest that all design codes provided conservative estimations of the bond strength between BFRP bars and GPC, where CSA S806, CSA S6 and JSCE seemed too conservative, with CSA

S6 being the most conservative one. ACI 440.1R offered still conservative but more accurate predictions of bond strength. It is also worth mentioning that, as shown in Fig. 6.15b and c, the predicted bond strengths are constant for higher values of concrete compressive strength, which is to be attributed to the limitations introduced by the design codes where CSA S806 and CSA S6 allow a maximum $\sqrt{f_c}$ of 8 MPa, while the limitation on $f_{bod} \leq 3.2$ MPa given by the JSCE leads to a constant value of the predicted bond strength for a concrete compressive strength higher than 57 MPa. It is worth noting that Saleh et al. (2019) also found that CSA S806 and CSA S6 provided overly conservative predictions for GFRP bars in high strength concrete compared to ACI 440.1R.

From Table 6.3, the predictions of bond strength using Eq. (6.38) show a closer estimation to experimental data, with an average ratio of experimental to predicted bond strength of 1.07 against those ranging from 2.47 to 5.49 obtained using the standard provisions. Nonetheless, some predicted values seemed non-conservative, especially those for the 6-mm bar samples that failed prematurely due to bar rupture and for the sample **10-15d** that failed due to concrete splitting. Therefore, Eq. (6.38) can be considered a preliminary prediction equation for the bond strength of BFRP bars in GPC, which can be modified by considering more experimental data for calibration and including safety factors.

Table 6.3 Comparison of experimental bond strength with predictions from standard codes and regression analysis equation.

Sample	EXP τ_{exp}	ACI 440.1R τ_{pred}	τ_{exp}/τ_{pred}	CSA S806 τ_{pred}	τ_{exp}/τ_{pred}	CSA S6 τ_{pred}	τ_{exp}/τ_{pred}	JSCE τ_{pred}	τ_{exp}/τ_{pred}	Regression τ_{pred}	τ_{exp}/τ_{pred}
6-5d	15.21	13.15	1.16	5.21	2.92	5.59	2.72	4.20	3.62	23.00	0.66
6-10d	13.91	7.90	1.76	5.21	2.67	5.59	2.49	4.20	3.31	20.88	0.67
6-15d	14.46	6.15	2.35	5.21	2.78	5.59	2.59	4.20	3.44	18.75	0.77
8-5d	42.11	13.15	3.20	5.21	8.08	5.59	7.53	4.20	10.03	23.38	1.80
8-10d	41.20	7.90	5.21	5.21	7.91	5.59	7.37	4.20	9.81	21.26	1.94
8-15d	18.81	6.15	3.06	5.21	3.61	5.59	3.36	4.20	4.48	19.13	0.98
10-5d	25.85	13.15	1.97	5.21	4.96	5.59	4.62	4.20	6.16	23.64	1.09
10-10d	22.41	7.90	2.84	5.21	4.30	5.59	4.01	4.20	5.34	21.51	1.04
10-15d	12.34	6.15	2.01	5.21	2.37	5.59	2.21	4.20	2.94	19.38	0.64
8-5d-S	22.08	13.15	1.68	5.47	4.04	5.59	3.95	4.20	5.26	23.38	0.94
GPC2-8-5d	27.59	14.05	1.96	5.57	4.95	5.97	4.62	4.58	6.02	23.38	1.18
AVERAGE			2.47		4.42		4.13		5.49		1.07
SD			1.10		1.98		1.84		2.45		0.44
COV			45%		45%		45%		45%		41%

(a)

(b)

(c)
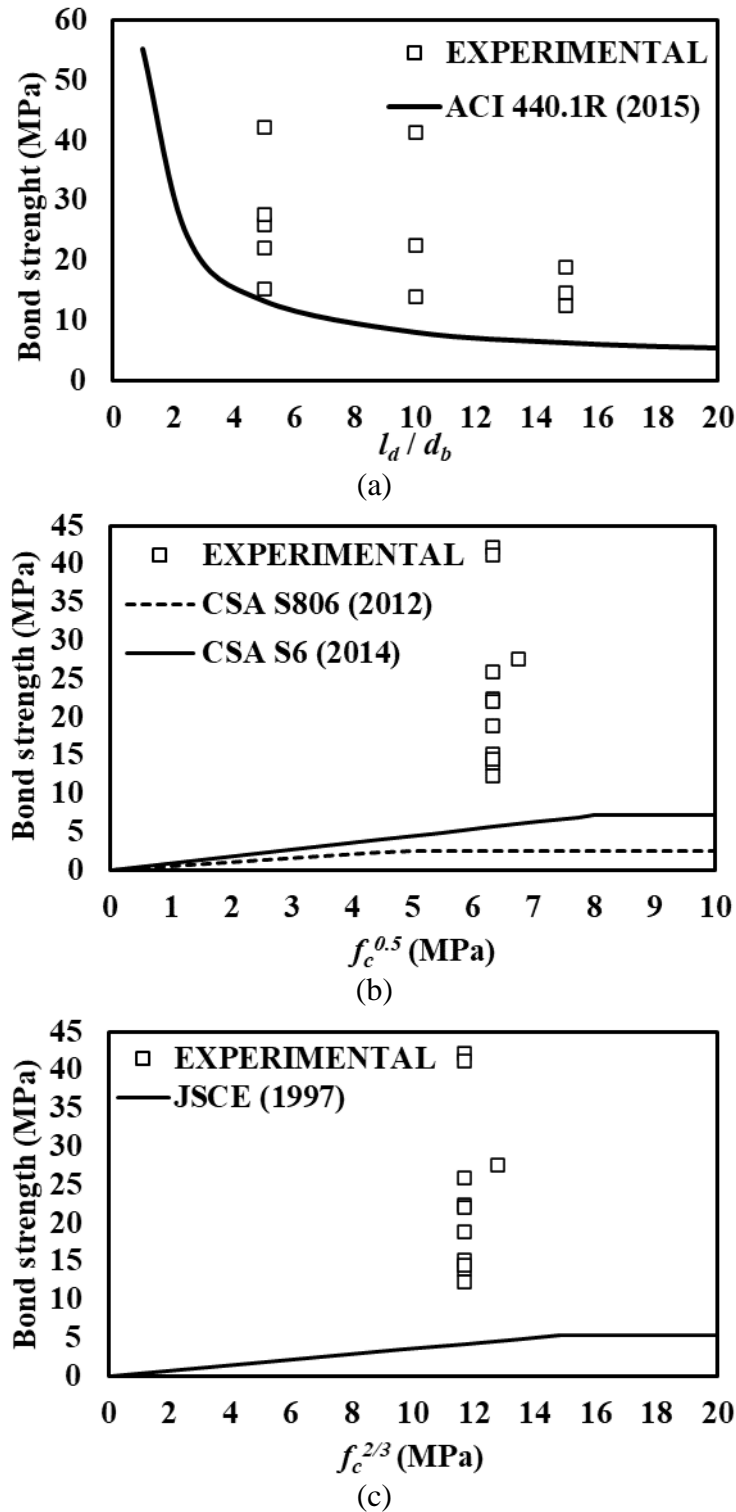
Fig. 6.15 Comparison between experimental data and bond strength predicted according to several design codes: (a) bond strength vs embedment length (ACI 440.1R, 2015); (b) bond strength vs concrete compressive strength square root (CAN/CSA S806-12, 2012; CAN/CSA-S6-14, 2017b); (c) bond strength vs concrete compressive strength (JSCE, 1997).

167

6.6 Concluding remarks

In this chapter, the bond behaviour of BFRP bars in GPC was investigated using an analytical model. The governing differential equation based on a bilinear bond stress-slip relationship was solved using boundary and continuity conditions to analyse the bond behaviour. First, the theoretical model was validated against the experimental and numerical results. Once validated, the theoretical formulation was used to run a stress analysis and a parametric study on influencing parameters affecting the maximum pull-out load. According to the theoretical analysis, the main conclusions are drawn as follows:

- The mean ratio of experimental to theoretical values for τ_m, $s_{m,FE}$, and $s_{m,LE}$ were respectively 1.09 (COV 8%), 1.17 (COV 16%), and 1.04 (COV 5%). In addition, regardless of the differences between the theoretical and numerical models, the $RMSPE$ ranged from 5% to 16%. Thus, the theoretical predictions of the bond stress-slip curve at both free and loaded ends compared well with the experimental and the numerical data. Furthermore, the analytical stress profiles and the parametric study results were consistent with the numerical results, indicating that the analytical formulation proposed was reliable in predicting the bond properties of BFRP bars in GPC.

- At low load levels K_b varied from 1.50 to 3.93, indicating a nonlinear distribution of bond stress along the embedded BFRP bars in GPC.

- The parametric study showed that the maximum pull-out load was mainly affected by bond strength, embedment length, and bar diameter. Bigger diameters, longer embedment lengths, and higher bond strengths increased the maximum pull-out load. The effect of slip at bond strength, ultimate slip and bar elastic modulus on the pull-out load was not remarkable. However, the bond stress profile exhibited by the BFRP bar was nonlinear compared to the more even offered by the steel bar, suggesting that the bond stress nonlinearity could be ascribed to the low BFRP bar elastic modulus.

- Following the parametric study results, an empirical equation was proposed to predict the bond strength of BFRP bars in GPC, considering the effects of bar diameter and embedment length. The predicted bond strength agreed well with experimental data, scoring a predicted to experimental bond strength ratio of 1.07. Furthermore, it was found that the estimated values based on the available design codes for FRP bars in concrete were too conservative.

Chapter 7 Conclusions and Perspectives

7.1 Conclusions

In this research, the bond of BFRP bars in GPC was systematically investigated for the first time based on experimental, numerical and theoretical studies. These two innovative materials have been coupled in a new system to offer a sustainable alternative to the more traditional steel reinforced PCC. This study provides an in-depth understanding of the bonding mechanisms of BFRP bars in GPC. The main research contributions are summarised below.

7.1.1 Research contributions

The contributions made to fill the knowledge gap of the bond behaviour of BFRP bars in GPC are the following:

- Firstly, given the novelty of the materials used in this research, the BFRP bars and GPC properties were characterised experimentally according to current standard methods. Additionally, the theoretical models to describe their properties were identified within those available for traditional materials, i.e. FRP reinforcement and PCC.

- Secondly, the bond properties of BFRP bars in GPC were investigated experimentally in a comprehensive manner, considering the effects of the main influencing parameters including bar diameter, embedment length, bar surface treatment and concrete compressive strength. This provided a thorough understanding of the average bond stress-slip curve, bond strength, bond ductility and failure modes.

- Thirdly, the first 3D finite element model of the bond of BFRP bars in concrete was developed, allowing the bond behaviour to be accurately characterised in terms of bond strength, failure patterns, and bond stresses development over the bar length.

- Fourth, an analytical bilinear bond stress-slip model was proposed to describe the bond of BFRP bars to GPC. Based on the bilinear bond stress-slip model, closed-form equations were developed considering boundary and continuity conditions, allowing to model the bond properties along the bar embedded portion.

- Finally, the dominant parameters affecting the bond strength were identified with a parametric study. As a result, a formula predicting the bond strength of BFRP bars in GPC was proposed and assessed against experimental data and existing guideline provisions.

7.1.2 Concluding remarks

According to the experimental, numerical and analytical results, the following conclusions can be drawn:

- Two GPC mixtures, e.g. GPC1 and GPC2, with a GGBS content of the total precursor of 15% and 20%, respectively, were tested and identified as suitable for the pull-out tests. The slump values indicated high workability of the mixtures, which reduced by increasing the slag content, thus fulfilling the requirement of workability. The concrete compressive strength at 28 d conformed to the basic requirements for normal and reinforced concrete. However, the two mixtures unexpectedly exhibited a similar compressive strength at 28 d, which was ascribed to a reduction of the strength development between 7 d and 28 d for the mixture GPC2. In addition, within the existing prediction equations for PCC, the Popovics model (1973) could predict the GPC compressive stress-strain relation, and the standard ACI 318-08 (2008) could be used to predict the splitting tensile strength and the elastic modulus from the compressive strength.

- The tensile strength of the BFRP bars ranged between 876 MPa and 1117 MPa, and the elastic modulus varied between 55 GPa and 58 GPa. The 6-mm bar exhibited a tensile strength 19% lower than the 8-mm bars and high variability in the stress-strain behaviour of different 6-mm bar samples at high stress levels. The lower mechanical properties of the 6-mm bar were attributed to the manufacturing process.

- For the majority of the pull-out test samples, the bond stress-slip curve consisted of a linear ascending branch followed by a sudden bond stress loss and minor slippage. Due to low chemical adhesion, the bond of BFRP bars in GPC was mainly attributed to the mechanical interlocking of the bar ribs. Considering the experimental results, a bilinear bond stress-slip curve was proposed and adopted for the finite element and the theoretical analyses.

- The difference in slips at the bar free and loaded ends observed experimentally suggested a nonlinear bond stress distribution along the BFRP bar. The results obtained with the finite element and analytical models confirmed the nonlinear distribution of tensile and bond stress along the bar axis, especially at low pull-out load levels and for longer embedment lengths, as also indicated by the study of the bond stress concentration factor (K_b). It appeared that with increasing load, the peak bond stress

migrates progressively from the loaded end towards the free end, reaching a more constant bond stress level along the embedment length.

- The parametric studies highlighted that increasing the bar diameter and embedment length reduced the bond strength, which effect was partially ascribed to the shear lag. Moreover, bar diameter and embedment length influenced the failure mode. For shorter embedment lengths ($5d_b$) the bar pull-out was due to the crushing of the concrete lugs between the bar ribs, suggesting high shear strength of the BFRP bar indentations. Conversely, for longer embedment lengths ($15d_b$), the sample failed due to concrete splitting while the bond interface remained intact. The above observation can be also discussed considering the finite element simulation, which indicated that in the sample with a longer embedment length, the splitting stress generated in the concrete by the radial bond stress was observed to lead to failure of the concrete elements in tension. Conversely, for a shorter embedment length, the normalised splitting stress value was insufficient to cause the cracking failure. It is also worth noting that, during the experimental pull-out test, the reduced mechanical properties of the 6-mm BFRP bars led to bar rupture, regardless of the embedment length.

- It was experimentally observed that the samples reinforced with ribbed and sand-coated bars exhibited a similar initial stiffness and failure mode (i.e. bar pull-out). However, the ribbed bars achieved higher bond strength than the sand-coated bars due to enhanced mechanical interlocking. Furthermore, the bond strength of the samples prepared with GPC2 was 34% lower than that of GPC1. This unexpected result was ascribed to the minor difference between the two concrete compressive strengths (~3 MPa) and possible concrete defects at the interface caused by the rapid setting time of GPC2 at the time of casting. Moreover, the steel-reinforced samples exhibited a bond strength 46% lower than BFRP bars and a more ductile bond behaviour.

- The parametric studies conducted with the finite element and analytical models indicated that within the bond stress-slip parameters, τ_m influenced the bond strength while s_m and s_u had no effect on the bond strength. In addition, no effect on the failure mode was observed. Moreover, the bar elastic modulus and the concrete compressive strength had no significant influence on the bond strength and the failure mode.

- Following the parametric study results, an empirical equation was proposed to predict the bond strength of BFRP bars in GPC, considering the effects of bar diameter and embedment length. The bond strength predictions agreed well with the experimental

data and with the standard code provisions for FRP bars, which were overly conservative for the BFRP-GPC system.

- More generally, the bond behaviour of BFRP bars in GPC was found similar to that of other FRP reinforcement in concrete, thus indicating its feasibility as a construction material.

7.2 Recommendations for future work

Considering the results and limitations of the current thesis, some recommendations for future investigations are suggested as follows:

- In this research, the experimental program focused on the centric pull-out test as it allows comparing the influence of different parameters. However, to fully understand the bond of BFRP bars to GPC under different conditions, it is recommended to run other types of testing such as eccentric pull-out, beam end, hinged beam and spliced beam testing.

- Both GPC and BFRP bars are characterised by variability that influences mechanical properties and bond behaviour. In the present research, the raw materials (i.e. precursors and BFRP bars) were obtained from one manufacturing company. The effect of the variability was thus investigated by adopting two GPC mixtures with different GGBS/FA ratios and two BFRP bars surface treatments. However, to fully establish the bond behaviour of BFRP bars in GPC, further aspects should be considered. For instance, for GPC, precursors obtained from different companies and different mix proportions could be adopted. Additionally, the BFRP bars could be manufactured using epoxy resin, and different surface treatments could be investigated, such as sand coating with various grain sizes or grooving surfaces with varying indentations.

- The bond performance of different bar surface configurations, different concrete compressive strengths and the comparison with the steel bar was assessed using limited data and thus provided only preliminary indications. Therefore, to draw more solid conclusions, it is recommended to further investigate the bond behaviour of BFRP bars to GPC, considering a broader data set that includes various bar diameters and embedment lengths. Furthermore, as the influence of the concrete cover and the transversal reinforcement was not explored, it should be included in future research, for instance, by conducting eccentric pull-out tests and adopting stirrups in the samples. The bond durability of BFRP bars in GPC should also be explored by exposing the

samples to aggressive environments (e.g. acid, alkaline and salty solutions) at different temperatures for different periods.

- In the present study, the numerical and theoretical models were based on a bilinear bond stress-slip curve. However, as per other FRP reinforcements in concrete, some nonlinearity could be observed running more experimental tests on the bond of BFRP bars to GPC. It is thus recommended to further develop the models proposed, considering the inclusion of a nonlinear bond stress-slip relationship for the interaction between BFRP bars and GPC. Furthermore, models that explicitly include the effect of the dominant parameters could also be proposed.

- A life cycle assessment of GPC reinforced with BFRP bars could quantify the sustainability and economic benefits deriving from its adoption compared to steel reinforced concrete.

Chapter 7 Conclusions and Perspectives

List of Publications

Peer-reviewed Journal Articles:

- Trabacchin, G., Sebastian, W. and Zhang, M. (2021). 'Experimental and analytical study of bond between basalt FRP bars and geopolymer concrete', *Construction and Building Materials*, https://doi.org/10.1016/j.conbuildmat.2021.125461.

- Trabacchin, G., Naderi, S., Sebastian, W. and Zhang, M. (2021). 'Modelling of pull-out behaviour of basalt fibre reinforced polymer bars embedded in geopolymer concrete', *Construction and Building Materials*, under review.

Peer-reviewed Conference Papers:

- Trabacchin, G., D'Ayala, D., Stegemann, J. and Zhang, M. (2019). 'Bond behaviour of basalt FRP bars in geopolymer concrete', *1st International Conference on innovation in low-carbon cement & concrete technology*, June 2019, London, UK

.

References

ABAQUS 6.14 User's Manual (2014) 'Dassault Systemes Simulia, Providence, RI, USA'.

Achillides, K. and Pilakoutas, Z. (2006) 'FE modeling of bond interaction of FRP bars to concrete', Structural Concrete, 7(1), pp. 7–16.

Achillides, Z. (1998) 'Bond behaviour of FRP bars in concrete', Ph.D. Thesis, Faculty of Engineering, University of Sheffield, UK.

Achillides, Z. and Pilakoutas, K. (2004a) 'Bond Behavior of Fiber Reinforced Polymer Bars under Direct Pullout Conditions', Journal of Composites for Construction, 8(2), pp. 173–181.

Achillides, Z. and Pilakoutas, K. (2004b) 'Bond behavior of FRP bars under direct pullout conditions', Journal of Composites for Construction, 8(2), pp. 173–181.

ACI (2004) ACI 440.3R-04 - Guide test methods for fiber-reinforced polymers (FRPs) for reinforcing or strengthening concrete structures, American Concrete Institute.

ACI 318 (2008) 'Building code requirements for structural concrete', American Concrete Institute, p. 465, ISBN: 9780870312649.

ACI 318 (2014) 'Building code requirements for structural concrete', American Concrete Institute, p. 520, ISBN: 9780870319303.

ACI 408R (2003) 'Bond and development of straight reinforcing bars in ension reported by ACI Committee 408', American Concrete Institute, ISBN: 9780870311338.

ACI 440.1R (2006) 'Guide for the design and construction of concrete reinforced with FRP bars', American Concrete Institute, ISBN: 978-0-7844-0753-0.

ACI 440.1R (2015) 'Guide for the design and construction of structural concrete reinforced with FRP bars', American Concrete Institute, p. 88, ISBN: 9781942727101.

Adetunji, I., Price, A., Fleming, P. and Kemp, P. (2003) 'Sustainability and the UK construction industry - A review', Proceedings of the Institution of Civil Engineers - Engineering Sustainability, 156(4), pp. 185–199.

Adhikari, S. (2009) Mechanical properties and flexural applications of basalt fiber reinforced polymer (BFRP) bars, Masters Thesis, University of Akron.

Ahmed, E. A., El-Salakawy, E. F. and Benmokrane, B. (2008) 'Bond Stress-Slip Relationship

References

and Development Length of FRP Bars Embedded in Concrete', HBRC Journal, 4(3).

Aiello, A. M., Leone, M. and Pecce, M. (2007) 'Bond performances of FRP rebars-reinforced concrete', Journal of Materials in Civil Engineering, 19(3), pp. 205–213.

AL-mahmoud, F., Castel, A., François, R. and Tourneur, C. (2007) 'Effect of surface pre-conditioning on bond of carbon fibre reinforced polymer rods to concrete', Cement and Concrete Composites, 29(9), pp. 677–689, ISBN: 0958-9465.

Al-Majidi, M. H., Lampropoulos, A., Cundy, A. and Meikle, S. (2016) 'Development of geopolymer mortar under ambient temperature for in situ applications', Construction and Building Materials, 120, pp. 198–211.

Albarrie (2018) 'Basalt continuous fibres: properties of basalt fibres', Canada.

Ali, A. H., Mohamed, H. M., Benmokrane, B., ElSafty, A. and Chaallal, O. (2019) 'Durability performance and long-term prediction models of sand-coated basalt FRP bars', Composites Part B: Engineering, 157(July 2018), pp. 248–258.

Alnajmi, L. and Abed, F. (2020) 'Evaluation of FRP bars under compression and their performance in RC columns', Materials, 13(20), pp. 1–19.

Altalmas, A., El Refai, A. and Abed, F. (2015) 'Bond degradation of basalt fiber-reinforced polymer (BFRP) bars exposed to accelerated aging conditions', Construction and Building Materials, 81, pp. 162–171.

Arias, J. P. M., Vazquez, A. and Escobar, M. M. (2012) 'Use of sand coating to improve bonding between GFRP bars and concrete', Journal of Composite Materials, 46(February), pp. 2271–2278, ISBN: 9789584496249.

AS 3600-2009 (2009) 'Concrete structures', Australian Standard, p. 213.

ASTM C127 (2015) 'Standard Test Method for Relative Density (Specific Gravity) and Absorption of Coarse Aggregate', ASTM International.

ASTM C128 (2015) 'Standard Test Method for Relative Density (Specific Gravity) and Absorption of Fine Aggregate', ASTM International, ISBN: 5919881100.

ASTM C143/C143M-15 (2015) 'Standard Test Method for Slump of Hydraulic-Cement Concrete'.

ASTM C33/C33M-11a (2011) 'Standard Specification for Concrete Aggregates'.

References

ASTM D7205 (2011) 'Standard test methods for tensile properties of fiber reinforced polymer matrix composite bars, American Society for Testing and Materials, Conshohocken, USA', ASTM International.

Aydin, F. (2018) 'Experimental investigation of thermal expansion and concrete strength effects on FRP bars behavior embedded in concrete', Construction and Building Materials, 163(January), pp. 1–8.

Baena, M. (2010) 'Study of bond behaviour between FRP reinforcement and concrete', Ph.D. Thesis, Universitat de Girona, ISBN: 9788469424841.

Baena, M., Torres, L., Turon, A. and Barris, C. (2009) 'Experimental study of bond behaviour between concrete and FRP bars using a pull-out test', Composites Part B, 40(8), pp. 784–797.

Banibayat, P. and Patnaik, A. (2015) 'Creep Rupture Performance of Basalt Fiber-Reinforced Polymer Bars', Journal of Aerospace Engineering, 28(3).

Bank, L. C. (2006) Composites for Construction: Structural Design with FRP Materials, John Willey and Sons, ISBN: 9780470121429.

Barcelo, L., Kline, J., Walenta, G. and Gartner, E. (2014) 'Cement and carbon emissions', Materials and Structures, 47(6), pp. 1055–1065.

Benmokrane, B., Tighiouart, B. and Chaallal, O. (1996) 'Bond Strength and Load Distribution of Composite GFRP Reinforcing Bars in Concrete', ACI Materials Journal, 93(3), pp. 254–259.

Bilek, V., Bonczková, S., Hurta, J., Pytlík, D. and Mrovec, M. (2017) 'Bond Strength between Reinforcing Steel and Different Types of Concrete', Procedia Engineering, 190, pp. 243–247.

Biscaia, H. C., Chastre, C. and Silva, M. A. G. (2013) 'Linear and nonlinear analysis of bond-slip models for interfaces between FRP composites and concrete', Composites Part B: Engineering, 45(1), pp. 1554–1568.

Bowman, E., Jacobson, G., Koch, G., Varney, J., Thopson, N., Moghissi, O., Gould, M. and Payer, J. (2016) NACE International IMPACT International Measures of Prevention, Application, and Economics of Corrosion Technologies Study, NACE International.

British Standards Institution BSI (2009a) BS EN 12390-3 - Testing hardened concrete - Part 3: Compressive strength of test specimens, BSI Standards Publication, ISBN: 9780580588006 0580588009.

References

British Standards Institution BSI (2009b) BS EN 12390-3 - Testing hardened concrete - Part 6: Tensile splitting strength of test specimens, BSI Standards Publication, ISBN: 9780580588006 0580588009.

British Standards Institution BSI (2013) BS EN 12390-13 - Testing hardened concrete - Part 13: Determination of secant modulus of elasticity in compression, BSI Standards Publication.

Broomfield, J. P. (1997) Corrosion of steel in concrete: Understanding, investigation and repair, London, E & FN Spon. London.

CAN/CSA-S6-06 (2006) 'Canadian Highway Bridge Design Code', Canadian Standard Association, p. 968, ISBN: 155397221X.

CAN/CSA-S6-14 (2017a) 'Canadian Highway Bridge Design Code', Canadian Standard Association, p. 894, ISBN: 9781771394123.

CAN/CSA-S6-14 (2017b) 'Canadian Highway Bridge Design Code', Canadian Standard Association, ISBN: 155397221X.

CAN/CSA-S807 (2015) 'Specification for fibre reinforced polymers', Canadian Standard Association, p. 44.

CAN/CSA S806-12 (2012) 'Design and construction of building structures with fibre-reinforced polymers', Canadian Standard Association, ISBN: 1553248538.

Castel, A. and Foster, S. J. (2015) 'Bond strength between blended slag and Class F fly ash geopolymer concrete with steel reinforcement', Cement and Concrete Research, 72, pp. 48–53, ISBN: 0008-8846.

CEB-FIP (2000) 'Bulletin 10 - Bond of reinforcement in concrete', fib Bulletin, 10, p. 427, ISBN: 2883940509.

CEB-FIP (2007) 'Bulletin 40 - FRP reinforcement for RC structures', fib Bulletin, p. 160, ISBN: 9782883940802.

CEB-FIP (2010) Model Code 2010, fib Model Code for Concrete Structures 2010, ISBN: 978-2-88394-050-5.

CEB - FIP (2010) 'Fib model code for concrete structures'.

Chaallal, O. and Benmokrane, B. (1996) 'Fiber-reinforced plastic rebars for concrete applications', Composites Part B: Engineering, 27(3–4), pp. 245–252, ISBN: 1359-8368.

References

Chamis, C. (1984) 'Mechanics of Composite Materials: Past, Present, and Future', NASA Technical Memorandum 100793.

Chang, E. H. (2009) 'Shear and bond behaviour of reinforced fly ash-based geopolymer concrete beams', PhD Thesis, Curtin University of Technology, Perth, Australia.

Cohn, M. Z. and Bartlett, M. (1982) 'Computer-simulated flexural tests of partially pre-stressed concrete sections', ASCE Journal of Structural Division, 108, pp. 2747 – 2765.

Collins, M. P. and Mitchell, D. (1991) Prestressed concrete structures, Prentice-Hall, Englewood Cliffs, NJ., ISBN: 013691635X 9780136916352.

Cosenza, E., Manfredi, G. and Realfonzo, R. (1995) 'Analytical modelling of bond between FRP reinforcing bars and concrete', Non-metalic (FRP) reinforcement for concrete structurestalic (FRP) reinforcement for concrete structures, (January), pp. 164–171, ISBN: 0360-1315.

Cosenza, E., Manfredi, G. and Realfonzo, R. (1996) 'Bond characteristics and anchorage length of FRP rebars.', in Proc., 2nd Int. Cant on Advanced Compos. Mat. in Bridge Struct., M. EI-Badry, ed.

Cosenza, E., Manfredi, G. and Realfonzo, R. (1997) 'Behavior and modeling of bond of FRP rebars to concrete', Journal of Composites for Construction, 1(2), pp. 40–51, ISBN: 10900268.

Cosenza, E., Manfredi, G. and Realfonzo, R. (2002) 'Development length of FRP straight rebars', Composites Part B: Engineering, 33(7), pp. 493–504, ISBN: 1359-8368.

Cui, Y., Zhang, P. and Bao, J. (2020) 'Bond Stress between Steel-Reinforced Bars and Fly Ash-Based Geopolymer Concrete', Advances in Materials Science and Engineering, 2020, p. 11.

Dattatreya, J. K., Rajamane, N. P., Sabitha, D., Ambily, P. S. and Nataraja, M. C. (2011) 'Flexural Behaviour of reinforced geopolymer concrete beams', International journal of civil and structural engineering.

Davidovits, J. (1993) 'Geopolymer cement to minimize carbon-dioxde greenhouse-warming', Ceramic Transactions ·, 37(1), pp. 165–182.

Desay, P. and Krishnan, S. (1964) 'Equation for the Stress-Strain Curve of Concrete', ACI Journal Proceedings, 61(3), p. 2019.

Van Deventer, J. S. J., Provis, J. L., Duxson, P. and Brice, D. G. (2010) 'Chemical research

References

and climate change as drivers in the commercial adoption of alkali activated materials', Waste and Biomass Valorization, 1(1), pp. 145–155.

Dong, M., Feng, W., Elchalakani, M., Li, G. (Kevin), Karrech, A. and May, E. F. (2017) 'Development of a High Strength Geopolymer by Novel Solar Curing', Ceramics International, 43(14), pp. 11233–11243.

Dong, Z., Wang, X. and Xu, B. (2018a) 'Bond performance of alkaline solution pre-exposed FRP bars with concrete', Magazine of Concrete Research, 70(17), pp. 894–904.

Dong, Z., Wu, G. and Lian, J. (2018b) 'Experimental study on the durability of FRP bars reinforced concrete beams in simulated ocean environment', IEEE Journal of Selected Topics in Quantum Electronics, 25(6), pp. 1123–1134.

Dong, Z., Wu, G., Xu, B., Wang, X. and Taerwe, L. (2016) 'Bond durability of BFRP bars embedded in concrete under seawater conditions and the long-term bond strength prediction', Materials and Design, 92, pp. 552–562.

Dwivedi, A. and Jain, M. (2014) 'Fly ash – waste management and overview : A Review.', Recent Research in Science and Technology, 6, pp. 30–35.

Elchalakani, M., Karrech, A., Dong, M., Mohamed Ali, M. S. and Yang, B. (2018) 'Experiments and Finite Element Analysis of GFRP Reinforced Geopolymer Concrete Rectangular Columns Subjected to Concentric and Eccentric Axial Loading', Structures, 14(February), pp. 273–289.

Elgabbas, F., Ahmed, E. A. and Benmokrane, B. (2015) 'Physical and mechanical characteristics of new basalt-FRP bars for reinforcing concrete structures', Construction and Building Materials, 95, pp. 623–635.

Eligehausen, R., Popov, E. P. and Bertero, V. V. (1983) 'Local bond stress-slip relationships of deformed bars under generalized excitations: Experimental results and analytical model.', UCB/EERC-83/23, Univ. of California, Earthquake Engineering Research Centre, Berkeley, CA., p. 1983.

Esfahani, M. R., Rakhshanimehr, M. and Mousavi, S. R. (2013) 'Bond Strength of Lap-Spliced GFRP Bars in Concrete Beams', Journal of Composites for Construction, 17(3), pp. 314–323.

Esfahani, M. R. and Rangan, B. V (1998) 'Bond between normal strength and high-strength concrete (HSC) and reinforcing bars in splices in beams', Structural Journal, 95(3).

References

European Standard EN 1992-1-1 (2004) Eurocode 2: Design of concrete structures, ISBN: 0580451917, 9780580451911.

Fan, X., Xu, T., Zhou, Z. and Zhou, X. (2017) 'Experimental Study on Basic Mechanical Properties of BFRP Bars', IOP Conference Series: Materials Science and Engineering, 250(1).

Fan, X. and Zhang, M. (2016a) 'Behaviour of inorganic polymer concrete columns reinforced with basalt FRP bars under eccentric compression: An experimental study', Composites Part B: Engineering, 104(March), pp. 44–56.

Fan, X. and Zhang, M. (2016b) 'Experimental study on flexural behaviour of inorganic polymer concrete beams reinforced with basalt rebar', Composites Part B: Engineering, 93, pp. 174–183.

Fan, X., Zhou, Z., Tu, W. and Zhang, M. (2021) 'Shear behaviour of inorganic polymer concrete beams reinforced with basalt FRP bars and stirrups', Composite Structures, 255(September 2020), p. 112901.

Fang, G. (2020) 'Multiscale Characterisation of Microstructure and Mechanical Properties of Alkali-Activated Fly Ash-Slag Concrete', Ph.D. thesis, University College London, UK.

Fang, G., Ho, W. K., Tu, W. and Zhang, M. (2018) 'Workability and mechanical properties of alkali-activated fly ash-slag concrete cured at ambient temperature', Construction and Building Materials, 172, pp. 476–487.

Fang, G. and Zhang, M. (2020) 'Multiscale micromechanical analysis of alkali-activated fly ash-slag paste', (June).

Fava, G., Carvelli, V. and Pisani, M. A. (2016) 'Remarks on bond of GFRP rebars and concrete', Composites Part B: Engineering, 93, pp. 210–220.

Fernández-Jiménez, A. and Palomo, A. (2003) 'Characterisation of fly ashes. Potential reactivity as alkaline cements', Fuel, 82(18), pp. 2259–2265.

Fernández-Jiménez, A. and Palomo, A. (2006) 'Engineering properties of alkali-activated fly', ACI Materials Journal, 103(2), pp. 106–112.

Focacci, F., Nanni, A. and Bakis, C. E. (2000) 'Local bond-slip relationship for FRP reinforcement in concrete', Journal of Composites for Construction, (February), pp. 24–31.

Ganesan, N., Abraham, R., Deepa Raj, S. and Sasi, D. (2014) 'Stress-strain behaviour of confined Geopolymer concrete', Construction and Building Materials, 73, pp. 326–331, ISBN:

References

0471253928.

Ganesan, N. and Indira, P. V (2014) 'Bond behaviour of reinforcing bars embedded in steel fibre reinforced geopolymer concrete', Magazine of Concrete Research, 67(1994), pp. 1–8, ISBN: 0024-9831r1751-763X.

Golla, S. K. and Prasanthi, P. (2016) 'Prediction of Micromechanical Behavior of Fiber (Glass/Basalt) Reinforced Polymer Composites', International Research Journal of Engineering and Technology (IRJET), 03(07).

Gooranorimi, O., Suaris, W. and Nanni, A. (2017) 'A model for the bond-slip of a GFRP bar in concrete', Engineering Structures, 146, pp. 34–42.

Habert, G., d'Espinose de Lacaillerie, J. B. and Roussel, N. (2011) 'An environmental evaluation of geopolymer based concrete production: reviewing current research trends', Journal of Cleaner Production, 19(11), pp. 1229–1238.

Hadi, M. N. S., Ahmad, J. and Yu, T. (2020) 'Investigation of BFRP bar reinforced geopolymer concrete filled BFRP tube columns', Proceedings of the Institution of Civil Engineers - Structures and Buildings, pp. 1–16.

Hamad, B. S. (1995) 'Bond strength improvement of reinforcing bars with specially designed rib geometries', ACI Structural Journal, 92(1), pp. 3–13.

Hao, Q., Wang, Y., He, Z. and Ou, J. (2009) 'Bond strength of glass fiber reinforced polymer ribbed rebars in normal strength concrete', Construction and Building Materials, 23(2), pp. 865–871.

Hardjito, D. and Rangan, B. V. (2005) 'Development and properties of low-calcium fly ash-based geopolymer concrete', Research Report GC1 Faculty of Engineering Curtin University of Technology.

Hardjito, D., Wallah, S. E., Sumajouw, D. M. J. and Rangan, B. V (2005) 'Introducing Fly Ash-Based Geopolymer Concrete: Manufacture and Engineering Properties', 30 th Conference on OUR WORLD IN CONCRETE & STRUCTURES, (January), pp. 23–24.

Hassan, A., Arif, M. and Shariq, M. (2020) 'A review of properties and behaviour of reinforced geopolymer concrete structural elements- A clean technology option for sustainable development', Journal of Cleaner Production, 245, p. 118762.

Hassan, M., Benmokrane, B., ElSafty, A. and Fam, A. (2016) 'Bond durability of basalt-fiber-

References

reinforced-polymer (BFRP) bars embedded in concrete in aggressive environments', Composites Part B: Engineering, 106, pp. 262–272.

Henault, J., Quiertant, M., Delepine-lesoille, S., Salin, J., Moreau, G., Taillade, F. and Benzarti, K. (2012) 'Quantitative strain measurement and crack detection in RC structures using a truly distributed fiber optic sensing system', Construction and Building Materials, 37, pp. 916–923.

Henriques, J., Simões, L. and Valente, I. B. (2013) 'Numerical modeling of composite beam to reinforced concrete wall joints Part I : Calibration of joint components', Engineering Structures, 52, pp. 747–761.

Hillerborg, A., Modeer, M. and Petersson, P. E. (1976) 'Analysis of crack formation and crack growth in concrete by means of fracture mechanics and finite elements', Cement and Concrete Research, 6, pp. 773–782.

Hossain, K. M. A., Ametrano, D. and Lachemi, M. (2017) 'Bond strength of GFRP bars in ultra-high strength concrete using RILEM beam tests', Journal of Building Engineering, 10(February), pp. 69–79.

Iervolino, I. and Galasso, C. (2012) 'Comparative assessment of load-resistance factor design of FRP-reinforced cross sections', Construction and Building Materials, 34, pp. 151–161, ISBN: 0817683488.

INFOMINE Research Group (2007) Basalt Fiber-Based Thermal Insulating Materials Market Research in Russia.

Inman, M., Thorhallsson, E. R. and Azrague, K. (2017) 'A mechanical and environmental assessment and comparison of basalt fibre reinforced polymer (BFRP) rebar and steel rebar in concrete beams', Energy Procedia, 111, pp. 31–40.

Janardhanan, T., Thaarrini, J., Dhivya, & S. and Dhivya, S. (2016) 'Comparative study on the production cost of geopolymer and conventional concretes', International Journal of Civil Engineering Research, 7(2), pp. 117–124.

Jang, J. G., Lee, N. K. and Lee, H. K. (2014) 'Fresh and hardened properties of alkali-activated fly ash/slag pastes with superplasticizers', Construction and Building Materials, 50, pp. 169–176.

Jankowiak, T. and Lodygowski, T. (2005) 'Identification of parameters of concrete damage plasticity constitutive model', Foundations of civil and environmental engineering, (6), pp. 53–69, ISBN: 1642-9303.

References

JSCE (1997) 'Recommendations for design and construction of concrete structures using continuous fiber reinforcing materials. Concrete Engineering Series, 23, Tokyo, Japan: Research Committee on Continuous Fiber Reinforcing Materials; 1997.', Japanese Society of Civil Engineers.

Karlsson, M. (1997) Bond between C-Bar FRP reinforcement and concrete, Graduation thesis, Chalmers University of Technology, Goteborg, Sweden.

Kim, J. S. and Park, J. H. (2015) 'An experimental investigation of bond properties of reinforcement in geopolymer concrete', pp. 96–99.

Krishnaraja, A. R., Sathishkumar, N. P., Kumar, T. S. and Kumar, P. D. (2014) 'Mechanical behaviour of geopolymer concrete under ambient curing', International Journal of Scientific Engineering and Technology, 3(2), pp. 130–132.

Lee, B. and Mulheron, M. (2012) 'Fluctuation of bond stress-slip behaviour of deformed bar under displacement control', Magazine of Concrete Research, 64(10), pp. 863–875.

Lee, B. and Mulheron, M. (2015) 'Measurement of bar strain during pull-out tests: Use of electrical resistance gauge methods under large displacement', Magazine of Concrete Research, 67(10), pp. 523–531.

Lee, J. J., Song, J. and Kim, H. (2014) 'Chemical stability of basalt fiber in alkaline solution', Fibers and Polymers, 15(11), pp. 2329–2334.

Lee, N. K. and Lee, H. K. (2013) 'Setting and mechanical properties of alkali-activated fly ash/slag concrete manufactured at room temperature', Construction and Building Materials, 47, pp. 1201–1209.

Lee, W. K. W. and Van Deventer, J. S. J. (2004) 'The interface between natural siliceous aggregates and geopolymers', 34, pp. 195–206.

Li, C., Gao, D., Wang, Y. and Tang, J. (2017) 'Effect of high temperature on the bond performance between basalt fibre reinforced polymer (BFRP) bars and concrete', Construction and Building Materials, 141, pp. 44–51.

Li, D., Xu, Z., Luo, Z., Pan, Z. and Cheng, L. (2002) 'The activation and hydration of glassy cementitious materials', Cement and Concrete Research, 32, pp. 1145–1152.

Li, G., Wu, J. and Ge, W. (2015) 'Effect of loading rate and chemical corrosion on the mechanical properties of large diameter glass/basalt-glass FRP bars', Construction and

References

Building Materials, 93, pp. 1059–1066.

Li, N., Shi, C., Zhang, Z., Wang, H. and Liu, Y. (2019) 'A review on mixture design methods for geopolymer concrete', Composites Part B: Engineering, 178(April), p. 107490.

Ling, Y., Wang, K., Li, W., Shi, G. and Lu, P. (2019) 'Effect of slag on the mechanical properties and bond strength of fly ash-based engineered geopolymer composites', Composites Part B: Engineering, 164(July 2018), pp. 747–757.

Liu, H., Yang, J. and Wang, X. (2017) 'Bond behavior between BFRP bar and recycled aggregate concrete reinforced with basalt fiber', Construction and Building Materials, 135, pp. 477–483.

Liu, X., Wang, X., Xie, K., Wu, Z. and Li, F. (2020) 'Bond Behavior of Basalt Fiber-Reinforced Polymer Bars Embedded in Concrete Under Mono-tensile and Cyclic Loads', International Journal of Concrete Structures and Materials, 14(1).

Lopresto, V., Leone, C. and De Iorio, I. (2011) 'Mechanical characterisation of basalt fibre reinforced plastic', Composites Part B: Engineering, 42, pp. 717–723, ISBN: 1359-8368.

Lu, Z. H., Wu, S. Y., Tang, Z., Zhao, Y. G. and Li, W. (2021) 'Effect of chloride-induced corrosion on the bond behaviors between steel strands and concrete', Materials and Structures/Materiaux et Constructions, 54(3), pp. 1–16, ISBN: 0123456789.

Malek, A., Scott, A., Pampanin, S. and Hoult, N. A. (2019) 'Postyield Bond Deterioration and Damage Assessment of RC Beams Using Distributed Fiber-Optic Strain Sensing System', Journal of Structural Engineering, 145(4), pp. 1–17.

Malvar, L. J. (1994) 'Bond stress-slip characteristics of FRP rebars', TR-2013-SHR Naval Facilities Engineering Service Center, Port Hueneme, CA.

Mander, J. b., Priestley, M. J. N. and Park, R. (1988) 'Theoretical Stress-Strain Model for Confined Concrete', Journal of Structural Engineering, 114(8).

Mara, V., Haghani, R. and Harryson, P. (2014) 'Bridge decks of fibre reinforced polymer (FRP): A sustainable solution', Construction and Building Materials, 50, pp. 190–199.

Maranan, G. B., Manalo, A. C., Karunasena, W. and Benmokrane, B. (2014) 'Bond-slip behaviour of GFRP bars into geopolymer concrete', The 7th International Conference on FRP composites in Civil Engineering.

Maranan, G. B., Manalo, A. C., Karunasena, W. and Benmokrane, B. (2015a) 'Bond stress-

References

slip behaviour: the case of GFRP bars in geopolymer concrete', Journal of Materials in Civil Engineering, 27.

Maranan, G. B., Manalo, A. C., Karunasena, W. and Benmokrane, B. (2015b) 'Pullout behaviour of GFRP bars with anchor head in geopolymer concrete', Composite Structures, 132(November), pp. 1113–1121.

Marchand, P., Baby, F., Khadour, A., Battesti, T., Rivillon, P., Quiertant, M., Nguyen, H.-H., Généreux, G., Deveaud, J.-P., Simon, A. and Toutlemonde, F. (2016) 'Bond behaviour of reinforcing bars in UHPFRC', Materials and Structures, 49(5), pp. 1979–1995.

Mazaheripour, H., Barros, J. A. O., Sena-Cruz, J., Pepe, M. and Martinelli, E. (2013a) 'Experimental study on bond performance of GFRP bars in self-compacting steel fiber reinforced concrete', Composite Structures, 95, pp. 202–212.

Mazaheripour, H., Barros, J. A. O., Sena-Cruz, J. and Soltanzadeh, F. (2013b) 'Analytical Bond Model for GFRP Bars to Steel Fiber Reinforced Self-Compacting Concrete', Journal of Composites for Construction, 17(6).

Michaud, D. and Fam, A. (2021) 'Development Length of Small-Diameter Basalt FRP Bars in Normal- and High-Strength Concrete', Journal of Composites for Construction, 25(1), p. 04020086, ISBN: 0000000183.

Militky, J. and Kovacic, V. (1996) 'Ultimate Mechanical Properties of Basalt Filaments', Textile Research Journal, 66(4), pp. 225–229.

Mohamed, O. A., Al Hawat, W. and Keshawarz, M. (2021) 'Durability and Mechanical Properties of Concrete Reinforced with Basalt Fiber-Reinforced Polymer (BFRP) Bars: Towards Sustainable Infrastructure', Polymers, 13(1402).

Mostafa, N. Y., El-Hemaly, S. A. S., Al-Wakeel, E. I., El-Korashy, S. A. and Brown, P. W. (2001) 'Characterization and evaluation of the hydraulic activity of water-cooled slag and air-cooled slag', Cement and Concrete Research, 31(6), pp. 899–904, ISBN: 1814865535.

Naderi, S., Tu, W. and Zhang, M. (2021) 'Meso-scale modelling of compressive fracture in concrete with irregularly shaped aggregates', Cement and Concrete Research, 140(November).

Nanni, A., Al-Zahrani, M. M., Al-Dulaijan, S. U., Bakis, C. E. and Boothby, T. E. . (1995) 'Bond of FRP reinforcement to concrete - experimental results', in Second International Symposium on Non-Metallic (FRP) Reinforcement for Concrete Structures, pp. 135 – 145.

References

Nath, P. and Sarker, P. (2012) 'Geopolymer concrete for ambient curing condition', Australasian Structural Engineering Conference 2012: The past, present and future of Structural Engineering, (January), pp. 1–9.

Nath, P. and Sarker, P. K. (2014) 'Effect of GGBFS on setting, workability and early strength properties of fly ash geopolymer concrete cured in ambient condition', Construction and Building Materials, 66, pp. 163–171.

Nuruddin, M. F., Malkawi, A. B., Fauzi, A., Mohammed, B. S. and Almattarneh, H. M. (2016) 'Geopolymer concrete for structural use: Recent findings and limitations', IOP Conference Series: Materials Science and Engineering, 133(1).

Okelo, R. and Yuan, R. L. (2005) 'Bond Strength of Fiber Reinforced Polymer Rebars in Normal Strength Concrete', Journal of Composites for Construction, 9(3), pp. 203–213, ISBN: 1090-0268.

Olivier, J. G. J., Janssens-Maenhout, G., Muntean, M. and Peters, J. A. H. W. (2016) 'Trends in global CO2 emissions 2016 report', ISBN: 9789491506512.

Ovitigala, T. (2012) 'Structural Behavior of Concrete Beams Reinforced with Basalt Fiber Reinforced Polymer (BFRP) Bars', Ph.D. Thesis University of Illinois, Chicago.

Oyebisi, S., Ede, A., Olutoge, F., Ofuyatan, O. and Alayande, T. (2019) 'Building a sustainable world: Economy index of geopolymer concrete', ISEC 2019 - 10th International Structural Engineering and Construction Conference, (June), ISBN: 9780996043762.

Palacios, M., Banfill, P. and Puertas, F. (2008) 'Rheology and setting of alkali-activated slag pastes and mortars: Effect of organ admixture', ACI Materials Journal, 105, pp. 140–148.

Patnaik, A., Banibayat, P., Adhikari, S. and Robinson, P. (2012) 'Mechanical Properties of Basalt Fiber Reinforced Polymer Bars Manufactured Using a Wet Layup Method', International Review of Civil Engineering (I.RE.C.E.), 3(5 (September)), pp. 412–417.

Pearson, M. C., Donchev, T. and Limbachiya, M. (2011) 'An Investigation Into the Sustainability of FRP Reinforcement Bars', in Conference: CDCC2011 - Durability and Sustainability of Fibre Reinforced Polymer (FRP) Composites for Construction and Rehabilitation.

Pecce, M., Manfredi, G., Realfonzo, R. and Cosenza, E. (2001) 'Experimental and analytical evaluation of bond properties of GFRP bars', Journal of Materials in Civil Engineering, (July/August), pp. 282–290, ISBN: 2840601710.

References

Pham, D. Q., Nguyen, T. N., Le, S. T., Pham, T. T. and Ngo, T. D. (2021) 'The structural behaviours of steel reinforced geopolymer concrete beams: An experimental and numerical investigation', Structures, 33(May), pp. 567–580.

Popovics, S. (1973) 'A numerical approach to the complete stress-strain curve of concrete', Cement and Concrete Research, pp. 583–599.

Provis, J. L. and Bernal, S. A. (2014) 'Geopolymers and related alkali-activated materials', Annual Review of Materials Research, 44, pp. 299–327.

Puertas, F., Martinez-Ramirez, S., Alonso, S. and Vazquez, T. (2000) 'Alkali-activated fly ash/slag cements. Strength behaviour and hydration products', Cement and Concrete Research, 30, pp. 1625–1632.

Rahman, M. M. and Sarker, P. K. (2013) 'Geopolymer concrete columns subjected under combined axial load and biaxial bending', (September).

Rangan, B. V., Hardjito, D., Wallah, S. E. and Sumajouw, D. M. J. (2005) 'Studies on fly ash-based geopolymer concrete', in Proceedings of the world congress geopolymer, Saint Quentin, France, pp. 133–137.

Rao, G. A. (2014) 'Parameters influencing bond strength of rebars in reinforced concrete', International Journal of Applied Engineering and Technology, 4(1), pp. 72–81.

Raoul, F., Laurens, S. and Deby, F. (2018) Corrosion and its consequences for reinforced concrete structures, ISTE Press - Elsevier, ISBN: 9781785482342.

Rashad, A. M. (2013) 'A comprehensive overview about the influence of different additives on the properties of alkali-activated slag - A guide for Civil Engineer', Construction and Building Materials, 47, pp. 29–55.

Rashad, A. M. (2018) 'An overview on rheology, mechanical properties and durability of high-volume slag used as a cement replacement in paste, mortar and concrete', Construction and Building Materials, pp. 89–117.

El Refai, A., Abed, F. and Altalmas, A. (2015a) 'Bond durability of basalt fiber–reinforced polymer bars embedded in concrete under direct pullout conditions', Journal of Composites for Construction, 19(5), p. 04014078.

El Refai, A., Ammar, M.-A. and Masmoudi, R. (2015b) 'Bond performance of basalt fiber-reinforced polymer bars to concrete', Journal of Composites for Construction, 19(3).

References

Rezazadeh, M., Carvelli, V. and Veljkovic, A. (2017) 'Modelling bond of GFRP rebar and concrete', Construction and Building Materials, 153, pp. 102–116.

RILEM TC (1994) 'RC 6 Bond test for reinforcement steel. 2. Pull-out test, 1983', in RILEM Recommendations for the Testing and Use of Constructions Materials, pp. 218–220, ISBN: 2351580117.

Rolland, A., Argoul, P., Benzarti, K., Quiertant, M., Chataigner, S. and Khadour, A. (2020) 'Analytical and numerical modeling of the bond behavior between FRP reinforcing bars and concrete', Construction and Building Materials, 231.

Rolland, A., Quiertant, M., Khadour, A., Chataigner, S., Benzarti, K. and Argoul, P. (2018) 'Experimental investigations on the bond behavior between concrete and FRP reinforcing bars', Construction and Building Materials, 173, pp. 136–148.

Russo, G., Zingone, G. and Romano, F. (1990) 'Analytical solution for bond-slip of reinforcing bars in R. C. joints', Journal of Structural Engineering, 116(2), pp. 336–355.

Saleh, N., Ashour, A., Lam, D. and Sheehan, T. (2019) 'Experimental investigation of bond behaviour of two common GFRP bar types in high-strength concrete', Construction and Building Materials, 201, pp. 610–622.

Saleh, N. M. (2018) 'Bond of glass fibre reinforced polymer bars in high strength concrete', Ph.D. Thesis, Faculty of Informatics, University of Bradford, UK.

Sarker, P. K. (2010) 'Bond strengths of geopolymer and cement concretes', 69, pp. 143–151.

Sarker, P. K. (2011) 'Bond strength of reinforcing steel embedded in fly ash-based geopolymer concrete', Materials and Structures, 44(5), pp. 1021–1030, ISBN: 1152701096.

Serbescu, A., Guadagnini, M. and Pilakoutas, K. (2014) 'Mechanical characterization of basalt FRP rebars and long-term strength predictive model', Journal of Composites for Construction, 19(2), ISBN: 8415683111.

Shen, D., Ojha, B., Shi, X., Zhang, H. and Shen, J. (2015) 'Bond stress-slip relationship between basalt fiber-reinforced polymer bars and concrete using a pull-out test', Journal of Reinforced Plastics and Composites, 35(9), pp. 747–763, ISBN: 0731-6844.

Shi, C., Jiménez, A. F. and Palomo, A. (2011) 'New cements for the 21st century: The pursuit of an alternative to Portland cement', Cement and Concrete Research, 41(7), pp. 750–763.

Shi, C. and Xie, P. (1998) 'Interface between cement paste and quartz sand in alkali-activated

References

slag mortars', Cement and Concrete Research, 28(6), pp. 887–896.

Smarter Building System (2017) 'Smarter building basalt FAQs'. Newport, Rhode Island, p. Newport, Rhode Island.

Sofi, M., Van Deventer, J. S. J., Mendis, P. A. and Lukey, G. C. (2007a) 'Bond performance of reinforcing bars in inorganic polymer concrete (IPC)', Journal of Materials Science, 42, pp. 3107–3116.

Sofi, M., Van Deventer, J. S. J., Mendis, P. A. and Lukey, G. C. (2007b) 'Engineering properties of inorganic polymer concretes (IPCs)', Cement and Concrete Research, 37(2), pp. 251–257.

Solyom, S. and Balázs, G. L. (2020) 'Bond of FRP bars with different surface characteristics', Construction and Building Materials, 264.

Sooriyaarachchi, H. (2006) 'Tension Stiffening Effect in GFRP Reinforced Concrete Elements', Ph.D. Thesis, University of Sheffield, UK, ISBN: 978-1-4020-5103-6 978-1-4020-5104-3.

Sturm, A. B. and Visintin, P. (2019) 'Local bond slip behavior of steel reinforcing bars embedded in ultra high performance fibre reinforced concrete', Structural Concrete, 20, pp. 108–122.

Sumajouw, D. M. J., Hardjito, D., Wallah, S. and Rangan, B. V. (2005a) 'Behaviour and strength of reinforced fly ash-based geopolymer concrete beams', Geopolymer.

Sumajouw, D. M. J., Hardjito, D., Wallah, S. and Rangan, B. V (2005b) 'Behavior of geopolymer concrete columns under equal load eccentricities', American Concrete Institute's Seventh International Symposium on Utilization of High-Strength/High-Performance Concrete.

Talha Junaid, M., Kayali, O., Khennane, A. and Black, J. (2015) 'A mix design procedure for low calcium alkali activated fly ash-based concretes', Construction and Building Materials, 79, pp. 301–310.

Tekle, B. H. (2017) Bond behaviour of GFRP bars embedded in alkali activated cement concrete, PhD Thesis, School of Engineering and Information Technology, The University of New South Wales.

Tekle, B. H. and Khennane, A. (2016) 'Comparison of Bond Properties of Steel and Sand-Coated GFRP Bars in Fly Ash-', Eighth International Conference on Fibre-Reinforced Polymer

References

(FRP) Composites in Civil Engineering, (14-16 December 2016).

Tekle, B. H., Khennane, A. and Kayali, O. (2016) 'Bond properties of sand-coated GFRP bars with fly ash-based geopolymer concrete', Journal of Composites for Construction, 20(5).

Tekle, B. H., Khennane, A. and Kayali, O. (2017) 'Bond of spliced GFRP reinforcement bars in alkali activated cement concrete', Construction and Building Materials, 154, pp. 972–982.

Tepfers, R. (1973) 'A Theory of Bond Applied to Overlapped Tensile Reinforcement Splices for Deformed Bars', Ph.D. Thesis, Chalmers University of Technology, pp. 1–330, ISBN: 99-0082857-7.

Tepfers, R. and Karlsson, M. . (1997) 'Pull-out and tensile reinforcement splice tests using FRP C-Bars', in Third International Symposium on Non-Metallic (FRP) Reinforcement for Concrete Structures, pp. 357–364.

Tepfers, T. (1979) 'Cracking of concrete cover along anchored deformed reinforcing bars', Magazine of Concrete Research, 31(106).

The MathWorks (2018) 'MATLAB and Statistics Toolbox Release, Inc., Natick, Massachusetts, United States'.

Thomas, R. J. and Peethamparan, S. (2015) 'Alkali-activated concrete: Engineering properties and stress-strain behavior', Construction and Building Materials, 93, pp. 49–56.

Tighiouart, B., Benmokrane, B. and Gao, D. (1998) 'Investigation of bond in concrete member with fibre reinforced polymer (FRP) bars', Construction and Building Materials, 12(8), pp. 453–462, ISBN: 0950-0618.

Topark-Ngarm, P., Chindaprasirt, P. and Sata, V. (2014) 'Setting time, strength, and bond of high-calcium fly ash geopolymer concrete', The Journal of Materials in Civil Engineering, 27(2011), pp. 1–7.

Turner, L. K. and Collins, F. G. (2013) 'Carbon dioxide equivalent (CO2-e) emissions: A comparison between geopolymer and OPC cement concrete', Construction and Building Materials, 43, pp. 125–130.

Veljkovic, A., Carvelli, V., Michal, M. and Pahn, M. (2017) 'Concrete cover effect on the bond of GFRP bar and concrete under static loading', Composites Part B, 124, pp. 40–53.

Vilanova, I., Torres, L., Baena, M. and Llorens, M. (2016) 'Numerical simulation of bond-slip interface and tension stiffening in GFRP RC tensile elements', Composite Structures, 153, pp.

References

504–513.

Wang, H., Sun, X., Peng, G., Luo, Y. and Ying, Q. (2015) 'Experimental study on bond behaviour between BFRP bar and engineered cementitious composite', Construction and Building Materials, 95, pp. 448–456, ISBN: 09500618.

Wang, L., Song, Z., Yi, J., Li, J., Fu, F. and Qian, K. (2019) 'Experimental Studies on Bond Performance of BFRP Bars Reinforced Coral Aggregate Concrete', International Journal of Concrete Structures and Materials, 13:52.

Wang, P. Z., Trettin, R. and Rudert, V. (2005) 'Effect of fineness and particle size distribution of granulated blast-furnace slag on the hydraulic reactivity in cement systems', Advances in Cement Research, 17(4), pp. 161–166.

Wei, W., Liu, F., Xiong, Z., Yang, F., Li, L. and Luo, H. (2020) 'Effect of loading rates on bond behaviour between basalt fibre- reinforced polymer bars and concrete', Construction and Building Materials, 231, p. 117138.

Winnefeld, F., Haha, M. Ben, Le Saout, G., Costoya, M., Ko, S. C. and Lothenbach, B. (2014) 'Influence of slag composition on the hydration of alkali-activated slags', Journal of Sustainable Cement-Based Materials, 4(2), pp. 85–100.

Wu, G., Dong, Z.-Q., Wang, X., Zhu, Y. and Wu, Z.-S. (2015a) 'Prediction of Long-Term Performance and Durability of BFRP Bars under the Combined Effect of Sustained Load and Corrosive Solutions', Journal of Composites for Construction, 19(3), p. 04014058.

Wu, G., Wang, X., Wu, Z., Dong, Z. and Xie, Q. (2015b) 'Degradation of basalt FRP bars in alkaline environment', Science and Engineering of Composite Materials, 22(6), pp. 649–657.

Wu, Z., Wang, X. and Wu, G. (2012) 'Advancement of structural safety and sustainability with basalt fiber reinforced polymers', Proceedings of the 6th International Conference on FRP Composites in Civil Engineering, CICE 2012, (June), pp. 13–15.

Yan, F. and Lin, Z. (2016) 'Bond behavior of GFRP bar-concrete interface: Damage evolution assessment and FE simulation implementations', Composite Structures, 155, pp. 63–76.

Yan, F., Lin, Z. and Yang, M. (2016) 'Bond mechanism and bond strength of GFRP bars to concrete: A review', Composites Part B: Engineering, 98, pp. 56–69.

Yang, S., Yang, C., Huang, M., Liu, Y., Jiang, J. and Fan, G. (2018) 'Study on bond performance between FRP bars and seawater coral aggregate concrete', Construction and

References

Building Materials, 173, pp. 272–288.

Yankelevsky, D. Z. (1985) 'Analytical model for bond-slip behavior under monotonic loading', Building and Environment, 20(3), pp. 163–168.

Yuan, H., Teng, J. G., Seracino, R., Wu, Z. S. and Yao, J. (2004) 'Full-range behavior of FRP-to-concrete bonded joints', 26, pp. 553–565.

Zanuy, C., Curbach, M. and Lindorf, A. (2013) 'Finite element study of bond strength between concrete and reinforcement under uneven confinement condition', Structural Concrete, 14(3), pp. 260–270.

Ziari, A. and Kianoush, M. R. (2014) 'Finite-Element Parametric Study of Bond and Splitting Stresses in Reinforced Concrete Tie Members', American Society of Civil Engineers, 140(5).